RAPID PATH-PLANNING ALGORITHMS FOR AUTONOMOUS PROXIMITY OPERATIONS OF SATELLITES

By

JOSUE DAVID MUÑOZ

A DISSERTATION PRESENTED TO THE GRADUATE SCHOOL
OF THE UNIVERSITY OF FLORIDA IN PARTIAL FULFILLMENT
OF THE REQUIREMENTS FOR THE DEGREE OF
DOCTOR OF PHILOSOPHY

UNIVERSITY OF FLORIDA

2011

To my dear mother and father

ACKNOWLEDGMENTS

I would first like to thank my advisor Dr. Norman G. Fitz-Coy, who I have had the honor of working with since my undergraduate career (and now seems so long ago). He has continually challenged me throughout the years and has also served as a role-model on many accounts. His passion for teaching and research has motivated me to pursue this degree, and his conscientious demeanor has made it a worthwhile experience.

I would like to express my thanks to my supervisory committee, Dr. Warren E. Dixon, Dr. Anil V. Rao, and Dr. Thomas F. Burks, who are some of the most brilliant minds I have had the pleasure of meeting. The knowledge they have instilled on me was pivotal for completing this work, and for that I am grateful.

I would also like to thank the agencies that have provided me with research and/or financial support throughout the years. Particularly, the University of Florida, the Defense Advanced Research Agency Projects, the South East Alliance for Graduate Education of the Professoriate Fellowship, the Lockheed Martin Corporation, the Air Force Research Lab/Space Vehicles Directorate, and the Science, Mathematics, and Research Transformation Scholarship.

Finally, I would like to thank my family, friends, and colleagues who have provided me with morale and/or research support throughout the years. Particularly, my brothers and sisters who have educated me in many ways, whether they realize it or not. Thanks go out to Shawn Johnson, who I met during my first week of college. Without his help, I would not have the study habits that allowed me to get this far in my career. Thanks to Ernesto del Castillo, who was always there to lift my spirits when I felt discouraged. Thanks to Dr. Nick Martinson, who I was able to brainstorm with and was always available to discuss research ideas. Thanks to Dr. Fred Leve, who always provided a different perspective, and our conversations always provoked new and interesting research ideas. Thanks to Dr. George Boyarko, who was always able to put things into

perspective, and helped bring a lot of my research together. And thanks to my friends and colleagues Shawn Allgeier, Sharanabasaweshwara Asundi, Dante Buckley, Katie Cason, Takashi Hiramatsu, Tzu-Yu Lin, Vivek Nagabhushan, Kunal Patankar, and Bungo Shiotani for the many long hours spent working together on our research and academic endeavors.

TABLE OF CONTENTS

LIST OF TABLES

LIST OF FIGURES

LIST OF ABBREVIATIONS

AAPF	Adaptive artificial potential function
ACL	Autonomous control level
ANGELS	Autonomous Nanosatellite Guardian for Evaluating Local Space
APF	Artificial potential function
APO	Autonomous proximity operation
CDM	Cell decomposition method
CM	Center of mass
CWH	Clohessy-Wiltshire-Hill
DART	Demonstration of Autonomous Rendezvous Technology
DOF	Degrees-of-freedom
DRE	Differential Riccati equation
ETS	Engineering Test Satellite
FREND	Front-end Robotic Enabling Near-term Demonstration
G&C	Guidance and control
GAS	Globally asymptotically stable
HC	Homotopy continuation
HTV	H-II transfer vehicle
ISS	International Space Station
KKT	Karush-Kuhn-Tucker
LCF	Lyapunov candidate function
LEO	Low Earth orbit

LQ	Linear quadratic
LTI	Linear time invariant
LTV	Linear time varying
MCS	Monte Carlo simulation
MSE	Maclaurin series expansion
NLP	Nonlinear program
OCM	Orthogonal collocation method
OCP	Optimal control problem
OEDS	Orbital Express Demonstration System
PI	Picard iteration
PID	Proportional-integral-derivative
PVT	Primer vector theory
SAA	Small angle approximation
SSA	Space situational awareness
STM	State transition matrix
SUMO	Satellite for the Universal Modification of Orbits
TPBVP	Two point boundary value problem
TSE	Taylor series expansion
UAV	Unmanned aerial vehicle
XSS	Experimental Satellite System
YATH	Yamanaka-Ankerson-Tschauner-Hempel

Abstract of Dissertation Presented to the Graduate School
of the University of Florida in Partial Fulfillment of the
Requirements for the Degree of Doctor of Philosophy

RAPID PATH-PLANNING ALGORITHMS FOR AUTONOMOUS PROXIMITY OPERATIONS OF SATELLITES

By

Josue David Muñoz

August 2011

Chair: Norman G. Fitz-Coy
Major: Aerospace Engineering

Autonomous proximity operations (APOs) can be bifurcated into two phases: (i) close-range rendezvous and (ii) final approach or endgame. For each APO phase, algorithms capable of real-time path planning provide the greatest ability to react to "unmodeled" events, thus enabling the highest level of autonomy. This manuscript explores methodologies for real-time computation of APO trajectories for both APO phases.

For the close-range rendezvous trajectories, an Adaptive Artificial Potential Function (AAPF) methodology is developed. The AAPF method is a modification of the Artificial Potential Function (APF) methodology which has favorable convergence characteristics. Building on these characteristics, the modification involves embedding the system dynamics and a performance criterion into the APF formulation resulting in a tunable system. Near-minimum time and/or near-minimum fuel trajectories are obtained by selecting the tuning parameter. Monte Carlo simulations are performed to assess the performance of the AAPF methodology.

For the final approach or endgame trajectories, two methodologies are considered: a Picard Iteration (PI) and a Homotopy Continuation (HC). Problems in this APO phase are typically solved as a finite horizon linear quadratic (LQ) problem, which essentially are solved as a final value problem with a Differential Riccati Equation (DRE). The PI and HC methods are well known tools for solving differential equations and are

utilized in this effort to provide solutions to the DRE which are amenable to real-time implementations; i.e., they provide solutions which are functionals to be evaluated real-time. Several cases are considered and compared to the classical DRE solution.

CHAPTER 1
INTRODUCTION

The paradigm of space technology is transitioning to enable autonomous on-orbit operations. [1, 2] One sign of this transition is the imminent retirement of the Space Shuttle. The Space Shuttle has carried many satellites and astronauts into space, which resulted in unprecedented missions and technological advancements. The Space Shuttle has also provided logistics to valuable space assets which would otherwise have been decommissioned. [3] The retirement of the Space Shuttle is a result of many years of high operation and maintenance costs. Autonomous spacecraft present an alternative for performing proximity operations that were previously done manually. [4] This would also allow manned space flight missions to focus on other space science missions rather than mundane resupply missions.

Another example of the transition in space technology is the rapidly increasing number of objects and debris in orbit. As space technology continues to mature, it is becoming easier to develop and launch space systems into orbit. In addition, collisions such as the Chinese ASAT test in 2007, the USA 193 intercept in 2008, and the Iridium 33/Cosmos 2251 collision in 2009 contribute greatly to orbital debris that could potentially be harmful to neighboring space assets. [5, 6] Currently, collisions are avoided by planning a series of maneuvers from a ground station and uplinking the commands. However, as the number of objects in orbit increases, it is becoming increasingly difficult to keep track of all objects and to solve for collision avoidance maneuvers with multiple constraints in a timely manner. The Iridium 33/Cosmos 2251 collision is a prime example of this, where the Iridium 33 satellite was a functional satellite, yet a collision was not avoided. This example shows why space situational awareness (SSA) is becoming critical to protect valuable space assets and to perform successful collision avoidance maneuvers. To supplement the SSA capabilities from

ground stations, satellites capable of performing autonomous proximity operations (APOs) can be used to accurately track objects in space or remove orbital debris. [7]

The responsive space initiative and small satellite technology also require the need for autonomy. One of the requirements of responsive space systems is autonomy such that they spacecraft is able to change its orbit or perform orbital stationkeeping onboard. [8, 9]. Likewise, small satellites or groups of fractionated small satellites can supplement or replace certain space assets. [10, 11] Small satellites can be used to perform APOs on other space assets as well. [12, 13]

APOs include (but are not limited to) close-range rendezvous, inspection, interception, docking, payload transfer, orbital station-keeping, formation flying, and on-orbit assembly. For the discussions in this manuscript, APOs are generalized and decomposed into two phases: (i) close-range rendezvous and (ii) final approach or endgame. Being able to accomplish APOs with the highest level of autonomy is pivotal for:

- Enabling APOs with spacecraft
- Giving heritage to technology developed for APOs
- Standardization for missions performing APOs
- Reduction in supervision needed for performing certain missions
- Increased robustness to communication constraints
- Enable servicing of spacecraft in orbit

A distinguishing feature of APOs is “autonomy”. Thus, it is necessary to define what is meant by autonomy in the context of APOs. A proposed definition for an autonomous system is a system that “*must perform well under significant uncertainties in the plant and the environment for extended periods of time and it must be able to compensate for system failures without external intervention.*” [14] This definition provides insight, yet it is too broad for the purpose of APOs. A different definition of autonomy has been proposed by the artificial intelligence, robotics, and intelligent systems community using three categorizations of model-based architectures: [15]

1. Model-based architecture: Ability to achieve prescribed objectives, all knowledge being in the form of models, as in the model-based architecture.
2. Adaptive model-based architecture: Ability to adapt to major environmental changes. This requires knowledge enabling the system to perform structure reconfiguration, i.e., it needs knowledge of structural and behavioral alternatives as can be represented in the system entity.
3. Generative model-based architecture: Ability to develop its own objectives. This requires knowledge to create new models to support the new objectives, that is a modeling methodology.

These three categories are useful for high-level analysis, yet a systematic approach of characterizing autonomy in space systems is desired. [16, 17] The approach taken by the Air Force Research Lab to characterize autonomy of Unmanned Aerial Vehicles (UAVs) uses Autonomous Control Levels (ACLs) ranging between 0-10. [18] The lowest ACL is Level 0, which corresponds to a vehicle that is remotely piloted and has no decision making capabilities. The highest ACL is Level 10 and is described as “Human-like”. The intermediate levels are defined for different ranges of abilities to “detect and track” other vehicles in close proximity and having “decision making capabilities on-board” with different amounts of “external supervision”. If a similar classification of autonomy is used for spacecraft, then being able to track objects in close proximity and rapidly plan optimized trajectories on-board (with minimal external supervision or intervention) is the level of autonomy desired for APOs.

On the other hand, performing tasks for proximity operation missions offline tends to have high operation costs. [19] Planning and scheduling offline is computationally costly and the additional communication constraints presents problems due to low-bandwidth, high-latency communication links. [20] An example of autonomous system with these capabilities is the Mars Exploration Rover which landed successfully on Mars in 2004. The latency of the communication (ranging from 8 to 42 minutes) required that a large number of tasks be planned and uplinked intermittently and executed without human monitoring or confirmation. [21] While the delays and communication constraints with a spacecraft in orbit are less severe, this example illustrates how scheduling

and planning autonomous tasks offline can be cumbersome. The communication constraints also vary depending on the orbit of the spacecraft. The spacecraft could be available for communication several times a day at best, while at other times it may not be accessible for long periods of times. Multiple ground stations can be used to alleviate the communication constraints, however, there is little freedom in strategically placing ground stations (due to monetary limits and property rights). On the other hand, increasing the level of autonomy would reduce the need for constant communication with a spacecraft.

1.1 Previous Missions

One of the first missions to attempt to demonstrate APOs was JAXA's Engineering Test Satellite VII (ETS-VII) in 1998. The ETS-VII is shown in Figure 1-1A and consists of a passive target satellite (ORIHIME) and an active satellite (HIKOBOSHI); both initially in a docked state. The main objective was to demonstrate relative approach, final approach, and docking between HIKOBOSHI and ORIHIME. The first experiment required that both spacecraft detach, fly in formation at a distance of two meters, and then demonstrate autonomous docking. [22, 23] The experience gained from this experiment would later be used on the H-II Transfer Vehicle (HTV) in 2009, which provides logistics to the International Space Station (ISS). [24] The HTV is shown in Figure 1-1B. The ETS-VII was also to demonstrate a relative approach trajectory between the two satellites, however, technical difficulties were experienced due to attitude deviations. In short, every time an orbital maneuver was executed, the thrusters would change the orientation of the chaser satellite which did not allow the chaser to track its predetermined trajectory. In order to alleviate this problem, a modification had to be made to the flight software. [23] Nevertheless, the lessons learned from the ETS-VII mission led to the success of the HTV. These two missions demonstrate how critical it is to perform an APO (particularly rendezvous and docking) with high precision and collision avoidance, especially when docking with a valued space asset like the ISS.

A Artist depiction of ETS-VII

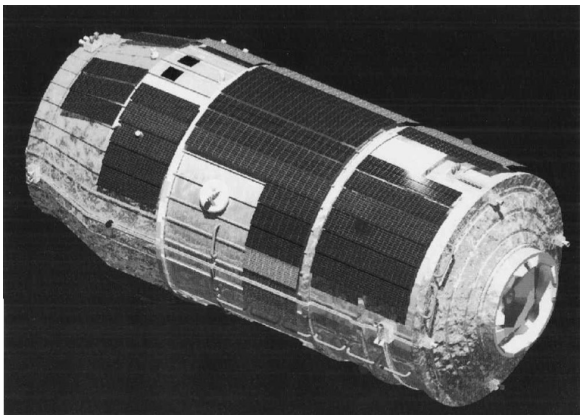

B Artist depiction of HTV

Figure 1-1. Illustration of JAXA's flight experiments

Another mission aimed at testing the ability to perform APOs was the Demonstration for Autonomous Rendezvous Technology (DART) project in 2005. [25] The main objective was to demonstrate long-range rendezvous, close-range rendezvous, and collision avoidance with the decommissioned MUBLCOM satellite which had been in orbit since 1999. [26] Both the DART spacecraft and MUBLCOM satellite are shown in Figure 1-2. The DART mission resulted in a mishap, where a "soft collision" between DART and MUBLCOM occurred after DART exhausted all of its propellant. Propellant management along with navigation and collision avoidance malfunctions caused the two spacecraft to collide, however, both spacecraft survived. [27]

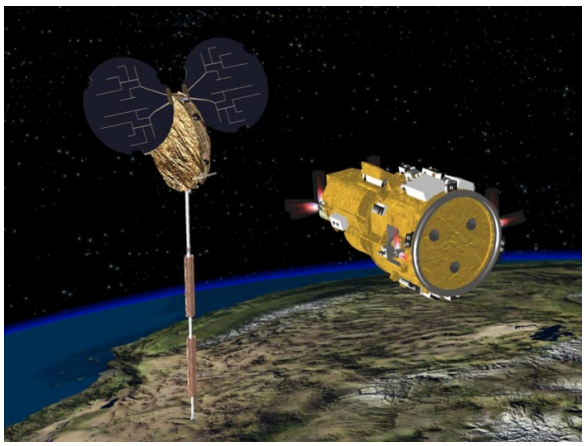

Figure 1-2. Illustration of DART mission

A concurrent mission with DART was the Experimental Satellite System-11 (XSS-11) in 2005 which followed its predecessor, the XSS-10. The XSS-11 mission was to further demonstrate capabilities for performing autonomous rendezvous and other APOs with the upper stage of its Minotaur I launch vehicle. [28, 29] Both XSS-10 and XSS-11 are depicted in Figure 1-3B and Figure 1-3A, respectively. The XSS-11 mission was successful in completing rendezvous and 75 natural motion circumnavigations. The XSS-11 spacecraft also conducted APOs with several US-owned decommissioned satellites, however, these results are not readily available in the public domain. [12, 29]

A Illustration of XSS-10

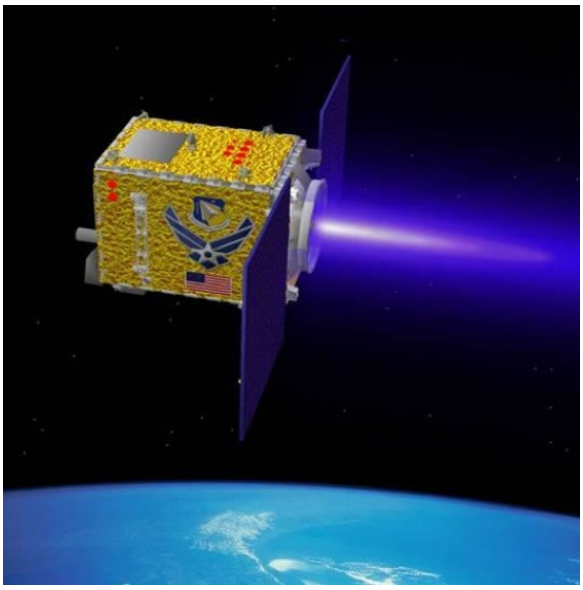

B Illustration of XSS-11

Figure 1-3. Illustration of the XSS missions

The Orbital Express Demonstration System (OEDS) mission in 2007 was successful and a landmark for APOs. This mission was able to demonstrate autonomous robotic payload transfer and reconfiguration of satellites. [30] The mission consisted of a servicing satellite (ASTRO) and a serviceable satellite (NextSat); both initially in a docked state. Both the ASTRO and NextSat satellites are shown in Figure 1-4. ASTRO was able to successfully perform APOs on NextSat including rendezvous at different ranges, capture, propellant and hardware transfer, which was a major milestone for

autonomous technology in space. However, the APOs were performed at a low level of autonomy, where several ground-based commands were required for OEDS to complete an operation. [30, 31]

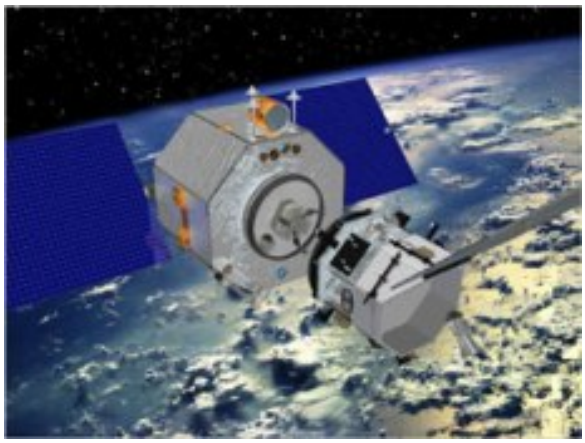

Figure 1-4. Illustration of OEDS mission

The most recent mission is the Prisma satellites, which were developed by the Swedish Space Corporation and launched on June 15, 2010. [32–34] The Prisma satellites consist of an active satellite (MANGO) and a passive satellite (TANGO); both initially in a docked state. MANGO and TANGO are shown in Figure 1-5. This mission will attempt to experimentally validate certain algorithms and hardware for APOs. The main directive is to perform a series of formation flying and rendezvous maneuvers at different ranges. The spacecraft will validate collision avoidance maneuvers when both are in proximity of each other. This mission will also give flight heritage to the smallest thrusters developed to date. [32]

There are future missions like the Satellite for the Universal Modification of Orbits/Front-end Robotic Enabling Near-term Demonstration (SUMO/FREND), the Autonomous Nanosatellite Guardian for Evaluating Local Space (ANGELS), and the most recently proposed venture, ViviSat. [35–37] SUMO/FREND is particularly interesting since details of the trajectory planning algorithms that will be used have been published in the public domain. [38] Each spacecraft will carry out specific missions for

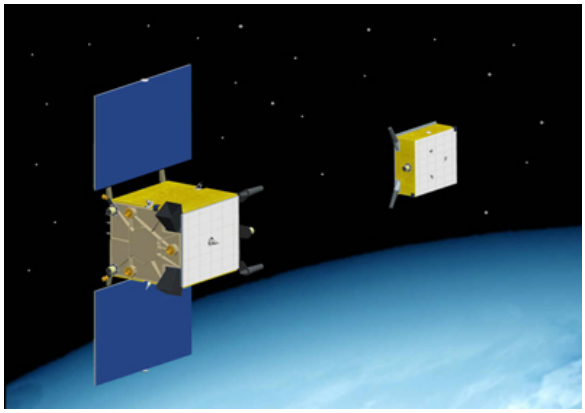

Figure 1-5. Illustration of Prisma mission

space application purposes, as opposed to testing concepts for APOs. These missions will also be milestones for determining the most appropriate APO methodologies.

1.2 State of the Art

Despite recent and future missions, the most effective path-planning methodology for APOs is still undetermined. While the methods used in the missions discussed are undisclosed, it is clear that the desired level of autonomy has not been demonstrated. To achieve this level of autonomy, there are different frameworks that have been suggested. One framework suggests developing faster microprocessors such that existing algorithms (that would normally be executed offline) would be simplified and executed on-board. Another framework suggests developing new algorithms that are capable of being executed in hardware that is readily available. While both frameworks are valid, verifying and validating either requires flight heritage.

Given the successes and/or shortcomings of the missions discussed in the previous section, the question of whether rapid path-planning algorithms need to be developed must to be investigated. While a level of autonomy has been demonstrated to be feasible for in-space operations, forthcoming demands require that certain missions have this capability of rapid path-planning for higher levels of autonomy. This is particularly true with the emergence of small satellite technology and the responsive space initiative. With both of these technical areas, success is measured from a

“cheaper, faster, and gets the job done” perspective. Since small satellite technology can be relatively “cheaper”, this would be an avenue that could be taken to ultimately determine the most effective path-planning methods for APOs.

In general, path-planning for the translational motion of spacecraft is referred to as orbital transfers. For this case, a distinction is made between maneuver planning and trajectory planning. Maneuver planning refers to a series of control actions for paths with long transfer times (on the order of the orbital period). The control actions are typically assumed to be impulsive since the engine burn time is a small fraction of the transfer time. [39, 40] In addition, the trajectory obtained is not as important as the terminal conditions of the trajectory. Trajectory planning refers to planning a series of control actions for paths with short transfer times (on the order of fractions of the orbital period). For this case, the control actions are not necessarily assumed impulsive and the trajectory obtained is relevant to the mission. Path-planning for the rotational motion of spacecraft is typically synonymous with trajectory planning since slew maneuvers have relatively short transfer times. In this manuscript, path-planning and trajectory planning are used interchangeably since the transfer times for APOs are small.

To this end, several algorithms have been used/proposed for path-planning of APOs. These algorithms are bifurcated into two groups: optimization methods and analytic methods. Optimization methods are methodologies derived from optimal control theory and historically have been studied to a greater extent. Some examples of optimization methods include Primer Vector Theory (PVT), cell decomposition methods (CDM), orthogonal collocation methods (OCM), the Inverse Dynamics in the Virtual Domain (IDVD) method, the Guidance using Analytic Solution (GAS) method, to name a few. For analytic methods, the word “analytic” is used in the sense that these methods have low complexity and the solutions are obtained using a fixed number of computations. Two prominent analytic methods are the glideslope method and artificial potential function (APF) method.

1.2.1 Optimization Methods

Optimal control theory is the default approach for computing optimal trajectories. [41–43] Using the calculus of variations, one can mathematically determine the necessary and sufficient conditions for an optimal trajectory based on the constraints on the system (i.e., dynamics, time, boundary, path, control effort, *etc.*). The study of optimal control theory applied to astrodynamics (particularly orbit transfers) is called Primer Vector Theory (PVT). [41, 42] The primer vector is nothing more than the costate associated with the velocity state of the satellite. It turns out that solutions to several relevant optimal trajectories depend on the solution to the primer vector. Despite its elegance, PVT (as well as general optimal control problems) still yields a two point boundary value problem (TPBVP) with both the states and costates, which can be difficult to solve. [42, 44] The coupled translational and rotational motion has also been posed as an optimal control problem (OCP) using a variational approach. [38, 45]

Cell decomposition methods attempt to facilitate solving the OCP by discretizing the state space. As a result, an exhaustive tree search is performed to determine the optimal trajectory. [46–48] Imposing additional system constraints is fairly easy and can be done without adding much complexity to the algorithm. However, the computational cost increases dramatically as the number of states increases. In addition, it is difficult to determine whether the solution obtained is the global optimizer. Although these exhaustive search methods have high computational cost, they always converge to a solution (if the problem is well-posed).

One of the most effective and computationally efficient ways to solve an optimal control problem is using orthogonal collocation methods (OCM). These methods essentially transcribe the infinite dimensional OCP to an equivalent finite dimensional nonlinear program (NLP). [49, 50] Reducing the dimensionality of an OCP using an OCM greatly reduces the computation needed to obtain a solution to an OCP. However, convergence times are still indeterminate and the solution is only known at the

collocation points. Moreover, it is difficult to determine whether the solution obtained is the global optimizer of the original OCP.

The IDVD method is similar to an OCM except the devised NLP involves solving for coefficients of a set of user-defined basis functions. This approach greatly reduces the dimensionality of the NLP and, in turn, the time needed to compute a solution. These basis functions are chosen based on known behavior of the dynamical system and known structure of the optimal control. The trajectories are obtained in the virtual domain (usually an affine transform of the time domain) and then mapped back to the time domain. While the IDVD method does not provide an exact solution to an OCP, the shape of the trajectories obtained are similar to the shape of the trajectories that would be obtained from solving an OCP (assuming appropriate basis functions are chosen). It has also been shown that these trajectories are near-optimal based on their performance index values. [51]

A framework that can be implemented for any optimization method is the receding horizon approach. [52] This approach attempts to segment the problem by considering a certain horizon of time rather than solving the OCP for the entire time horizon. As a result, the OCP is solved sequentially until the terminal conditions are met at the final time. The intent of this approach is to reduce convergence times. However, since the problem is being solved sequentially, it is suboptimal according to the “Principle of Optimality”. [44]

The GAS method is an ad hoc method that reduces the dimensionality of an OCP by employing the receding horizon framework and performing an optimization only in the time domain. This method requires that an analytic solution be known for the dynamics of the system. [53] This approach greatly reduces the dimensionality of the problem. However, an optimization problem still needs to be solved iteratively. While this method obtains a solution with relatively small computational load, the end result is suboptimal due to the receding horizon framework.

1.2.2 Analytic Methods

The first (and most widely used) analytic method discussed is the glideslope algorithm. [54] This method is commonly used since it can easily be implemented due to its low complexity. The cornerstone of this algorithm is the classic two-impulse rendezvous solution. [55] This algorithm is effective yet the performance obtained is suboptimal, since there is no consideration of a cost metric. There is also no collision avoidance logic in the algorithm which does not make it favorable for APOs.

Another analytic method is the APF method, which can be thought of as an automated way of computing maneuvers for the glideslope method. The APF method has also been considered as a single-step solution to a local optimization problem (i.e., infinitesimally small receding horizon), since only local gradient information is used to plan a maneuver. [52] If the artificial potential is defined with certain characteristics, then these maneuvers have been shown to yield favorable convergence properties. [56–61] A collision avoidance logic can be included by augmenting the APF with artificial potentials representing avoidance regions. The APF method, however, does not include system dynamics nor a performance metric and is thus suboptimal. As a result, the trajectories generated for APOs are not well defined, which is important when being used on a conservative system such as a spacecraft.

1.3 Technical Challenges

Certain considerations need to be taken with the algorithm development for APOs. The priority for any APO should be safety and conservation of the space assets their resources. Therefore, an algorithm used for APOs should be robust to "unmodeled" events (i.e., rapidly generate new or corrected trajectories) and have a collision avoidance logic. In addition, the algorithm should optimize the trajectories to be cost-effective (i.e., with respect to control effort, power, time, computation, *etc.*).

A challenge with which one is faced when developing algorithms is the tradeoff between computational efficiency and optimality illustrated in Figure 1-6. Ideally,

an algorithm would have the computational efficiency of an analytic method while maintaining the performance characteristics from optimization methods. Given that computational efficiency plays a role in APOs, it is difficult to characterize different algorithms based on a single performance index. Thus, when considering algorithms for APOs, a posterior ancillary performance index must be considered which quantifies the computations performed and the convergence time to obtain a solution. Measuring floating point operations is not practical for optimization methods since their convergence times are indeterminate. [52, 62] Moreover, the conservative computation environment on flight hardware requires that power and system resources required be taken into account. In addition to the constraints on radiation-hardened hardware, only a fraction of the computation resources would be available since other flight operations must be executed as well.

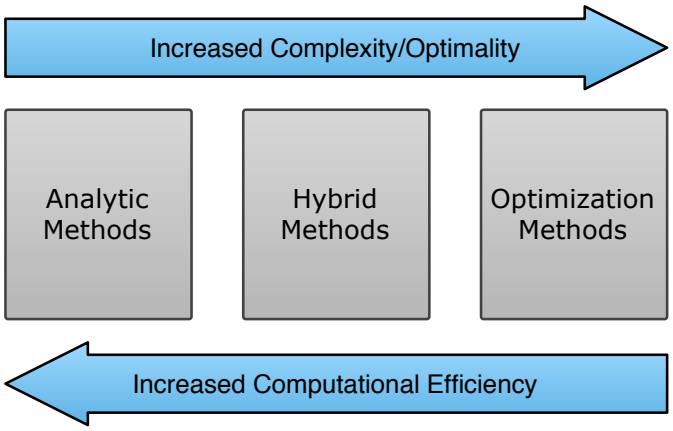

Figure 1-6. Computational efficiency vs. optimality tradeoff

The challenge of developing an algorithm that is both optimal and computationally efficient is daunting. The default solution is deferring to Moore's Law and standing by for flight hardware that guarantees real-time execution of existing algorithms. However, implementing existing algorithms on-board flight hardware would result in excess computations since trajectories would continuously need to be updated. Using analytic methodologies is more favorable since trajectories are obtained using a fixed number

of computations (i.e., functional evaluations); which is readily implementable with existing hardware. However, the trajectories obtained can still be optimized and their robustness needs to be verified. Different avenues for developing algorithms must be continuously explored to determine the most suitable algorithms for APOs. The need for accurate absolute and relative navigation is an additional challenge. [63] It is essential to have continuous knowledge of the states and objects in proximity of the autonomous spacecraft to ensure autonomy.

1.4 Research Scope

The dynamics (for both translational and rotational motion) of a rigid body orbiting the Earth are presented in Chapter 2. For both types of motion, the governing equations are presented along with the environmental disturbances experienced in orbit. Different parameterizations for describing the orientation of a rigid body are then discussed along with the kinematics for each parameterization.

The development of a high fidelity simulation environment is discussed in Chapter 3. This includes the Simulink model based on the dynamic models discussed in Chapter 2. Detailed actuator models are developed for reaction jets and reaction wheels. The reaction jets are the linear momentum exchange devices used to effect an orbital maneuver. Reaction wheels are the angular momentum exchange devices used to effect a change in orientation. The simulation environment is later used in Chapter 8 to characterize optimal trajectories and to determine how the APF and AAPF methods perform under higher fidelity dynamics.

Chapter 4 discusses some of the properties associated with the pertinent optimal trajectories for APOs. Namely, these trajectories are minimum time trajectories, fixed time minimum control effort trajectories, and finite horizon linear quadratic (LQ) trajectories. It is also shown in Chapter 4 that solving a finite horizon LQ problem reduces to solving a final value problem with the Differential Riccati Equation (DRE). The optimal trajectories for rendezvous and slew maneuvers are computed in Chapter 4.

A rendezvous maneuver with a path constraint (representative of an obstacle) is also computed.

The APF algorithm is discussed in Chapter 5 and the adaptive artificial potential function (AAPF) method is presented in Chapter 6. The AAPF method, which is a modification of the APF method, is developed to exploit the computational efficiency of the APF method and increase its optimality by choosing a time dependent form of the artificial potentials. A stability analysis is performed for both the APF and AAPF methods in Chapter 6. Two numerical examples are provided for both the APF and AAPF methods to demonstrate both algorithms' effectiveness.

Chapter 7 discusses methods for solving finite horizon LQ OCPs. The solution for an LQ OCP with a linear time invariant (LTI) Hamiltonian matrix is obtained using a state transition matrix (STM) representation. Two new methodologies are developed for obtaining the solution to a LQ OCP with a linear time varying (LTV) Hamiltonian matrix using: the Picard Iteration (PI) and the Homotopy Continuation (HC). A numerical example with a LTV system is then solved using the PI and three different HC mappings. An example representing a final approach scenario is solved using the Yamanaka-Ankerson-Tschauner-Hempel (YATH) relative motion model using the HC.

Chapter 8 presents the results from the numerical analyses performed. First, the results of two Monte Carlo simulations are presented to verify that the AAPF has improved performance and convergence characteristics over the APF method. Next, the results obtained from the simulations performed using the high fidelity model are presented. The optimal trajectories obtained in Chapter 4 for both the rotational and translational problems are tracked in the high fidelity simulation environment to determine whether the trajectories are feasible and to characterize any performance degradation. The APF and AAPF methods are also implemented in the high fidelity simulation environment to determine how these methods perform in a high fidelity model. A set of results for rendezvous with obstacle avoidance is also presented, where

tracking a trajectory and the APF and AAPF methods are implemented. Lastly, a final approach scenario is simulated by using a finite horizon LQ control law in the high fidelity model. Finally, Chapter 9 presents conclusions from the analyses done in the previous chapters.

CHAPTER 2
SYSTEM DYNAMICS

The dynamics equations governing the coupled six degrees-of-freedom (DOF) motion of a spacecraft in orbit are discussed in this chapter. The spacecraft is assumed to be a rigid body, thus the motion of a rigid body can be bifurcated into translational motion and rotational motion. The dynamics associated with both motions are discussed along with the environmental disturbances that affect an object in orbit. The dynamics equations are used in the Chapter 3 to model the spacecraft and its environment and in Chapter 4 as the dynamics constraint to obtain optimal trajectories.

2.1 Orbital Mechanics

Assuming a spherically homogeneous central body (i.e., Earth), which is significantly larger than the orbiting body (i.e., spacecraft), the motion of the smaller body with respect to the larger body can be modeled as

$$\ddot{\mathbf{r}} + \frac{\mu_\oplus}{\|\mathbf{r}\|^3}\mathbf{r} = \mathbf{f} + \mathbf{a}_d \ , \tag{2–1}$$

where $\mathbf{r}$ is the position of the spacecraft relative to the center of mass (CM) of the Earth, $\mu_\oplus$ is the Earth's gravitational parameter, $\mathbf{f}$ is the control action (i.e., specific thrust) applied by the satellite, and $\mathbf{a}_d$ is the sum of disturbing accelerations acting on the satellite. When $\mathbf{a}_d = \mathbf{0}$, this is known as the Keplerian model. [39, 40] The coupling between rotational motion and translational motion is introduced in $\mathbf{f}$ and $\mathbf{a}_d$ since these terms depend on the orientation of the spacecraft. The disturbing accelerations are caused by the environment experienced in orbit. In particular, the disturbances discussed are higher order gravitational effects, atmospheric drag, solar drag, and third body effects (i.e., gravitational effects from the Moon and Sun in particular).

2.1.1 Zonal Harmonics

Modeling the Earth as a distributed mass system (which is not spherically homogeneous), the gravity effect of the Earth can be determined as the negative

gradient of gravity potentials. Using spherical harmonics (zonal, sectoral, and tesseral) to section the Earth, the gravity potential of the zonal harmonics (which have the dominating disturbing effect) is

$$V(\mathbf{r}) = \frac{\mu_\oplus}{\|\mathbf{r}\|}\left[1 - \sum_{k=2}^{\infty} J_k \left(\frac{R_\oplus}{\|\mathbf{r}\|}\right)^k P_k(\cos(\phi_{gc}))\right],$$

where J_k is the empirically determined constant for the kth zonal harmonic, $R_\oplus$ is the equatorial radius of Earth, P_k is the kth order Legendre polynomial, and ϕ_{gc} is the geocentric latitude of the satellite. [39, 40] The negative gradient of this potential yields the effective gravitational specific force from the zonal harmonics on the spacecraft. Note that the potential term outside of the series yields the gravity term for the restricted two-body model (i.e., spherically homogeneous Earth). The sectoral and tesseral harmonics are omitted since the zonal harmonics have the largest disturbing effect (i.e., the spherically homogeneous Earth term and the J_2 effect). In fact, the J_2 effect is up to 1000 times greater than the next most dominating effect. [39] The decrease in gravitational effect can also be seen in the subsequent zonal terms since when $k \to \infty$, then $\left(\frac{R_\oplus}{\|\mathbf{r}\|}\right)^k \to 0$. The J_2 effect represented in the Earth-Centered Earth-Fixed (ECEF) frame is

$$\mathbf{a}_{J_2} = -\frac{3J_2\mu_\oplus R_\oplus^2}{2r^5}\begin{bmatrix} r_I\left(1 - \frac{5r_K^2}{r^2}\right) & r_J\left(1 - \frac{5r_K^2}{r^2}\right) & r_K\left(3 - \frac{5r_K^2}{r^2}\right)\end{bmatrix}^T,$$

where r_I, r_J, and r_K are the components of $\mathbf{r}$ represented in the ECEF frame. For the purposes of modeling, the first six zonal harmonics are used (pp. 550-552 of [39]).

2.1.2 Aerodynamic Drag

The surfaces of the spacecraft are discretized into n faces to determine the aerodynamic drag. For a convex spacecraft structure, the aggregate aerodynamic drag is

$$\mathbf{a}_{ad} = -\left(\frac{1}{2}\frac{\rho(h)}{m}\|\mathbf{v}_{rel}\|^2 \sum_{i=1}^{n} \gamma_i A_i C_{D,i}\hat{\mathbf{n}}_i \cdot \hat{\mathbf{v}}_{rel}\right)\hat{\mathbf{v}}_{rel}, \tag{2–2}$$

where m is the mass of the spacecraft, $\rho(h)$ is the air density as a function of altitude h, A_i is the area of face i, $C_{D,i}$ is the drag coefficient of face i, $\mathbf{n}_i$ is the unit vector normal to face i, and γ_i is defined below. [39, 64]

$$\gamma_i = \begin{cases} 1 & \text{if } \hat{\mathbf{n}}_i \cdot \hat{\mathbf{v}}_{rel} > 0 \\ 0 & \text{otherwise} \end{cases}$$

An illustration of the vectors $\mathbf{n}_i$ is shown in Figure 2-1 for a spacecraft with a cube structure. The coupling between translational and rotational motion is evident in this disturbance since the orientation of the spacecraft determines the aerodynamic drag. Likewise, the aerodynamic drag may cause a moment which affects the rotational motion of the spacecraft. The parameter $\hat{\mathbf{v}}_{rel}$ is the unit vector parallel to $\mathbf{v}_{rel}$, which is the relative velocity between the satellite and the Earth's atmosphere. It is assumed that the atmosphere has the same rotational velocity as the Earth. As a result, $\mathbf{v}_{rel}$ is defined as

$$\mathbf{v}_{rel} = \dot{\mathbf{r}} - \boldsymbol{\omega}_{\oplus} \times \mathbf{r} \ ,$$

where $\boldsymbol{\omega}_{\oplus}$ is the rotation rate of the Earth.

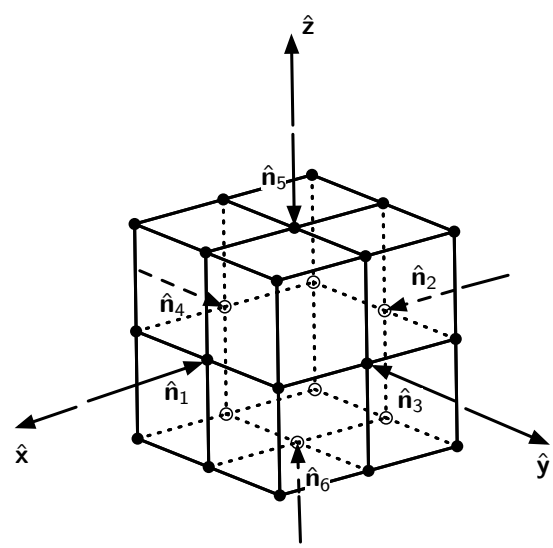

Figure 2-1. Surface discretization of spacecraft with unit normal vectors

Different models exist for describing the air density as a function of height. The model used is the Exponential Atmosphere Model, which is simple yet fairly accurate for altitudes $h \leq 1000$ km. Using this model, the air density is defined as

$$\rho(h) = \rho_0 \exp\left(-\frac{h - h_0}{H}\right) ,$$

where h_0, ρ_0, and H are tabulated parameters and also depend on the the altitude. Values for these parameters can be found in [39].

2.1.3 Solar Drag

Using the same discretization of the surfaces of the spacecraft, the aggregate solar drag is

$$\mathbf{a}_{sd} = -\left(\frac{SP}{m}\sum_{i=1}^{n}\eta_i A_i C_{R,i}\hat{\mathbf{n}}_i \cdot \hat{\mathbf{r}}_{sun}\right)\hat{\mathbf{r}}_{sun} , \tag{2–3}$$

where $SP = 4.57 \times 10^{-6}$ N/m^2 is the mean solar pressure, $\hat{\mathbf{r}}_{sun}$ is the unit vector pointing from the Sun to the satellite's CM, $C_{R,i}$ is the coefficient of reflectivity of face i, and η_i is defined as below. [39, 64]

$$\eta_i = \begin{cases} 1 & \text{if } \hat{\mathbf{n}}_i \cdot \hat{\mathbf{r}}_{sun} > 0 \\ 0 & \text{otherwise} \end{cases}$$

The coupling between translational and rotational motion is evident in this disturbance as well. It should be noted that this disturbance is only active when the spacecraft is not in eclipse. [39, 64] The condition for determining whether a spacecraft is in eclipse is

$$\sin^{-1}\left(\frac{R_\oplus}{\|\mathbf{r}\|}\right) \geq \cos^{-1}\left(\frac{\mathbf{r}}{\|\mathbf{r}\|} \cdot \hat{\mathbf{r}}_{sun}\right) .$$

2.1.4 Third Body Disturbances

Third body disturbances are gravitational effects caused by objects other than the Earth. In particular, the objects that have the most influence on an Earth spacecraft are the Sun and the Moon. [39] The gravitational effect of the Sun on a body orbiting the

Earth is

$$\mathbf{a}_{\odot} = \mu_{\odot} \left(\frac{\mathbf{R}_{\odot} - \mathbf{r}}{\|\mathbf{R}_{\odot} - \mathbf{r}\|^3} - \frac{\mathbf{R}_{\odot}}{\|\mathbf{R}_{\odot}\|^3} \right) ,$$

where $\mu_{\odot}$ is the gravitational parameter of the Sun and $\mathbf{R}_{\odot}$ is the position of the Sun relative to the Earth's center. The gravitational effect of the Moon on a body orbiting the Earth is

$$\mathbf{a}_{☾} = \mu_{☾} \left(\frac{\mathbf{R}_{☾} - \mathbf{r}}{\|\mathbf{R}_{☾} - \mathbf{r}\|^3} - \frac{\mathbf{R}_{☾}}{\|\mathbf{R}_{☾}\|^3} \right) ,$$

where $\mu_{☾}$ is the gravitational parameter of the Moon and $\mathbf{R}_{☾}$ is the position of the moon relative to the Earth's center. The models used for determining the position of the Sun and Moon as a function of time are presented in [39].

2.2 Attitude Dynamics

The rotational motion of a rigid body can be modeled using Euler's second law. [64, 65] The angular momentum of a rigid body about its CM is

$$\mathbf{H} = \mathbf{J} \cdot \boldsymbol{\omega} ,$$

where $\mathbf{J}$ is the centroidal inertia dyadic of the rigid body and $\boldsymbol{\omega}$ is the angular velocity relative to an inertial reference frame. Thus, the time rate of change of the angular momentum is equal to the sum of external torques

$$\frac{d\mathbf{H}}{dt} = \mathbf{J} \cdot \dot{\boldsymbol{\omega}} + \boldsymbol{\omega} \times \mathbf{J} \cdot \boldsymbol{\omega} = \boldsymbol{\tau} + \boldsymbol{\tau}_d , \tag{2–4}$$

where $\boldsymbol{\tau}$ is the control torque and $\boldsymbol{\tau}_d$ is the sum of external disturbing torques acting on the satellite. During flight, a spacecraft is subjected to external disturbance torques which affect its motion. For completeness, the disturbing torques discussed are the gravity gradient torque, aerodynamic torque, and solar torque. A detailed exposé of these disturbances can be found in [39, 64].

2.2.1 Gravity Gradient Torque

A gravity gradient torque is experienced when a body is not symmetric (about any axis) and does not have a homogeneous mass distribution. The gravity gradient torque is defined as

$$\boldsymbol{\tau}_{gg} = 3\frac{\mu_{\oplus}}{\|\mathbf{r}\|^3}\hat{\mathbf{c}} \times (\mathbf{J} \cdot \hat{\mathbf{c}}) \ ,$$

where $\hat{\mathbf{c}}$ is the unit vector in the nadir direction.

2.2.2 Aerodynamic Torque

An aerodynamic torque results from the aerodynamic drag in equation (2–2), which does not act along the CM of the spacecraft (i.e., the CM and geometric center are distinct). For these cases, the aerodynamic torque is modeled as

$$\boldsymbol{\tau}_{at} = -\frac{1}{2}\frac{\rho(h)}{m}\|\mathbf{v}_{rel}\|^2 \sum_{i=1}^{n} \gamma_i A_i C_{D,i} \left(\hat{\mathbf{n}}_i \cdot \hat{\mathbf{v}}_{rel}\right)^2 \left(\hat{\mathbf{v}}_{rel} \times \mathbf{r}_{cp,i}\right) \ ,$$

where $\mathbf{r}_{cp,i}$ is the vector from the CM to the center of pressure of face i. Specifically, this vector is defined as

$$\mathbf{r}_{cp,i} = l_i \hat{\mathbf{n}}_i - \mathbf{r}_{cm} \ ,$$

where l_i is the distance from the geometric center to the center of pressure of face i and $\mathbf{r}_{cm}$ is the position of the spacecraft's CM relative to the geometric center of the spacecraft. [39, 64]

2.2.3 Solar Torque

Solar wind has an effect similar to that of atmospheric wind. Thus, solar drag produces a torque when the center of pressure is distinct from the CM For these cases, the solar torque is modeled as

$$\boldsymbol{\tau}_{st} = -\frac{SP}{m} \sum_{i=1}^{n} \eta_i A_i C_{R,i} \left(\hat{\mathbf{n}}_i \cdot \hat{\mathbf{r}}_{sun}\right)^2 \left(\hat{\mathbf{r}}_{sun} \times \hat{\mathbf{r}}_{cp,i}\right) \ .$$

2.3 Attitude Representations

Numerous parameterizations exist to describe the orientation of a rigid body. [66] First, the classical Euler angles are discussed. The Euler angle representation is used in Appendix A to derive a set of equations for relative rotational motion. Next, the axis-angle representation and the unit quaternion are discussed. These attitude representations are intimately related and are used to define relative orientations and the scalar metric to measure for relative orientation errors.

2.3.1 Euler Angles

The orientation of one coordinate system relative to another can be described using at most a sequence of three Euler rotations. [66, 67] An Euler rotation is a rotation about one of the axes that defines the orthonormal basis of the coordinate system. This rotation is represented by a matrix operation. The matrix that rotates a vector about the first axis is

$$\mathbf{C}(1,\theta) = \begin{bmatrix} 1 & 0 & 0 \\ 0 & \cos\theta & \sin\theta \\ 0 & -\sin\theta & \cos\theta \end{bmatrix},$$

about the second axis is

$$\mathbf{C}(2,\theta) = \begin{bmatrix} \cos\theta & 0 & -\sin\theta \\ 0 & 1 & 0 \\ \sin\theta & 0 & \cos\theta \end{bmatrix},$$

and about the third axis is

$$\mathbf{C}(3,\theta) = \begin{bmatrix} \cos\theta & \sin\theta & 0 \\ -\sin\theta & \cos\theta & 0 \\ 0 & 0 & 1 \end{bmatrix}.$$

Consequently, a rotation matrix relating vector representations in frames $\mathcal{A}$ and $\mathcal{B}$ is defined by a rotation sequence about the i, j, and k axes with angles ϕ, θ, and ψ,

respectively (as seen in equation (2–5)). [65–67]

$$\mathbf{C}_{\mathcal{BA}} = \mathbf{C}(k, \psi)\mathbf{C}(j, \theta)\mathbf{C}(i, \phi) \tag{2–5}$$

Thus, a vector represented in frame $\mathcal{A}$ can now be represented in frame $\mathcal{B}$ as

$$^{\mathcal{B}}\mathbf{v} = \mathbf{C}_{\mathcal{BA}}{}^{\mathcal{A}}\mathbf{v} \ .$$

The kinematics of the Euler angles can be derived by summing all the rotation rates (represented in the same coordinate system). [66] This results in the expression

$$\boldsymbol{\omega} = \mathbf{S}(\phi, \theta, \psi) \begin{bmatrix} \dot{\phi} \\ \dot{\theta} \\ \dot{\psi} \end{bmatrix} \ ,$$

where the definition of $\mathbf{S}(\phi, \theta, \psi)$ depends on the rotation sequence used.

2.3.2 Axis-Angle

The same rotation matrix can be derived by performing a single rotation about a unit vector $\hat{\mathbf{e}}$ (i.e., eigenaxis) by an angle θ (i.e., eigenangle), and is defined as

$$\mathbf{C}_{\mathcal{BA}} = \mathbf{C}(\hat{\mathbf{e}}, \theta) = \cos\theta\mathbf{I} + (1 - \cos\theta)\hat{\mathbf{e}}\hat{\mathbf{e}}^T - \sin\theta\hat{\mathbf{e}}^\times \ ,$$

where $\mathbf{e}^\times$ is the skew operator and is defined for an arbitrary column matrix

$$\mathbf{a} = \begin{bmatrix} a_1 & a_2 & a_3 \end{bmatrix}^T$$

below. [65, 66]

$$\mathbf{a}^\times = \begin{bmatrix} 0 & -a_3 & a_2 \\ a_3 & 0 & -a_1 \\ -a_2 & a_1 & 0 \end{bmatrix}$$

The kinematics for this parameterization are given below. [66]

$$\dot{\theta} = \hat{\mathbf{e}} \cdot \boldsymbol{\omega}$$
$$\dot{\hat{\mathbf{e}}} = \frac{1}{2}\left[\hat{\mathbf{e}}^{\times}\boldsymbol{\omega} - \cot\left(\frac{\theta}{2}\right)\hat{\mathbf{e}}^{\times}(\hat{\mathbf{e}}^{\times}\boldsymbol{\omega})\right]$$

This representation is useful since the angle can be used as a scalar metric for the relative orientation between two orientations.

2.3.3 Unit Quaternion

A unit quaternion is a set of four parameters used to represent the orientation of a rigid body

$$\mathbf{q} = \begin{bmatrix} \boldsymbol{\epsilon} \\ \eta \end{bmatrix} , \tag{2–6}$$

where $\boldsymbol{\epsilon}$ is the vector component and η is the scalar component. The unity constraint requires that $\mathbf{q}^T\mathbf{q} = 1$. Unit quaternions are related to the axis-angle representation by

$$\boldsymbol{\epsilon} = \sin\left(\frac{\theta}{2}\right)\hat{\mathbf{e}}$$
$$\eta = \cos\left(\frac{\theta}{2}\right) .$$

The relationship between Euler angles and quaternions is not direct and can be found in [67] or [66].

Given a quaternion that relates coordinate system $\mathcal{A}$ to coordinate system $\mathcal{B}$, the rotation matrix using this quaternion is defined as

$$\mathbf{C}_{\mathcal{BA}}(\mathbf{q}) = \boldsymbol{\Xi}^T(\mathbf{q})\boldsymbol{\Psi}(\mathbf{q}) ,$$

where $\boldsymbol{\Xi}(\mathbf{q})$ and $\boldsymbol{\Psi}(\mathbf{q})$ are defined below. [66, 68]

$$\boldsymbol{\Psi}(\mathbf{q}) = \begin{bmatrix} \eta \mathbf{I} - \boldsymbol{\epsilon}^{\times} \\ -\boldsymbol{\epsilon}^{T} \end{bmatrix}$$

$$\boldsymbol{\Xi}(\mathbf{q}) = \begin{bmatrix} \eta \mathbf{I} + \boldsymbol{\epsilon}^{\times} \\ -\boldsymbol{\epsilon}^{T} \end{bmatrix}$$

A favorable attribute of quaternions is that the inverse relationship between the rotation matrix and the quaternion is nonsingular. This means that a unique quaternion can be extracted from the rotation matrix which represents the original orientation. [66] Another favorable attribute is that the quaternion kinematics are bilinear (in the quaternion and the angular velocity) and are represented as

$$\dot{\mathbf{q}} = \frac{1}{2}\boldsymbol{\Xi}(\mathbf{q})\boldsymbol{\omega} = \frac{1}{2}\boldsymbol{\Omega}(\boldsymbol{\omega})\mathbf{q} \ , \tag{2–7}$$

where

$$\boldsymbol{\Omega}(\boldsymbol{\omega}) = \begin{bmatrix} -\boldsymbol{\omega}^{\times} & \boldsymbol{\omega} \\ -\boldsymbol{\omega}^{T} & 0 \end{bmatrix} \ .$$

Quaternions are particularly useful since an error quaternion between two orientations can be defined. To define an error quaternion, the quaternion product operation is first defined as

$$\mathbf{q}_1 \otimes \mathbf{q}_2 = \begin{bmatrix} \boldsymbol{\Psi}(\mathbf{q}_1) & \mathbf{q}_1 \end{bmatrix} \mathbf{q}_2 = \begin{bmatrix} \boldsymbol{\Xi}(\mathbf{q}_2) & \mathbf{q}_2 \end{bmatrix} \mathbf{q}_1 \ .$$

As a result, the quaternion inverse is defined as

$$\mathbf{q}^{-1} = \begin{bmatrix} -\boldsymbol{\epsilon} \\ \eta \end{bmatrix} \ ,$$

such that the quaternion product of a quaternion and its inverse is the zero quaternion $\begin{bmatrix} \mathbf{0}^T & 1 \end{bmatrix}^T$. This way, the error quaternion is

$$\mathbf{q}_e = \mathbf{q}_1 \otimes \mathbf{q}_2^{-1} \ , \tag{2–8}$$

since the zero quaternion is obtained when $\mathbf{q}_1$ and $\mathbf{q}_2$ are equivalent. An error angle is also defined based on the relationship between the axis-angle representation and unit quaternions

$$\theta_e = 2\cos^{-1}(\eta_e) \ ,$$

where η_e is the scalar component of the error quaternion. This error angle represents a scalar metric for the relative orientation between two orientations described by $\mathbf{q}_1$ and $\mathbf{q}_2$.

In conclusion, the dynamics associated with both translational and rotational motion of a spacecraft in orbit are presented in this chapter. The translational motion includes disturbances from the Earth's oblateness, aerodynamic and solar drag, and third body gravitational effects. The rotational motion includes disturbances from the gravity gradient and aerodynamic and solar drag. Different sets of parameterizations for representing an orientation are also discussed. The dynamics discussed in this chapter are used to develop a high fidelity model of a spacecraft. They are also used for obtaining optimal trajectories (while neglecting disturbances) for rendezvous and slew maneuvers.

CHAPTER 3
SYSTEM MODELING

The high fidelity simulation environment developed in Simulink is discussed in this chapter. The simulation environment is used for characterizing performance of different algorithms by applying them in the high fidelity model of the spacecraft. The simulation environment includes models for two spacecraft (i.e., chaser and target), where each spacecraft is modeled using the dynamics discussed in Chapter 2. The chaser satellite has thrusters for translational control and reaction wheels for attitude control, where a model for these devices is also discussed in this chapter. These models are important since the actuator dynamics determine whether the commands from a controller are realizable. The high level Simulink diagram of the simulation environment is shown in Figure 3-1.

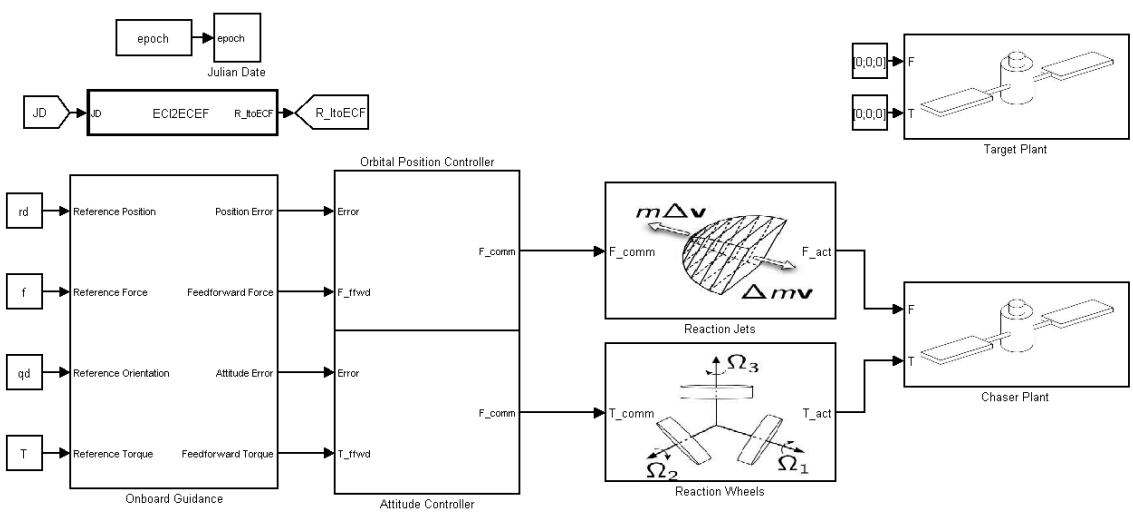

Figure 3-1. High level Simulink diagram

3.1 Target/Chaser Plant

The satellite geometry for both the target and chaser is based on a cube structure with side length $l = 1$ m. The structure is important because it dictates the effects of the disturbances experienced. The actuator geometry assumes unidirectional thrusters on each face that have a line of action along the center of mass (CM) of the spacecraft.

Figure 3-2 illustrates the arrangement of the six thrusters in the body frame. The reaction wheel system is such that the spin axis of each reaction wheel is aligned with each axis of the body frame.

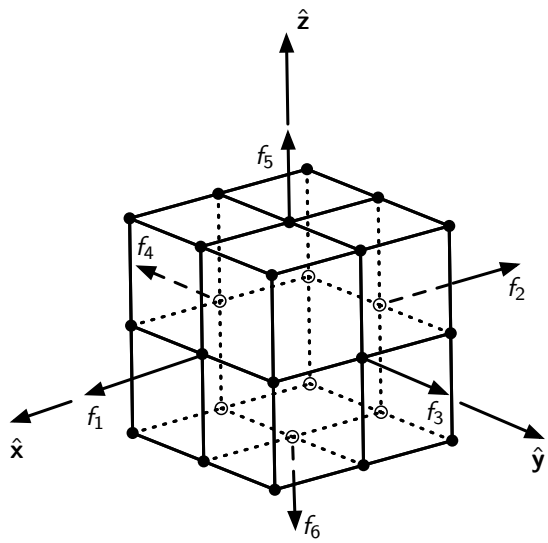

Figure 3-2. Geometry of spacecraft and reaction jets

It should be noted that the mass is not modeled as a variable quantity. In reality, the mass is variable since the reaction jets expend fuel to produce a force. [69] This extra degree of freedom does have considerable effect on the dynamics, however, it is difficult to determine how to model this without having a preliminary design of the spacecraft. Having a variable mass and inertia matrix affects the magnitude of some disturbing forces and the attitude dynamics. The reaction jets are also affected since they would have a limited supply of fuel to burn. [69]

The motion of both spacecraft is modeled using the equations discussed in Chapter 2. Particularly, the translational motion is modeled using the restricted two-body model while including disturbances. A model of the Sun and Moon position is given in [39] (as a function of the Julian Date), which determines the solar drag, solar torque, and third body gravitational effects. The rotational motion is modeled using Euler's second law while including the disturbing torques. As a result, the satellite plant is grouped into

one block as shown in Figure 3-3, where the only inputs are the force and torque from the actuators.

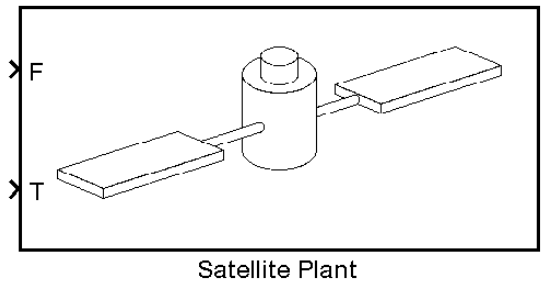

Figure 3-3. Simulink satellite model block

3.2 Actuator Dynamics and Model

The actuators chosen for the chaser are low-thrust reaction jets for orbital maneuvers and reaction wheels for attitude maneuvers. The dynamics and constraints for both the reaction jets and the reaction wheels are discussed including any delays, saturation limits, and/or deadband limits. Modeling actuators assist in determining whether the commanded actions by a particular controller are realizable.

3.2.1 Reaction Jets

Reaction jets are linear momentum exchange devices that generate the force required for performing orbital maneuvers. Depending on the configuration of the jets on the spacecraft, they can impart a force and/or moment. In general, the relationship between each individual reaction jet force, and the resultant force and moment can be expressed as

$$\begin{bmatrix} \mathbf{F} \\ \mathbf{M} \end{bmatrix} = \mathbf{L}\mathbf{f} \ ,$$

where **F** and **M** are the force and moment (expressed in the body fixed frame), respectively, **L** is the configuration matrix that determines each individual reaction jet's contribution to the force and moment, and **f** is a column matrix containing the force magnitudes from each reaction jet.

The configuration of the reaction jets chosen is illustrated in Figure 3-2. This configuration is chosen for simplicity and to avoid controllability issues. The matrix $\mathbf{L}$ for this configuration matrix is decomposed as

$$\mathbf{L} = \begin{bmatrix} \mathbf{L}_1 \\ \mathbf{L}_2 \end{bmatrix} ,$$

where

$$\mathbf{L}_1 = \begin{bmatrix} 1 & -1 & 0 & 0 & 0 & 0 \\ 0 & 0 & 1 & -1 & 0 & 0 \\ 0 & 0 & 0 & 0 & 1 & -1 \end{bmatrix}$$

and $\mathbf{L}_2 = \mathbf{0}$ since the reaction jet forces act along the CM and do not produce a moment. Thus, given a commanded force $\mathbf{F}_{comm}$, the individual reaction jet forces can be determined using the min-norm solution

$$\mathbf{f} = \mathbf{L}_1^T (\mathbf{L}_1 \mathbf{L}_1^T)^{-1} \mathbf{F}_{comm} .$$

To enforce the unidirectional constraint (i.e., reaction jets can only produce positive forces), the following conditions are enforced on the min-norm solution

$$f_{2i-1}^* = \begin{cases} f_{2i-1} + |f_{2i}| & \text{if } f_{2i-1} \geq 0 \text{ and } f_{2i} \leq 0 \\ 0 & \text{otherwise} \end{cases} \quad \text{for } i = 1, 2, 3$$

$$f_{2i}^* = \begin{cases} f_{2i} + |f_{2i-1}| & \text{if } f_{2i} \geq 0 \text{ and } f_{2i-1} \leq 0 \\ 0 & \text{otherwise} \end{cases} \quad \text{for } i = 1, 2, 3 .$$

Thus, the actual force from the reaction jet solution

$$\mathbf{f}^* = \begin{bmatrix} f_1^* & f_2^* & f_3^* & f_4^* & f_5^* & f_6^* \end{bmatrix}^T$$

is

$$\mathbf{F}_{act} = \mathbf{L}_1 \mathbf{f}^* \ .$$

The inherent delays and dynamics associated with the chemical, electrical, and mechanical processes of the jets are modeled as well. An example of a typical thrust profile is shown in Figure 3-4. [64] First, a force is commanded at time t_0. However, due to the processes required for turning on the reaction jet there is a delay and is instead turned on at time t_1. Next, the force from the reaction jet must ramp up to the commanded value which is achieved at time t_2. The same delay is seen when the force commanded is changed at time t_3 yet the change begins at time t_4. The thrust then ramps down to the new commanded value at t_5. The values for these delays, growth, and decay times range from a few milliseconds to hundreds of milliseconds. [64] The block diagram in Figure 3-5 illustrates how this thrust profile is achieved, where the delay used is 1 ms and the transfer function used is

$$G(s) = \frac{100}{s + 100} \ ,$$

which yields a growth and decay time of about 100 ms.

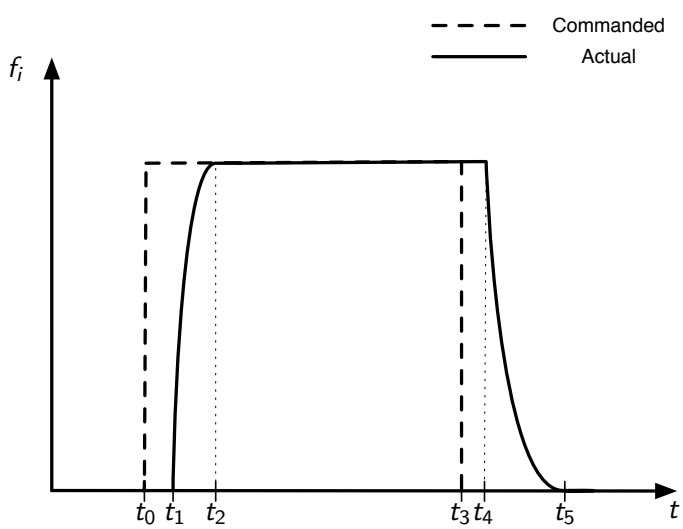

Figure 3-4. Thrust profile of reaction jets

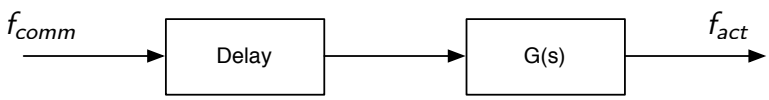

Figure 3-5. Block diagram to achieve thrust profile

A saturation and deadband limit is imposed on each reaction jet as well. Figure 3-6 illustrates a generic commanded signal that contains both these limits and the resulting achievable thrust profile. In order to achieve this thrust profile, a three-part switch is used to distinguish between the three different cases and is illustrated in Figure 3-7. From Figure 3-7, the first case corresponds to the saturation limit being active, the second case is when the deadband limit is active, and the third case is when neither is active. Figure 3-7 also shows the delay and the transfer function discussed previously. The saturation limit and deadband limits used are $f_{max} = \sqrt{3}$ N and $f_{db} = 0.01$ N, respectively.

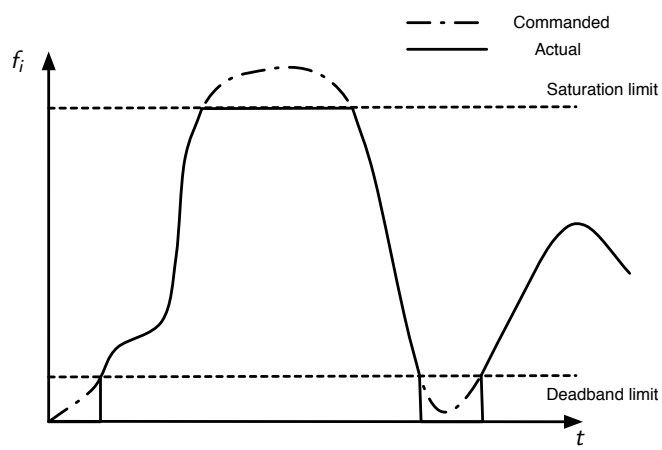

Figure 3-6. Illustration of saturation and deadband limits

3.2.2 Reaction Wheels

Reaction wheels are angular momentum exchange devices that distribute angular momentum of the satellite by spinning up or down the reaction wheels. Initially, these

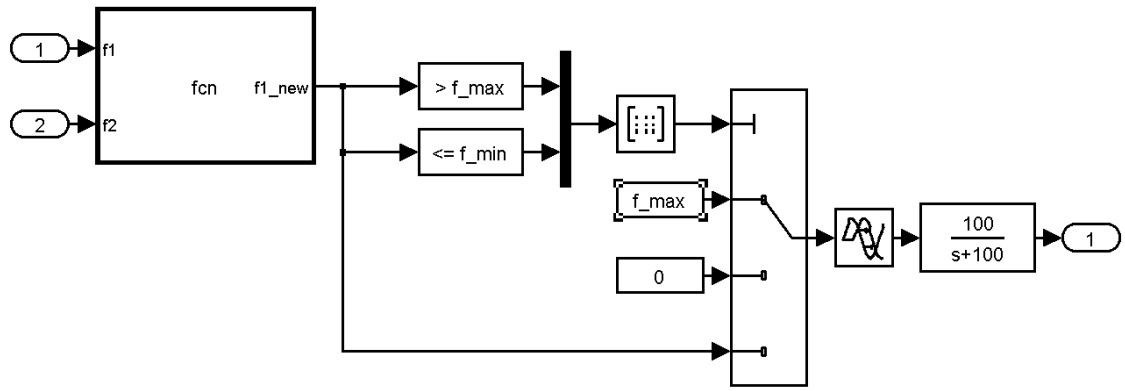

Figure 3-7. Switch to impose saturation and deadband limits

devices contain a portion of the satellite's angular momentum. Since angular momentum is conserved, when the reaction wheels are spun up (or down), the angular momentum of the remaining components of the satellite has to be adjusted to maintain a total constant value. [64, 70] As a result, the orientation of the satellite changes. In general, the angular momentum of a reaction wheel device can be expressed as the sum of angular momenta of the reaction wheels

$$\mathbf{h} = \sum_{i=1}^{N} \mathbf{C}(3, \phi_i)\mathbf{C}(2, \theta_i)\mathbf{C}(3, \delta_i) \begin{bmatrix} I_{fw,i}\Omega_i \\ 0 \\ 0 \end{bmatrix},$$

where ϕ_i is the separation angle, θ_i is the inclination angle, δ_i is the gimbal angle, $I_{fw,i}$ is the moment of inertia of the reaction wheel about its spin axis, and Ω_i is the angular velocity of the reaction wheel. The rotation matrices express the angular momentum of each reaction wheel in the body fixed frame. The only time-varying quantity in this expression is the angular velocities of the reaction wheels. Thus, the time derivative of

the angular momentum of the reaction wheel device is

$$\dot{\mathbf{h}} = \sum_{i=1}^{N} \mathbf{C}(3,\phi_i)\mathbf{C}(2,\theta_i)\mathbf{C}(3,\delta_i) \begin{bmatrix} I_{fw,i}\dot{\Omega}_i \\ 0 \\ 0 \end{bmatrix} ,$$

where $\dot{\Omega}_i$ is the angular acceleration of the reaction wheel which produces the effect of a torque.

Typically, the geometry of the reaction wheel system used has each reaction wheel's spin axis aligned with each principal axis of the principal body fixed frame (i.e., three reaction wheels). If a redundant wheel is used, it is typically skewed such that its direction is along the diagonal of the principal body fixed frame directions. The configuration used in the simulation environment is a three reaction wheel attitude control system with each reaction wheel's spin axis aligned with each of the axes of the body fixed frame. As a result, the angular momentum of the reaction wheel system expressed in the chaser's body fixed frame is

$$\begin{aligned} \mathbf{h} &= \begin{bmatrix} I_{fw,1} & 0 & 0 \\ 0 & I_{fw,2} & 0 \\ 0 & 0 & I_{fw,3} \end{bmatrix} \begin{bmatrix} \Omega_1 \\ \Omega_2 \\ \Omega_3 \end{bmatrix} \\ \Rightarrow \mathbf{h} &= \mathbf{I}_{fw}\boldsymbol{\Omega} \ . \end{aligned} \tag{3–1}$$

Likewise, the derivative of the angular momentum is expressed as

$$\dot{\mathbf{h}} = \mathbf{I}_{fw}\dot{\boldsymbol{\Omega}} \ . \tag{3–2}$$

To derive the control methodology to realize a commanded torque using a reaction wheel system, the rotational equations of motion are revisited. The angular momentum of a spacecraft about its CM is expressed as

$$\mathbf{H} = \mathbf{J}\boldsymbol{\omega} + \mathbf{h} \ ,$$

where the centroidal inertia matrix $\mathbf{J}$ does not include the reaction wheels. Assuming no external torques are acting on the satellite (i.e., no disturbing torques), then the total angular momentum is conserved. Thus, the inertial time derivative of the total angular momentum is

$$\begin{aligned} \dot{\mathbf{H}} &= \mathbf{J}\dot{\boldsymbol{\omega}} + \dot{\mathbf{h}} + \boldsymbol{\omega}^{\times}(\mathbf{J}\boldsymbol{\omega} + \mathbf{h}) = \mathbf{0} \\ &\Rightarrow \mathbf{J}\dot{\boldsymbol{\omega}} + \boldsymbol{\omega}^{\times}\mathbf{J}\boldsymbol{\omega} = -\dot{\mathbf{h}} - \boldsymbol{\omega}^{\times}\mathbf{h} \ . \end{aligned} \tag{3–3}$$

Coulomb and viscous friction and stiction are considerable torques that affect the performance of the reaction wheels. [64] Stiction is not easily modeled and is ignored since it only affects the reaction wheels when they are at low spin rates. The friction model used on the reaction wheels is the sum of coulomb and viscous friction

$$\boldsymbol{\tau}_{friction} = \tau_c sgn(\boldsymbol{\Omega}) + \tau_v \boldsymbol{\Omega} \ ,$$

where τ_c is the Coulomb friction coefficient and τ_v is the viscous friction coefficient.

Recalling equation (3–3), the internal torque from the reaction wheels is obtained as

$$\boldsymbol{\tau}_{comm} - \boldsymbol{\tau}_{friction} = -\dot{\mathbf{h}} - \boldsymbol{\omega}^{\times}\mathbf{h} \ .$$

where $\boldsymbol{\tau}_{comm}$ is the desired torque from the reaction wheel system. Given an attitude controller $\boldsymbol{\tau}_{comm}$ and feedback of reaction wheel angular velocities, the reaction wheels' angular acceleration that would produce the commanded torque is found using equation (3–1) and equation (3–2), and is

$$\dot{\boldsymbol{\Omega}} = \mathbf{I}_{fw}^{-1}\left[-\boldsymbol{\tau}_{comm} + \boldsymbol{\tau}_{friction} - \boldsymbol{\omega}^{\times}\mathbf{I}_{fw}\boldsymbol{\Omega}\right] \ .$$

The parameters and constraints used for the reaction wheel device are shown in Table 3-1. These include saturation limits placed on the angular velocity and angular acceleration of the reaction wheels.

Table 3-1. Reaction wheel system parameters and constraints

Parameter	Value	Units
$I_{fw,i}$	0.625	$\mathrm{kg} \cdot \mathrm{m}^2$
τ_c	7.06×10^{-4}	$\mathrm{N} \cdot \mathrm{m}$
τ_v	1.16×10^{-5}	$(\mathrm{N} \cdot \mathrm{m})/(\mathrm{rad}/\mathrm{s})$
$\dot{\Omega}_{max}$	100	$\mathrm{rad}/\mathrm{s}^2$
Ω_{max}	524	rad/s

In this chapter, a simulation environment developed to model two spacecraft in close proximity is discussed. Included is a plant model for both the chaser and target spacecrafts. The coupled six degrees-of-freedom dynamics discussed in Chapter 2 are used for both spacecraft. The dynamics and constraints associated with the actuators on the chaser are also discussed. This model is later used to determine whether optimal trajectories are realizable and to characterize differences between theoretical performance and actual performance. It is also used to determine whether the algorithms developed using linearized models are still valid in a higher fidelity model.

CHAPTER 4
OPTIMAL TRAJECTORIES

Solutions to an optimal control problem (OCP) can be used for obtaining optimal trajectories. In this chapter, a general form of an OCP is presented. The OCPs of particular interest that are discussed are the minimum time OCP, fixed time minimum control effort OCP, and finite horizon linear quadratic (LQ) OCP. Minimum time and fixed time minimum control effort trajectories are typically used for close-range rendezvous. Finite horizon LQ trajectories are typically used for the final approach or endgame of a proximity operation. It is shown that solving a finite horizon LQ OCP is equivalent to solving a final value problem with the Differential Riccati Equation (DRE). Finally, the three pertinent optimal trajectories for both the translational and rotational motion are computed. In addition, a fixed time minimum control effort problem is solved which includes an obstacle.

4.1 Optimal Control Problem

Without loss of generality, the continuous time OCP is posed as

$$\min_{\mathbf{u} \in \mathbb{R}^m} J = \Phi(\mathbf{x}(t_0), \mathbf{x}(t_f), t_0, t_f) + \int_{t_0}^{t_f} \mathcal{L}(\mathbf{x}(t), \mathbf{u}(t), t)\ dt\ ,$$

subject to

$$\begin{aligned}
\dot{\mathbf{x}}(t) &= \mathbf{f}(\mathbf{x}(t), \mathbf{u}(t), t) \\
\phi(\mathbf{x}(t_0), \mathbf{x}(t_f), t_0, t_f) &= \mathbf{0} \\
\mathbf{c}(\mathbf{x}(t), \mathbf{u}(t), t) &\leq \mathbf{0}\ ,
\end{aligned}$$

where $\Phi : \mathbb{R}^n \times \mathbb{R}^n \times \mathbb{R} \times \mathbb{R} \to \mathbb{R}$ is the cost incurred from the boundary conditions, $\mathcal{L} : \mathbb{R}^n \times \mathbb{R}^m \times \mathbb{R} \to \mathbb{R}$ is the Lagrangian, $\mathbf{f} : \mathbb{R}^n \times \mathbb{R}^m \times \mathbb{R} \to \mathbb{R}^n$ is the derivative constraint (i.e., dynamics) on $\mathbf{x}$, $\phi : \mathbb{R}^n \times \mathbb{R}^n \times \mathbb{R} \times \mathbb{R} \to \mathbb{R}^k$ is the column matrix of constraints at the boundary conditions, and $\mathbf{c} : \mathbb{R}^n \times \mathbb{R}^m \times \mathbb{R} \to \mathbb{R}^l$ ($l \leq m$) is the column matrix of state and/or control constraints. [41, 43, 44] It is important to note that the "less than or

equal to" in $\mathbf{c}(\mathbf{x}(t), \mathbf{u}(t), t) \leq \mathbf{0}$ (and when used with vectors or matrices in the rest of this chapter) is a component-wise operator.

The calculus of variations is used to determine the necessary and sufficient conditions to solve an OCP. [41, 44] First, an augmented cost function is defined as

$$J_a = \Phi + \boldsymbol{\nu}^T \boldsymbol{\phi} + \int_{t_0}^{t_f} \mathcal{L} + \boldsymbol{\lambda}^T \mathbf{f} + \boldsymbol{\mu}^T \mathbf{c} \; dt \; ,$$

where $\boldsymbol{\nu} \in \mathbb{R}^k$, $\boldsymbol{\lambda} \in \mathbb{R}^n$, and $\boldsymbol{\mu} \in \mathbb{R}^l$ are the costates associated with the constraints $\boldsymbol{\phi}$, $\mathbf{f}$, and $\mathbf{c}$, respectively. The costate $\boldsymbol{\mu}$ has the property

$$\begin{aligned} \boldsymbol{\mu} &\geq \mathbf{0} \;\; \text{if } \mathbf{c} = \mathbf{0} \\ \boldsymbol{\mu} &= \mathbf{0} \;\; \text{if } \mathbf{c} \leq \mathbf{0} \; . \end{aligned} \tag{4–1}$$

As a result, the Hamiltonian is defined as the integrand of the augmented cost as

$$\mathcal{H} = \mathcal{L} + \boldsymbol{\lambda}^T \mathbf{f} \; .$$

The necessary conditions for optimality are given in equation (4–2) and the transversality conditions are given in equation (4–3). [43, 44]

$$\begin{aligned} \dot{\mathbf{x}} &= \left(\frac{\partial \mathcal{H}}{\partial \boldsymbol{\lambda}} \right)^T \\ \dot{\boldsymbol{\lambda}} &= -\left(\frac{\partial \mathcal{H}}{\partial \mathbf{x}} \right)^T \\ \mathbf{0} &= \left(\frac{\partial \mathcal{H}}{\partial \mathbf{u}} \right)^T \end{aligned} \tag{4–2}$$

$$\begin{aligned} \boldsymbol{\lambda}(t_0) + \left(\frac{\partial \Phi}{\partial \mathbf{x}(t_0)} \right)^T + \left(\frac{\partial \boldsymbol{\phi}}{\partial \mathbf{x}(t_0)} \right)^T \boldsymbol{\nu} &= \mathbf{0} \;\; \text{if } \mathbf{x}(t_0) \text{ is unspecified} \\ -\boldsymbol{\lambda}(t_f) + \left(\frac{\partial \Phi}{\partial \mathbf{x}(t_f)} \right)^T + \left(\frac{\partial \boldsymbol{\phi}}{\partial \mathbf{x}(t_f)} \right)^T \boldsymbol{\nu} &= \mathbf{0} \;\; \text{if } \mathbf{x}(t_f) \text{ is unspecified} \end{aligned} \tag{4–3}$$

$$-\mathcal{H}(t_0) + \frac{\partial \Phi}{\partial t_0} + \left(\frac{\partial \boldsymbol{\phi}}{\partial t_0}\right)^T \boldsymbol{\nu} = 0 \text{ if } t_0 \text{ is unspecified}$$
$$\mathcal{H}(t_f) + \frac{\partial \Phi}{\partial t_f} + \left(\frac{\partial \boldsymbol{\phi}}{\partial t_f}\right)^T \boldsymbol{\nu} = 0 \text{ if } t_f \text{ is unspecified .}$$

Note that there is no explicit condition for the costate associated with the state and/or control constraints (i.e., $\boldsymbol{\mu}$). This costate is determined by equation (4–1) when the constraint is inactive (i.e., $\mathbf{c} < \mathbf{0}$) or by equation (4–1) and equation (4–2) simultaneously when the constraint is active (i.e., $\mathbf{c} = \mathbf{0}$). [43]

When state and/or control constraints are imposed and/or when the Hamiltonian is affine in the control, the Minimum Principle of Pontryagin (MPP) must be used since the necessary conditions for optimality cannot be employed. [43, 44] In essence, the MPP provides an additional necessary condition to determine the optimal control. This principle is stated as

$$\mathcal{H}(\mathbf{x}^*, \boldsymbol{\lambda}^*, \mathbf{u}^*, t^*) \leq \mathcal{H}(\mathbf{x}^*, \boldsymbol{\lambda}^*, \mathbf{u}, t^*) \;\; \forall\, \mathbf{u} \in \mathcal{U} \;,$$

where $\mathcal{U} = \{\mathbf{u} \in \mathbb{R}^m \mid \mathbf{c}(\mathbf{x}^*, \mathbf{u}, t^*) \leq \mathbf{0}\}$ is the set of admissible control inputs. The " * " superscript here and henceforth denotes the optimal solution of the variable.

Using the calculus of variations approach to solve the OCP increases the dimensionality by introducing new variables (i.e., costates) for each set of constraints. [44] Solving for the costates is necessary since they determine the optimal control as well as unknown boundary conditions. Also, the transversality conditions show that the boundary conditions for the states and costates are not known at the same boundary, making it difficult to solve for both states and costates simultaneously.

4.1.1 Minimum Time Problem

The minimum time problem can be stated as

$$\min_{\mathbf{u} \in \mathcal{U}} J = \int_{t_0}^{t_f} 1 \; dt = t_f - t_0 \;, \tag{4–4}$$

subject to

$$\dot{\mathbf{x}}(t) = \mathbf{a}(\mathbf{x}(t), t) + \mathbf{B}(\mathbf{x}(t), t)\mathbf{u}(t)$$

$$\mathbf{x}(t_0),\ \mathbf{x}(t_f),\ t_0 \text{ are specified}$$

$$u_{min} \leq u_i \leq u_{max} \text{ for } i = 1, 2, \ldots, m\ ,$$

where $\mathbf{a} : \mathbb{R}^n \times \mathbb{R} \rightarrow \mathbb{R}^n$ and $\mathbf{B} : \mathbb{R}^n \times \mathbb{R} \rightarrow \mathbb{R}^{n\times m}$. [44] Note that the dynamics constraint is affine in the control, which is a fair assumption for most dynamical systems. It is inherent that the final time be unspecified and that saturation limits be placed on the control. Otherwise, the solution would yield an infinite control action to reach the terminal condition immediately. Also, given the initial condition and the control constraint, the final condition $\mathbf{x}_f$ must to be reachable from the initial condition $\mathbf{x}_0$. [44, 71]

The Hamiltonian for this problem is defined as

$$\mathcal{H} = 1 + \boldsymbol{\lambda}^T \left[\mathbf{a} + \mathbf{B}\mathbf{u}\right]\ .$$

The MPP must be applied and results in the following condition

$$\boldsymbol{\lambda}^{*T}\mathbf{B}(\mathbf{x}^*, t^*)\mathbf{u}^* \leq \boldsymbol{\lambda}^{*T}\mathbf{B}(\mathbf{x}^*, t^*)\mathbf{u}\ . \tag{4–5}$$

If the matrix $\mathbf{B}$ is written as

$$\mathbf{B}(\mathbf{x}^*, t^*) = \begin{bmatrix} \mathbf{b}_1(\mathbf{x}^*, t^*) & \mathbf{b}_2(\mathbf{x}^*, t^*) & \cdots & \mathbf{b}_m(\mathbf{x}^*, t^*) \end{bmatrix}\ ,$$

where $\mathbf{b}_i \in \mathbb{R}^{n\times 1}$ are column matrices, then the product in equation (4–5) can be expressed as

$$\boldsymbol{\lambda}^{*T}\mathbf{B}(\mathbf{x}^*, t^*)\mathbf{u} = \sum_{i=1}^{m} \boldsymbol{\lambda}^{*T}\mathbf{b}_i(\mathbf{x}^*, t^*)u_i\ . \tag{4–6}$$

Substituting equation (4–6) into equation (4–5), the optimal control that satisfies the MPP is given as

$$u_i^* = \begin{cases} u_{max} & \text{if } \boldsymbol{\lambda}^{*T}\mathbf{b}_i(\mathbf{x}^*, t^*) < 0 \\ u_{min} & \text{if } \boldsymbol{\lambda}^{*T}\mathbf{b}_i(\mathbf{x}^*, t^*) > 0 \\ \text{undetermined} & \text{if } \boldsymbol{\lambda}^{*T}\mathbf{b}_i(\mathbf{x}^*, t^*) = 0 \end{cases} \quad \text{for } i = 1, 2, \ldots, m \,.$$

Note that this problem results in a "bang-bang" control structure. [43, 44] This means that the control lies on the boundary of $\mathcal{U}$ throughout the trajectory until the terminal conditions are reached. The optimal control depends on the values of the costates, thus the costates still need to be determined.

4.1.2 Fixed Time Minimum Control Effort Problem

The fixed time minimum control effort problem can be stated as

$$\min_{\mathrm{u} \in \mathcal{U}} J = \int_{t_0}^{t_f} \|\mathbf{u}(t)\| \, dt \,, \tag{4–7}$$

subject to

$$3 \tag{4–8}$$

Note that the final time is specified in this problem. If the final time was not specified, then the solution would be to apply an infinitesimal control action over an infinite amount of time. [44] Again, since there is a constraint on the control, the final condition $\mathbf{x}_f$ must be reachable from the initial condition $\mathbf{x}_0$. [44, 71]

The Hamiltonian for this problem is defined as

$$\mathcal{H} = \|\mathbf{u}\|_1 + \boldsymbol{\lambda}^T \left[\mathbf{a} + \mathbf{B}\mathbf{u}\right] \,,$$

The MPP must be applied and results in the following condition

$$\|\mathbf{u}^*\|_1 + \boldsymbol{\lambda}^{*T}\mathbf{B}(\mathbf{x}^*, t^*)\mathbf{u}^* \leq \|\mathbf{u}\|_1 + \boldsymbol{\lambda}^{*T}\mathbf{B}(\mathbf{x}^*, t^*)\mathbf{u} \,. \tag{4–9}$$

Using equation (4–6) and the definition of the 1-norm, the right hand side can be written as

$$\|\mathbf{u}\|_1 + \boldsymbol{\lambda}^{*T}\mathbf{B}(\mathbf{x}^*, t^*)\mathbf{u} = \sum_{i=1}^{m} |u_i| + \boldsymbol{\lambda}^{*T}\mathbf{b}_i(\mathbf{x}^*, t^*)u_i \ .$$

The optimal control that satisfies the MPP in equation (4–9) is obtained as

$$u_i^* = \begin{cases} u_{max} & \text{if } \boldsymbol{\lambda}^{*T}\mathbf{b}_i(\mathbf{x}^*, t^*) < -1 \\ 0 & \text{if } -1 < \boldsymbol{\lambda}^{*T}\mathbf{b}_i(\mathbf{x}^*, t^*) < 1 \\ u_{min} & \text{if } \boldsymbol{\lambda}^{*T}\mathbf{b}_i(\mathbf{x}^*, t^*) > 1 \\ \text{undetermined} & \text{if } \boldsymbol{\lambda}^{*T}\mathbf{b}_i(\mathbf{x}^*, t^*) = \pm 1 \end{cases} \quad \text{for } i = 1, 2, \ldots, m \ .$$

Note that this problem results in a "bang-off-bang" control structure. [43, 44] An interesting result that also arises from this problem is the tradeoff between the final time specified and the total control effort as depicted in Figure 4-1. [44] As noted in the figure, there is a lower bound on the final time specified due to the dynamics and control constraints. For linear systems, this bound can be determined and is a function of the initial conditions. [44] This bound exists for nonlinear systems, but it is not as easily determined. Another interesting result is if there are no path constraints, then the solution can be approximated using two impulses (at the initial and final time). [53, 72] This approximation, along with the tradeoff between the fixed time and control effort, is used later in the algorithm development in Chapter 6.

4.1.3 Finite Horizon Linear Quadratic Problem

The finite horizon LQ problem can be stated as

$$\min_{\mathbf{u} \in \mathcal{U}} J = \frac{1}{2}\mathbf{x}^T(t_f)\mathbf{S}_f\mathbf{x}(t_f) + \frac{1}{2}\int_{t_0}^{t_f} \mathbf{x}^T(t)\mathbf{Q}(t)\mathbf{x}(t) + \mathbf{u}^T(t)\mathbf{R}(t)\mathbf{u}(t)\ dt \ , \tag{4–10}$$

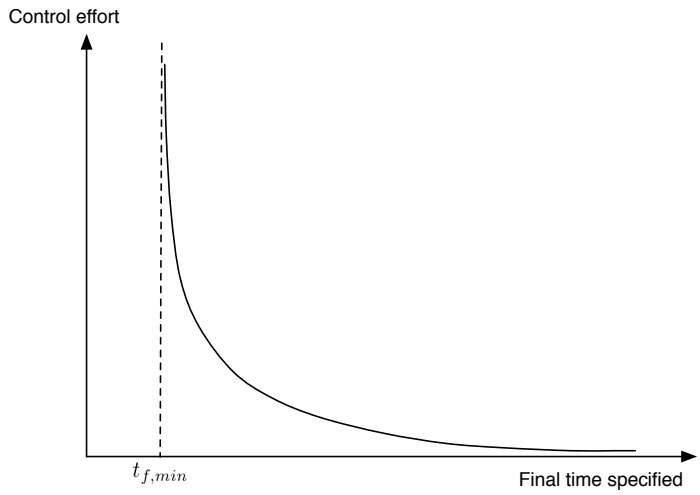

Figure 4-1. Tradeoff between final time and control effort

subject to

$$\dot{\mathbf{x}}(t) = \mathbf{A}(t)\mathbf{x}(t) + \mathbf{B}(t)\mathbf{u}(t)$$

$$\mathbf{x}(t_0),\ t_0,\ t_f \text{ are specified ,}$$

where $\mathbf{A}(t) \in \mathbb{R}^{n\times n}$, $\mathbf{B}(t) \in \mathbb{R}^{n\times m}$, $\mathbf{S}_f \in \mathbb{R}^{n\times n}$ is symmetric positive-semidefinite, $\mathbf{Q}(t) \in \mathbb{R}^{n\times n}$ is symmetric positive-semidefinte, and $\mathbf{R}(t) \in \mathbb{R}^{m\times m}$ is symmetric positive-definite. This LQ problem is entitled “finite horizon” since the final time is specified and finite, “linear” since the dynamics constraint is linear, and “quadratic” since the cost function is a quadratic function. It is also required that the pair $(\mathbf{A}, \mathbf{B})$ be controllable and the pair $(\mathbf{A}, \mathbf{Q})$ be observable. [43, 44, 71]

The Hamiltonian for this problem is defined as

$$\mathcal{H} = \frac{1}{2}(\mathbf{x}^T\mathbf{Q}\mathbf{x} + \mathbf{u}^T\mathbf{R}\mathbf{u}) + \boldsymbol{\lambda}^T(\mathbf{A}\mathbf{x} + \mathbf{B}\mathbf{u})\ .$$

One of the necessary conditions for optimality states

$$\left(\frac{\partial \mathcal{H}}{\partial \mathbf{u}}\right)^T = \mathbf{0}$$
$$\Rightarrow \mathbf{R}\mathbf{u}^* + \mathbf{B}^T\boldsymbol{\lambda}^* = \mathbf{0}\ ,$$

and leading to the optimal control law

$$\mathbf{u}^* = -\mathbf{R}^{-1}\mathbf{B}^T\boldsymbol{\lambda}^*\ .$$

Note that the MPP did not have to be employed here since there are no control constraints and the Hamiltonian is not affine in the control. From the transversality conditions, the boundary condition of the costate at the final time is given by

$$\boldsymbol{\lambda}^*(t_f) = \mathbf{S}_f\mathbf{x}_f\ . \tag{4–11}$$

The other two necessary conditions for optimality yield

$$\dot{\mathbf{x}}^* = \left(\frac{\partial \mathcal{H}}{\partial \boldsymbol{\lambda}}\right)^T = \mathbf{A}\mathbf{x}^* + \mathbf{B}\mathbf{u}^*$$
$$\dot{\boldsymbol{\lambda}}^* = -\left(\frac{\partial \mathcal{H}}{\partial \mathbf{x}}\right)^T = -\mathbf{Q}\mathbf{x}^* - \mathbf{A}^T\boldsymbol{\lambda}^*\ .$$

Substituting equation (4–16) for the control and writing in state space form yields the following system

$$\begin{bmatrix} \dot{\mathbf{x}}^* \\ \dot{\boldsymbol{\lambda}}^* \end{bmatrix} = \begin{bmatrix} \mathbf{A} & -\mathbf{B}\mathbf{R}^{-1}\mathbf{B}^T \\ -\mathbf{Q} & -\mathbf{A}^T \end{bmatrix} \begin{bmatrix} \mathbf{x}^* \\ \boldsymbol{\lambda}^* \end{bmatrix}\ ,\quad \begin{bmatrix} \mathbf{x}(t_0) \\ \boldsymbol{\lambda}(t_f) \end{bmatrix} = \begin{bmatrix} \mathbf{x}_0 \\ \mathbf{S}_f\mathbf{x}_f \end{bmatrix}\ , \tag{4–12}$$

where the state matrix is the Hamiltonian matrix.

Given the transversality condition in equation (4–11), the existence of a continuous linear mapping that relates the costates to the states is explored. This mapping is assumed to be of the form

$$\boldsymbol{\lambda}^*(t) = \mathbf{S}(t)\mathbf{x}^*(t)\ , \tag{4–13}$$

where $\mathbf{S}(t_f) = \mathbf{S}_f$. The time derivative of equation (4–13) yields

$$\dot{\boldsymbol{\lambda}}^* = \dot{\mathbf{S}}\mathbf{x}^* + \mathbf{S}\dot{\mathbf{x}}^* \ . \tag{4–14}$$

Substituting the expressions for the derivatives in equation (4–12) into equation (4–14) and using the relationship in equation (4–13) yields

$$\left[\dot{\mathbf{S}} + \mathbf{Q} - \mathbf{S}\mathbf{B}\mathbf{R}^{-1}\mathbf{B}^T\mathbf{S} + \mathbf{S}\mathbf{A} + \mathbf{A}^T\mathbf{S}\right]\mathbf{x}^* = \mathbf{0} \ .$$

Thus, the nontrivial solution (i.e., $\mathbf{x}^* \neq \mathbf{0}$) is given by

$$\dot{\mathbf{S}} + \mathbf{Q} - \mathbf{S}\mathbf{B}\mathbf{R}^{-1}\mathbf{B}^T\mathbf{S} + \mathbf{S}\mathbf{A} + \mathbf{A}^T\mathbf{S} = \mathbf{0} \ , \quad \mathbf{S}(t_f) = \mathbf{S}_f \ , \tag{4–15}$$

where this equation is the DRE. The DRE is a nonlinear matrix differential equation and an analytic solution cannot be determined in general. Also, since it only has a boundary condition specified at the final time, the DRE needs to be integrated backwards in time. [43, 68] Solving this equation also allows for the optimal control law to be written in state feedback form as

$$\mathbf{u}^* = -\mathbf{R}^{-1}\mathbf{B}^T\mathbf{S}\mathbf{x} \ . \tag{4–16}$$

4.2 Methods for Solving Optimal Control Problems

This section discusses the shooting method which is used for solving an OCP indirectly (i.e., via the calculus of variations approach). This method requires that the necessary conditions for optimality be set up, and that an initial guess for the unknown boundary conditions be guessed. A collocation method which is used for solving an OCP directly (i.e., without introducing costates) is also discussed. This method entails performing a transcription of the continuous time OCP to a finite dimensional nonlinear program (NLP) which makes solving the optimization problem more tractable.

4.2.1 Indirect Method: Shooting

Recall that the transversality conditions assert that if the state and/or time is specified at boundary, then the costate and/or Hamiltonian is not specified at that boundary. Additionally, note that if the Hamiltonian is not an explicit function of time, then it is constant since

$$\begin{aligned}
\frac{d\mathcal{H}}{dt} &= \frac{\partial H}{\partial t} + \frac{\partial H}{\partial \mathbf{x}}\dot{\mathbf{x}} + \frac{\partial \mathcal{H}}{\partial \boldsymbol{\lambda}}\dot{\boldsymbol{\lambda}} \\
\Rightarrow \frac{d\mathcal{H}}{dt} &= 0 + \frac{\partial H}{\partial \mathbf{x}}\left(\frac{\partial \mathcal{H}}{\partial \boldsymbol{\lambda}}\right)^T - \frac{\partial \mathcal{H}}{\partial \boldsymbol{\lambda}}\left(\frac{\partial H}{\partial \mathbf{x}}\right)^T \\
\Rightarrow \frac{d\mathcal{H}}{dt} &= 0\ .
\end{aligned}$$

To describe the process of applying the shooting method, an example is used for a general Hamiltonian boundary value problem (HBVP) where the initial state and time are specified and the final state and time are unspecified. A similar process can be applied if a different set of boundary conditions are known. First, the HBVP is established based on the necessary conditions for optimality as

$$\begin{bmatrix} \dot{\mathbf{x}} \\ \dot{\boldsymbol{\lambda}} \\ \dot{H} \end{bmatrix} = \begin{bmatrix} \left(\frac{\partial \mathcal{H}}{\partial \boldsymbol{\lambda}}\right)^T \\ -\left(\frac{\partial \mathcal{H}}{\partial \mathbf{x}}\right)^T \\ 0 \end{bmatrix}_{\mathrm{u}=\mathrm{u}^*}, \tag{4–17}$$

with $\mathbf{x}_0$ and t_0 specified.

The principal step of the shooting method is that a guess is made for the unknown initial values of $\boldsymbol{\lambda}(t_0)$ and $\mathcal{H}(t_0)$. Subsequently, equation (4–17) is integrated forward in time until the values obtained for $\boldsymbol{\lambda}(t_f)$ and $\mathcal{H}(t_f)$ from the transversality conditions are obtained. If they are not obtained, then a new guess is needed and the process should be repeated. A root-finding scheme can be employed to make refined guesses for subsequent iterations. However, if a poor initial guess is made, then it is unlikely that the shooting method converges. Unfortunately, there is no specific way of choosing a

"good" initial guess. In addition, each iteration of the shooting method requires numerical integration, which becomes computationally costly if multiple iterations are required. [73]

4.2.2 Direct Method: Collocation

Different approaches for collocation have been proposed and studied for solving OCPs. [49, 50, 74] The foundation of these approaches lies in choosing a finite set of collocation points and setting up an optimization problem (equivalent to the OCP), where the constraints of the OCP are enforced at the collocation points. This is done by first approximating the state at the N collocation points using a function approximation

$$\mathbf{x}(t) \approx \sum_{i=1}^{N} L_i(t)\mathbf{x}(t_i) \ , \tag{4–18}$$

where t_i are the collocation points, $\mathbf{x}(t_i)$ is the value of the state at the collocation point, and $L_i(t)$ is the Lagrange polynomial

$$L_i(t) = \prod_{\substack{j=1 \\ j\neq i}}^{N} \frac{t - t_j}{t_i - t_j} \ .$$

The collocation points are usually determined as roots of a special kind of polynomial. One approach is to use the roots of an orthogonal polynomial; this is called an orthogonal collocation method (OCM). [49, 50]

Differentiating equation (4–18) yields

$$\dot{\mathbf{x}}(t) \approx \sum_{i=1}^{N} \dot{L}_i(t)\mathbf{x}(t_i) = \sum_{i=1}^{N} \mathbf{f}(\mathbf{x}(t_i), \mathbf{u}(t_i), t_i) \ . \tag{4–19}$$

The dynamics constraint is now enforced using an algebraic equation at each collocation point. Next, a matrix is defined where the values of the state (which are still to be

determined) are concatenated as

$$\mathbf{X} = \begin{bmatrix} \mathbf{x}^T(t_1) \\ \mathbf{x}^T(t_2) \\ \vdots \\ \mathbf{x}^T(t_N) \end{bmatrix} .$$

Similarly, a matrix is defined where the values of the control (which are still to be determined) are concatenated as

$$\mathbf{U} = \begin{bmatrix} \mathbf{u}^T(t_1) \\ \mathbf{u}^T(t_2) \\ \vdots \\ \mathbf{u}^T(t_N) \end{bmatrix} ,$$

and the values of the dynamic constraints are concatenated as

$$\mathbf{F}(\mathbf{X}, \mathbf{U}, t_1, t_2, \dots, t_N) = \begin{bmatrix} \mathbf{f}^T(\mathbf{x}(t_1), \mathbf{u}(t_1), t_1) \\ \mathbf{f}^T(\mathbf{x}(t_2), \mathbf{u}(t_2), t_2) \\ \vdots \\ \mathbf{f}^T(\mathbf{x}(t_N), \mathbf{u}(t_N), t_N) \end{bmatrix} .$$

Thus, the dynamic constraint at each collocation points is written as

$$\mathbf{DX} = \mathbf{F}(\mathbf{X}, \mathbf{U}, t_1, t_2, \dots, t_N) ,$$

where the matrix **D** includes the derivatives of the Lagrangian polynomials evaluated at the collocation points. This matrix is not unique and depends on the collocation scheme used. [49, 50] The state and/or control constraints are employed in a similar manner, where the constraint is applied at each collocation point. This means the state and/or

control constraints are written as

$$\mathbf{C}(\mathbf{X}, \mathbf{U}, t_1, t_2, \dots, t_N) = \begin{bmatrix} \mathbf{c}^T(\mathbf{x}(t_1), \mathbf{u}(t_1), t_1) \\ \mathbf{c}^T(\mathbf{x}(t_2), \mathbf{u}(t_2), t_2) \\ \vdots \\ \mathbf{c}^T(\mathbf{x}(t_N), \mathbf{u}(t_N), t_N) \end{bmatrix} \leq \mathbf{0} \ .$$

In addition, the integral part of the cost functional is now approximated using a quadrature rule as

$$\int_{t_0}^{t_f} \mathcal{L}(\mathbf{x}, \mathbf{u}, t) \ dt \approx \sum_{i=1}^{N} w_i \mathcal{L}(\mathbf{x}(t_i), \mathbf{u}(t_i), t_i) \ ,$$

where w_i are the quadrature weights. [49, 50, 73] Now, the cost functional and constraints are all functions of the finite set of collocation points. The result is a finite dimensional optimization problem (i.e., NLP) of the form

$$\min_{\substack{\mathbf{X} \in \mathbb{R}^{N \times n} \\ \mathbf{U} \in \mathbb{R}^{N \times m}}} J = J(\mathbf{X}, \mathbf{U})$$

subject to

$$\mathbf{D}\mathbf{X} = \mathbf{F}(\mathbf{X}, \mathbf{U}, t_1, t_2, \dots, t_N)$$

$$\phi(\mathbf{x}(t_0), \mathbf{x}(t_N), t_0, t_N) = \mathbf{0}$$

$$\mathbf{C}(\mathbf{X}, \mathbf{U}, t_1, t_2, \dots, t_N) \leq \mathbf{0} \ .$$

The solution to a NLP is such that parameters $\mathbf{X}$ and $\mathbf{U}$ satisfy the Karush-Kuhn-Tucker (KKT) conditions. [75] However, since the KKT conditions are only enforced at the collocation points, global optimality (with respect to the original OCP) can not be guaranteed. Also, collocation methods still require an initial guess at each of the collocation points, where the convergence time to solve the NLP depends on the quality of the initial guess. [49, 50, 75]

A powerful tool that is available free-of-charge and works in the Matlab environment in conjunction with the Sparse Nonlinear Optimization (SNOPT) solver is the Gauss Pseudospectral Optimal Control Software (GPOPS). [76, 77] The GPOPS software allows the user to easily transcribe a continuous OCP to a NLP and solve the NLP using SNOPT. GPOPS is used to obtain the optimal trajectories in the following section. These trajectories are also used in Chapter 8 to determine whether there are performance differences in a higher fidelity model.

4.3 Optimal Rendezvous Trajectories

Four examples of optimal rendezvous trajectories are presented in this section. The rendezvous problem involves a passive spacecraft (i.e., target) and an active spacecraft (i.e., chaser). The translational motion for both spacecraft is governed by the Keplerian model in equation (2–1) (i.e., no disturbing accelerations). The objective of the rendezvous problem is

$$\mathbf{r}_{rel} = \mathbf{r}_c - \mathbf{r}_t \to \mathbf{0}$$
$$\dot{\mathbf{r}}_{rel} = \dot{\mathbf{r}}_c - \dot{\mathbf{r}}_t \to \mathbf{0}\ ,$$

where $\mathbf{r}_c$ and $\mathbf{r}_t$ are the position of the chaser and target, respectively. The parameters used are given in Table 4-1. The initial conditions of the target place it in a circular orbit with a 600 km altitude. The initial conditions of the chaser are chosen such that the relative position between the chaser and target (in the target's orbital frame) is

$$\mathbf{r}(t_0) = \begin{bmatrix} 500 & -500 & 500 \end{bmatrix}^T \text{ m}$$

and the relative velocity is zero. The following path constraint is also imposed on the chaser to ensure that it stays in low Earth orbit.

$$200 \text{ km} \leq \|\mathbf{r}_c\| - R_\oplus \leq 1000 \text{ km}$$

Similarly, the control constraint below is imposed

$$|f_i| \leq f_{max} \text{ for } i = 1, 2, 3 \ ,$$

which is representative of a control constraint for reaction jets. The markers in the plots for each example represent the collocation points used by GPOPS.

Table 4-1. Optimal rendezvous parameters

Parameter	Value	Units
$\mathbf{r}_c(t_0)$	$\begin{bmatrix}-1182.339411 & 6816.939420 & 904.891745\end{bmatrix}^T$	km
$\mathbf{v}_c(t_0)$	$\begin{bmatrix}0.175776 & -0.963776 & 7.494102\end{bmatrix}^T$	km/s
$\mathbf{r}_t(t_0)$	$\begin{bmatrix}-1182.959348 & 6817.396210 & 904.495486\end{bmatrix}^T$	km
$\mathbf{v}_t(t_0)$	$\begin{bmatrix}0.175776 & -0.963776 & 7.494102\end{bmatrix}^T$	km/s
f_{max}	0.001	km/s^2

4.3.1 Minimum Time Rendezvous

The minimum time problem specified in equation (4–4) requires that both the initial and final states be specified. The initial states are specified, yet the final states for the individual spacecraft are free. What is specified, is a relative position and velocity of zero at the final time. The relative trajectory, relative position, relative velocity, and control history are shown in Figure 4-2. The relative trajectory shown in Figure 4-2A indicates how the chaser approaches the target. The relative position and relative velocity plots in Figure 4-2B and Figure 4-2C, respectively, indicate that the final boundary conditions are satisfied. The control history plot in Figure 4-2D shows that a control structure similar to "bang-bang" is obtained. Recall that the optimal control is unspecified when the control is switched. The minimum time (which is also the cost) for rendezvous is $t_f^* = 49.86$ s.

4.3.2 Fixed Time Minimum Control Effort Rendezvous

The minimum control effort rendezvous problem specified in equation (4–7) requires that both the initial and final states be specified along with a final time. The initial states are specified, but the final states for the individual spacecraft are free. What is specified is a relative position and velocity of zero at the final time. The final time

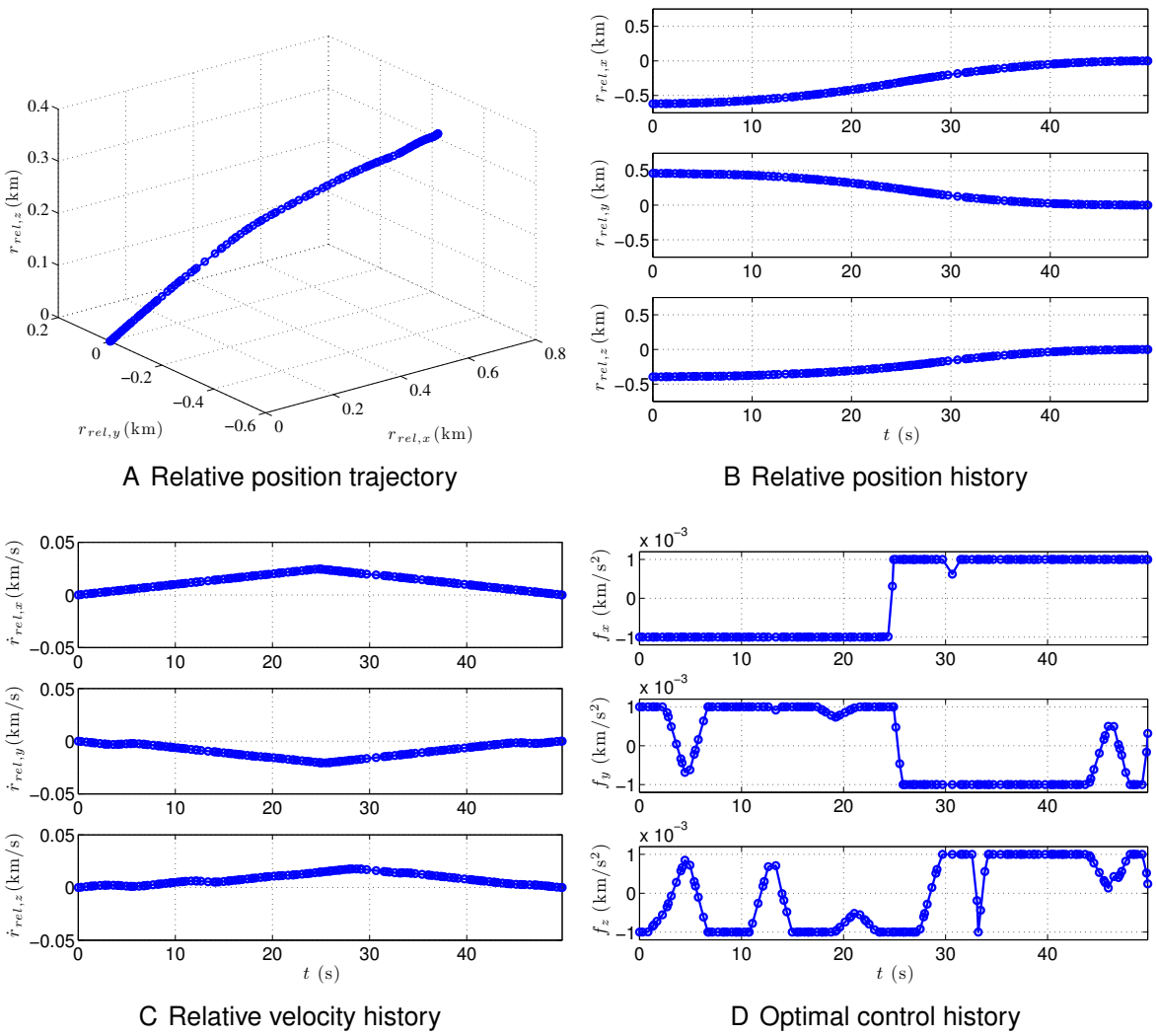

Figure 4-2. Minimum time rendezvous results

chosen for this problem is $t_f = 500$ s. The relative trajectory, relative position, relative velocity, and control history are shown in Figure 4-3. The relative trajectory shown in Figure 4-3A indicates how the chaser approaches the target. The relative position and relative velocity plots in Figure 4-3B and Figure 4-3C, respectively, indicate that the final boundary conditions are satisfied at the final time. The control history plot in Figure 4-3D shows that a similar control structure to “bang-off-bang” is obtained. Recall that the optimal control is unspecified when the control switches. The cost obtained (or total control effort) for this problem is $J = 6.61$ m/s. It should be noted that this problem

required less collocation points since the time range was longer and the optimal control was zero for a majority of the collocation points.

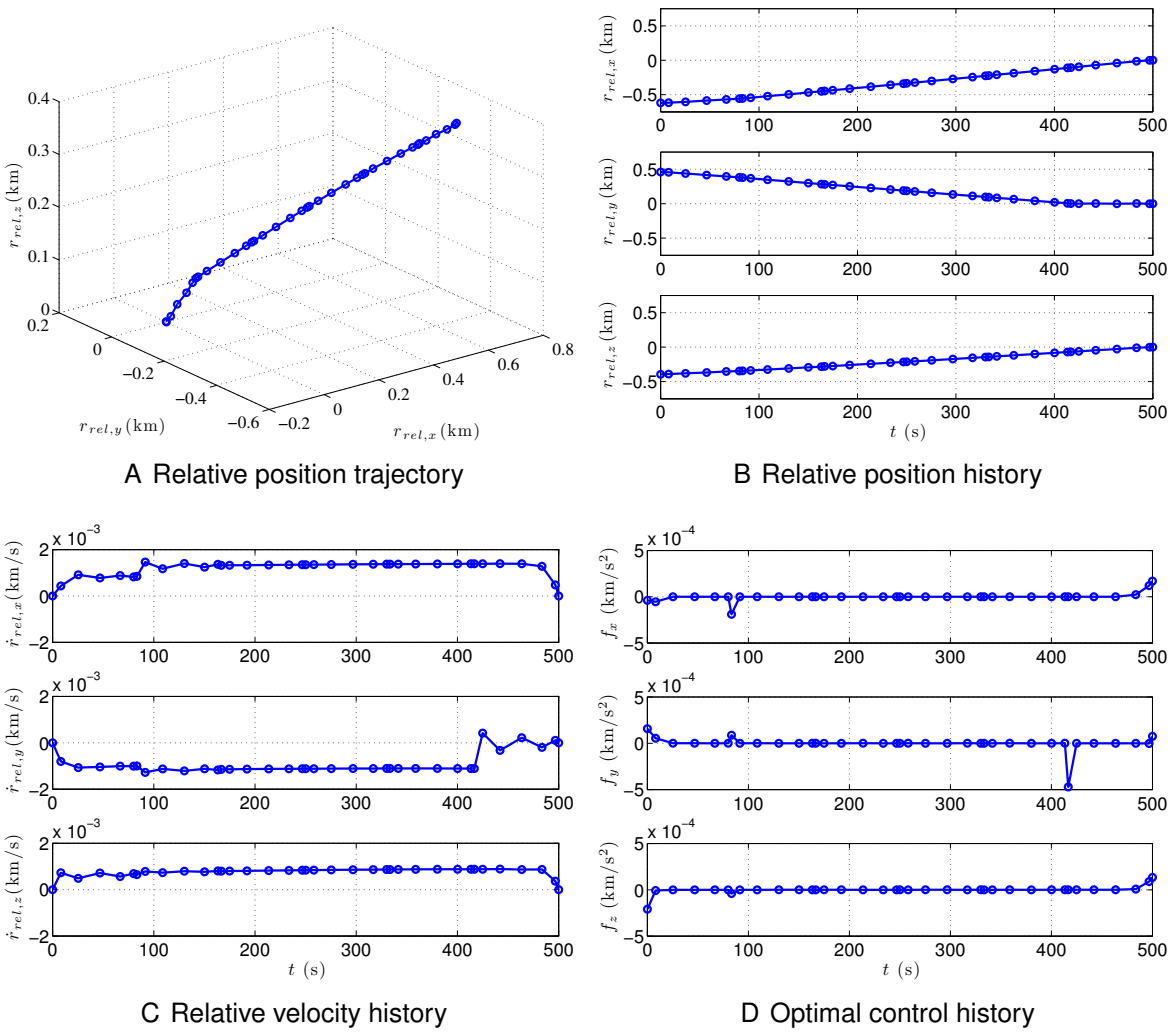

A Relative position trajectory

B Relative position history

C Relative velocity history

D Optimal control history

Figure 4-3. Fixed time minimum control effort rendezvous results

4.3.3 Finite Horizon Quadratic Cost Rendezvous

The quadratic problem specified in equation (4–10) requires that only the initial states be specified along with a final time. Instead, a cost is added for the initial and terminal boundary conditions desired. The time horizon chosen is the same as the minimum fuel problem (i.e., $t_f = 500$ s). The values used for the matrices that define the

cost functional are

$$\mathbf{S}_f = \mathbf{Q} = \begin{bmatrix} 10^4 \times \mathbf{I} & \mathbf{0} \\ \mathbf{0} & 10^2 \times \mathbf{I} \end{bmatrix} \in \mathbb{R}^{6\times 6}$$
$$\mathbf{R} = 10^{-1} \times \mathbf{I} \in \mathbb{R}^{3\times 3} \ .$$

The relative trajectory, relative position, relative velocity, and control history are shown in Figure 4-4. The relative trajectory shown in Figure 4-4A indicates how the chaser approaches the target. The relative position and relative velocity plots in Figure 4-4B and Figure 4-4C, respectively, indicate that the desired final states are virtually obtained at the final time. The control history plot in Figure 4-4D shows that the control decays as the terminal conditions are approached.

4.3.4 Constrained Fixed Time Minimum Fuel Rendezvous

The same cost is used as the fixed time minimum control effort problem with the added path constraint of

$$\|\mathbf{r}_c(t) - \mathbf{r}_o(t)\| \geq 100 \text{ m} \ ,$$

where $\mathbf{r}_o(t)$ is the position of an obstacle and is governed by the two body relative motion model in equation (2–1) (neglecting disturbances). The initial conditions used for the obstacle are

$$\mathbf{r}_o(t_0) = \begin{bmatrix} -1182.649497 & 6817.167778 & 904.693252 \end{bmatrix}^T \text{ km}$$
$$\mathbf{v}_o(t_0) = \begin{bmatrix} 0.175775 & -0.963776 & 7.494102 \end{bmatrix}^T \text{ km/s} \ .$$

The relative position trajectories of the chaser are shown at different instances in time in Figure 4-5. These figures indicate how the chaser is able to avoid the obstacle and reach the target. The relative position, relative velocity, and control history are shown in Figure 4-6. The relative position and relative velocity plots shown in Figure 4-6A and Figure 4-6B, respectively, indicate that the final boundary conditions

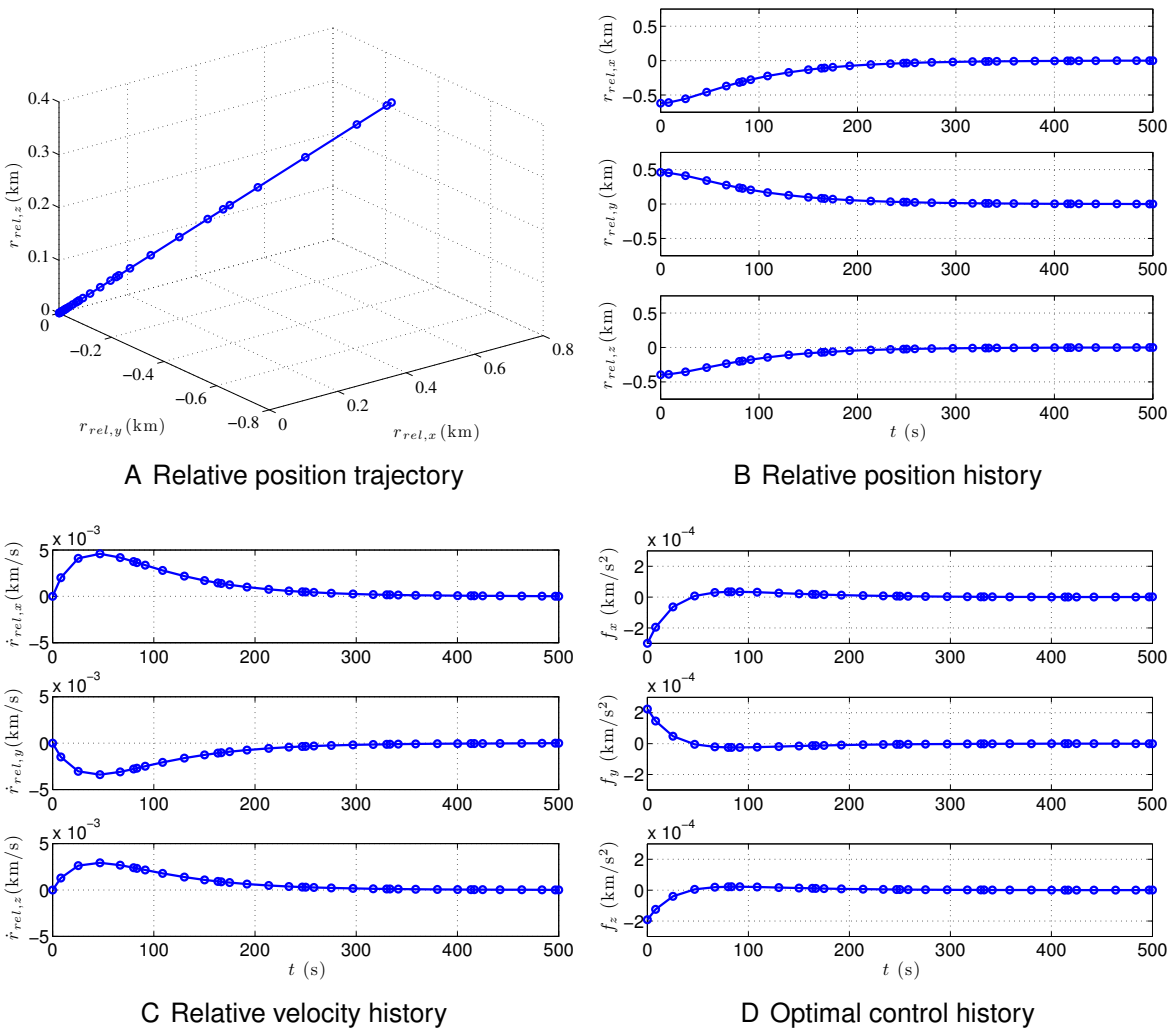

Figure 4-4. Finite horizon quadratic cost rendezvous results

are satisfied at the final time. The control history in Figure 4-6C that a “bang-off-bang” control structure is obtained, with a midcourse correction in the “z” direction.

4.4 Optimal Slew Maneuvers

Three examples of optimal slew maneuvers are presented in this section. Neglecting disturbances, the equations of motion used are the quaternion kinematics in equation (2–7) and the equations of motion in equation (2–4). The parameters used for

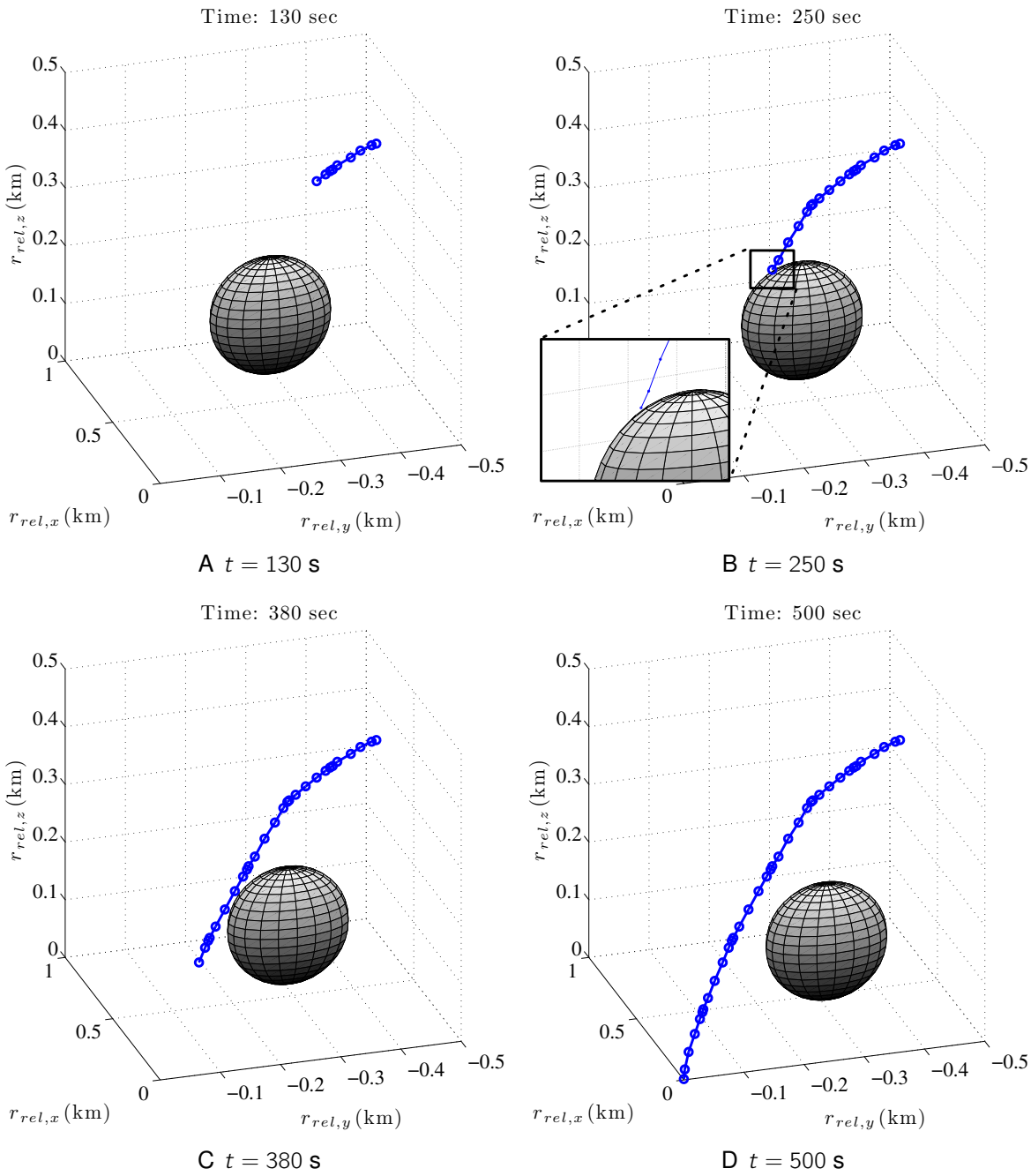

A $t = 130$ s

B $t = 250$ s

C $t = 380$ s

D $t = 500$ s

Figure 4-5. Constrained fixed time minimum control effort trajectories

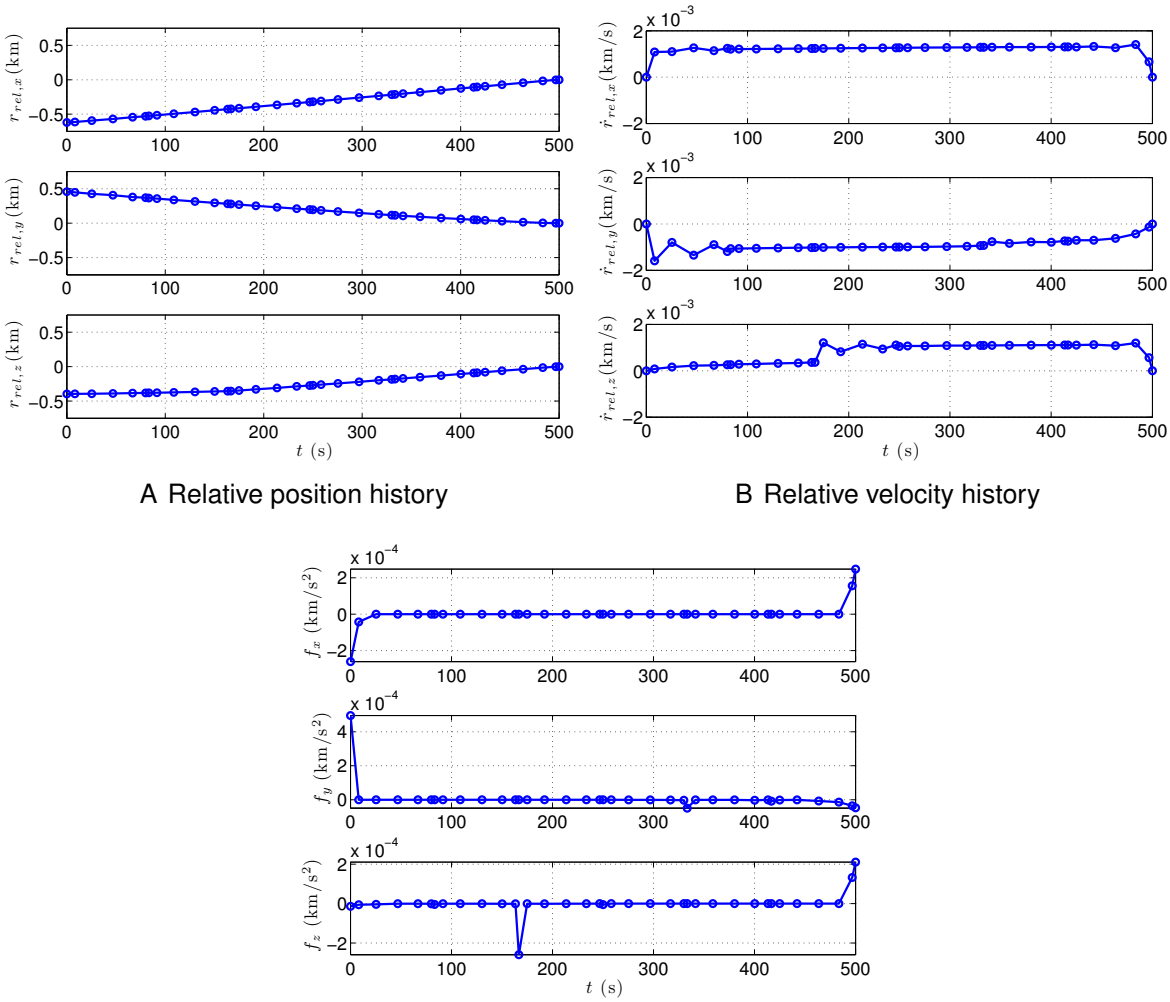

A Relative position history

B Relative velocity history

C Optimal control history

Figure 4-6. Constrained fixed time minimum control effort rendezvous results

the examples are given in Table 4-2. The objective of the slew maneuver is

$$\boldsymbol{\epsilon}, \boldsymbol{\omega} \to \mathbf{0}$$

$$\eta \to 1 \ .$$

These parameters define a 180° slew maneuver about the first body axis. The control constraint shown below is enforced

$$|\tau_i| \leq \tau_{max} \text{ for } i = 1, 2, 3 \ ,$$

which is representative of a control constraint for a reaction wheel attitude control system. The markers in the figures for each example represent the collocation points used by GPOPS.

Table 4-2. Optimal slew parameters

Parameter	Value	Units
$\mathbf{J}$	$\begin{bmatrix} 300 & 20 & 10 \\ 20 & 100 & 0 \\ 10 & 0 & 200 \end{bmatrix}$	$\mathrm{kg} \cdot \mathrm{m}^2$
$\mathbf{q}(t_0)$	$\begin{bmatrix} 1 & 0 & 0 & 0 \end{bmatrix}^T$	–
$\boldsymbol{\omega}(t_0)$	$\begin{bmatrix} 0 & 0 & 0 \end{bmatrix}^T$	rad/s
τ_{max}	1	$\mathrm{N} \cdot \mathrm{m}$

4.4.1 Minimum Time Slew

The minimum time problem specified in equation (4–4) requires that the initial and final states be specified, thus the final states are given by the control objective. The quaternion, angular velocity, and control history are shown in Figure 4-7. The quaternion and angular velocity plots in Figure 4-7A and Figure 4-7B, respectively, indicate that the final boundary conditions are obtained. The control history plot in Figure 4-7C shows that a control structure similar to “bang-bang” is obtained. The resulting minimum time (which is also the cost) for the slew maneuver is $t_f^* = 48.70$ s.

4.4.2 Fixed Time Minimum Control Effort Slew

The minimum control effort problem is specified in equation (4–7) had the same boundary conditions as the minimum time slew maneuver. The final time specified for this problem is $t_f = 100$ s. The quaternion, angular velocity, and control history are shown in Figure 4-8. The quaternion and angular velocity plots in Figure 4-8A and Figure 4-8B, respectively, indicate that the final boundary conditions are obtained at the final time specified. The control history plot in Figure 4-8C shows that a similar control structure to “bang-off-bang” is obtained. It is interesting to note that a large number of collocation points were required, and as a result the solution took a long time to obtain. This may be due to the fact that the optimal control is unspecified at the switching times.

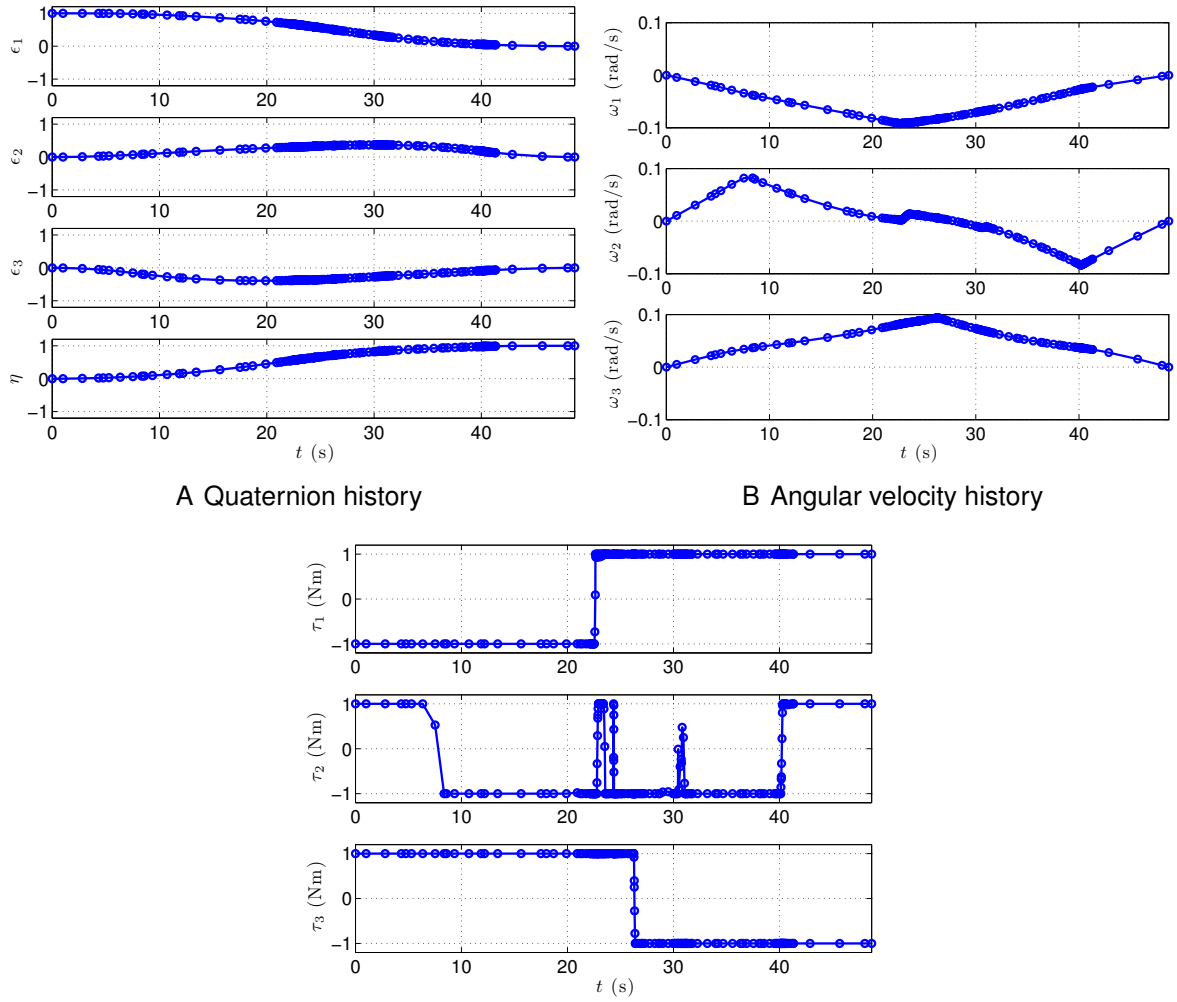

A Quaternion history

B Angular velocity history

C Optimal control history

Figure 4-7. Minimum time slew results

The interval where the control is unspecified also has some finite width. The optimal control solution also had small values in between the initial and final switches in the control. The final cost (and also the control effort) obtained is $J = 24.37$ N $\cdot$ m.

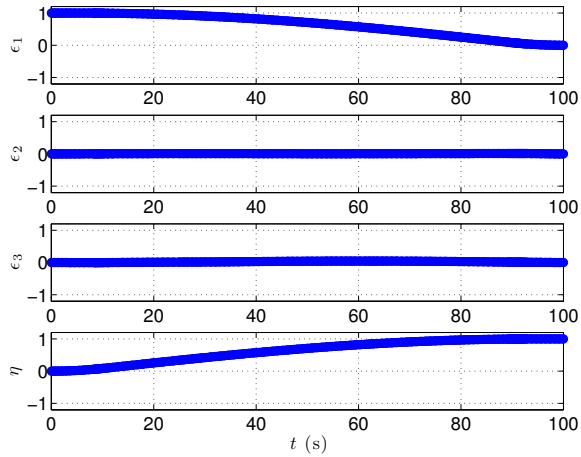

A Quaternion history

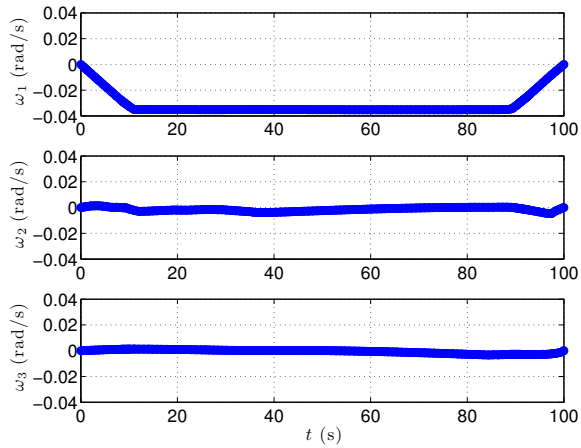

B Angular velocity history

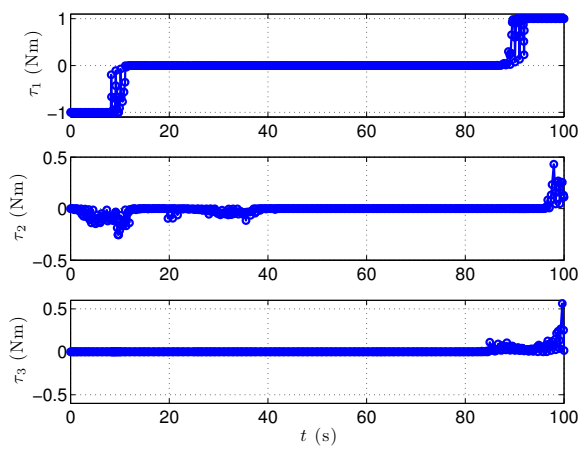

C Optimal control history

Figure 4-8. Fixed time minimum control effort slew results

4.4.3 Finite Horizon Quadratic Cost Slew

The finite horizon quadratic cost requires that only the initial conditions on the state and the final time be specified. The cost used for this problem is

$$J = \frac{1}{2}\left[\boldsymbol{\epsilon}^T(t_f)\mathbf{S}_{f,1}\boldsymbol{\epsilon}(t_f) + s_f(1-\eta(t_f))^2 + \boldsymbol{\omega}^T(t_f)\mathbf{S}_{f,2}\boldsymbol{\omega}(t_f)\right] + \ldots$$
$$\frac{1}{2}\int_{t_0}^{t_f} \boldsymbol{\epsilon}^T(t)\mathbf{Q}_1\boldsymbol{\epsilon}(t) + q(1-\eta(t))^2 + \boldsymbol{\omega}^T(t)\mathbf{Q}_2\boldsymbol{\omega}(t) + \boldsymbol{\tau}^T(t)\mathbf{R}\boldsymbol{\tau}(t)dt\ ,$$

where the values used for the matrices are

$$\mathbf{S}_{f,1} = \mathbf{S}_{f,2} = \mathbf{Q}_1 = \mathbf{Q}_2 = \mathbf{I} \in \mathbb{R}^{3\times 3}$$

$$\mathbf{R} = 10 \times \mathbf{I} \in \mathbb{R}^{3\times 3}$$

$$s_f = q = 1 \ .$$

The final time specified is the same as the minimum control effort problem (i.e., $t_f = 100$ s). The quaternion, angular velocity, and control history are shown in Figure 4-9. The quaternion and angular velocity plots in Figure 4-9A and Figure 4-9B, respectively, indicate that the desired final conditions are virtually obtained. The control history plot in Figure 4-9C indicates that the control is saturated for the initial onset of the maneuver, and then ramped down. This is attributed to the conservative saturation limits on the torque given the size of the spacecraft.

In conclusion, the theory related to generating optimal trajectories is presented in this chapter. In particular, the pertinent OCPs for close-range rendezvous are the minimum time problem and minimum control effort problem, and the pertinent OCP for the final approach or endgame of a proximity operation is the finite horizon LQ problem. A set of trajectories for each OCP is obtained for rendezvous and slew maneuvers. These trajectories are later used as baseline comparisons for the algorithms developed. It is also later determined whether these trajectories are realized using a high fidelity model.

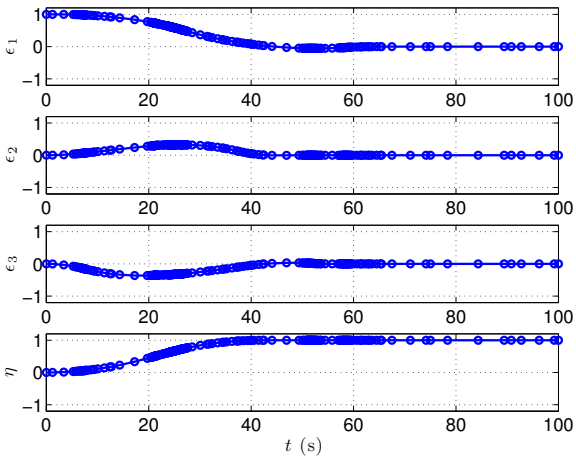

A Quaternion history

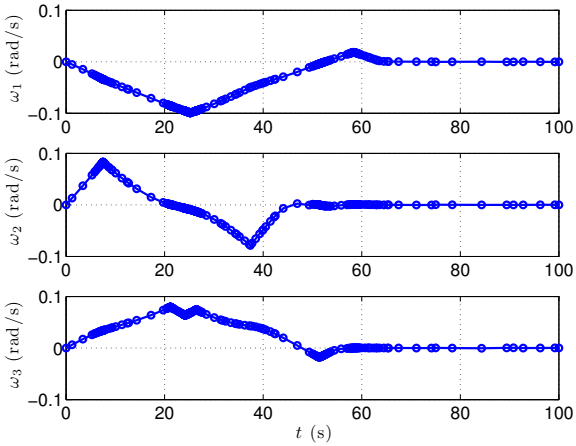

B Angular velocity history

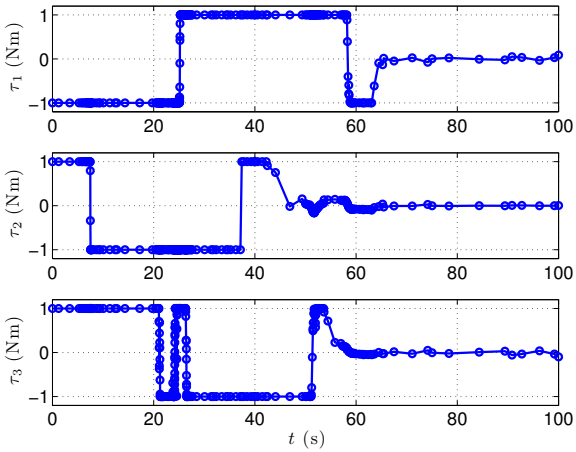

C Optimal control history

Figure 4-9. Finite horizon quadratic cost slew results

CHAPTER 5
ARTIFICIAL POTENTIAL FUNCTION METHOD

Using an artificial potential is an effective method for deriving guidance laws. Just as a potential shapes certain force fields (e.g., gravity, electromagnetism, etc.), an artificial potential can be defined to shape an artificial force field for determining a control law. The artificial potential must have certain properties such that the resulting control law provides stable results. This chapter discusses the APF methodology. Two sets of examples are presented where the APF method is applied to the Clohessy-Wiltshire-Hill (CWH) equation and the small angle approximation (SAA) equation derived in Appendix A.

5.1 Development

An artificial potential is defined by superimposing attractive and repulsive potentials. The purpose of the attractive potential is to impose a global minimum at the desired terminal position $\mathbf{x}_f$. The repulsive potentials create regions of high potential at positions $\mathbf{x}_i$ of the state space that are to be avoided. [56–59, 78]

Different forms of artificial potentials have been explored. One form is to use harmonic functions (i.e., satisfy Laplace's equation) as potentials since these functions do no exhibit local minima when superimposed. [79–81] However, the gradient of sinks and sources (which are typical harmonic functions used for attractive and repulsive potentials, respectively) is undefined at their center and is near zero away from their center. Thus, scaling the sinks and sources can be difficult.

Another typical choice for an attractive potential function (and the one used in this work) is a quadratic function

$$\phi_a(\mathbf{x}) = \frac{1}{2}(\mathbf{x} - \mathbf{x}_f)^T \mathbf{P}(\mathbf{x} - \mathbf{x}_f) \ , \tag{5–1}$$

where $\mathbf{P}$ is a symmetric positive-definite weighting matrix that shapes the attractive potential. A typical choice for defining repulsive potentials (and the one used in this

work) is using Gaussian functions

$$\phi_r(\mathbf{x}) = \sum_{i=1}^{N} \psi_i \exp\left[-\frac{(\mathbf{x}-\mathbf{x}_i)^T \mathbf{N}_i (\mathbf{x}-\mathbf{x}_i)}{\sigma_i}\right] ,$$

where ψ_i and σ_i are the height and width parameters, respectively, and $\mathbf{N}_i$ is a symmetric positive-definite weighting matrix that shapes the ith repulsive potential. [57, 59]. Using these functions might yield local minima in the artificial potential (depending on the parameters chosen for the repulsive potential), which may cause convergence problems. [82, 83] Regardless of the choice of APFs used, the total artificial potential is defined as the sum of the attractive and repulsive potentials.

$$\phi = \phi_a + \phi_r \tag{5–2}$$

An example of an APF consisting of a quadratic attractive potential and two Gaussian repulsive potentials for a two degree of freedom system is illustrated in Figure 5-1.

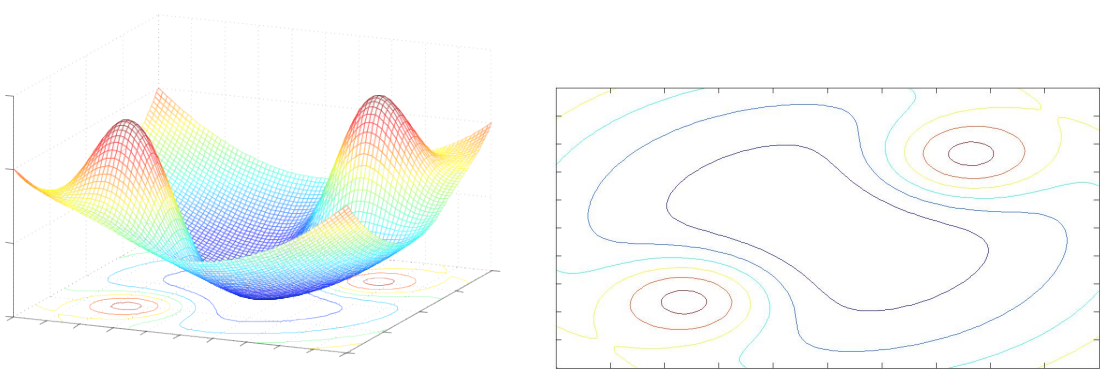

A 3D surface plot with contour outline

B 2D contour plot

Figure 5-1. Artificial potential function (APF) example

Several combinations of the types of APFs have been used to alleviate some of the drawbacks associated with each of them. [56, 58, 60, 84–86] Systematically resolving the local minima problem is beyond the scope of this work. However, since the close-range rendezvous workspace is sparse, there is a considerable separation between obstacles and the goal. Thus, local minimum are avoided for most sets of

obstacle parameters. If the local minima problem cannot be avoided, then different forms of potentials should be used.

A feedback controller can be developed from the definition of the APF, where a force in the opposite direction of the local gradient of the artificial potential is applied when the rate of change of the artificial potential is positive. This feedback controller is defined as

$$\mathbf{u}(\mathbf{x}, \dot{\mathbf{x}}) = \begin{cases} -k\boldsymbol{\nabla}_{\mathrm{x}}\phi - (\dot{\mathbf{x}} - \dot{\mathbf{x}}_f) & \text{if } \dot{\phi} \geq 0 \\ \mathbf{0} & \text{otherwise} \end{cases}, \tag{5–3}$$

where k is a positive gain, and

$$\begin{aligned}
\boldsymbol{\nabla}_{\mathrm{x}}\phi &= \left(\frac{\partial\phi}{\partial\mathbf{x}}\right)^T \\
\Rightarrow \boldsymbol{\nabla}_{\mathrm{x}}\phi &= \mathbf{P}(\mathbf{x} - \mathbf{x}_f) - \sum_{i=1}^{N} 2\frac{\psi_i}{\sigma_i} \exp\left[-\frac{(\mathbf{x} - \mathbf{x}_i)^T\mathbf{N}_i(\mathbf{x} - \mathbf{x}_i)}{\sigma_i}\right] \mathbf{N}_i(\mathbf{x} - \mathbf{x}_i) \\
\dot{\phi} &= \left(\frac{\partial\phi}{\partial\mathbf{x}}\right)\frac{d\mathbf{x}}{dt} + \left(\frac{\partial\phi}{\partial\mathbf{x}_f}\right)\frac{d\mathbf{x}_f}{dt} + \sum_{i=1}^{N}\left(\frac{\partial\phi}{\partial\mathbf{x}_i}\right)\frac{d\mathbf{x}_i}{dt} \\
\Rightarrow \dot{\phi} &= (\mathbf{x} - \mathbf{x}_f)^T\mathbf{P}\left(\dot{\mathbf{x}} - \dot{\mathbf{x}}_f\right) - \sum_{i=1}^{N} 2\frac{\psi_i}{\sigma_i}(\mathbf{x} - \mathbf{x}_i)^T \exp\left[-\frac{(\mathbf{x} - \mathbf{x}_i)^T\mathbf{N}_i(\mathbf{x} - \mathbf{x}_i)}{\sigma_i}\right] \mathbf{N}_i\left(\dot{\mathbf{x}} - \dot{\mathbf{x}}_i\right) .
\end{aligned}$$

5.2 Numerical Examples

Two sets of numerical examples are presented to demonstrate the APF method. In the first example, the APF method is applied to the CWH equation with a grid of 14 static obstacles in the state space. In the second example, the APF method is applied to the SAA equation with a tumbling satellite.

5.2.1 Clohessy-Wiltshire-Hill Example

The parameters used in this example are given in Table 5-1. The goal of the chaser (initially located at the relative position $\mathbf{r}_0$) is to reach the target (located at the origin) while avoiding the obstacles. A set of 14 static obstacles are placed in the state space at the positions shown below.

$$\mathbf{r}_1 = \begin{bmatrix} 500 & 0 & 0 \end{bmatrix}^T \quad \mathbf{r}_2 = \begin{bmatrix} -500 & 0 & 0 \end{bmatrix}^T \quad \mathbf{r}_3 = \begin{bmatrix} 0 & 500 & 0 \end{bmatrix}^T$$

$$\mathbf{r}_4 = \begin{bmatrix} 0 & -500 & 0 \end{bmatrix}^T \quad \mathbf{r}_5 = \begin{bmatrix} 0 & 0 & 500 \end{bmatrix}^T \quad \mathbf{r}_6 = \begin{bmatrix} 0 & 0 & -500 \end{bmatrix}^T$$

$$\mathbf{r}_7 = \begin{bmatrix} 250 & 250 & 250 \end{bmatrix}^T \quad \mathbf{r}_8 = \begin{bmatrix} 250 & -250 & 250 \end{bmatrix}^T \quad \mathbf{r}_9 = \begin{bmatrix} 250 & 250 & -250 \end{bmatrix}^T$$

$$\mathbf{r}_{10} = \begin{bmatrix} 250 & -250 & -250 \end{bmatrix}^T \quad \mathbf{r}_{11} = \begin{bmatrix} -250 & 250 & 250 \end{bmatrix}^T \quad \mathbf{r}_{12} = \begin{bmatrix} -250 & -250 & 250 \end{bmatrix}^T$$

$$\mathbf{r}_{13} = \begin{bmatrix} -250 & 250 & -250 \end{bmatrix}^T \quad \mathbf{r}_{14} = \begin{bmatrix} -250 & -250 & -250 \end{bmatrix}^T$$

These positions define an obstacle grid that does not yield local minima, yet still clutters the state space. Static obstacles are practical for avoiding spacecraft that are tethered or flying in formation. Otherwise, these obstacles would not be static and would drift. However, static obstacles are used for simplicity and to demonstrate the collision avoidance abilities of the APF algorithm.

Table 5-1. Relative translation parameters

Parameter	Value	Units
n	0.0012	rad/s
$\mathbf{r}_0$	$\begin{bmatrix} -750 & 500 & -750 \end{bmatrix}^T$	m
$\mathbf{v}_0$	$\begin{bmatrix} 0.5 & -2 & 0 \end{bmatrix}^T$	m/s
$\mathbf{r}_f$	$\begin{bmatrix} 0 & 0 & 0 \end{bmatrix}^T$	m
f_{max}	1	m/s
$\mathbf{P}$	$\mathbf{I} \in \mathbb{R}^{3\times3}$	s^{-2}
$\mathbf{N}_i$	$\mathbf{I} \in \mathbb{R}^{3\times3}$	s^{-2}
ψ_i	1.5×10^5	–
σ_i	1.0×10^4	m^2
k	0.002	–

For this example, the control constraint shown below is enforced.

$$\|\mathbf{f}\|_2 \leq f_{max}$$

Settling time is used as a performance metric, where the trajectory obtained is considered settled when $\|\mathbf{r}\| \leq 10$ m. The running control effort cost is also used as

a performance metric and is defined as

$$V(t) = \int_{t_0}^{t} \|\mathbf{u}\|_1 \, d\varepsilon \, .$$

The results obtained are displayed in Figure 5-2. The trajectory plot in Figure 5-2A shows that an obstacle is encountered and the chaser is able to maneuver around it. The position and velocity plots in Figure 5-2B and Figure 5-2C, respectively, indicate that the chaser is able to reach the target with zero velocity. The corresponding control history is given in Figure 5-2D.

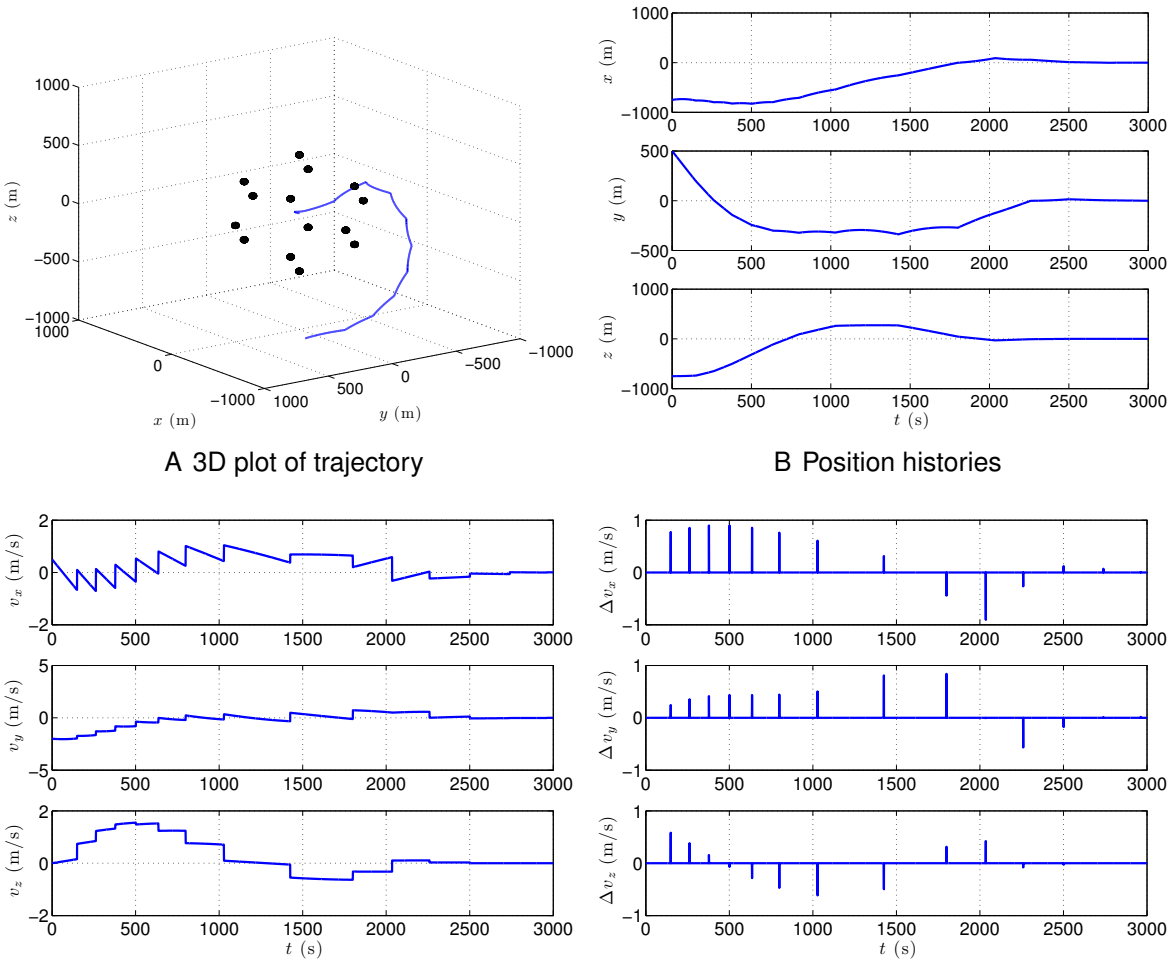

A 3D plot of trajectory

B Position histories

C Velocity histories

D Control histories

Figure 5-2. APF method results using Clohessy-Wiltshire-Hill (CWH) equation

The settling time obtained is 2620 s and the control effort at the settling time is 16.94 m/s^2. The running cost is shown in Figure 5-3 which illustrates how the cost increases with every control action.

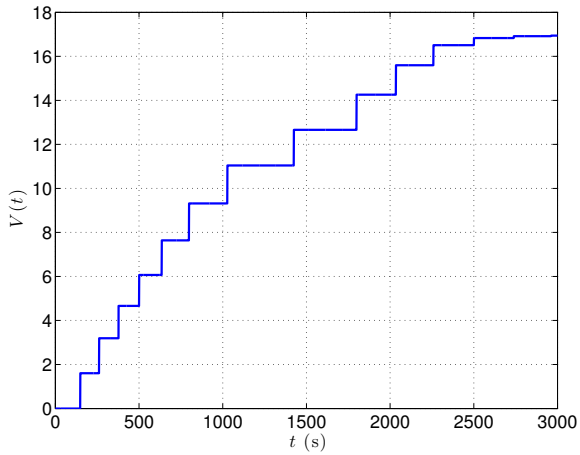

Figure 5-3. APF method running cost using CWH equation

5.2.2 Small Angle Approximation Example

The parameters used in this example are shown in Table 5-2. The goal of the chaser (with initial relative orientation $\boldsymbol{\alpha}_0$ to the target) is to reach a relative orientation of $\boldsymbol{\alpha} = \mathbf{0}$ rad with the target that is tumbling at the rate $\boldsymbol{\omega}_{\mathrm{t}}$. The control constraint shown below is enforced.

$$|\tau_i| \leq \tau_{max} \text{ for } i = 1, 2, 3$$

Settling time is used as performance metric where the trajectory obtained is considered settled when $\|\boldsymbol{\alpha}\| \leq 0.01$ rad. The running control effort cost is also used as a performance metric and is defined as

$$V(t) = \int_{t_0}^{t} \|\boldsymbol{\tau}\|_1 \, d\varepsilon \, .$$

The results for this example are displayed in Figure 5-4. The relative orientation and relative angular velocity plots in Figure 5-4A and Figure 5-4B, respectively, indicate that both these parameters converge to zero. The corresponding control history is

Table 5-2. Relative orientation parameters

Parameter	Value	Units
$\mathbf{J}$	$\begin{bmatrix} 300 & 20 & 10 \\ 20 & 100 & 0 \\ 10 & 0 & 200 \end{bmatrix}$	$\mathrm{kg} \cdot \mathrm{m}^2$
$\boldsymbol{\omega}_t$	$\begin{bmatrix} 0.25 & -0.25 & 0.25 \end{bmatrix}^T$	rad/s
$\boldsymbol{\alpha}_0$	$\begin{bmatrix} 0.3 & -0.2 & -0.15 \end{bmatrix}^T$	rad
$\dot{\boldsymbol{\alpha}}_0$	$\begin{bmatrix} 0 & 0 & 0 \end{bmatrix}^T$	rad/s
$\boldsymbol{\alpha}_f$	$\begin{bmatrix} 0 & 0 & 0 \end{bmatrix}^T$	rad
τ_{max}	20	$\mathrm{N} \cdot \mathrm{m}$
$\mathbf{P}$	$\mathbf{I} \in \mathbb{R}^{3\times3}$	s^{-2}
k	2	–

given in Figure 5-4C. The settling time obtained is 22.7 s. Note that the running cost in Figure 5-4D linearly increases with time since the controller continuously compensates for the tumbling satellite.

In conclusion, the APF method is discussed in this chapter. The procedure for defining an APF and the corresponding control law is presented. Two examples of the APF method are also presented using the CWH and SAA equations. From the discussion and examples in this chapter, the APF method is a useful tool for computing guidance laws as long as its restrictions are understood.

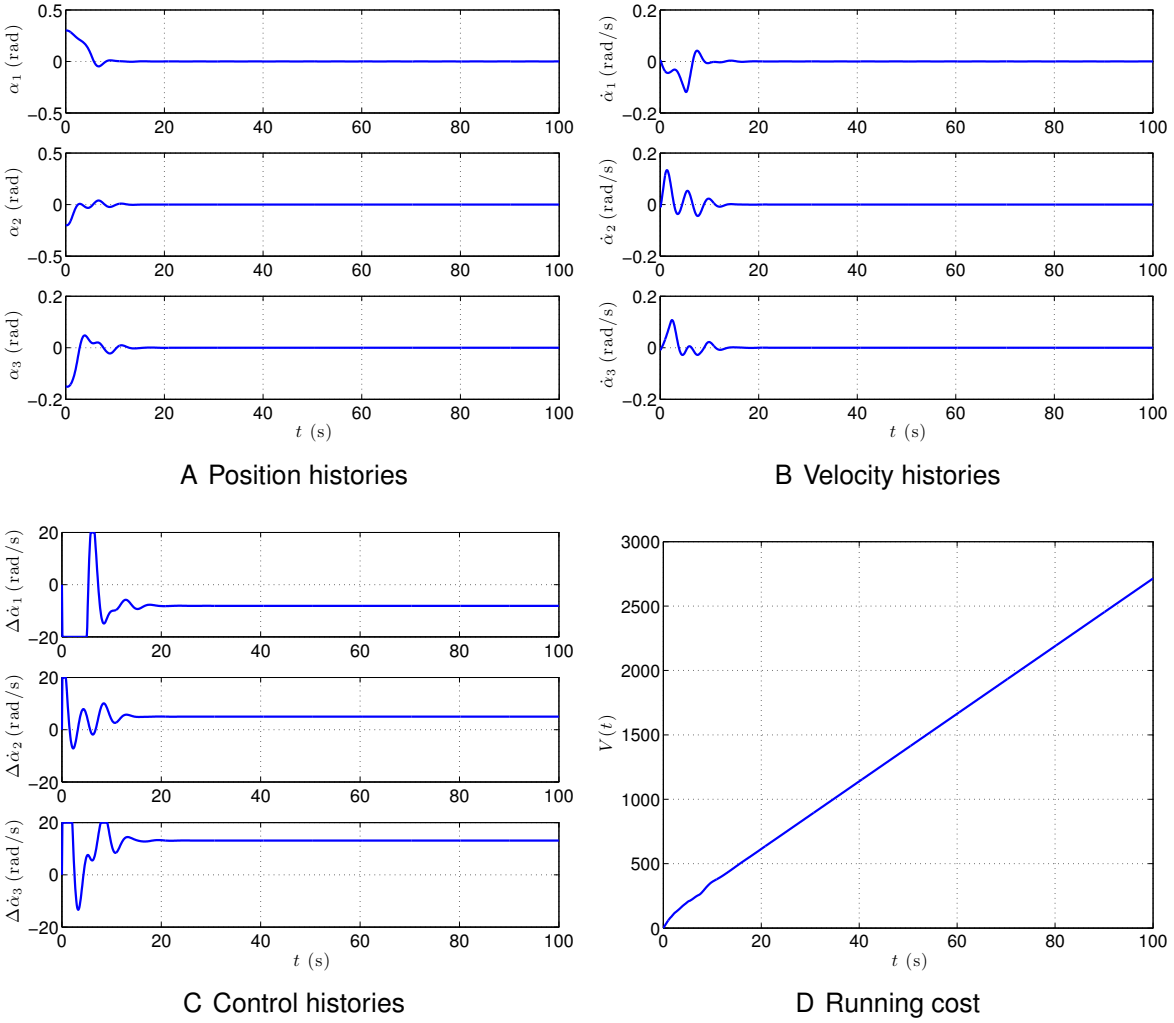

Figure 5-4. APF method results using small angle approximation (SAA) equation

CHAPTER 6
ADAPTIVE ARTIFICIAL POTENTIAL FUNCTION METHOD

The artificial potential function (APF) method discussed in Chapter 5 is a method that can be used in a rapid path-planning framework. It was shown that the APF method is well-suited for close-range rendezvous scenarios and relative orientation problems. However, a drawback of the APF method is that it has no consideration of the dynamics or a performance index. The adaptive artificial potential function (AAPF) method is a modification of the APF method with the intent of embedding the dynamics and performance index in the formulation. The APF framework is adopted because of its low complexity and favorable convergence characteristics. The development of the AAPF method and the adaptive update law used to determine the weighting parameters of the APF is discussed in this chapter. A stability analysis is also presented which shows that stability is obtained for unconstrained cases (i.e., no obstacle regions), but that stability cannot be proven for constrained cases (i.e., with obstacle regions). Finally, two numerical examples are presented where the AAPF method is applied to the Clohessy-Wiltshire-Hill (CWH) equation and the small angle approximation (SAA) equation derived in Appendix A.

6.1 Development

It was shown in Chapter 5 that different forms of APFs exist. However, there is no systematic approach for defining an APF for a particular set of dynamics or performance criteria. The parameters that define APFs are chosen ad hoc, thus it is difficult to determine the parameters which yield the best performance with least control effort. Additionally, since there is no consideration of the dynamics, the trajectories obtained from the APF method are not defined such that the goal is reached at a specified time. These factors are particularly important with close-range rendezvous of spacecraft, where control effort, power, and time must be conserved. Therefore, path-planning algorithms for close-range rendezvous must take these factors into account. To remedy

the drawbacks of using the APF method for close-range rendezvous, the AAPF method is developed by embedding the dynamics and a performance criteria in the formulation.

To embed the dynamics in the formulation of the AAPF method, the relative motion models discussed in Appendix A are used. These models are used since the two point boundary value problem (TPBVP) solutions are obtained analytically and the TPBVP solution is used in the formulation to include the dynamics. To do this, consider the same form of the attractive potential in equation (5–1) except let the attractive weighting matrix be time dependent (i.e., $\mathbf{P} = \mathbf{P}(t)$). To enforce the symmetric positive-definite condition, a Cholesky factorization $\mathbf{P}(t) = \mathbf{R}^T(t)\mathbf{R}(t)$ is used,where $\mathbf{R}(t)$ is the upper triangular matrix termed the "Cholesky factor" and is defined as

$$\mathbf{R}(t) = \begin{bmatrix} \rho_{11}(t) & \rho_{12}(t) & \rho_{13}(t) \\ 0 & \rho_{22}(t) & \rho_{23}(t) \\ 0 & 0 & \rho_{33}(t) \end{bmatrix}.$$

Due to the adaptation, the time derivative of the attractive potential now contains additional terms as shown below.

$$\begin{aligned} \dot{\phi}_a &= \frac{\partial \phi_a}{\partial t} + \left(\frac{\partial \phi_a}{\partial \mathbf{x}}\right)\frac{d\mathbf{x}}{dt} + \left(\frac{\partial \phi_a}{\partial \mathbf{x}_f}\right)\frac{d\mathbf{x}_f}{dt} \\ \Rightarrow \dot{\phi}_a &= \frac{1}{2}(\mathbf{x}-\mathbf{x}_f)^T(\dot{\mathbf{R}}^T\mathbf{R} + \mathbf{R}^T\dot{\mathbf{R}})(\mathbf{x}-\mathbf{x}_f) + (\mathbf{x}-\mathbf{x}_f)^T\mathbf{R}^T\mathbf{R}\,(\dot{\mathbf{x}}-\dot{\mathbf{x}}_f) \end{aligned}$$

A time dependent attractive is used since this is what governs how the goal is approached. Using a time dependent repulsive potential simply changes the shape and size of the obstacle region and does not necessarily improve performance. As a result, the form of the repulsive potential remains the same.

Since the form of the APF is the same, the form of the control law also remains the same as shown in equation (5–3). The difference is that the weights in $\mathbf{R}(t)$ must be chosen effectively to improve performance. This is achieved by allowing the negative gradient of the attractive potential to adapt to the velocity profile of the TPBVP solution.

The formulation of the TPBVP velocity profile is presented in Appendix B. The velocity profile obtained in equation (B–6) must then be written in a feedback form by letting the time $t_0 = t$ and the initial condition $\mathbf{x}_0 = \mathbf{x}$. [40]

$$\dot{\mathbf{x}}_d(\mathbf{x}, t) = \mathbf{\Phi}_{22}(-T)\mathbf{\Phi}_{12}^{-1}(-T)\mathbf{x} + \mathbf{\Phi}_{12}^{-1}(T)\left[\mathbf{x}_f - \mathbf{x}_t\right] \tag{6–1}$$

Note that $\mathbf{x}_t$ is now time dependent and is shown below.

$$\mathbf{x}_t = \int_t^T \mathbf{\Phi}_{12}(T - \varepsilon)\mathbf{B}_2\mathbf{u}\, d\varepsilon$$

For the relative translation problem, the states in question are the components of the relative position (i.e., $\mathbf{x} = \mathbf{r}$). To obtain the velocity profile, equation (6–1) is used and is defined as

$$\mathbf{v}_d = \mathbf{\Phi}_{22}(-T)\mathbf{\Phi}_{12}^{-1}(-T)\mathbf{r} - \mathbf{\Phi}_{12}^{-1}(T)\mathbf{r}_f \ ,$$

where $\mathbf{\Phi}_{12}, \mathbf{\Phi}_{22}$ are blocks of the STM for the CWH equation and T is the transfer time of the TPBVP solution for the CWH equations. Note that $\mathbf{r}_t = \mathbf{0}$ since $\mathbf{u} = \mathbf{0}$ (i.e., no constant forcing term). Also, note that the velocity profile depends on T, where this parameter is chosen such that $\mathbf{\Phi}_{12}^{-1}(T)$ exists.

The relative orientation problem is similar where the states in question are the components of the relative orientation (i.e., $\mathbf{x} = \boldsymbol{\alpha}$). To obtain the velocity profile, equation (6–1) is used and is defined as

$$\dot{\boldsymbol{\alpha}}_d = \mathbf{\Phi}_{22}(-T)\mathbf{\Phi}_{12}^{-1}(-T)\boldsymbol{\alpha} + \mathbf{\Phi}_{12}^{-1}(T)\boldsymbol{\alpha}_f \ ,$$

where $\mathbf{\Phi}_{12}, \mathbf{\Phi}_{22}$ are blocks of the STM for the SAA equation and T is the transfer time of the TPBVP solution for the SAA equations. Note that $\boldsymbol{\alpha}_t = \mathbf{0}$ which corresponds to always having a compensation for the constant forcing term $\mathbf{u} = -\boldsymbol{\omega}_t^{\times}\mathbf{J}\boldsymbol{\omega}_t$. Also, note that the velocity profile depends on the choice of T, where this parameter is chosen such that $\mathbf{\Phi}_{12}^{-1}(T)$ exists. This transfer time and the transfer time of the TPBVP solution

for the CWH equations is distinct since the STMs are different. For the remainder of the derivation, an arbitrary state $\mathbf{x}$ is used since the velocity profile for both the CWH equation and the SAA equation is of the same form.

The adaptive update law is now developed to choose the weights of the attractive artificial potential. First, an error variable is defined as

$$\begin{aligned} \mathbf{e} &= \dot{\mathbf{x}}_d - (-\boldsymbol{\nabla}_x \phi_a) \\ \Rightarrow \mathbf{e} &= \boldsymbol{\Phi}_{22}(-T)\boldsymbol{\Phi}_{12}^{-1}(-T)\mathbf{x} + \boldsymbol{\Phi}_{12}^{-1}(T)\mathbf{x}_f + \mathbf{R}^T\mathbf{R}(\mathbf{x} - \mathbf{x}_f) \ . \end{aligned} \tag{6–2}$$

Next, the time derivative of equation (6–2) yields

$$\dot{\mathbf{e}} = \boldsymbol{\Phi}_{22}(-T)\boldsymbol{\Phi}_{12}^{-1}(-T)\dot{\mathbf{x}} + \boldsymbol{\Phi}_{12}^{-1}(T)\dot{\mathbf{x}}_f + (\dot{\mathbf{R}}^T\mathbf{R} + \mathbf{R}^T\dot{\mathbf{R}})(\mathbf{x} - \mathbf{x}_f) + \mathbf{R}^T\mathbf{R}\,(\dot{\mathbf{x}} - \dot{\mathbf{x}}_f) \ ,$$

which is linearly parameterized as

$$\dot{\mathbf{e}} = \boldsymbol{\Phi}_{22}(-T)\boldsymbol{\Phi}_{12}^{-1}(-T)\dot{\mathbf{x}} + \boldsymbol{\Phi}_{12}^{-1}(T)\dot{\mathbf{x}}_f + (\mathbf{Y} + \mathbf{Z})\dot{\boldsymbol{\theta}} + \mathbf{R}^T\mathbf{R}(\dot{\mathbf{x}} - \dot{\mathbf{x}}_f) \ ,$$

where

$$\mathbf{Y} = \begin{bmatrix} \xi_1 & 0 & 0 & 0 & 0 & 0 \\ 0 & \xi_1 & 0 & \xi_2 & 0 & 0 \\ 0 & 0 & \xi_1 & 0 & \xi_2 & \xi_3 \end{bmatrix}$$

$$\mathbf{Z} = \begin{bmatrix} \rho_{11}(x_1 - x_{f,1}) & \rho_{11}(x_2 - x_{f,2}) & \rho_{11}(x_3 - x_{f,3}) & 0 & 0 & 0 \\ \rho_{12}(x_1 - x_{f,1}) & \rho_{12}(x_2 - x_{f,2}) & \rho_{12}(x_3 - x_{f,3}) & \rho_{22}(x_2 - x_{f,2}) & \rho_{22}(x_3 - x_{f,3}) & 0 \\ \rho_{13}(x_1 - x_{f,1}) & \rho_{13}(x_2 - x_{f,2}) & \rho_{13}(x_3 - x_{f,3}) & \rho_{23}(x_2 - x_{f,2}) & \rho_{23}(x_3 - x_{f,3}) & \rho_{33}(x_3 - x_{f,3}) \end{bmatrix}$$

$$\boldsymbol{\theta} = \begin{bmatrix} \rho_{11} & \rho_{12} & \rho_{13} & \rho_{22} & \rho_{23} & \rho_{33} \end{bmatrix}^T \ .$$

The terms ξ_i for $i = 1, 2, 3$ are defined below.

$$\xi_1 = \rho_{11}(x_1 - x_{f,1}) + \rho_{12}(x_2 - x_{f,2}) + \rho_{13}(x_3 - x_{f,3})$$

$$\xi_2 = \rho_{22}(x_2 - x_{f,2}) + \rho_{23}(x_3 - x_{f,3})$$

$$\xi_3 = \rho_{33}(x_3 - x_{f,3})$$

An adaptive update law is then defined for the weights as

$$\dot{\boldsymbol{\theta}} = -(\mathbf{Y} + \mathbf{Z})^{\#} \left[\boldsymbol{\Phi}_{22}(-T)\boldsymbol{\Phi}_{12}^{-1}(-T)\dot{\mathbf{x}} + \boldsymbol{\Phi}_{12}^{-1}(T)\dot{\mathbf{x}}_f + \mathbf{R}^T\mathbf{R}\left(\dot{\mathbf{x}} - \dot{\mathbf{x}}_f\right) + \mathbf{e} \right] , \tag{6–3}$$

where

$$(\mathbf{Y} + \mathbf{Z})^{\#} = (\mathbf{Y} + \mathbf{Z})^T((\mathbf{Y} + \mathbf{Z})(\mathbf{Y} + \mathbf{Z})^T)^{-1}$$

which drives $\mathbf{e} \to \mathbf{0}$ as $t \to \infty$. Note that the matrix $(\mathbf{Y} + \mathbf{Z})$ is full rank except when $\mathbf{x} = \mathbf{x}_f$. However, this only occurs at $t = \infty$ in the APF framework since the controller results in $\mathbf{x} \to \mathbf{x}_f$ asymptotically. Therefore, $(\mathbf{Y} + \mathbf{Z})$ is nonsingular except at $t = \infty$. This indicates that this algorithm should only be used for close-range rendezvous or intercept or until the chaser is within a threshold of $\mathbf{x}_f$. In addition, a nonzero initial condition for $\boldsymbol{\theta}$ is needed to initially have a positive-definite weighting matrix.

Since an adaptation is being done with a time-varying signal (i.e, the velocity profile), a discontinuous projection algorithm is employed to ensure that the adaptive estimates are bounded. [87, 88] First, if "close proximity" situations are only considered, then there exists $\delta \in \mathbb{R}$ such that

$$\|\mathbf{x}(t) - \mathbf{x}_f\| \leq \delta \;\; \forall \; t \in [t_0, \infty) \; .$$

As a result, the velocity profile in equation (6–1) is also bounded. Thus, there exists an upper and lower bound $\overline{\theta}_i, \underline{\theta}_i \in \mathbb{R}$ for $i = 1, 2, \ldots, 6$, such that a convex set can be defined

for each estimate as

$$\Lambda_i = \{\nu \in \mathbb{R} \mid \underline{\theta}_i \leq \nu \leq \overline{\theta}_i\} \text{ for } i = 1, 2, \ldots, 6 \,.$$

The projection operator is defined based on the definition of the convex set as

$$\dot{\hat{\theta}}_i = \text{Proj}(\dot{\theta}_i) = \begin{cases} \dot{\theta}_i & \text{if } \theta_i \in \Lambda_i \\ \dot{\theta}_i & \text{if } \theta_i = \underline{\theta}_i \text{ and } \dot{\theta}_i \geq 0 \\ \dot{\theta}_i & \text{if } \theta_i = \overline{\theta}_i \text{ and } \dot{\theta}_i \leq 0 \\ 0 & \text{otherwise} \end{cases} \quad \text{for } i = 1, 2, \ldots, 6 \,, \tag{6–4}$$

where $\dot{\theta}_i$ for $i = 1, 2, \ldots, 6$ is defined in equation (6–3). Figure 6-1 shows an illustration of the resultant adaptive estimate trajectory using the projection algorithm. Using the adaptive update law in equation (6–3) with the artificial projection algorithm in equation (6–4), the AAPF control law is

$$\mathbf{u}(\mathbf{x}, \dot{\mathbf{x}}) = \begin{cases} -\mathbf{R}^T\mathbf{R}\,(\mathbf{x} - \mathbf{x}_f) - k\boldsymbol{\nabla}_x\phi_r - (\dot{\mathbf{x}} - \dot{\mathbf{x}}_f) & \text{if } \dot{\phi} \geq 0 \\ \mathbf{0} & \text{otherwise} \end{cases} \,, \tag{6–5}$$

where the matrix $\mathbf{R}$ contains the adaptive estimates.

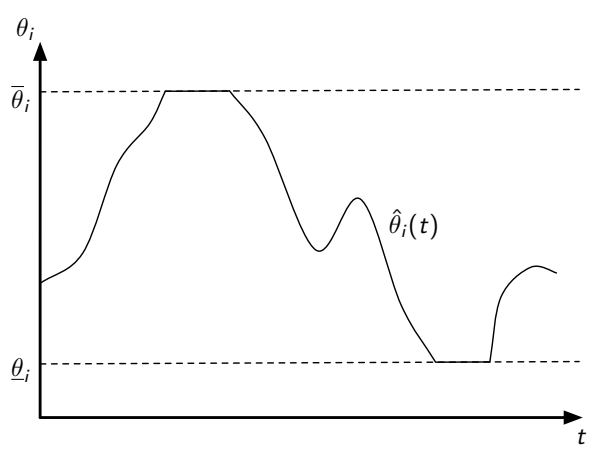

Figure 6-1. Illustration of adaptive estimate trajectory

6.2 Stability Analysis

To analyze the stability of the APF and AAPF method, the unconstrained case (i.e., obstacle-free) is first considered. Consider a Lyapunov candidate function (LCF) that has the same form as the quadratic attractive potential

$$V(\boldsymbol{\epsilon}) = \frac{1}{2}\boldsymbol{\epsilon}^T\boldsymbol{\epsilon} \ ,$$

where $\boldsymbol{\epsilon} = \mathbf{x} - \mathbf{x}_f \rightarrow \mathbf{0}$ is the control objective. Given a LCF, the sufficient conditions for a globally asymptotically stable (GAS) equilibrium point at $\boldsymbol{\epsilon} = \mathbf{0}$ are: [89]

1. $V(\mathbf{0}) = 0$
2. $V(\boldsymbol{\epsilon}) > 0 \ \ \forall\, \mathbf{x} \in \mathbb{R}^n - \{\mathbf{0}\}$
3. $V(\boldsymbol{\epsilon})$ is radially unbounded (i.e., $V(\boldsymbol{\epsilon}) \rightarrow \infty$ as $\|\boldsymbol{\epsilon}\| \rightarrow \infty$)
4. $\dot{V}(\boldsymbol{\epsilon}) < 0 \ \ \forall\, \boldsymbol{\epsilon} \in \mathbb{R}^n - \{\mathbf{0}\}$

The first three conditions are satisfied based on the choice of the LCF. For the fourth condition, the derivative of the LCF is

$$\dot{V} = \boldsymbol{\epsilon}^T(\dot{\mathbf{x}} - \dot{\mathbf{x}}_f) \ .$$

If the control action is impulsive, then the velocity at any instant in time can be described as the velocity plus the magnitude of the impulse (given the impulse is nonzero at that instant in time). [71] To ensure the fourth condition is satisfied, an impulsive control action (i.e., $\Delta\dot{\mathbf{x}}$) is defined according to the control law in equation (5–3) or equation (6–5) that occurs when $\dot{\phi} \geq 0$. Thus, the velocity after the impulsive action occurs is defined as

$$\dot{\mathbf{x}} - \dot{\mathbf{x}}_f + \Delta\dot{\mathbf{x}} = -k\nabla_{\mathrm{x}}\phi(\boldsymbol{\epsilon}) = -k\mathbf{P}\boldsymbol{\epsilon} \ ,$$

where k is a positive scalar. [57] Note that $\nabla_{\mathrm{x}}\phi = \mathbf{P}\nabla_{\mathrm{x}}V$. Thus, defining the controller in equation (5–3) or equation (6–5) ensures the velocity is a scalar multiple of the negative

gradient of the APF (and LCF) when $\dot{\phi} \geq 0$. The derivative of the LCF then becomes

$$\dot{V} = \begin{cases} -k\boldsymbol{\epsilon}^T \mathbf{P} \boldsymbol{\epsilon} & \text{if } \dot{\phi} \geq 0 \\ \boldsymbol{\epsilon}^T (\dot{\mathbf{x}} - \dot{\mathbf{x}}_f) & \text{if } \dot{\phi} < 0 \end{cases} < 0 \ ,$$

and satisfies the fourth condition. Therefore, all the conditions are met and the point $\boldsymbol{\epsilon} = \mathbf{0}$ is a GAS equilibrium point.

When considering obstacle regions, the same stability analysis cannot be used. For one, choosing a LCF becomes difficult since the same form of the APF does not satisfy the first two conditions for a GAS equilibrium point. One way to remedy this is to define the APF as

$$\phi = \frac{1}{2}(\mathbf{x} - \mathbf{x}_f)^T \left[\mathbf{P} + \sum_{i=1}^{N} \psi_i \exp\left[-\frac{(\mathbf{x} - \mathbf{x}_i)^T \mathbf{N}_i (\mathbf{x} - \mathbf{x}_i)}{\sigma_i} \right] \mathbf{I} \right] (\mathbf{x} - \mathbf{x}_f) \ ,$$

and use a LCF of this form as well. However, this still does not resolve the local minima problem. [90] In fact, it is known that stability cannot be proven with a general set of obstacle regions and parameters. [82] Consider a two degrees-of-freedom system example illustrated in Figure 6-2A. If the obstacles are arranged as illustrated and the obstacle parameters are defined such that the repulsive potentials are not sensed until the chaser is near the “barricade” of obstacles, then the chaser would not be able to escape the “barricade” of obstacles. Another example shown in Figure 6-2B occurs when the dynamics of the system are negligible (e.g., the double integrator) and the obstacle is along the line of sight of the target. In this scenario, if the obstacle region is defined symmetrically and it lies along the line of sight of the chaser to the target, then the attractive and repulsive potentials eventually counteract each other and the control is null at this point.

Regrettably, the stability for an obstacle avoidance problem using the APF or AAPF method is based on intuition. The intuitive nature of the APF method gives a notion that by defining the APF appropriately, the solution converges to the goal position. The two

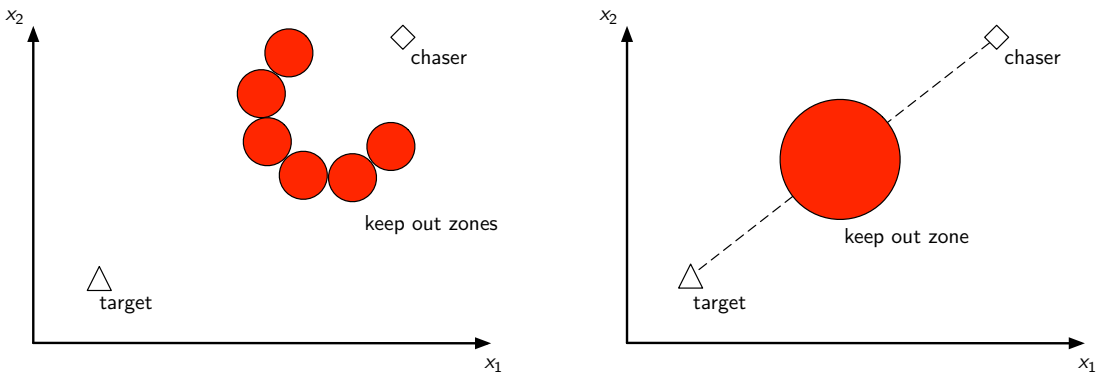

A Local minimum example

B Counteracting obstacle example

Figure 6-2. Examples where APF does not guarantee convergence

examples demonstrate how the APF method does not yield convergence for an arbitrary dynamical system with arbitrary artificial potential parameters. These types of problems can be dealt with in an ad hoc manner where the appropriate parameters are used such that local minima are avoided. [53, 84] The AAPF method, however, considers the dynamics which alleviates some of the local minima problems. In addition, the close-range rendezvous scenario has free-floating target and obstacles which reduces the probability of local minima as well.

6.3 Numerical Examples

Two sets of numerical examples are presented in this section to demonstrate the AAPF method. In the first example, the AAPF method is applied to the CWH equation with a grid of 14 static obstacle in the state space. In the second example, the AAPF method is applied to the SAA equation with a tumbling satellite.

6.3.1 Clohessy-Wiltshire-Hill Example

The parameters used in this example are given in Table 6-1. The goal of the chaser (initially located at the relative position $\mathbf{r}_0$) is to reach the target (located at the origin) while avoiding the obstacles. A set of 14 static obstacles are placed in the state space at the positions shown below.

$$\mathbf{r}_1 = \begin{bmatrix} 500 & 0 & 0 \end{bmatrix}^T \quad \mathbf{r}_2 = \begin{bmatrix} -500 & 0 & 0 \end{bmatrix}^T \quad \mathbf{r}_3 = \begin{bmatrix} 0 & 500 & 0 \end{bmatrix}^T$$

$$\mathbf{r}_4 = \begin{bmatrix} 0 & -500 & 0 \end{bmatrix}^T \quad \mathbf{r}_5 = \begin{bmatrix} 0 & 0 & 500 \end{bmatrix}^T \quad \mathbf{r}_6 = \begin{bmatrix} 0 & 0 & -500 \end{bmatrix}^T$$

$$\mathbf{r}_7 = \begin{bmatrix} 250 & 250 & 250 \end{bmatrix}^T \quad \mathbf{r}_8 = \begin{bmatrix} 250 & -250 & 250 \end{bmatrix}^T \quad \mathbf{r}_9 = \begin{bmatrix} 250 & 250 & -250 \end{bmatrix}^T$$

$$\mathbf{r}_{10} = \begin{bmatrix} 250 & -250 & -250 \end{bmatrix}^T \quad \mathbf{r}_{11} = \begin{bmatrix} -250 & 250 & 250 \end{bmatrix}^T \quad \mathbf{r}_{12} = \begin{bmatrix} -250 & -250 & 250 \end{bmatrix}^T$$

$$\mathbf{r}_{13} = \begin{bmatrix} -250 & 250 & -250 \end{bmatrix}^T \quad \mathbf{r}_{14} = \begin{bmatrix} -250 & -250 & -250 \end{bmatrix}^T$$

For this example, the control constraint shown below is enforced.

$$\|\mathbf{f}\| \leq f_{max}$$

Settling time is used as a performance metric where the trajectory obtained is considered settled when $\|\mathbf{r}\| \leq 10$ m. The running control effort cost is also used as a performance metric and is defined as

$$V(t) = \int_{t_0}^{t} \|\mathbf{u}\|_1 \, d\varepsilon \, .$$

Table 6-1. Relative translation parameters

Parameter	Value	Units
n	0.0012	rad/s
$\mathbf{r}_0$	$\begin{bmatrix} 750 & 0 & -500 \end{bmatrix}^T$	m
$\mathbf{v}_0$	$\begin{bmatrix} 0.5 & 2 & 0 \end{bmatrix}^T$	m/s
$\mathbf{r}_f$	$\begin{bmatrix} 0 & 0 & 0 \end{bmatrix}^T$	m
f_{max}	1	$\mathrm{m/s^2}$
$\boldsymbol{\theta}_0$	$0.002 \times \begin{bmatrix} 1 & 0 & 0 & 1 & 0 & 1 \end{bmatrix}^T$	$\mathrm{s^{-2}}$
$\mathbf{N}_i$	$\mathbf{I} \in \mathbb{R}^{3\times 3}$	$\mathrm{s^{-2}}$
ψ_i	1.5×10^5	–
σ_i	1.0×10^4	$\mathrm{m^2}$
k	0.002	–
T	1000	s

The results obtained are displayed in Figure 6-3. The trajectory plot in Figure 6-3A shows that an obstacle is encountered and the chaser is able to maneuver around it. The position and velocity plots in Figure 6-3B and Figure 6-3C, respectively, indicate that the chaser reaches the origin with zero velocity. The corresponding control history is given in Figure 6-3D.

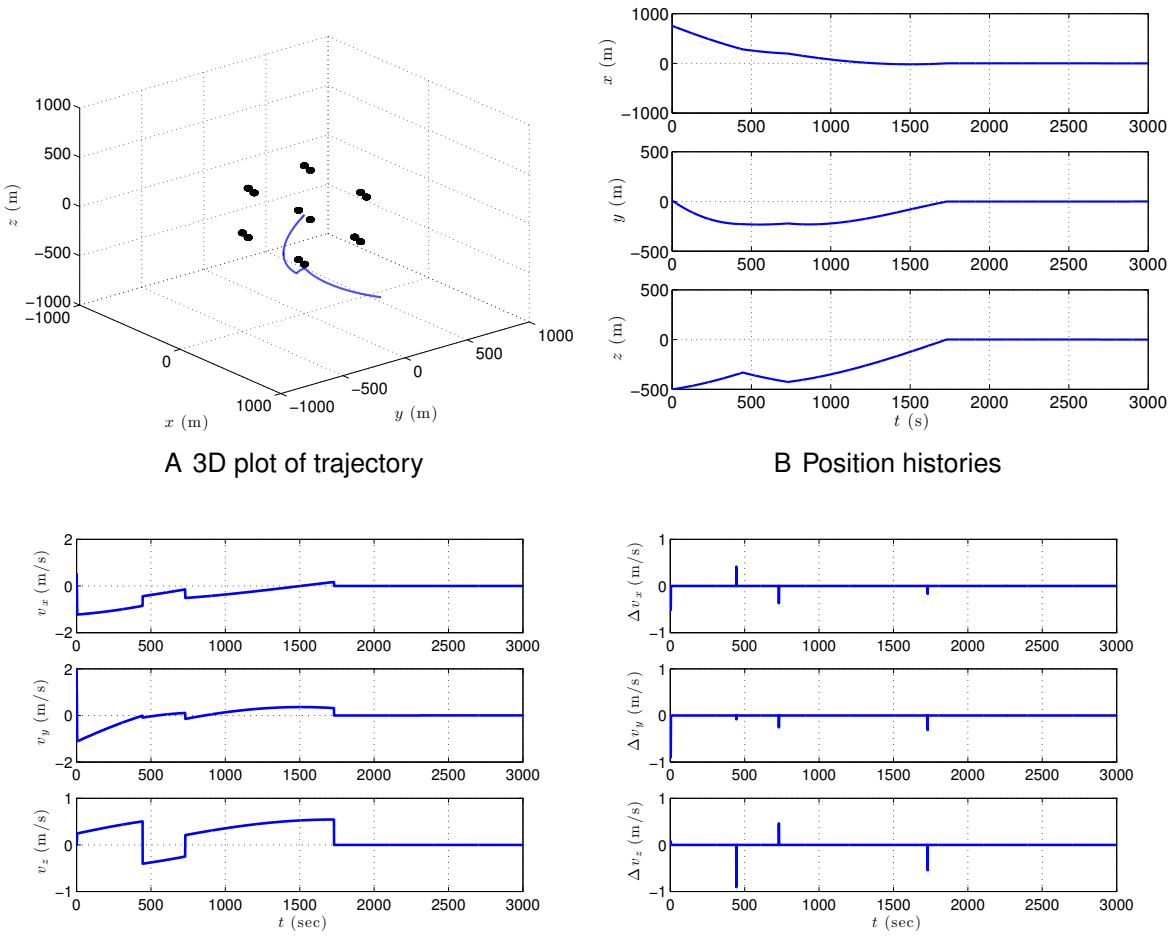

A 3D plot of trajectory

B Position histories

C Velocity histories

D Control histories

Figure 6-3. Adaptive artificial potential function (AAPF) method results using CWH equation

The settling time obtained is 1715 s and the control effort at the settling time is 8.63 m/s. The running cost is shown in Figure 6-4, which illustrates how the cost increases with every control action.

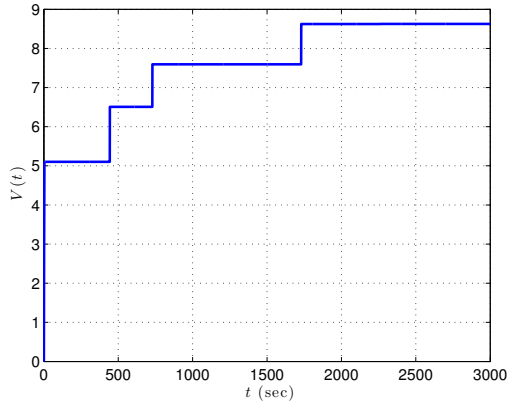

Figure 6-4. AAPF running cost using CWH equation

The plot of the adaptive estimates is shown in Figure 6-5. These plots indicate that the adaptive estimates continue to change depending on the chaser's position in the state space. This reinforces the fact that the magnitude of the commanded force should depend on the dynamics and the location of the chaser.

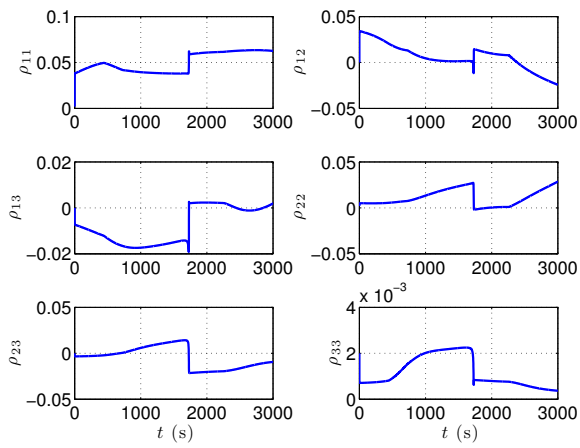

Figure 6-5. AAPF adaptive estimates using CWH equation

6.3.2 Small Angle Approximation Example

The parameters used in this example are shown in Table 6-2. The goal of the chaser (with initial relative orientation α_0 to the target) is to reach a relative orientation of $\alpha = \mathbf{0}$ rad with the target that is tumbling at the rate ω_t. The control constraint shown

below is enforced.

$$|\tau_i| \leq \tau_{max} \text{ for } i = 1, 2, 3$$

Settling time is used as a performance metric where the trajectory obtained is considered settled when $\|\boldsymbol{\alpha}\| \leq 0.01$ rad. The running control effort cost is also used as performance metric and is defined as

$$V(t) = \int_{t_0}^{t} \|\boldsymbol{\tau}\|_1 \, d\varepsilon \, .$$

Table 6-2. Relative orientation parameters

Parameter	Value	Units
$\mathbf{J}$	$\begin{bmatrix} 300 & 20 & 10 \\ 20 & 100 & 0 \\ 10 & 0 & 200 \end{bmatrix}$	$\text{kg} \cdot \text{m}^2$
$\boldsymbol{\omega}_t$	$\begin{bmatrix} 0.25 & -0.25 & 0.25 \end{bmatrix}^T$	rad/s
$\boldsymbol{\alpha}_0$	$\begin{bmatrix} 0.3 & -0.2 & -0.15 \end{bmatrix}^T$	rad
$\dot{\boldsymbol{\alpha}}_0$	$\begin{bmatrix} 0 & 0 & 0 \end{bmatrix}^T$	rad/s
$\boldsymbol{\alpha}_f$	$\begin{bmatrix} 0 & 0 & 0 \end{bmatrix}^T$	rad
τ_{max}	20	$\text{N} \cdot \text{m}$
$\boldsymbol{\theta}_0$	$0.002 \times \begin{bmatrix} 1 & 0 & 0 & 1 & 0 & 1 \end{bmatrix}^T$	s^{-2}
T	5	s

The results for this example are displayed in Figure 6-6. The relative orientation and relative angular velocity plots in Figure 6-6A and Figure 6-6B, respectively, indicate that both these parameters converge to zero. The corresponding control history is given in Figure 6-6C. The settling time obtained is approximately 20.1 s. Note that the running cost in Figure 6-6D increases linearly with time since the controller continues to compensate for the tumbling satellite.

The plots of the adaptive estimates are shown in Figure 6-7. These plots indicate that the adaptive estimates continue to change depending on the spacecrafts relative orientation. This reinforces the fact that the magnitude of the commanded torque should depend on the dynamics and the relative orientation.

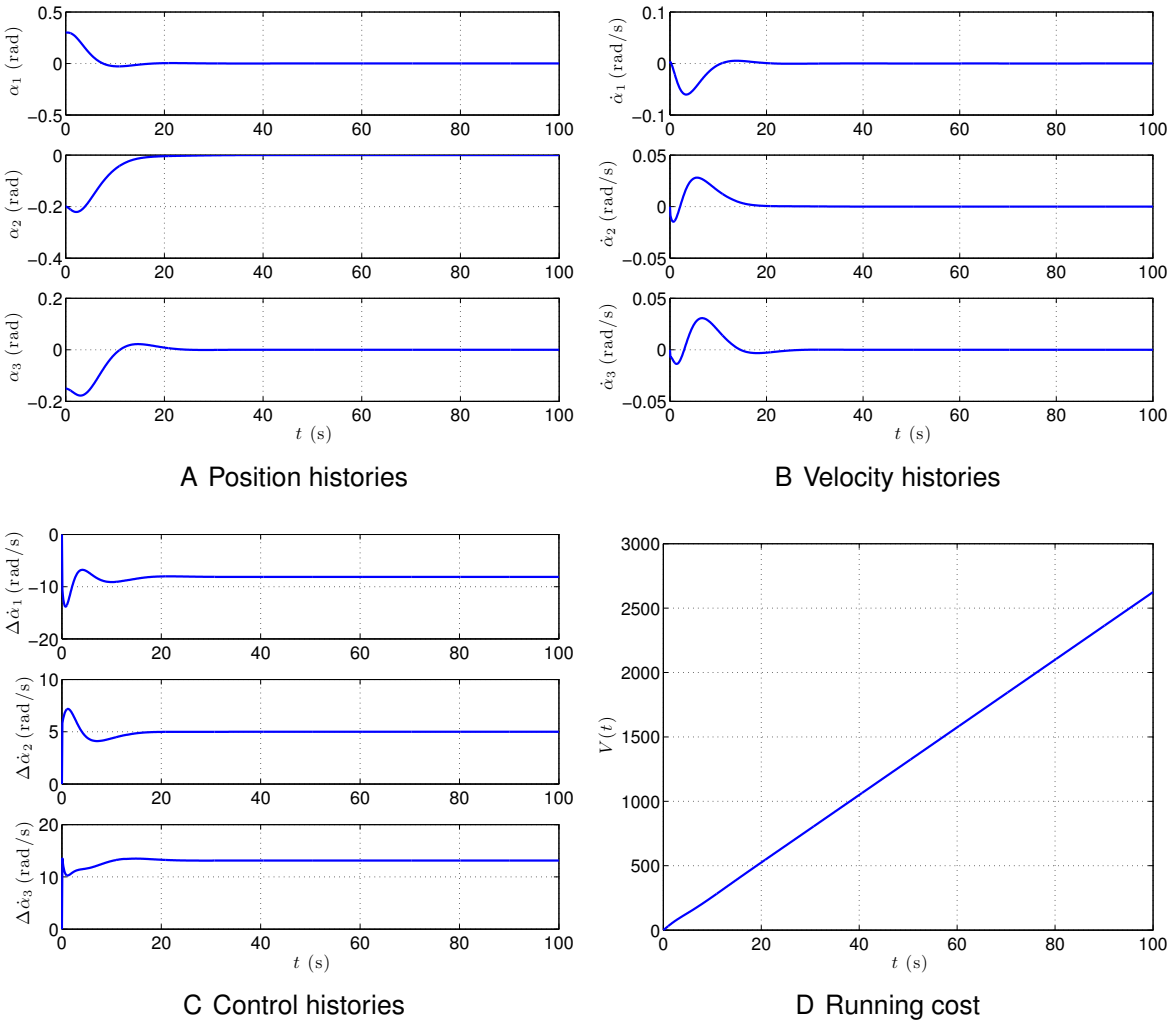

Figure 6-6. AAPF results using SAA equation

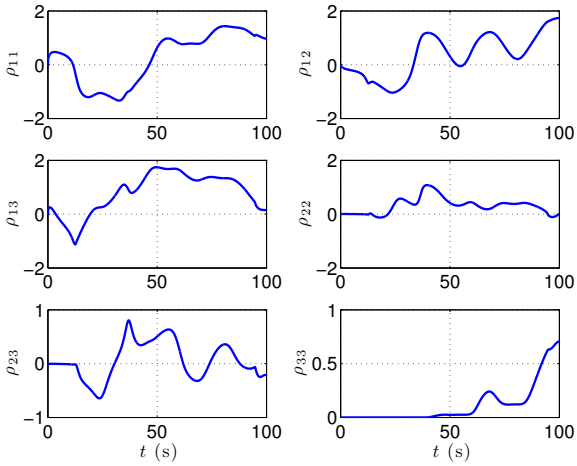

Figure 6-7. AAPF adaptive estimates using SAA equation

In conclusion, a modification to the APF method is presented in this chapter. This modification is done in an effort to implement a performance metric for tuning the APF method. As a result, an adaptive update law is used to vary the weights on the attractive APF. The velocity profile of the TPBVP is used in the derivation since this solution is a good approximation to the fixed time minimum control effort problem. A stability analysis is also presented, where it is demonstrated that convergence is only guaranteed for obstacle-free (unconstrained) cases. Finally, two examples are performed to demonstrate the AAPF method. The first is a relative translation problem in a cluttered environment and the second is a relative orientation problem with a tumbling spacecraft.

CHAPTER 7
FINITE HORIZON LINEAR QUADRATIC PROBLEMS

In the previous chapter, the close-range rendezvous trajectories were addressed by developing the adaptive artificial potential function (AAPF) method. However, the AAPF method is not well-suited for the final approach or endgame of an autonomous proximity operation (APO). Trajectories obtained from solving a linear quadratic (LQ) optimal control problems (OCPs) are typically used for the final approach or endgame. Moreover, solving a finite horizon LQ OCP augments the problem with a time constraint which is necessary for certain APOs (i.e., intercept, rendezvous with uncooperative target, docking, *etc.*). This chapter discusses the methods for solving finite horizon LQ problems. First, the Differential Riccati Equation (DRE) is adopted from equation (4–15). It is shown that there exists a system of linear matrix differential equations which are intimately related to the DRE. Furthermore, when the Hamiltonian matrix is time invariant, the DRE is solved using using a state transition matrix (STM) representation of the linear system of matrix differential equations. When the Hamiltonian is time varying, the solution cannot be obtained using a STM representation. As a result, two methods of solving are developed using: Picard Iteration (PI) and Homotopy Continuation (HC). A numerical example is presented to demonstrate the effectiveness of solving the DRE for a LTV system using PI and HC. Finally, a final approach trajectory is obtained using HC with the Yamanaka-Ankerson-Tschauner-Hempel (YATH) equation derived in Appendix A.

7.1 Development

Trajectories for the final approach or endgame of an APO are typically obtained by solving a LQ optimal control problem (OCP). This is because a linearized model serves as a good approximation in this level of proximity and using a linearized model simplifies the solution process. Moreover, the control law obtained from an LQ problem is in the state feedback form which makes it compliant for implementation. It was shown in

Chapter 4 that solving a finite horizon LQ OCP in equation (4–10) amounts to solving a final value problem with the DRE in equation (4–15). The difficulty here is that the DRE is a nonlinear equation, which in general, cannot be analytically solved. Thus, solving a final value problem with the DRE requires that the DRE be integrated backwards in time every time a new solution is needed.

An interesting property of the DRE is that it is intimately related to the system of linear matrix differential equations

$$\begin{bmatrix} \dot{\mathbf{U}} \\ \dot{\mathbf{V}} \end{bmatrix} = \begin{bmatrix} \mathbf{A} & -\mathbf{B}\mathbf{R}^{-1}\mathbf{B}^T \\ -\mathbf{Q} & -\mathbf{A}^T \end{bmatrix} \begin{bmatrix} \mathbf{U} \\ \mathbf{V} \end{bmatrix} , \quad \begin{bmatrix} \mathbf{U}(t_f) \\ \mathbf{V}(t_f) \end{bmatrix} = \begin{bmatrix} \mathbf{I} \\ \mathbf{S}_f \end{bmatrix} , \tag{7–1}$$

where $\mathbf{V}, \mathbf{U} \in \mathbb{R}^{n \times n}$. [91, 92] Note that the state matrix is the Hamiltonian matrix from equation (4–12). If $\mathbf{U}^{-1}$ exists, then the solution to the DRE can be written using the variable transformation

$$\mathbf{S} = \mathbf{V}\mathbf{U}^{-1} . \tag{7–2}$$

This is seen if equation (7–1) is substituted into the time derivative of equation (7–2) as shown below.

$$\begin{aligned}
\dot{\mathbf{S}} &= \dot{\mathbf{V}}\mathbf{U}^{-1} - \mathbf{V}\mathbf{U}^{-1}\dot{\mathbf{U}}\mathbf{U}^{-1} \\
\Rightarrow \dot{\mathbf{S}} &= \left[-\mathbf{Q}\mathbf{U} - \mathbf{A}^T\mathbf{V}\right]\mathbf{U}^{-1} - \mathbf{V}\mathbf{U}^{-1}\left[\mathbf{A}\mathbf{U} - \mathbf{B}\mathbf{R}^{-1}\mathbf{B}^T\mathbf{V}\right]\mathbf{U}^{-1} \\
\Rightarrow \dot{\mathbf{S}} &= -\mathbf{Q} - \mathbf{A}^T\left(\mathbf{V}\mathbf{U}^{-1}\right) - \left(\mathbf{V}\mathbf{U}^{-1}\right)\mathbf{A} - \left(\mathbf{V}\mathbf{U}^{-1}\right)\mathbf{B}\mathbf{R}^{-1}\mathbf{B}^T\left(\mathbf{V}\mathbf{U}^{-1}\right) \\
\Rightarrow \dot{\mathbf{S}} &= -\mathbf{Q} - \mathbf{A}^T\mathbf{S} - \mathbf{S}\mathbf{A} + \mathbf{S}\mathbf{B}\mathbf{R}^{-1}\mathbf{B}^T\mathbf{S}
\end{aligned}$$

Note that the boundary condition on the DRE is also satisfied using the variable transformation in equation (7–2) as shown below.

$$\mathbf{S}(t_f) = \mathbf{V}(t_f)\mathbf{U}^{-1}(t_f) = \mathbf{S}_f$$

Therefore, if the solution for $\mathbf{U}$ and $\mathbf{V}$ can be obtained, then the optimal control law is defined using the variable transformation in equation (7–2). As a result, the optimal control law from equation (4–16) is defined as

$$\mathbf{u} = -\mathbf{R}^{-1}\mathbf{B}^{T}\mathbf{V}\mathbf{U}^{-1}\mathbf{x}\,.$$

7.2 Linear Time-Invariant System

When the Hamiltonian matrix is time invariant, equation (7–1) can be solved using a STM representation. [92–94] In particular, for the constant Hamiltonian matrix

$$\mathbf{H}_c = \begin{bmatrix} \mathbf{A} & -\mathbf{B}\mathbf{R}^{-1}\mathbf{B}^{T} \\ -\mathbf{Q} & -\mathbf{A}^{T} \end{bmatrix}\,,$$

the solution to equation (7–1) is written as

$$\begin{bmatrix} \mathbf{U}(t) \\ \mathbf{V}(t) \end{bmatrix} = \exp\left(\mathbf{H}_c(t-t_f)\right) \begin{bmatrix} \mathbf{I} \\ \mathbf{S}_f \end{bmatrix} = \mathbf{\Phi}(t,t_f) \begin{bmatrix} \mathbf{I} \\ \mathbf{S}_f \end{bmatrix}\,, \tag{7–3}$$

where $\mathbf{\Phi}(t,t_f)$ is the STM of the system of linear matrix differential equations in equation (7–1).

7.3 Linear Time-Varying System

When the Hamiltonian matrix is time varying, the STM is not easily solved for in general. In principle, the STM does exist, however, the difficulty is in obtaining the actual form of the STM. To address this difficulty, two methods are investigated for solving the DRE: PI and HC. Both PI and HC are known to be convergent in general. [95, 96] Thus, obtaining the solution using PI and/or HC can be used rather than having to integrate the DRE backwards in time.

7.3.1 Picard Iteration

The PI is a fixed point iterative technique for solving differential or integral equations. [95] Note that the final value problem with equation (7–1) is a differential equation. Thus, if the Hamiltonian matrix is time varying, then the final value problem in

equation (7–1) can be solved using PI. First, the variable $\mathbf{X}$ is defined as

$$\mathbf{X} = \begin{bmatrix} \mathbf{U} \\ \mathbf{V} \end{bmatrix} ,$$

so that equation (7–1) is written as

$$\dot{\mathbf{X}} = \mathbf{H}_t \mathbf{X} \ , \quad \mathbf{X}(t_f) = \mathbf{X}_f \ , \tag{7–4}$$

where $\mathbf{H}_t$ is the time varying Hamiltonian matrix. Using PI, the solution to the $(k+1)^{\text{th}}$ iteration is written as

$$\mathbf{X}^{(k+1)}(t) = \mathbf{X}_f + \int_{t_f}^{t} \mathbf{H}_t(\varepsilon) \mathbf{X}^{(k)}(\varepsilon) \ d\varepsilon \ .$$

The PI requires an initial guess (i.e., the fixed point). Using $\mathbf{X}^{(0)} = \mathbf{0}$ as the initial guess, the solution as $k \to \infty$ is

$$\begin{aligned} \mathbf{X}(t) = \Bigg[\mathbf{I} + \int_{t_f}^{t} \mathbf{H}_t(\varepsilon_1) d\varepsilon_1 + \int_{t_f}^{t} \mathbf{H}_t(\varepsilon_2) \left[\int_{t_f}^{\varepsilon_2} \mathbf{H}_t(\varepsilon_1) d\varepsilon_1 \right] d\varepsilon_2 + \ldots \\ \int_{t_f}^{t} \mathbf{H}_t(\varepsilon_3) \left[\int_{t_f}^{\varepsilon_3} \mathbf{H}_t(\varepsilon_2) \left[\int_{t_f}^{\varepsilon_2} \mathbf{H}_t(\varepsilon_1) d\varepsilon_1 \right] d\varepsilon_2 \right] d\varepsilon_3 + \cdots \Bigg] \mathbf{X}_f \\ \Rightarrow \mathbf{X}(t) = \mathbf{\Phi}(t, t_f) \mathbf{X}_f \ . \end{aligned}$$

The integral terms can be computed analytically using a symbolic manipulator or a quadrature rule for a numerical approximation. However, analytic expressions are favorable since the quadrature rule would have to be done at each time step and recursively for each additional term. Note that if the Hamiltonian matrix is constant, then the solution simply becomes the Taylor Series Expansion (TSE) of the matrix exponential about $t = t_f$ (which is the solution in equation (7–3)). However, if the Hamiltonian is not constant, then the Picard Iteration provides a solution for the STM.

7.3.2 Homotopy Continuation

Given a smooth nonlinear operator $N(\mathbf{x})$, the HC can be used to solve

$$N(\mathbf{x}) = \mathbf{0} \ , \tag{7–5}$$

which can not be analytically solved in general. [97] This is done by defining a homotopy, which is a continuous topological map that injects $L(\mathbf{x}) \ \rightarrow \ N(\mathbf{x})$ as the embedding parameter $p \rightarrow 1$. The idea is to continuously embed the solution of $L(\mathbf{x}) = \mathbf{0}$ (which is known) to the solution of $N(\mathbf{x}) = \mathbf{0}$. [96, 97] The benefit that HC has over other perturbation techniques is that the radius and rate of convergence can be increased depending on the parameters chosen in the solution formulation. [96] It is known that HC is an effective tool for solving a wide range of problems (e.g., algebraic, ordinary differential, partial differential, boundary value, *etc.*). [96] The approach for solving the DRE using HC is discussed in this section.

First, the convex homotopy is defined

$$H(\mathbf{x}, p) = (1 - p)\left[L(\mathbf{x}) - L(\mathbf{y}_0)\right] - ph\mathbf{\Psi}(t)\left[N(\mathbf{x})\right] = \mathbf{0} \ , \tag{7–6}$$

where $p \in \{\nu \in \mathbb{R} \mid 0 \leq \nu \leq 1\}$ is the embedding parameter, $h \neq 0$ is the auxiliary parameter, $\mathbf{\Psi}(t) \neq \mathbf{0}$ is the auxiliary function, and $\mathbf{y}_0$ is an initial guess. [96] Note that the homotopy has the property

$$\begin{aligned} H(\mathbf{x}, 0) &= L(\mathbf{x}) - L(\mathbf{y}_0) = \mathbf{0} \\ H(\mathbf{x}, 1) &= N(\mathbf{x}) = \mathbf{0} \ . \end{aligned}$$

Next, the parameter $\mathbf{x}$ is written as a Maclaurin Series Expansion (MSE) in the embedding parameter

$$\mathbf{x} = \mathbf{x}_0 + p\mathbf{x}_1 + p^2\mathbf{x}_2 + \cdots \ , \tag{7–7}$$

where the parameters $\mathbf{x}_0, \mathbf{x}_1, \mathbf{x}_2, \ldots$ are to be determined. Note that the solution to $N(\mathbf{x}) = \mathbf{0}$ can now be written as

$$\mathbf{x} = \lim_{p \to 1} \mathbf{x}_0 + p\mathbf{x}_1 + p^2\mathbf{x}_2 + \cdots = \sum_{i=0}^{\infty} \mathbf{x}_i \ .$$

Therefore, solving equation (7–5) amounts to solving for the parameters $\mathbf{x}_0, \mathbf{x}_1, \mathbf{x}_2, \ldots$. These parameters are solved for by substituting equation (7–7) into equation (7–6). Appendix C discusses the solution derivation using the original DRE as the operator

$$N(\mathbf{S}) = \dot{\mathbf{S}} + \mathbf{Q} - \mathbf{S}\mathbf{B}\mathbf{R}^{-1}\mathbf{B}^T\mathbf{S} + \mathbf{A}^T\mathbf{S} + \mathbf{S}\mathbf{A} = \mathbf{0} \ , \tag{7–8}$$

while choosing

$$L(\mathbf{S}) = \dot{\mathbf{S}} \ . \tag{7–9}$$

Appendix D discusses the solution derivation using the operator

$$N(\mathbf{X}) = \dot{\mathbf{X}} - \mathbf{H}_t\mathbf{X} = \mathbf{0} \ , \tag{7–10}$$

which is the system of linear matrix differential equations related to the DRE, and choosing

$$L(\mathbf{X}) = \dot{\mathbf{X}} \ . \tag{7–11}$$

Appendix E discusses the solution derivation using equation (7–10) as the operator and choosing

$$L(\mathbf{X}) = \dot{\mathbf{X}} - \mathbf{X} \ . \tag{7–12}$$

Based on the formulation, there are free parameters that can be manipulated. Namely, these are the operator $L(\mathbf{x})$, the initial guess $\mathbf{y}_0$, the auxiliary parameter h, and the auxiliary function $\mathbf{\Psi}(t)$. These parameters can be chosen such that the radius and rate of convergence is improved (depending on the problem being solved). [96] In the

solution derivations in the appendices, these parameters are chosen by default (except for the auxiliary parameter h). However, a thorough analysis should be performed to determine the set of parameters that yield the desired results.

A feature of the PI and HC is the parametric solution structure of the Riccati matrix. Since the solutions are functions of the time horizon and the state, input, and LQ matrices, then the solution is easily updated. This makes the solution structure amenable to changes in the time horizon, dynamics model, and/or performance index.

7.4 Numerical Examples

An example is presented to demonstrate how well the solution to the DRE can be approximated using PI and the HC. This example is used since linearized models of dynamical systems tend to have oscillatory components in their dynamics. In particular, this is true for models of relative translational motion in orbit (as shown in Appendix A). [98, 99]

A two degrees-of-freedom linear system is used with the dynamics

$$\begin{bmatrix} \dot{x}_1 \\ \dot{x}_2 \end{bmatrix} = \begin{bmatrix} 0 & 1 \\ sin(t) & 0 \end{bmatrix} \begin{bmatrix} x_1 \\ x_2 \end{bmatrix} + \begin{bmatrix} 0 \\ 1 \end{bmatrix} u \ , \quad \begin{bmatrix} x_1(t_0) \\ x_2(t_0) \end{bmatrix} = \begin{bmatrix} 2 \\ 1 \end{bmatrix}$$

$$\Rightarrow \dot{\mathbf{x}} = \mathbf{A}(t)\mathbf{x} + \mathbf{B}u \ , \quad \mathbf{x}(t_0) = \mathbf{x}_0$$

The parameters and matrices that are associated with the finite horizon LQ problem are given in Table 7-1.

Table 7-1. Finite horizon linear quadratic parameters

Parameters	Value	Units
$\mathbf{S}_f$	$\mathbf{I} \in \mathbb{R}^{2\times 2}$	–
$\mathbf{Q}$	$\mathbf{I} \in \mathbb{R}^{2\times 2}$	–
$\mathbf{R}$	$\mathbf{I} \in \mathbb{R}^{1\times 1}$	–
t_0	0	s
t_f	20	s

7.4.1 Picard Iteration

Using the PI approach to solve the DRE, the results are shown in Figure 7-1. The results were computed for 0th to 7th order approximations. The four components of the Riccati matrix $\mathbf{S}$ are shown in Figure 7-1A thru Figure 7-1D, where $\mathbf{S}^*_{i,j}$ indicates the optimal solution. The plots indicate that adding an order of approximation does not necessarily yield a better result. In fact, it is shown that only the even ordered approximations yielded favorable estimates. The max difference between the components of $\mathbf{S}^{(k)}$ and $\mathbf{S}^*$ is shown in Table 7-2. It is shown that increasing the order of approximation did improve the solution about the boundary condition at $t = t_f$.

Table 7-2. Maximum difference of Riccati matrix components (PI)

Approximation order	$\Delta S_{1,1}$	$\Delta S_{1,2}$	$\Delta S_{2,2}$	$\Delta S_{2,2}$
0	2.28	2.29	2.29	1.35
1	46.04	44.36	45.66	43.82
2	2.21	2.10	2.05	1.19
3	22.99	14.88	20.52	13.07
4	2.11	1.84	1.89	1.03
5	$6.35e3$	$4.44e3$	$6.09e3$	$4.26e3$
6	2.12	1.80	1.73	1.04
7	90.45	68.80	80.38	61.00

The resulting solutions were then used to determine the control, and in turn the response of the states. The states are shown in Figure 7-1E and the control is shown in Figure 7-1F, where $\mathbf{x}^*$ and u^* indicate the optimal states and optimal control, respectively. The states converge to the optimal solution, but at the cost of a large initial control value. The set of states that converged faster were for the even numbered approximations (since the Riccati matrices for these cases were fair approximations). The resulting costs obtained for each approximation are given in Table 7-3 where J^* indicates the optimal cost. The lowest cost was obtained for the 3rd order approximation, however, this is still far from the optimal cost. Note that the 5th order approximation resulted in a large cost. It was determined that this was caused by the $\mathbf{U}$ becoming ill-conditioned.

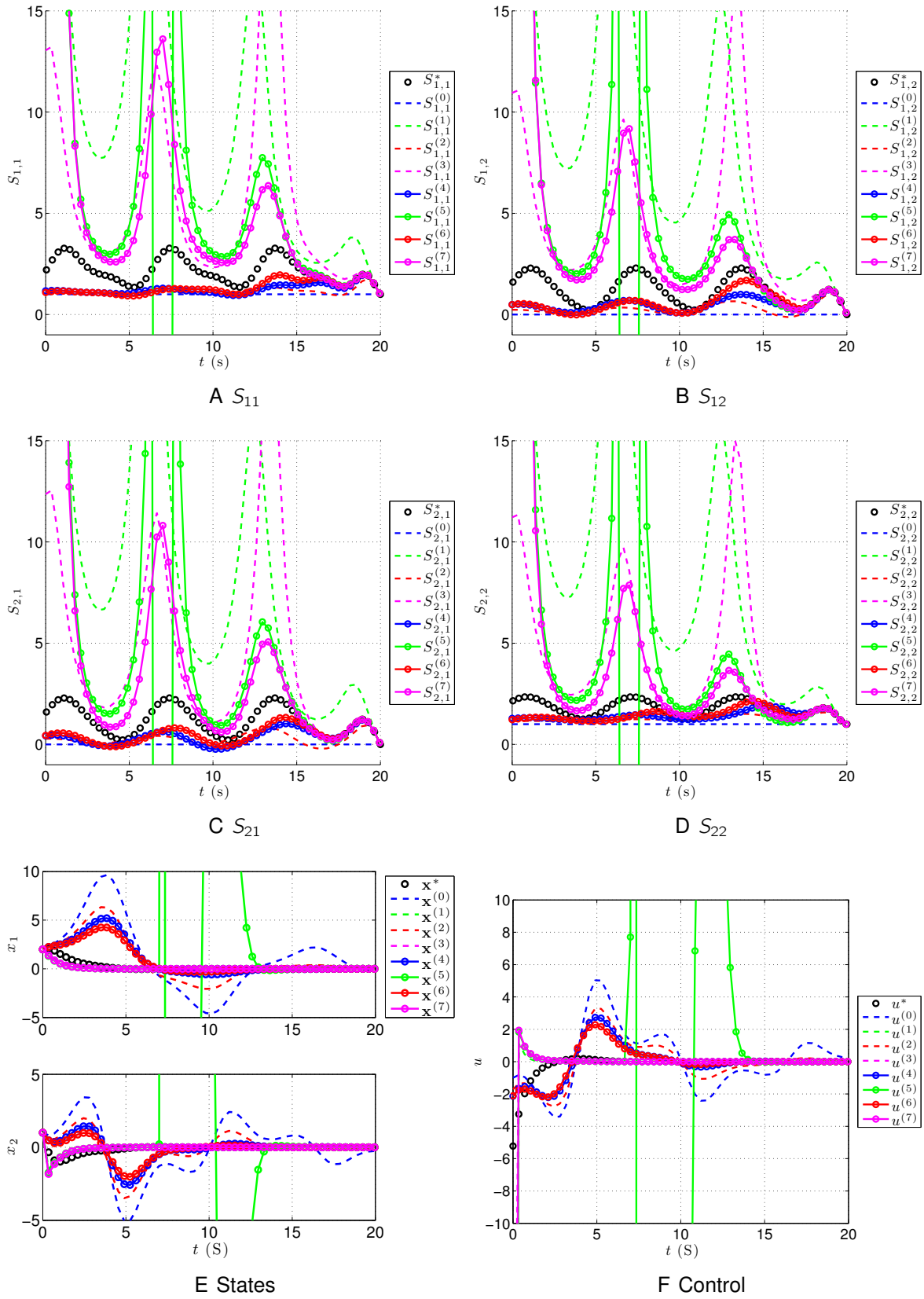

Figure 7-1. Picard Iteration results

Table 7-3. Costs for each approximating method

Cost	PI	HC (case 1)	HC (case 2)	HC (case 3)
J^*	8.44	8.44	8.44	8.44
$J^{(0)}$	223.18	223.18	223.18	223.18
$J^{(1)}$	92.34	229.20	31.93	15.67
$J^{(2)}$	91.35	240.02	41.18	11.13
$J^{(3)}$	29.78	243.15	8.80	11.70
$J^{(4)}$	59.12	250.03	11.73	11.73
$J^{(5)}$	$1.25e32$	282.32	9.36	11.41
$J^{(6)}$	43.76	369.90	8.90	-.-
$J^{(7)}$	57.43	-.-	-.-	-.-

7.4.2 Homotopy Continuation

Three different cases of HC were attempted for solving the DRE. The first case is for the homotopy defined by the operators in equation (7–8) and equation (7–9). The results obtained are shown in Figure 7-2, where the value for the auxiliary parameter used is $h = -1/20$. The results were computed for the 0th to 6th order approximations. The four components of the Riccati matrix $\mathbf{S}$ are shown in Figure 7-2A thru Figure 7-2D. The results indicate that this HC approach does not improve as the order of the approximation increases. Also, the results obtained do not seem to have the same trend as the optimal solution. The max difference between the components of $\mathbf{S}^{(k)}$ and $\mathbf{S}^*$ is shown in Table 7-4.

Table 7-4. Maximum difference of Riccati matrix components (HC case 1)

Approximation order	$\Delta S_{1,1}$	$\Delta S_{1,2}$	$\Delta S_{2,2}$	$\Delta S_{2,2}$
0	2.28	2.29	2.29	1.35
1	1.97	1.67	2.29	1.35
2	1.68	2.50	2.28	1.34
3	1.92	3.39	2.26	1.33
4	2.99	4.09	2.24	1.32
5	4.08	4.68	2.22	1.36
6	5.16	5.21	2.22	1.51

The resulting solutions are then used to determine the control, and in turn the response of the states. The states are shown in Figure 7-2E and the control is shown in Figure 7-2F. The results converge for each case, but do not necessarily improve

as the order of approximation increases. This can be improved by choosing a better combination of the operator $L(\mathbf{S})$, the auxiliary parameter h, the auxiliary function $\mathbf{\Psi}(t)$, and the initial approximation $\mathbf{Y}_0$. The resulting costs obtained for each order approximation are given in Table 7-3. The best results were obtained for the 1st order approximation since this gave the best approximation for the Riccati matrix at the initial time. Notice that since the DRE is being solved directly, there is no concern for ill-conditioned matrices.

The second case is for the homotopy defined by the operators in equation (7–10) and equation (7–11). The results obtained are shown in Figure 7-3 where the value for the auxiliary parameter used is $h = -1/2$. The results were computed for the 0th to 6th order approximations. The four components of the Riccati matrix $\mathbf{S}$ are shown in Figure 7-3A thru Figure 7-3D. The results indicate that this HC approach does have consistent improvement as the order of the approximation increases. The results tend to have the same trend as the optimal solution as well. The max difference between the components of $\mathbf{S}^{(k)}$ and $\mathbf{S}^*$ is shown in Table 7-5.

Table 7-5. Maximum difference of Riccati matrix components (HC case 2)

Approximation order	$\Delta S_{1,1}$	$\Delta S_{1,2}$	$\Delta S_{2,2}$	$\Delta S_{2,2}$
0	2.28	2.29	2.29	1.35
1	12.92	12.17	12.54	11.67
2	2.13	1.88	1.84	0.98
3	1.03	0.99	0.99	0.48
4	1.55	1.16	1.13	0.39
5	1.12	1.00	0.92	0.46
6	1.05	0.84	0.72	0.26

The resulting solutions were then used to determine the control, and in turn the response of the states. The states are shown in Figure 7-3E and the control is shown in Figure 7-3F. The results do converge and stay near the optimal solution as the order of the approximation increases. The resulting costs obtained for each order approximation are given in Table 7-3. The best results were obtained for the 3rd order approximation. This again might be coincidental since this approximation might have yielded a good

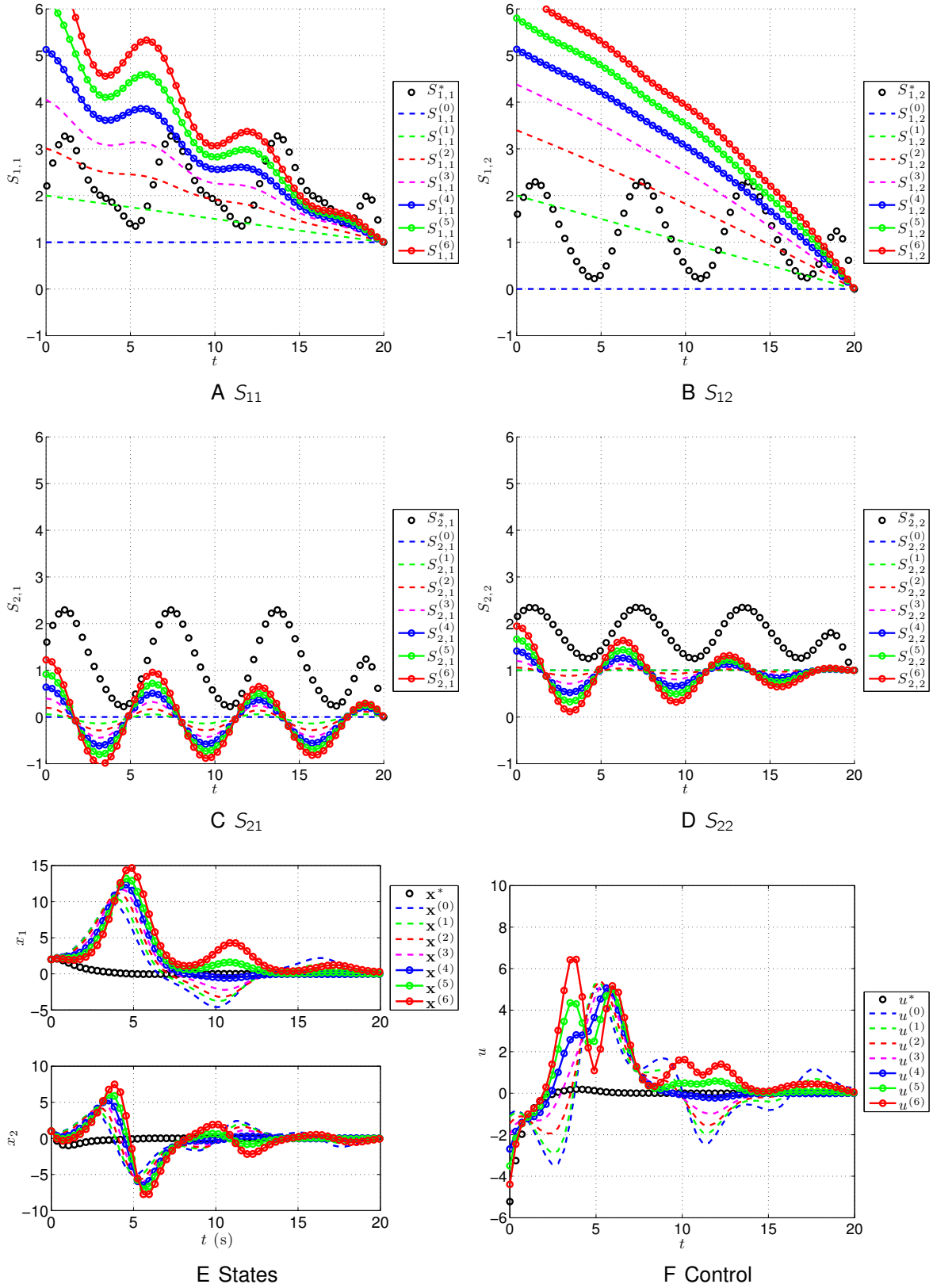

Figure 7-2. Homotopy continuation (case 1) results ($h = -1/20$)

approximation for the initial value of the Riccati matrix. Despite this, it is shown that the homotopy used yields a good approximation to the solution to the DRE.

The third case is for the homotopy defined by the operators in equation (7–10) and equation (7–12). The results obtained are shown in Figure 7-4 where the value for the auxiliary parameter used is $h = -1/2$. The results were computed for the 0th to 5th order approximations. The four components of the Riccati matrix $\mathbf{S}$ are shown in Figure 7-4A thru Figure 7-4D. The results indicate that this HC solution shows improvement immediately after the 0th approximation. However, the improvements with the subsequent approximations seem to plateau. However, the results do have the same trend as the optimal solution. The max differences between the components of $\mathbf{S}^{(k)}$ and $\mathbf{S}^*$ are shown in Table 7-6.

Table 7-6. Maximum difference of Riccati matrix components (HC case 3)

Approximation order	$\Delta S_{1,1}$	$\Delta S_{1,2}$	$\Delta S_{2,2}$	$\Delta S_{2,2}$
0	2.28	2.29	2.29	1.35
1	1.53	1.54	1.54	1.01
2	1.34	1.16	1.14	0.63
3	1.44	1.18	1.16	0.55
4	1.44	1.19	1.16	0.56
5	1.41	1.17	1.14	0.56

The resulting solutions were then used to determine the control, and in turn the response of the states. The states are shown in Figure 7-4E and the control is shown in Figure 7-4F. The results do converge and stay near the optimal solution as the order of the approximation increases. The resulting costs obtained for each order approximation are given in Table 7-3. The best results were obtained for the 2nd order approximation. This again might be coincidental since this approximation might have yielded a good approximation for the initial value of the Riccati matrix.

7.5 Yamanaka-Ankerson-Tschauner-Hempel Example

An example using the YATH equation derived in Appendix A is presented in this section. Based on the example in the previous section, the HC (Case 2) yielded the

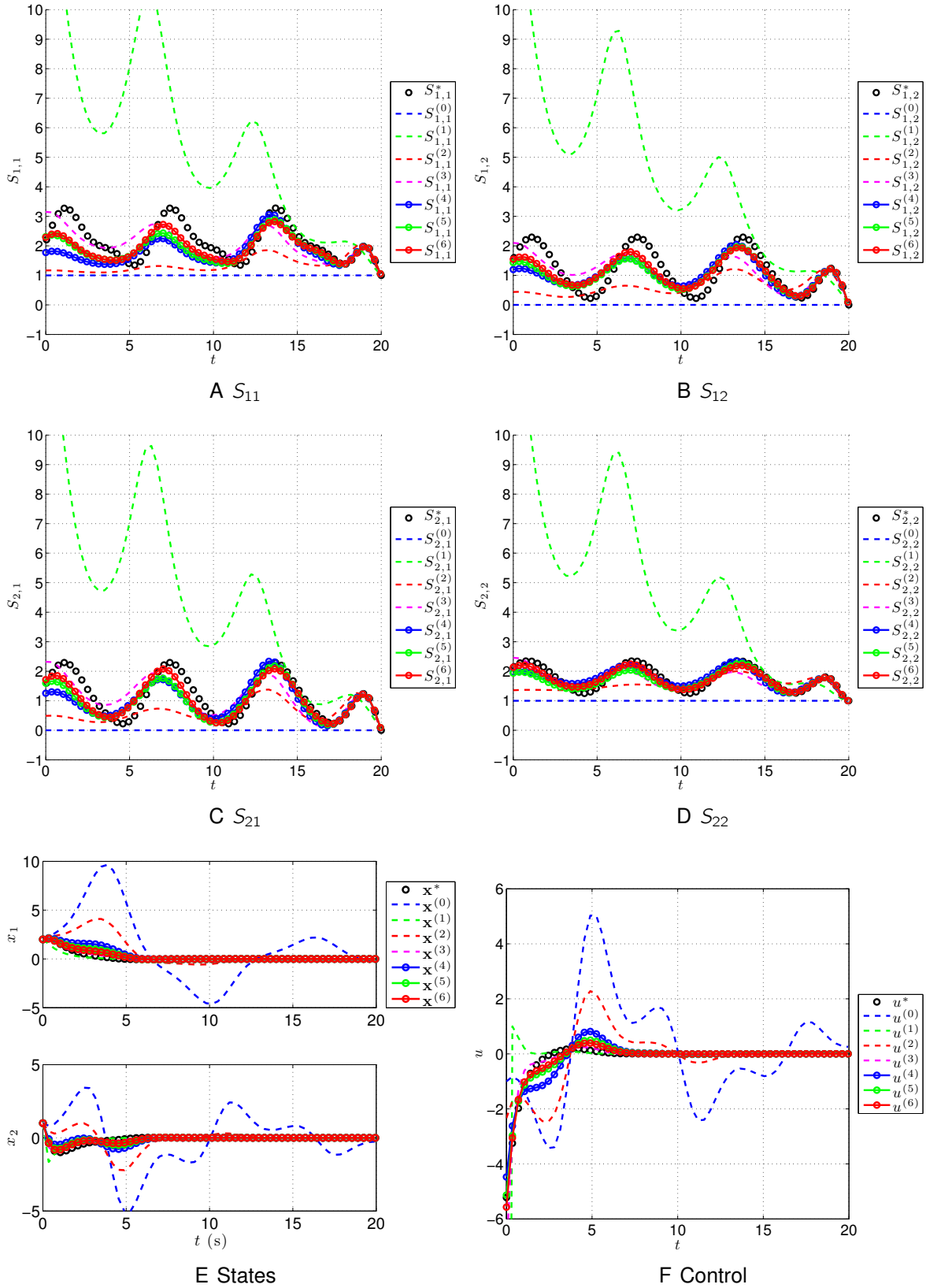

Figure 7-3. Homotopy continuation (case 2) results ($h = -1/2$)

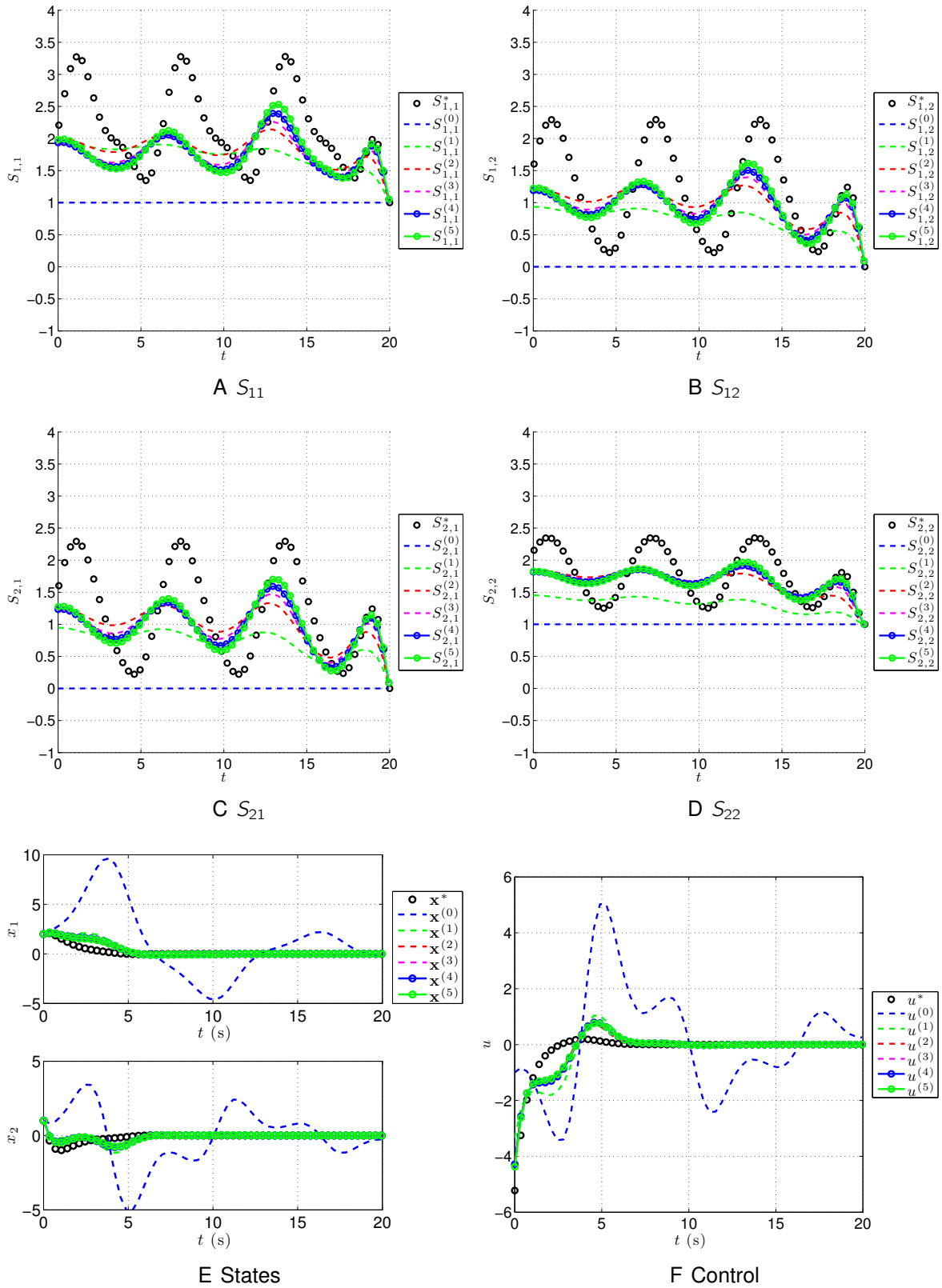

Figure 7-4. Homotopy continuation (case 3) results ($h = -1/2$)

closest result to the optimal solution. In this section, the HC (Case 2) approach shown in Appendix D is used where the solution is obtained up to the fourth order approximation. The value of the auxiliary parameter used is $h = -1/10$. The parameters associated with the LQ problem are given in Table 7-7. Note that the independent variable for this set of equations is the true anomaly of the target.

Table 7-7. Final approach parameters

Parameters	Value	Units
$\mathbf{S}_f$	$\begin{bmatrix} 10^3 \times \mathbf{I} & \mathbf{0} \\ \mathbf{0} & 10^{-3} \times \mathbf{I} \end{bmatrix} \in \mathbb{R}^{6\times 6}$	–
$\mathbf{Q}$	$\begin{bmatrix} 10^3 \times \mathbf{I} & \mathbf{0} \\ \mathbf{0} & 10^{-2} \times \mathbf{I} \end{bmatrix} \in \mathbb{R}^{6\times 6}$	–
$\mathbf{R}$	$10^{-3} \times \mathbf{I} \in \mathbb{R}^{3\times 3}$	–
e	0.15	–
k	0.0256	$\sqrt{\text{rad/s}}$
$\mathbf{r}_0$	$\begin{bmatrix} 10 & -10 & 10 \end{bmatrix}^T$	m
$\mathbf{v}_0$	$\begin{bmatrix} 0 & -0 & 0 \end{bmatrix}^T$	m/s
θ_0	0	deg
θ_f	10	deg

The results obtained are shown in Figure 7-5. The relative position history is shown in Figure 7-5A where the black line represents the optimal solution and the other lines represent the different approximation orders. This figure shows that the solutions begin to converge after the first order approximation. In addition, the solution gets close to the optimal solution as the order of the approximation increases. The relative velocity histories are shown in Figure 7-5B. These results indicate that the velocity converges to zero after the first order approximation as well. The corresponding control histories are shown in Figure 7-5C and a zoomed view of this plot is shown in Figure 7-5D. These plots show that the approximations require a relatively large initial control action. This is likely due to a poor approximation to the Riccati matrix at the initial time. Despite this, the trajectories were shown to converge to the origin. The costs associated with each trajectory are shown in Table 7-8. This table shows the cost continues to decrease as the order of the approximation increases.

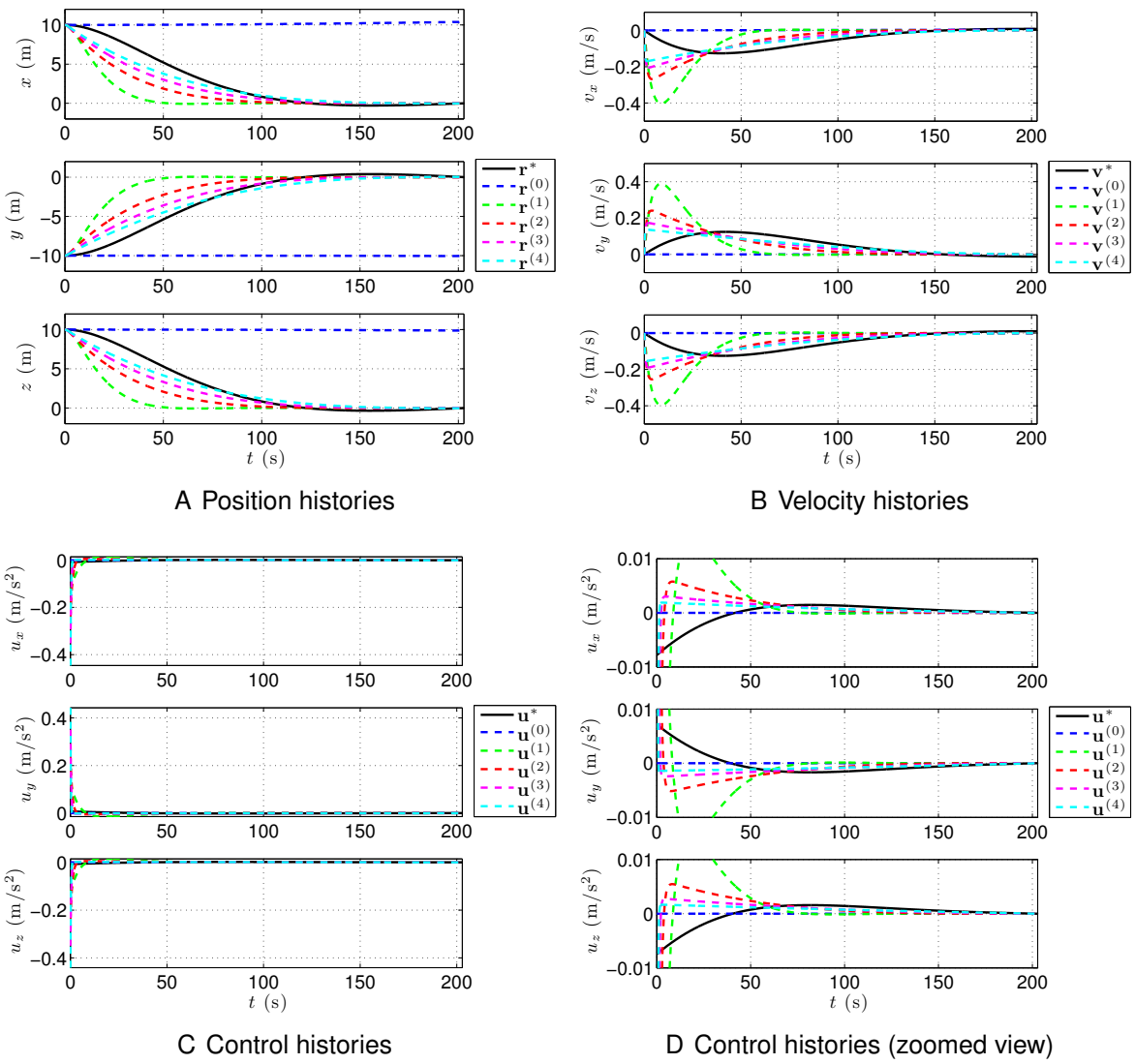

Figure 7-5. Homotopy continuation results for final approach example ($h = -1/10$)

Table 7-8. Costs for final approach using HC

Cost	HC (case 2)
J^*	$6.74e3$
$J^{(0)}$	$1.78e5$
$J^{(1)}$	$7.72e4$
$J^{(2)}$	$7.41e4$
$J^{(3)}$	$7.13e4$
$J^{(4)}$	$7.08e4$

In this chapter, the methods for solving a finite horizon LQ problem for both an LTI and LTV systems are discussed. For the case where the Hamiltonian matrix is constant, it is shown that solution is determined by obtaining the STM of linear system of matrix differential equations related to the DRE. When the Hamiltonian matrix is not constant, two methods are presented for obtaining the solution. For the numerical example shown in this chapter, the best result is obtained by using the HC approach with the mapping between equation (7–10) and equation (7–11). This mapping is then used to solve the final approach problem with the YATH equations presented in Appendix A. It is shown that the after the first order approximation, the solutions converge to the origin. In addition, as the order of the approximation increased, the solution matches more closely to the optimal solution.

CHAPTER 8
NUMERICAL RESULTS

The results from the numerical analyses performed are presented and discussed in this chapter. First, the results of the Monte Carlo simulations (MCSs) performed characterize the performance and convergence characteristics for the Artificial Potential Function (APF) and Adaptive Artificial Potential Function (AAPF) methods. The MCSs are performed with both the Clohessy-Wiltshire-Hill (CWH) and small angle approximation (SAA) equations. Next, the results of implementing the optimal solutions obtained in Chapter 4 in the high fidelity model are presented. Two methods of tracking are used: “trajectory tracking” and “force tracking”. The aim of this study is to determine how well the spacecraft is able to track the trajectories obtained and to characterize the discrepancies between the optimal trajectory and the realized trajectory. The APF and AAPF methods are also implemented in the high fidelity model to determine how these methods perform in a higher fidelity model. Next, a close-range rendezvous scenario with obstacle avoidance is presented. The scenario is simulated with a planned trajectory, the APF method, and the AAPF method. Lastly, a final approach scenario is presented which uses the finite horizon LQ solution using the CWH equation and the state transition matrix (STM) solution presented in Chapter 7.

8.1 Monte Carlo Simulations

It was shown in Chapter 6 that a stability proof for the APF and AAPF methods only exists for the obstacle-free case. Moreover, there is no methodology to characterize the performance of these methods. As a result, MCSs are performed to demonstrate performance and convergence characteristics of the APF and AAPF methods. Two MCSs are performed for relative translation (i.e., CWH equation) and relative orientation (i.e., SAA equation).

In the relative translation MCS, the initial conditions of the chaser are varied. The initial conditions are chosen as normally distributed random vectors with $\mathbf{r}_0 \sim \mathcal{N}(\mathbf{0}, 500\mathbf{I})$,

$\mathbf{v}_0 \sim \mathcal{N}(\mathbf{0}, \mathbf{I})$, and with the constraints

$$250 \text{ m} \leq \|\mathbf{r}_0\| \leq 1000 \text{ m}$$

$$\|\mathbf{r}_0 - \mathbf{r}_i\| \geq 50 \text{ m for } i = 1, 2, 3, \ldots, 14 \ .$$

These constraints are enforced to ensure that there is a considerable separation initially between the chaser, target, and obstacles while maintaining the close proximity assumption. A set of 14 static obstacles are placed in the state space at the positions shown below.

$$\mathbf{r}_1 = \begin{bmatrix} 500 & 0 & 0 \end{bmatrix}^T \quad \mathbf{r}_2 = \begin{bmatrix} -500 & 0 & 0 \end{bmatrix}^T \quad \mathbf{r}_3 = \begin{bmatrix} 0 & 500 & 0 \end{bmatrix}^T$$

$$\mathbf{r}_4 = \begin{bmatrix} 0 & -500 & 0 \end{bmatrix}^T \quad \mathbf{r}_5 = \begin{bmatrix} 0 & 0 & 500 \end{bmatrix}^T \quad \mathbf{r}_6 = \begin{bmatrix} 0 & 0 & -500 \end{bmatrix}^T$$

$$\mathbf{r}_7 = \begin{bmatrix} 250 & 250 & 250 \end{bmatrix}^T \quad \mathbf{r}_8 = \begin{bmatrix} 250 & -250 & 250 \end{bmatrix}^T \quad \mathbf{r}_9 = \begin{bmatrix} 250 & 250 & -250 \end{bmatrix}^T$$

$$\mathbf{r}_{10} = \begin{bmatrix} 250 & -250 & -250 \end{bmatrix}^T \quad \mathbf{r}_{11} = \begin{bmatrix} -250 & 250 & 250 \end{bmatrix}^T \quad \mathbf{r}_{12} = \begin{bmatrix} -250 & -250 & 250 \end{bmatrix}^T$$

$$\mathbf{r}_{13} = \begin{bmatrix} -250 & 250 & -250 \end{bmatrix}^T \quad \mathbf{r}_{14} = \begin{bmatrix} -250 & -250 & -250 \end{bmatrix}^T$$

The initial positions and obstacles are illustrated in Figure 8-1A where the blue circles represent the initial positions and the black dots represent the static obstacles. The parameters used in this MCS are given in Table 8-1.

Table 8-1. Monte Carlo simulation parameters (CWH equation)

Parameter	APF Value	AAPF Value	Units
n	0.0012	0.0012	rad/s
$\mathbf{r}_f$	$\mathbf{0}$	$\mathbf{0}$	m
f_{max}	1	1	m/s
$\mathbf{P}$	$\mathbf{I} \in \mathbb{R}^{3\times3}$	–	s^{-2}
$\boldsymbol{\theta}_0$	–	$0.002 \times \begin{bmatrix} 1 & 0 & 0 & 1 & 0 & 1 \end{bmatrix}^T$	s^{-2}
$\mathbf{N}_i$	$\mathbf{I} \in \mathbb{R}^{3\times3}$	$\mathbf{I} \in \mathbb{R}^{3\times3}$	s^{-2}
ψ_i	1.5×10^5	1.5×10^5	–
σ_i	1.0×10^4	1.0×10^4	m^2
k	0.002	0.002	–
T	–	1000	s

In the relative orientation MCS, the initial conditions of the chaser and tumbling rate of the target are varied. The initial conditions were chosen as normally distributed random vectors with $\boldsymbol{\alpha}_0 \sim \mathcal{N}(\mathbf{0}, 0.1\mathbf{I})$, $\dot{\boldsymbol{\alpha}}_0 \sim \mathcal{N}(\mathbf{0}, 0.1\mathbf{I})$, $\boldsymbol{\omega}_t \sim \mathcal{N}(\mathbf{0}, 0.05\mathbf{I})$, and the constraints

$$\begin{aligned} 0.1 \text{ rad} \leq \|\boldsymbol{\alpha}_0\| &\leq 0.25 \text{ rad} \\ \|\dot{\boldsymbol{\alpha}}_0\| &\leq 0.25 \text{ rad/s} \\ \|\boldsymbol{\omega}_t\| &\leq 0.25 \text{ rad/s} \ . \end{aligned}$$

The constraints are enforced to maintain the small angle assumption yet have a distinct initial relative orientation and tumbling rate between the chaser and target. Obstacles are not included in this MCS. However, they could have been included to represent "keep out zones" in the relative orientation states. The initial orientations used are illustrated in Figure 8-1B. The parameters used in this MCS are given in Table 8-2.

Table 8-2. Monte Carlo simulation parameters (SAA equation)

Parameter	APF Value	AAPF Value	Units
$\boldsymbol{\alpha}_f$	$\mathbf{0}$	$\mathbf{0}$	rad
τ_{max}	20	20	m/s
$\mathbf{P}$	$\mathbf{I} \in \mathbb{R}^{3\times3}$	–	s^{-2}
$\boldsymbol{\theta}_0$	–	$0.002 \times \begin{bmatrix} 1 & 0 & 0 & 1 & 0 & 1 \end{bmatrix}^T$	s^{-2}
k	2	–	–
T	–	5	s

Settling time is used to characterize convergence where the solution is assumed to have settled when $\mathbf{r} \leq 10$ m for the relative translation case and $\boldsymbol{\alpha} \leq 0.01$ rad for the relative orientation case. Performance is characterized based on the control effort cost

$$J = \int_{t_0}^{t_f} \|\mathbf{u}\|_1 dt \ ,$$

where $\mathbf{u}$ is the control parameter and t_f is the settling time.

The results obtained for the relative translation MCS are shown in Figure 8-2. The cost data is shown in Figure 8-2A where the average cost obtained using the APF

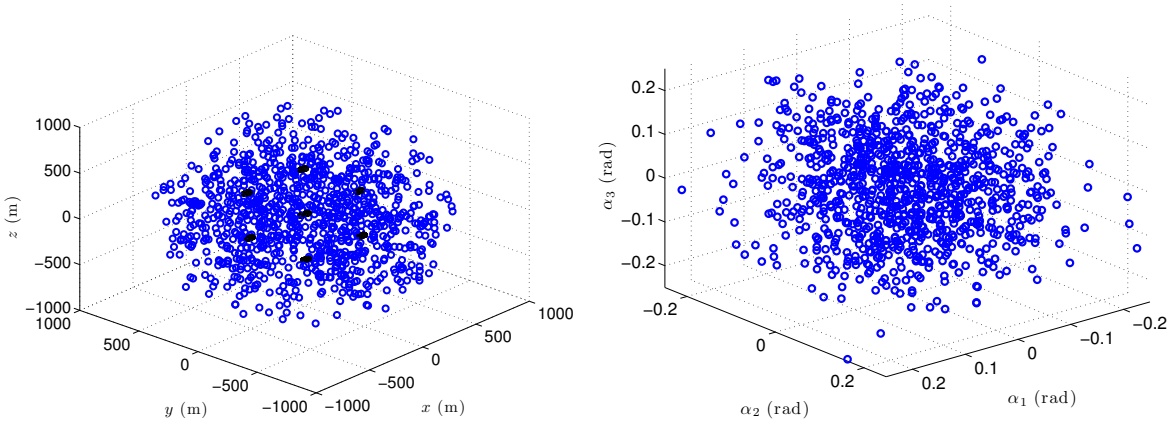

A CWH initial positions and obstacle positions

B SAA initial orientations

Figure 8-1. Initial relative position/orientations used in Monte Carlo simulations

method is 8.60 m/s and the average cost obtained using the AAPF method is 4.12 m/s. The settle time data is shown in Figure 8-2B where the average settling time obtained with the APF method is 1315 s and the average settling time obtained using the AAPF method was 1209 s. These results indicate that the AAPF method commands less control effort than the APF method in the relative translation scenario. In addition, the AAPF method is able to specify a time constraint based on the largely skewed (to the right) data in Figure 8-2B for the AAPF method. A large majority of the data points centered around the 1000 s is a result of choosing the transfer time $T = 1000$ s. The results of the MCS indicate that the AAPF method commands less control effort globally while being able to choose a time criterion in the transfer time T.

The results obtained for the relative orientation MCS are shown in Figure 8-2. The cost data is shown in Figure 8-2C where the average cost obtained using the APF method is 207.7 N $\cdot$ m while the average cost obtained using the AAPF method is 65.03 N $\cdot$ m. The settle time data is shown in Figure 8-2D where the average settling time obtained using the APF method is 6.85 s and the average settling time obtained using the AAPF method is 8.97 s. These results indicate that the AAPF method commands less control effort than the APF method in the relative orientation scenario. However, a

firm time constraint is not seen based on the transfer time chosen for the AAPF method. This is due to the linearized model (i.e., SAA equation) and the constant compensation for the tumbling rates of each sample point. Although the average settling time was slightly larger for the AAPF method, the control effort was considerably lower.

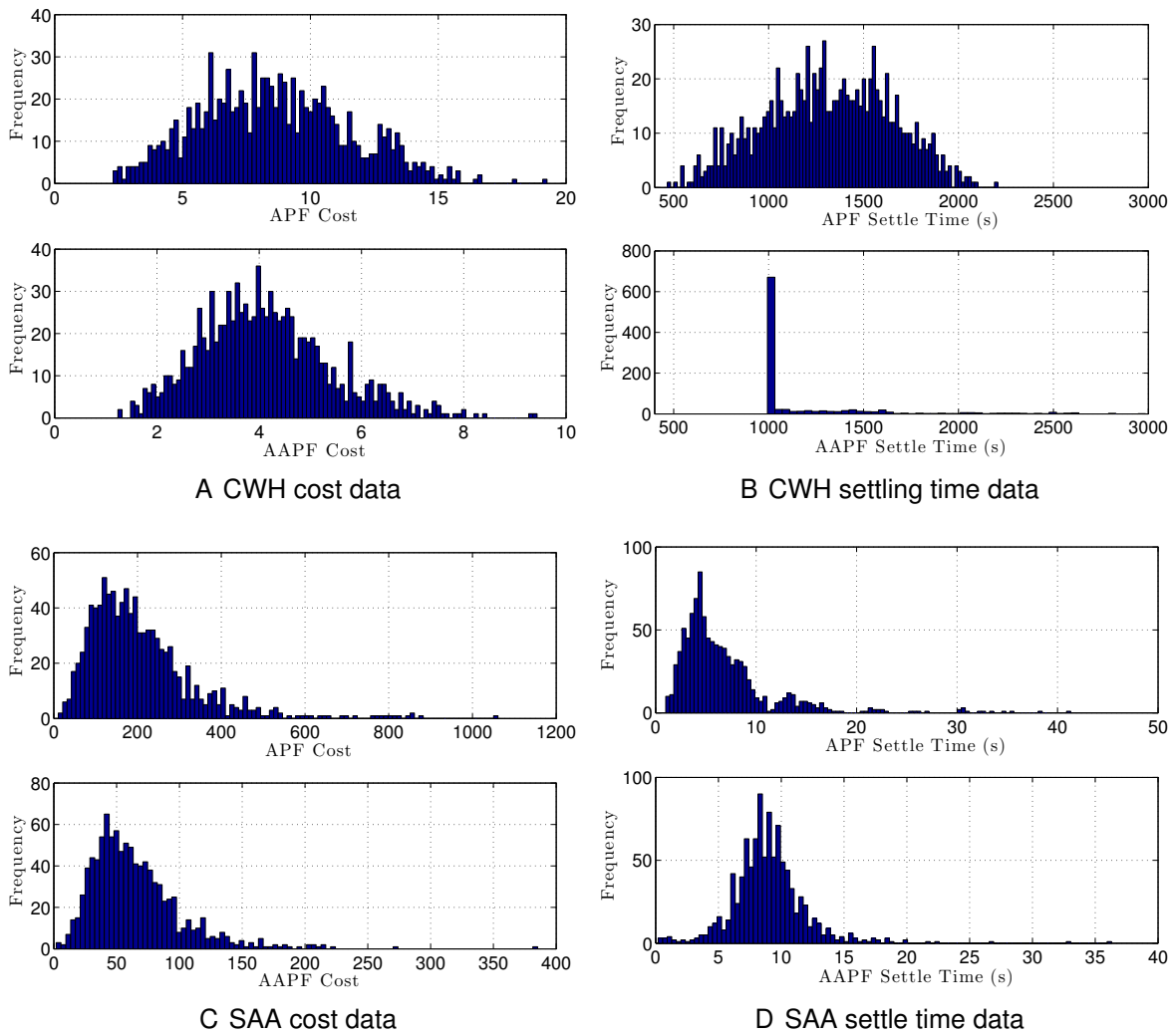

Figure 8-2. Costs and settling times data from Monte Carlo simulations

8.2 High Fidelity Simulations

The simulation results presented in this section are generated using the high fidelity model discussed in Chapter 3. The parameters used for the target and chaser spacecraft are given in Table 8-3 and Table 8-4, respectively. In the simulations, the optimal trajectories obtained in Chapter 4 are implemented using two methods of

tracking: “trajectory tracking” and “force tracking”. Since the trajectories obtained in Chapter 4 are only defined at the collocation points, interpolation is used for both tracking methods to obtain a continuous reference signal.

Table 8-3. Target spacecraft parameters

Parameter	Value	Units
m_t	100	kg
l_t	3	m
$\mathbf{r}_t(t_0)$	$\begin{bmatrix}-1182.959348 & 6817.396210 & 904.495486\end{bmatrix}^T$	km
$\mathbf{v}_t(t_0)$	$\begin{bmatrix}0.175776 & -0.963776 & 7.494102\end{bmatrix}^T$	km/s
$\mathbf{J}_t$	$\begin{bmatrix}300 & 20 & 10 \\ 20 & 100 & 0 \\ 10 & 0 & 200\end{bmatrix}$	$\mathrm{kg} \cdot \mathrm{m}^2$
$\mathbf{q}_t(t_0)$	$\begin{bmatrix}0 & 0 & 0 & 1\end{bmatrix}^T$	–
$\boldsymbol{\omega}_t(t_0)$	$\begin{bmatrix}0 & 0 & 0\end{bmatrix}^T$	rad/s

Table 8-4. Chaser spacecraft parameters

Parameter	Value	Units
m_c	100	kg
l_c	3	m
$\mathbf{r}_c(t_0)$	$\begin{bmatrix}-1182.339411 & 6816.939420 & 904.891745\end{bmatrix}^T$	km
$\mathbf{v}_c(t_0)$	$\begin{bmatrix}0.175776 & -0.963776 & 7.494102\end{bmatrix}^T$	km/s
f_{max}	$\sqrt{3}$	$\mathrm{m/s^2}$
f_{db}	0.01	$\mathrm{m/s^2}$
$\mathbf{J}_c$	$\begin{bmatrix}300 & 20 & 10 \\ 20 & 100 & 0 \\ 10 & 0 & 200\end{bmatrix}$	$\mathrm{kg} \cdot \mathrm{m}^2$
$\mathbf{q}_c(t_0)$	$\begin{bmatrix}1 & 0 & 0 & 0\end{bmatrix}^T$	–
$\boldsymbol{\omega}_c(t_0)$	$\begin{bmatrix}0 & 0 & 0\end{bmatrix}^T$	rad/s
Ω_{max}	5000	rad/s
$\dot{\Omega}_{max}$	100	$\mathrm{rad/s^2}$

The “trajectory tracking” method involves tracking the optimal states obtained from the optimal solution. A cubic spline is used to interpolate between the collocation points of the optimal trajectory since cubic splines are smooth (i.e., ensure the derivative of the interpolating polynomial is continuous) and do not have the oscillatory behavior of

high-degree polynomial interpolation. [73] To track a position, the error is defined as

$$\mathbf{e}_d = \mathbf{r}_c^* - \mathbf{r}_c \ ,$$

where $\mathbf{r}_c^*$ is the optimal position of the chaser. As a result, the proportional-integral-derivative (PID) controller

$$\mathbf{f} = k_p \mathbf{e}_d + k_i \int_{t_0}^{t} \mathbf{e}_d \ d\varepsilon + k_d \dot{\mathbf{e}}_d$$

is used, where $k_p = 0.6$, $k_i = 0.06$, and $k_d = 1.5$ are the tuned PID controller gains. [71] The PID controller defines the force required to track the optimal chaser position based on the true chaser position. To track an orientation, the error quaternion is defined according to equation (2–8)

$$\mathbf{q}_e = \mathbf{q}_c^* \otimes \mathbf{q}_c^{-1} \ ,$$

where $\mathbf{q}_c^*$ is the optimal attitude trajectory of the chaser. As a result, the eigenaxis attitude controller

$$\boldsymbol{\tau} = -k \mathbf{J}_c \boldsymbol{\epsilon}_e - c \mathbf{J}_c \boldsymbol{\omega}_c + \boldsymbol{\omega}_c^{\times} \mathbf{J}_c \boldsymbol{\omega}_c$$

is used, where $\boldsymbol{\epsilon}_e$ is the vector component of the error quaternion and $k = 9.54$, $c = 5.5$ are gains. [100] The eigenaxis controller generates the torque required to perform an eigenaxis slew (i.e., “minimum eigenangle” slew) towards the optimal chaser orientation based on the true chaser orientation. [100]

The “force tracking” method involves tracking the optimal control and torque profiles using the respective actuators. A piecewise cubic Hermite interpolating polynomial is used to interpolate between the collocation points of the control. This method of interpolation is chosen since the optimal control is sometimes discontinuous and piecewise polynomials can handle this phenomenon. [73] As a result, the interpolated optimal control is fed forward to the actuators as the commanded control action.

The APF and AAPF methods are also implemented in the high fidelity model. These simulations are performed to determine how well the APF and AAPF methods perform in a high fidelity model. Both methods are designed to “re-plan” trajectories until the terminal conditions are met. A close-range rendezvous scenario with obstacle avoidance is also simulated. The trajectory obtained in Chapter 4 is implemented using “trajectory tracking”. The APF and AAPF methods are also implemented to demonstrate close-range rendezvous with obstacle avoidance.

The last set of results presented are the final approach scenario. The final approach is done using the finite horizon LQ solution using the CWH equation. The feedback control law for this approach is developed in Chapter 7. This controller is implemented to demonstrate how using a linearized model can be used to develop a feedback controller which is implementable in higher fidelity dynamics.

8.2.1 Minimum Time Trajectories

Figure 8-3 shows the results of implementing the minimum time trajectories using “trajectory tracking” in the high fidelity model. The magnitude of the relative position is shown in Figure 8-3A where the blue line represents the relative position between the chaser and target and the green line represents the relative position between the chaser and the optimal trajectory. This figure indicates that the optimal trajectory is tracked within 5 m and the distance between the chaser and the optimal trajectory is approximately 0.5 m at the final time. However, the distance between the chaser and the target is approximately 10 m. This deviation is small and is due to disturbances and/or inaccuracies in the optimal solution.

The orientation error is shown in Figure 8-3B where the blue line represents the error angle between the chaser and target and the green line represents the error angle between the chaser and optimal trajectory. This figure indicates that the attitude trajectory can be tracked within a 10° error angle. The error angle between the chaser

and target and between the chaser and optimal trajectory is virtually the same (i.e., about $1°$) at the final time. The deviation is due inaccuracies in the optimal solution.

The relative position plots are shown in Figure 8-3C and the quaternion trajectories are shown in Figure 8-3D. Both match closely to the optimal trajectories, which indicates that the respective dynamic models used are accurate for minimum time trajectories. The force plot is shown in Figure 8-3E and the torque plot is shown in Figure 8-3F. The force plot indicates that "trajectory tracking" leads to a control history similar to the optimal control history. The torque plot indicates that "trajectory tracking" does not necessarily lead to a control history similar to the optimal control history. In particular, the first component of the torque matches the optimal control; however, the second and third components do not.

Next, Figure 8-4 shows the results of implementing the minimum time trajectories using "force tracking" with the high fidelity model. The relative position magnitude is shown in Figure 8-4A where the blue line represents the relative position between the chaser and target and the green line represents the relative position between the chaser and the optimal trajectory. This figure indicates that the optimal force does not yield the same response in a higher fidelity model. At the final time, the relative position between the chaser and the optimal trajectory is approximately 10 m and the relative position between the chaser and the target is approximately 3 m. It is equivocal as to why "force tracking" yields a better response in the high fidelity model.

The orientation error plot is shown in Figure 8-4B where the blue line represents the error angle between the chaser and target and the green line represents the error angle between the chaser and the optimal trajectory. This figure indicates that the error angle between the chaser and target and between the chaser and the optimal trajectory are virtually the same (approximately $5°$) at the final time. This is evidence that the optimal control does not yield the same response in the high fidelity model and as a result the terminal conditions are not satisfied. This is likely due to a drift in the attitude

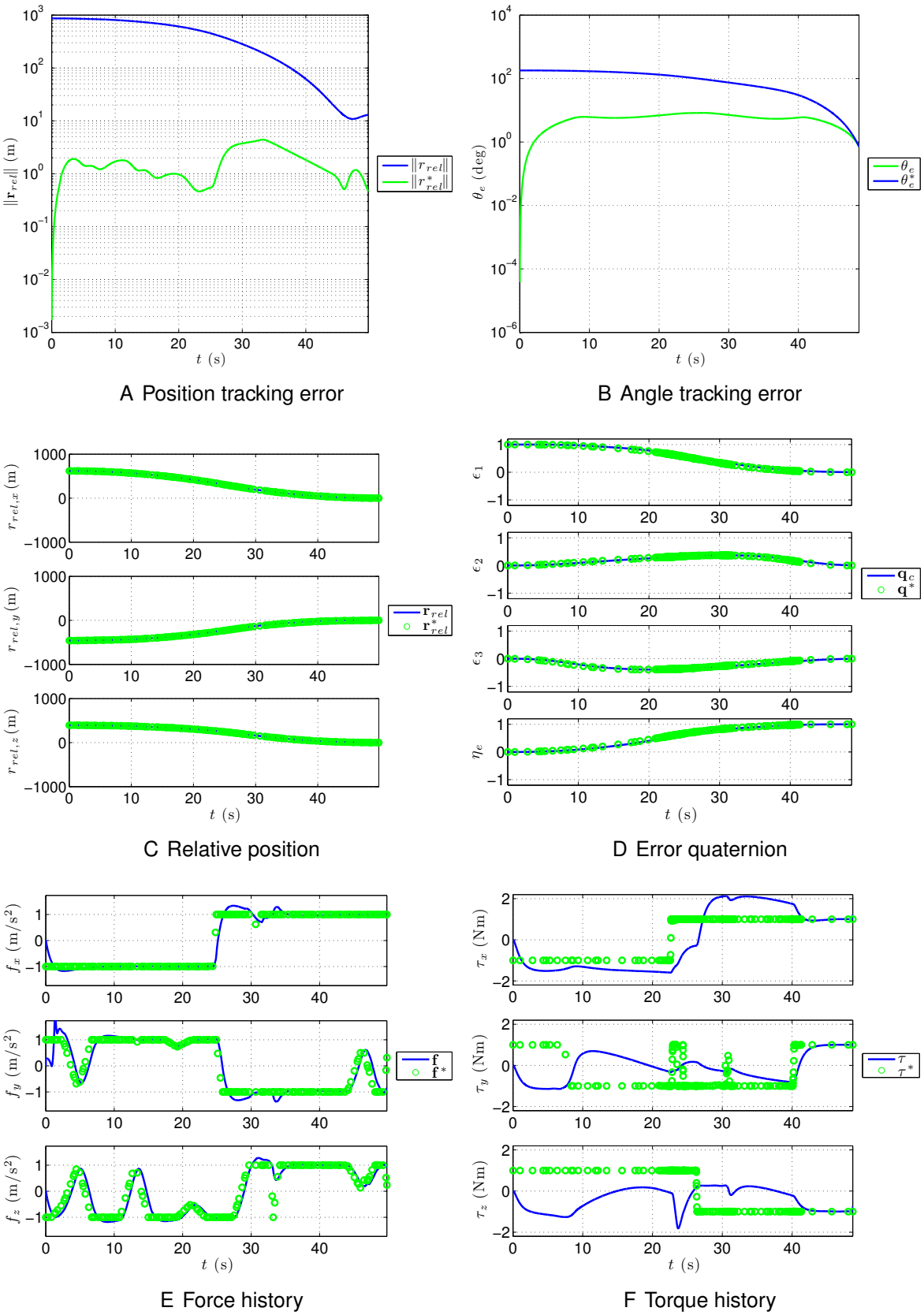

Figure 8-3. Minimum time “trajectory tracking” results

of the target caused by disturbances. Another source of error might be the “bang-bang” control structure. This control structure requires that a discontinuous jump be made in the control which is not physically realizable with the reaction wheels.

The relative position plots are shown in Figure 8-4C and the quaternion trajectories are shown in Figure 8-4D. Both plots indicate that the resultant trajectory is similar to the optimal trajectory. This indicates that the models used for generating the optimal solutions are accurate for minimum time problems. The force plot is shown in Figure 8-4E and the torque plot is shown in Figure 8-4F. These plots indicate that the optimal control can be tracked accurately by the actuators.

8.2.2 Fixed Time Minimum Control Effort Trajectories

Figure 8-5 shows the results of implementing the fixed time minimum control effort trajectories using “trajectory tracking” with the high fidelity model. The magnitude of the relative position is shown in Figure 8-5A where the blue line represents the relative position between the chaser and target and the green line represents the relative position between the chaser and the optimal trajectory. This figure indicates that the optimal trajectory is tracked accurately (i.e., within a 1 m error). The plot shows a high frequency low amplitude tracking signal which implies the PID controller is accurately tracking the trajectory. However, the position of the chaser is not nearly the same as the position of the target (approximately 1 km away) at the final time. This is due to secular disturbing effects which were not modeled in the reference trajectories.

The orientation error is shown in Figure 8-5B where the blue line represents the error angle between the chaser and target and the green line represents the error angle between the chaser and optimal trajectory. This error plot is evidence that the optimal attitude trajectory can be tracked within a 1° error angle and that the final orientation matches the results from the higher fidelity model (within a 0.1° error angle) at the final time.

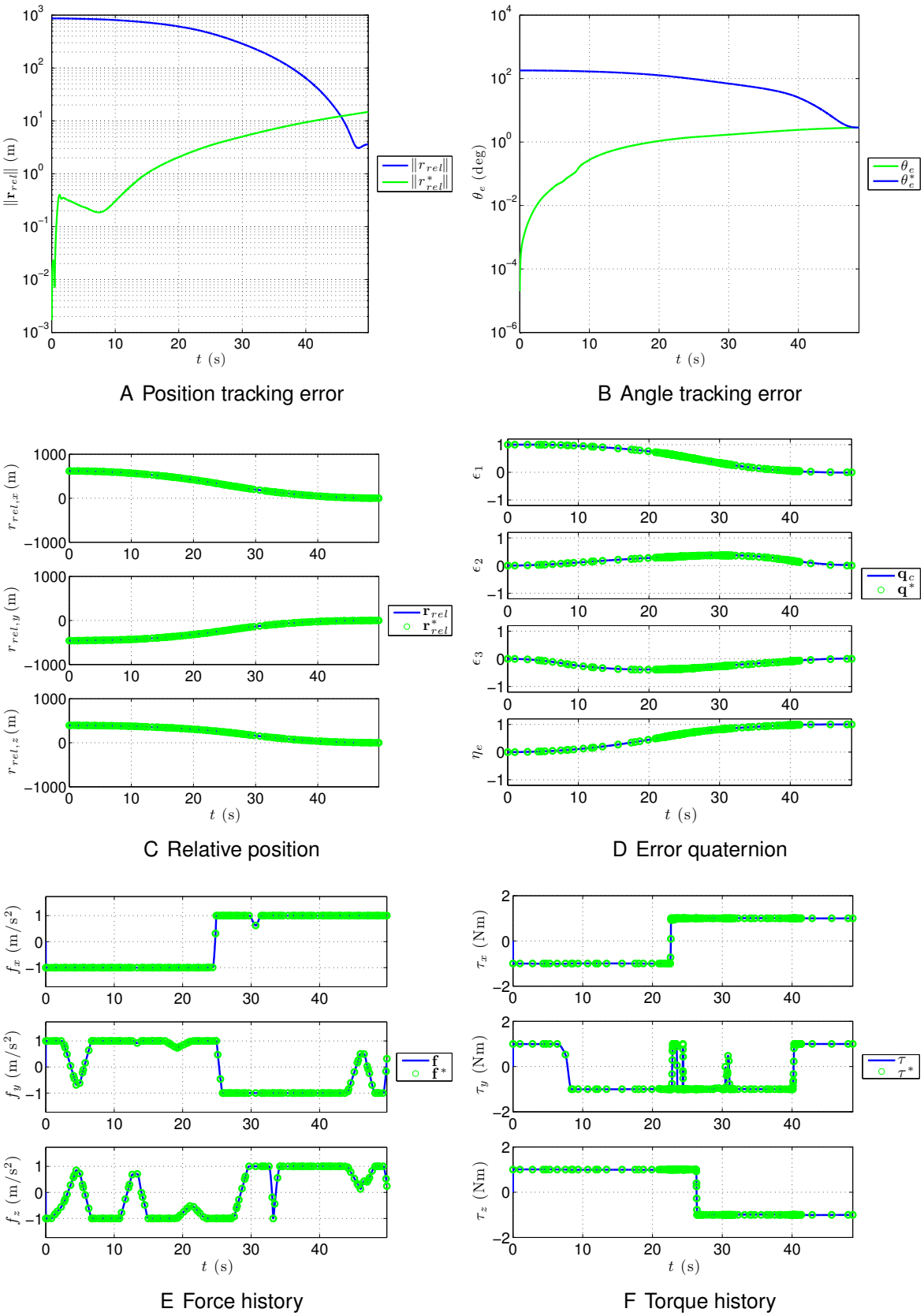

Figure 8-4. Minimum time “force tracking” results

The relative position plots shown in Figure 8-5C illustrate the secular disturbing effects. The trajectories are initially coincident and begin to drift after approximately 100 s. Since the disturbances affect the chaser and the target, the error goes unaccounted for in both spacecraft. This result is motivation for a need to “re-plan” for “unmodeled” effects.

The quaternion trajectories shown in Figure 8-5D match closely which agrees with the results in Figure 8-5B. This indicates that the model used for rotational motion is accurate. The force plot is shown in Figure 8-5E and the torque plot is shown in Figure 8-5F. Both the force and torque plots indicate that “trajectory tracking” leads to a control history similar to the optimal control history.

Next, Figure 8-6 shows the results of implementing the fixed time minimum control effort trajectories using “force tracking” with the high fidelity model. The relative position magnitude is shown in Figure 8-6A where the blue line represents the relative position between the chaser and target and the green line represents the relative position between the chaser and the optimal trajectory. The green line indicates that optimal control does not yield the same response in a higher fidelity model. This is due to the secular disturbing effects acting on the chaser. However, the chaser is closer to the target at the final time (approximately 300 m). This is a result of the “bang-off-bang” control structure being fully captured when using “force tracking”.

The orientation error plot is shown in Figure 8-6B where the blue line represents the error angle between the chaser and target and the green line represents the error angle between the chaser and the optimal trajectory. This figure indicates that the error between the chaser and target and the error between the chaser and the optimal trajectory are about the same (approximately $10°$) at the final time. This is evidence that the optimal control history does not yield the desired terminal conditions in a higher fidelity model. This may be due to a drift in the orientation of the target or the “bang-off-bang” control structure. Since there is a finite width in between the switching

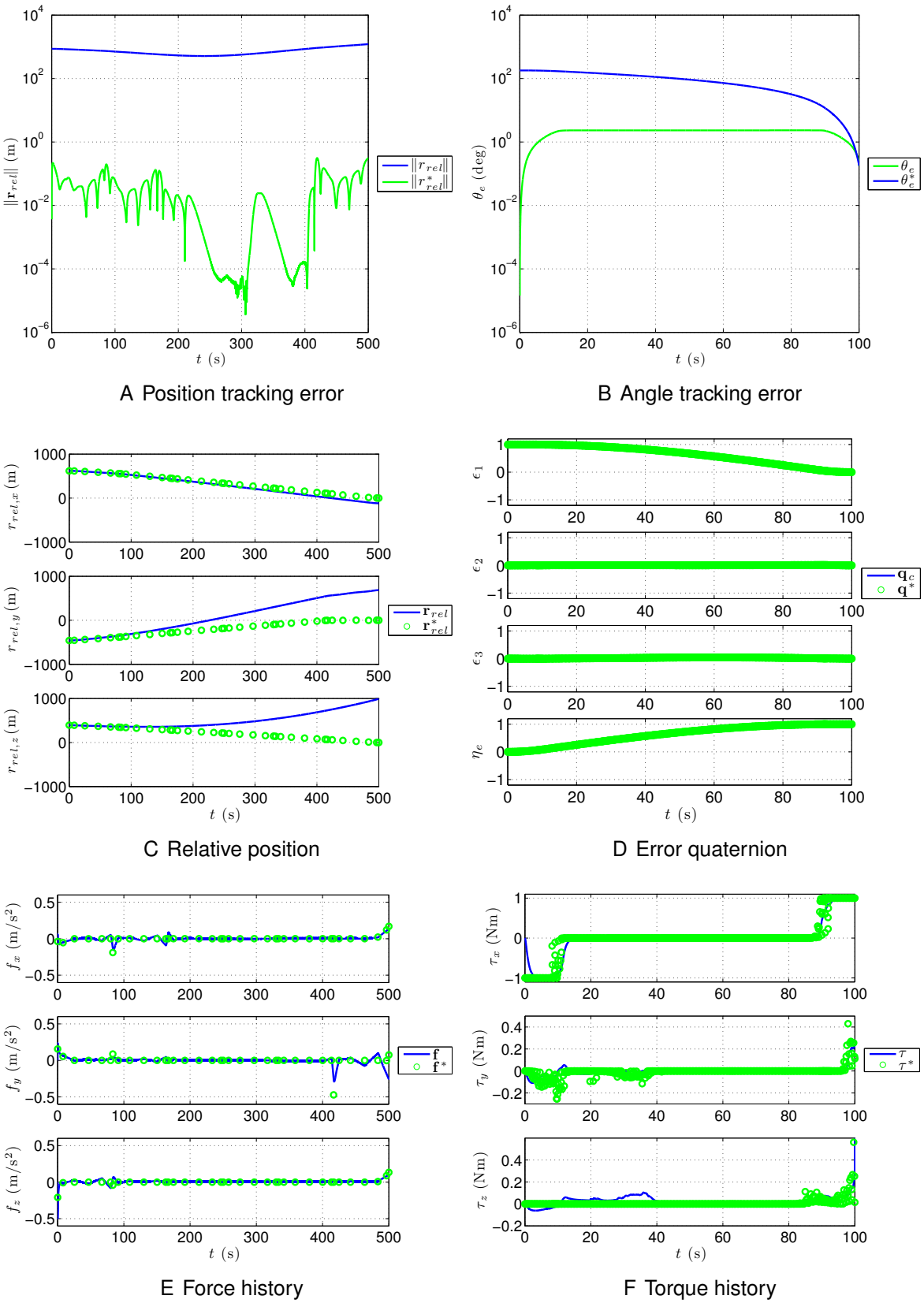

Figure 8-5. Fixed time minimum control effort “trajectory tracking” results

points of the control, the interpolated values at the switching points add an error to the response.

The relative position plots shown in Figure 8-6C illustrate the secular disturbing effects. It is shown that the trajectories are initially coincident and begin to drift after approximately 100 s. This figure also illustrates that the terminal condition obtained using “force tracking” are better than those obtained using “trajectory tracking”. However, the error at the final time is still large. The quaternion plot shown in Figure 8-6D indicates that the the trajectories are similar, yet there is a 10° error at the terminal condition which is evident in Figure 8-6B. The force plot is shown in Figure 8-6E and the torque plot is shown in Figure 8-6F. These plots indicate that the optimal control histories are tracked accurately by the actuators.

8.2.3 Finite Horizon Quadratic Cost Trajectories

Figure 8-7 shows the results of implementing the finite horizon quadratic cost trajectories using “trajectory tracking” with the high fidelity model. The magnitude of the relative position is shown in Figure 8-7A where the blue line represents the relative position between the chaser and target and the green line represents the relative position between the chaser and the optimal trajectory. This figure indicates that the optimal trajectory is tracked accurately (i.e., under a 0.01 m error). However, the relative position between the chaser and target is not close to zero (approximately 1 km) at the final time. This is again due to secular disturbing effects.

The orientation error is shown in Figure 8-7B where the blue line represents the error angle between the chaser and target and the green line represents the error angle between the chaser and optimal trajectory. This plot is evidence that the optimal trajectory can be tracked within a 1° error angle, and that the final orientation matches the results from the higher fidelity model (within a 0.1° error) at the final time. This result indicates that disturbances have less effect on the rotational motion.

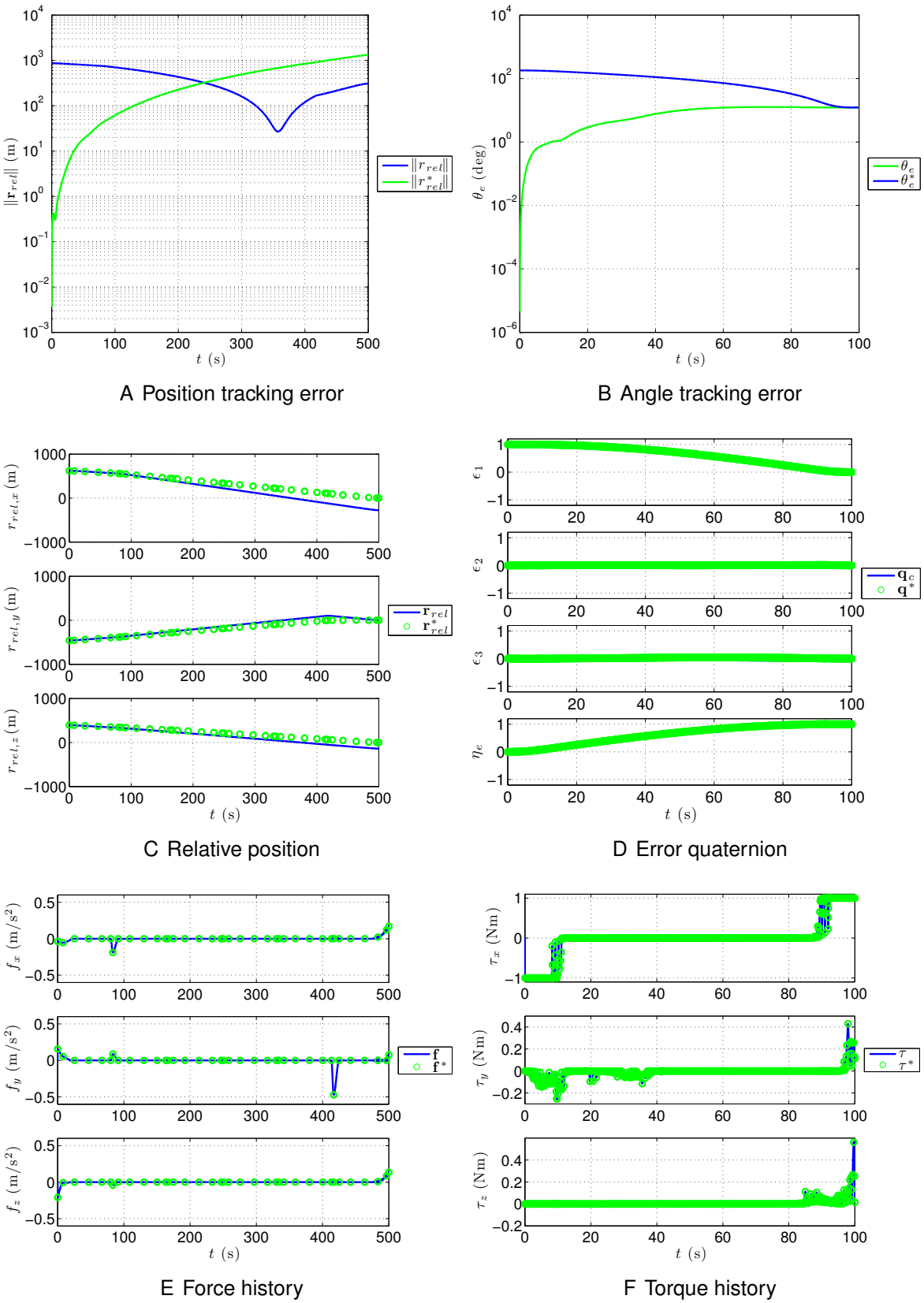

Figure 8-6. Fixed time minimum control effort “force tracking” results

The relative position plots shown in Figure 8-7C illustrate how the chaser drifts as it tracks the optimal trajectory. Initially the trajectories are coincident and begin to drift after approximately 100 s. The quaternion trajectories shown in Figure 8-7D match closely, which is reinforced by the results in Figure 8-7B. The force plot is shown in Figure 8-7E and the torque plot is shown in Figure 8-7F. The force plot indicates that "trajectory tracking" leads to a control history similar to the optimal control history. The torque plot is another example where "trajectory tracking" does not necessarily lead to a control history similar to the optimal control history.

Next, Figure 8-8 shows the results of implementing the finite horizon quadratic cost trajectories using "force tracking" with the high fidelity model. The relative position magnitude is shown in Figure 8-8A where the blue line represents the relative position between the chaser and target and the green line represents the relative position between the chaser and the optimal trajectory. The green line indicates that optimal control does not yield the same response in a higher fidelity model. However, the chaser is closer to the target at the final time (approximately 300 m). This is again due to the secular disturbing effects.

The orientation error plot is shown in Figure 8-8B where the blue line represents the error angle between the chaser and target and the green line represents the error angle between the chaser and the optimal trajectory. This figure indicates that the error between the chaser and target and the error between the chaser and the optimal trajectory are about the same (about $10°$) at the final time. This is evidence that the optimal control history does not yield the terminal conditions in a higher fidelity model. This is due to a drift in the orientation of the target and the initial "bang-bang" control structure when the control is saturated.

The relative position plots shown in Figure 8-8C illustrate the secular disturbing effects. The trajectories are initially coincident and begin to drift after approximately 100 s. The quaternion plots shown in Figure 8-8D indicate that the trajectories

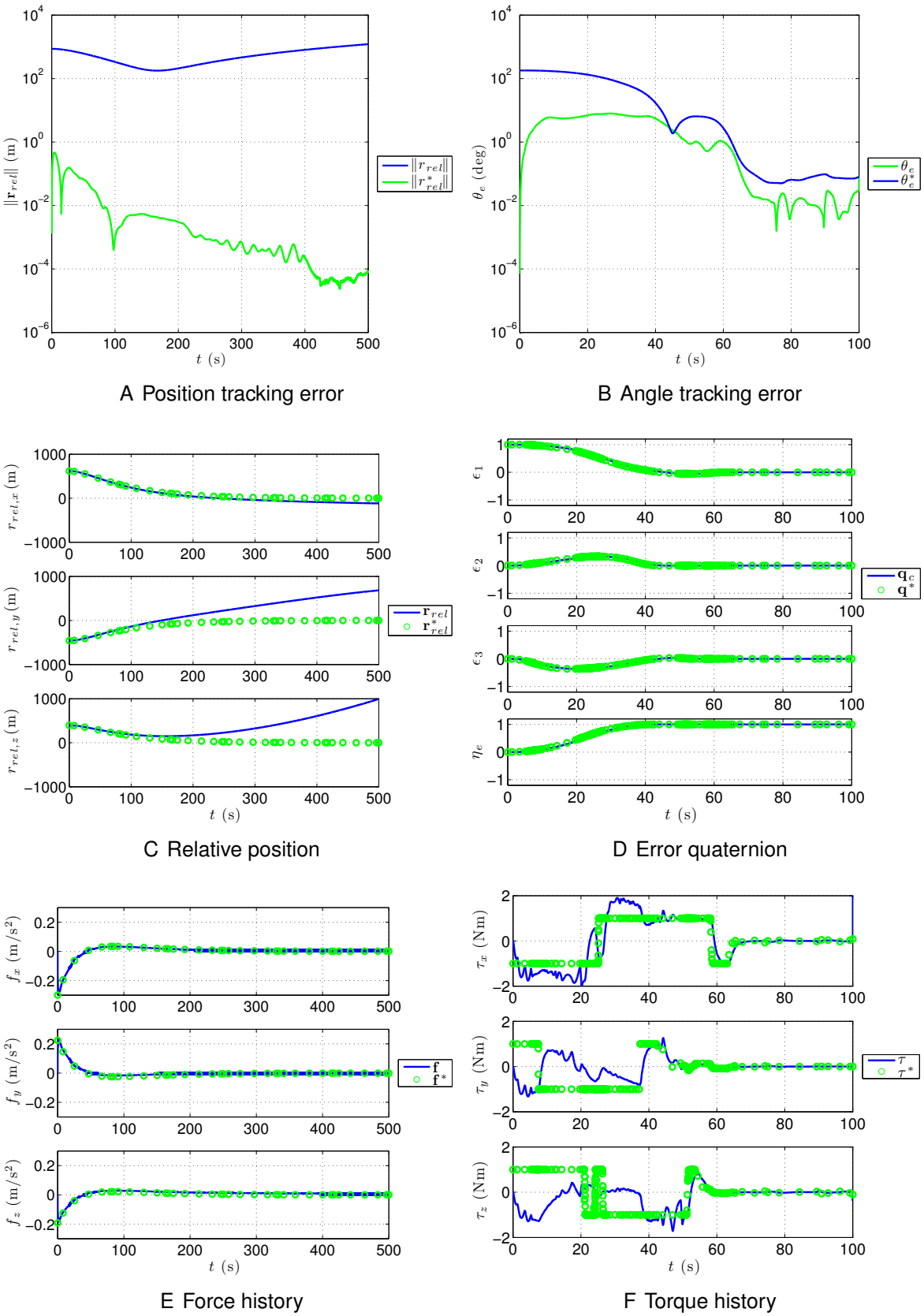

Figure 8-7. Finite horizon quadratic cost “trajectory tracking” results

are similar. The force plot is shown in Figure 8-8E and the torque plot is shown in Figure 8-8F. These plots indicate that the optimal control histories can be tracked accurately by the actuators.

8.2.4 Disturbance-Free Trajectories

To determine the extent to which disturbances, inaccuracies in optimal solutions, and the control structure contribute to the drifting trajectories, two additional examples are performed while disabling disturbances. The first example is implementing the fixed time minimum control effort trajectories using “trajectory tracking”. Figure 8-9 shows the results obtained for this example. The magnitude of the relative position is shown in Figure 8-9A where the blue line represents the relative position between the chaser and target and the green line represents the relative position between the chaser and the optimal trajectory. This figure indicates that the optimal trajectory is tracked accurately (i.e., under a 0.1 m error). The relative position between the chaser and target and between the chaser and optimal trajectory are virtually the same (approximately 0.3 m) at the final time. Figure 8-9C also supports this since both trajectories are similar and they both are near the origin at the final time.

The orientation error is shown in Figure 8-7B where the blue line represents the error angle between the chaser and target and the green line represents the error angle between the chaser and optimal trajectory. The quaternion plots are shown in Figure 8-9D. The effects of removing disturbances is not evident in these plots since disturbances did not have a large effect on the rotational motion in the first place. The force plot is shown in Figure 8-9E and the torque plot is shown in Figure 8-9F. The control history here is similar to the control history with disturbances.

The next example is implementing the finite horizon quadratic cost trajectories using “force tracking”. Figure 8-10 shows the results for this example. The results indicate that the “force tracking” method does not give favorable results without disturbances. Figure 8-10A and Figure 8-10C show that the terminal conditions are

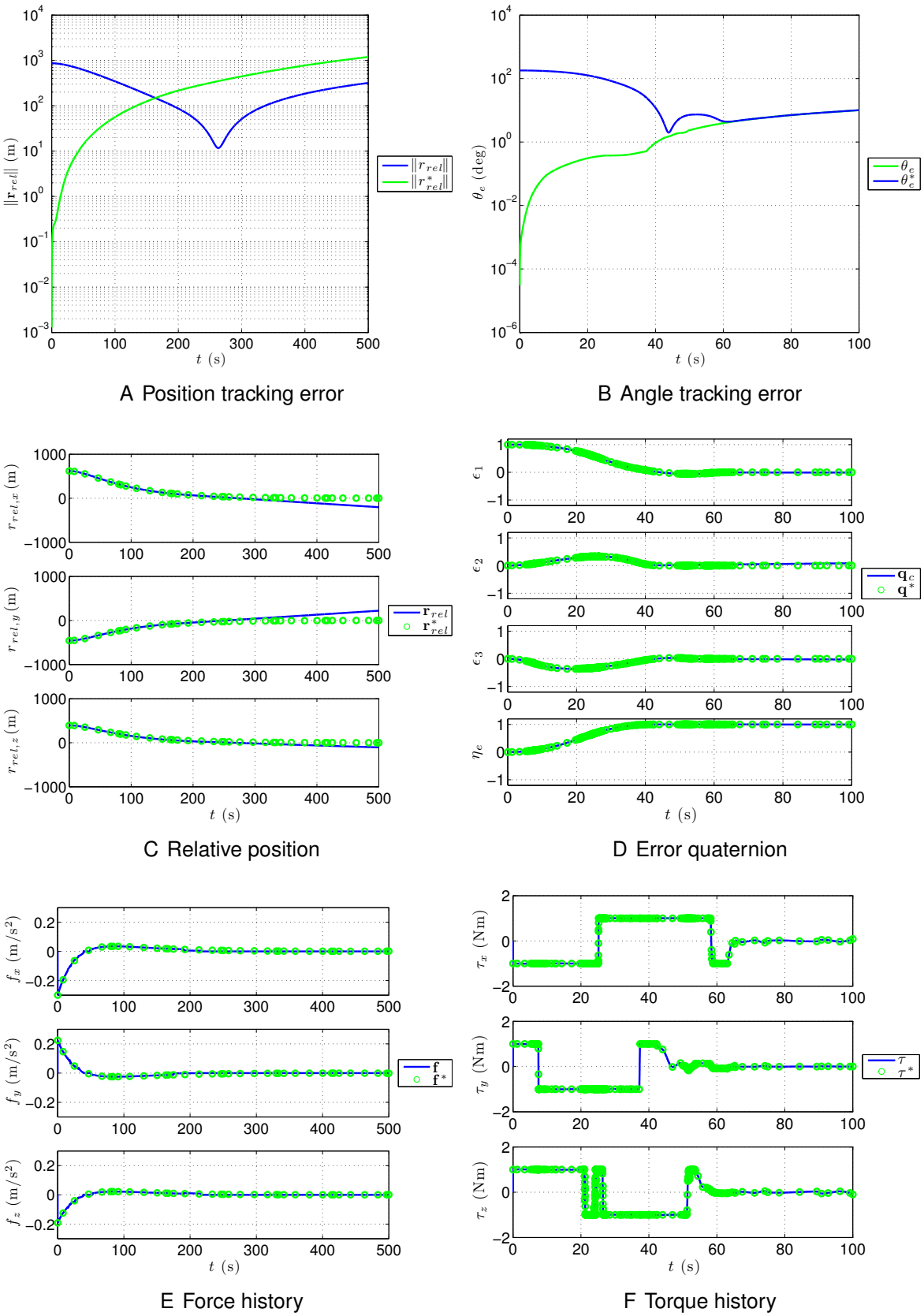

Figure 8-8. Finite horizon quadratic cost “force tracking” results

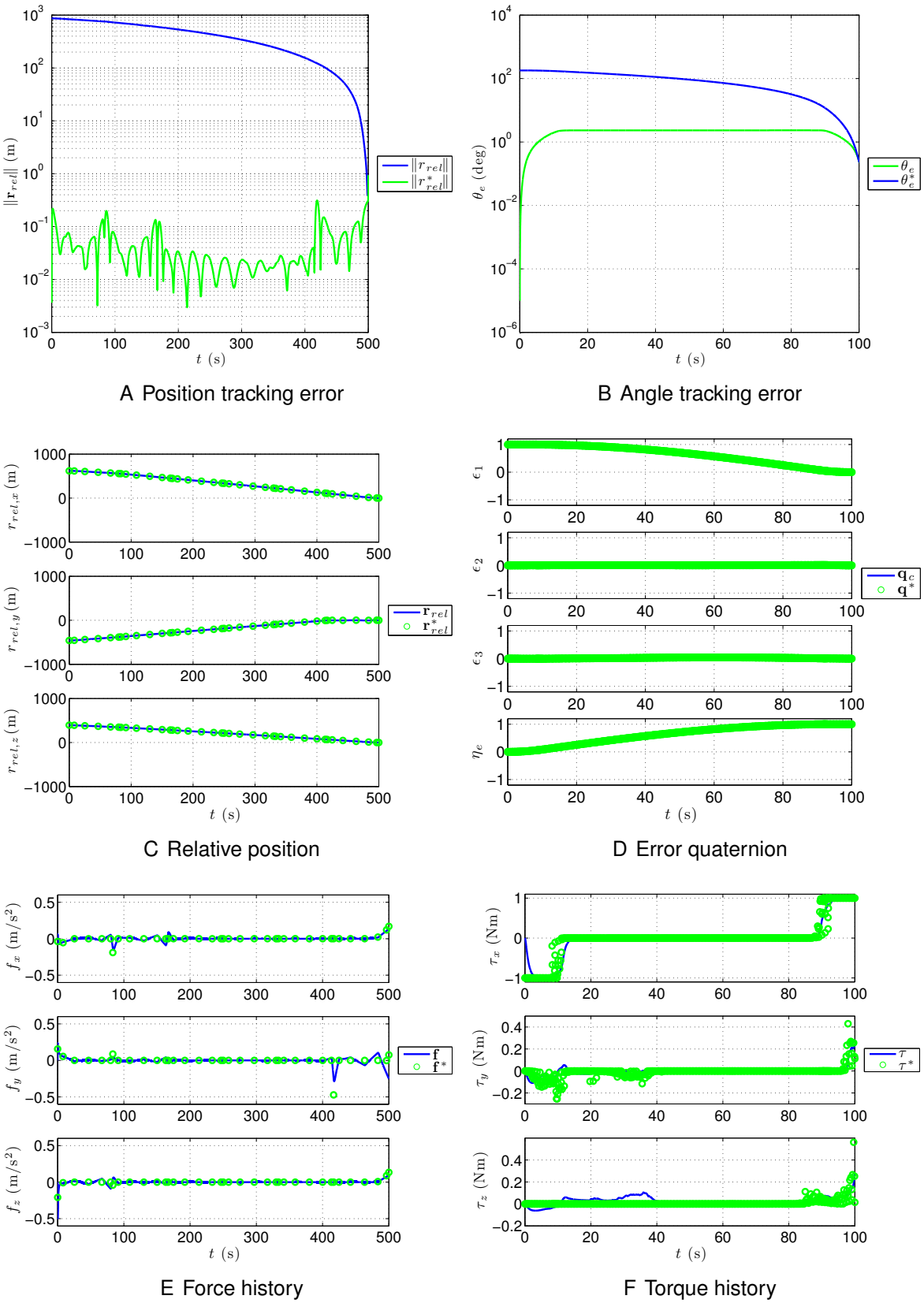

Figure 8-9. Fixed time minimum control effort “trajectory tracking” results (no disturbances)

not obtained. Moreover, Figure 8-10B and Figure 8-10D show results similar to the results in Figure 8-8 which include disturbances. Thus, deviations using "force tracking" are caused by inaccuracies in the optimal solutions. These inaccuracies are due to the interpolation since the solutions are only known at the collocation points. This result is motivation for the need to "re-plan" when there are inaccuracies in a solution.

8.2.5 Artificial Potential Function Trajectory

The target and chaser parameters used are the same as given in Table 8-3 and Table 8-4, respectively. The APF parameters used for this example are give in Table 8-5. Figure 8-11 shows the results of implementing the APF method in the high fidelity model. Figure 8-11A is a plot of the magnitude of the relative position versus time. This figure indicates that the magnitude of the relative position continues to decrease with every maneuver. Figure 8-11B shows the relative position history and the corresponding control history is shown in Figure 8-11C. These results indicate that the chaser continuously approaches the target with every maneuver.

Table 8-5. APF method parameters

Parameter	Value	Units
$\mathbf{r}_f$	$\mathbf{0}$	m
$\mathbf{P}$	$\mathbf{I} \in \mathbb{R}^{3\times3}$	s^{-2}
k	0.002	–

8.2.6 Adaptive Artificial Potential Function Trajectory

The target and chaser parameters used are the same as given in Table 8-3 and Table 8-4, respectively. The AAPF parameters used for this example are give in Table 8-6. Figure 8-12 shows the results of implementing the AAPF method in the high fidelity model. Figure 8-12A is a plot of the magnitude of the relative position versus time. This figure indicates that the magnitude of the relative position continues to decrease and that a maneuver is executed approximately every 200 s. This is no coincidence since the transfer time chosen was $T = 200$ s. Figure 8-12B shows the relative position history and the corresponding control history is shown in Figure 8-12C.

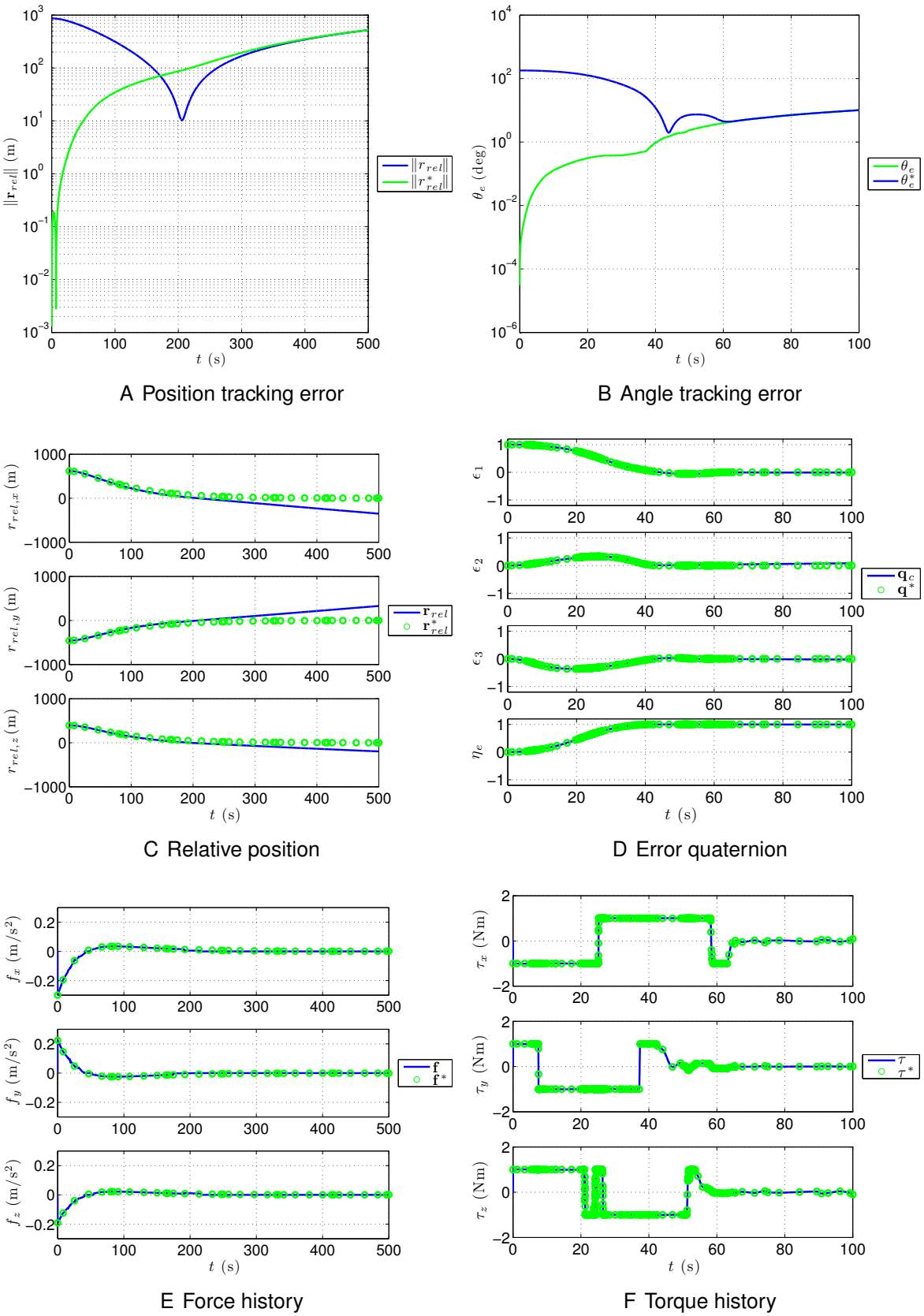

Figure 8-10. Finite horizon quadratic cost “force tracking” results (no disturbances)

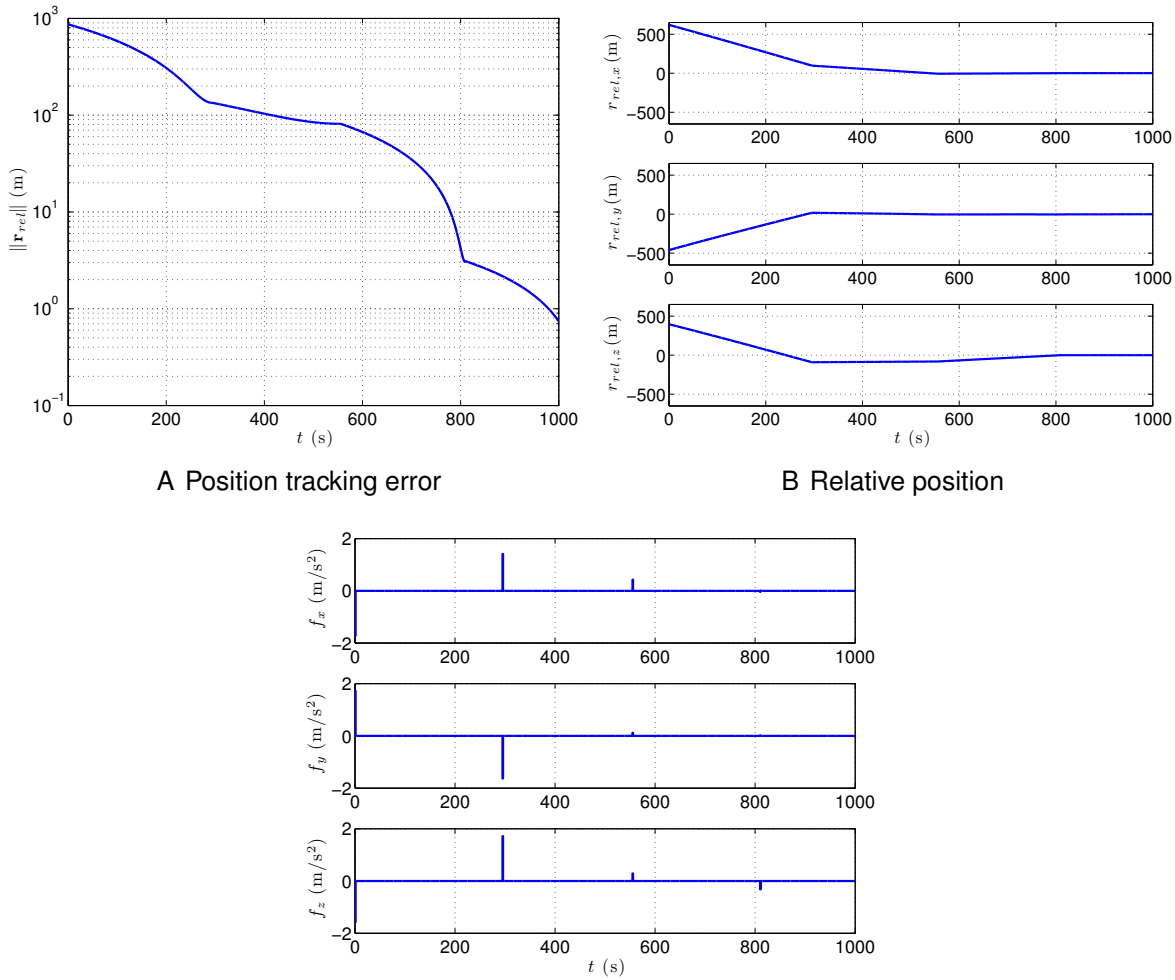

A Position tracking error

B Relative position

C Control history

Figure 8-11. APF method results

These results indicate that the chaser continuously approaches the target with every maneuver. Moreover, the AAPF method is suitable for rendezvous in a high fidelity model despite its development using a linearized model.

Table 8-6. AAPF method parameters

Parameter	Value	Units
$\mathbf{r}_f$	$\mathbf{0}$	m
$\boldsymbol{\theta}_0$	$0.002 \times \begin{bmatrix} 1 & 0 & 0 & 1 & 0 & 1 \end{bmatrix}^T$	s^{-2}
T	200	s

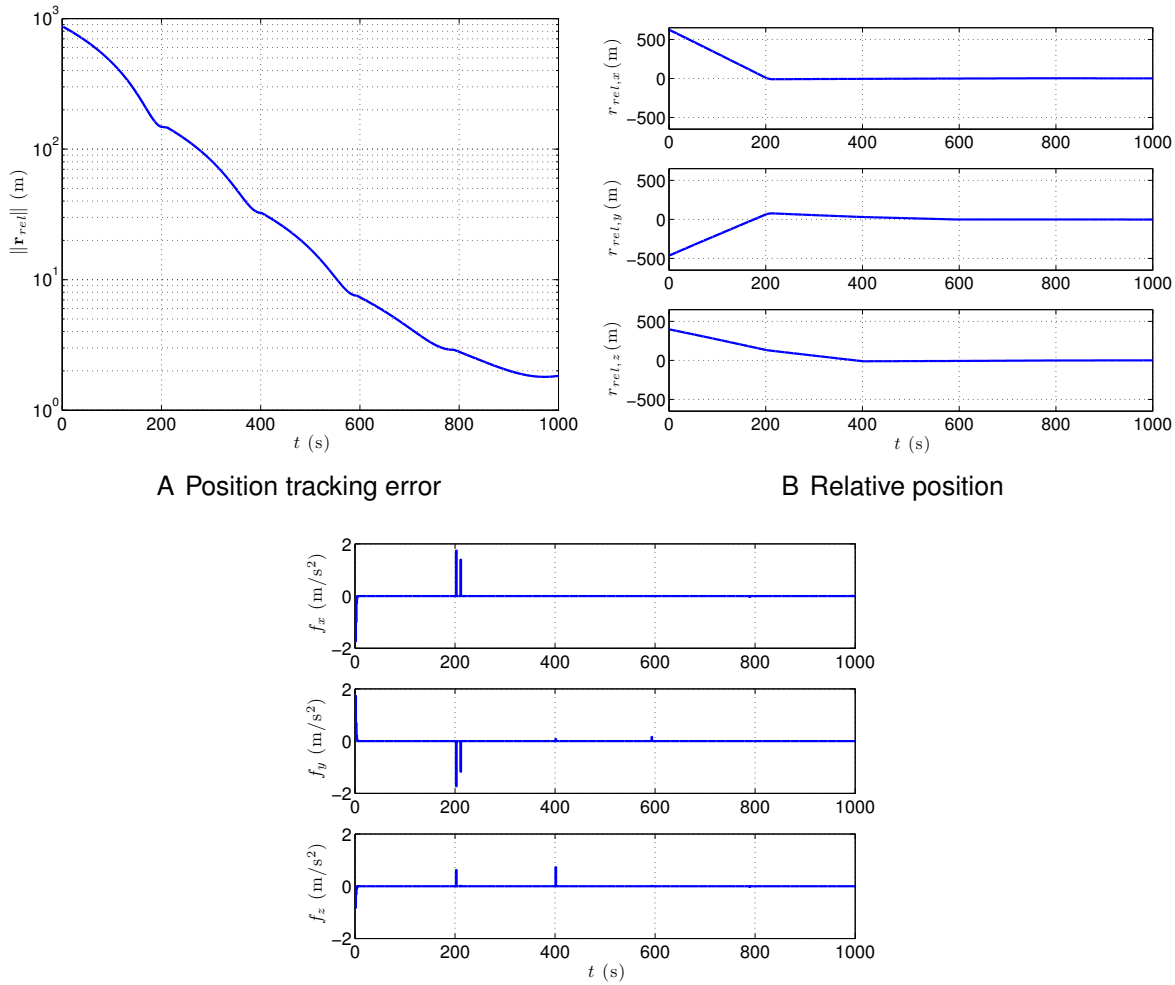

A Position tracking error

B Relative position

C Control history

Figure 8-12. AAPF method results

8.2.7 Obstacle Avoidance Trajectories

The results obtained for the close-range rendezvous scenario with obstacle avoidance are presented in this section. The chaser and target have the same parameters shown in Table 8-4 and Table 8-3, respectively. The obstacle has the parameters shown in Table 8-7 and is modeled the same as the chaser and target. The optimal solution obtained in Chapter 4 is implemented using “trajectory tracking”.

The results obtained from implementing the constrained fixed time minimum control effort trajectory using “trajectory tracking” are shown in Figure 8-13 and Figure 8-14. The relative position trajectories of the chaser are shown at different instances in

Table 8-7. Obstacle spacecraft parameters

Parameter	Value	Units
m_o	100	kg
l_o	3	m
$\mathbf{r}_o(t_0)$	$\begin{bmatrix}-1182.649497 & 6817.167778 & 904.693252\end{bmatrix}^T$	km
$\mathbf{v}_o(t_0)$	$\begin{bmatrix}0.175775 & -0.963776 & 7.494102\end{bmatrix}^T$	km/s
$\mathbf{J}_o$	$\begin{bmatrix}300 & 20 & 10 \\ 20 & 100 & 0 \\ 10 & 0 & 200\end{bmatrix}$	$\text{kg} \cdot \text{m}^2$
$\mathbf{q}_o(t_0)$	$\begin{bmatrix}0 & 0 & 0 & 1\end{bmatrix}^T$	–
$\boldsymbol{\omega}_o(t_0)$	$\begin{bmatrix}0 & 0 & 0\end{bmatrix}^T$	rad/s

Figure 8-13A thru Figure 8-13D. These figures support the results that were shown previously. That is, while the optimal trajectory can tracked accurately, there is disparity between the optimal trajectory and the actual trajectory. In this case, tracking the trajectory did not result in a collision between the chaser and the target. However, if the chaser did approach the obstacle due to drifting effects, then a correction would must be made to the trajectory to avoid a collision.

The magnitude of the relative position is shown in Figure 8-14A where the blue line represents the relative position between the chaser and the target and the green line represents the relative position between the chaser and the optimal trajectory. This figure indicates that the trajectory can be tracked accurately. The relative position plots shown in Figure 8-14B illustrate the drifting that occurs from tracking a planned trajectory. The force plot is shown in Figure 8-14C. The commanded force is similar to the optimal force solution which is the same result for the previous “trajectory tracking” results presented.

The parameters used for implementing the APF method for close-range rendezvous with obstacle avoidance are shown in Table 8-8. Recall that the path constraint for the obstacle required that the chaser be more that 100 m from the obstacle at all times. Thus, the APF parameters are chosen such that the repulsive potential roughly represents a “sphere” with radius of 100 m.

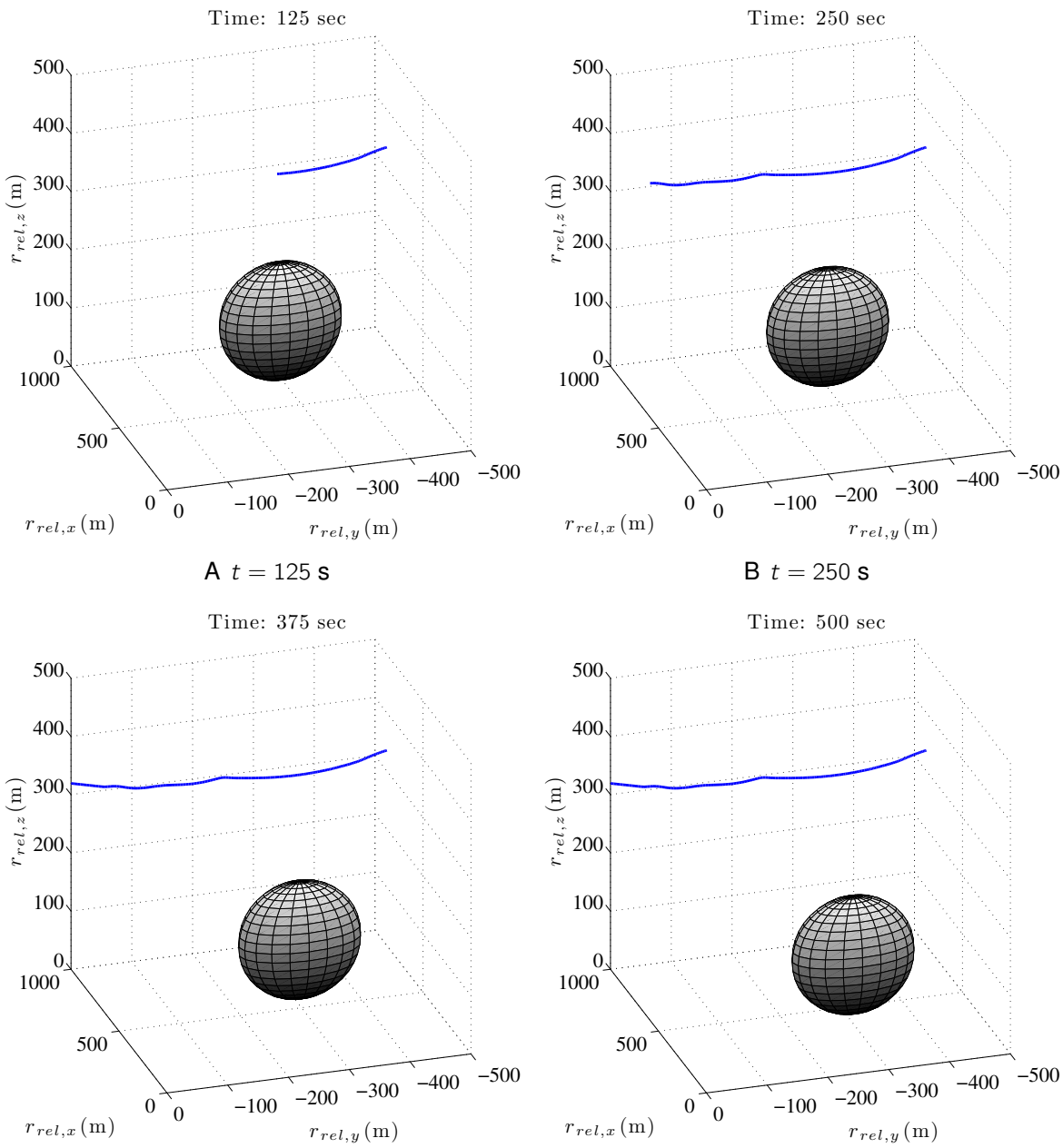

A $t = 125$ s

B $t = 250$ s

C $t = 375$ s

D $t = 500$ s

Figure 8-13. Constrained fixed time minimum control effort trajectories

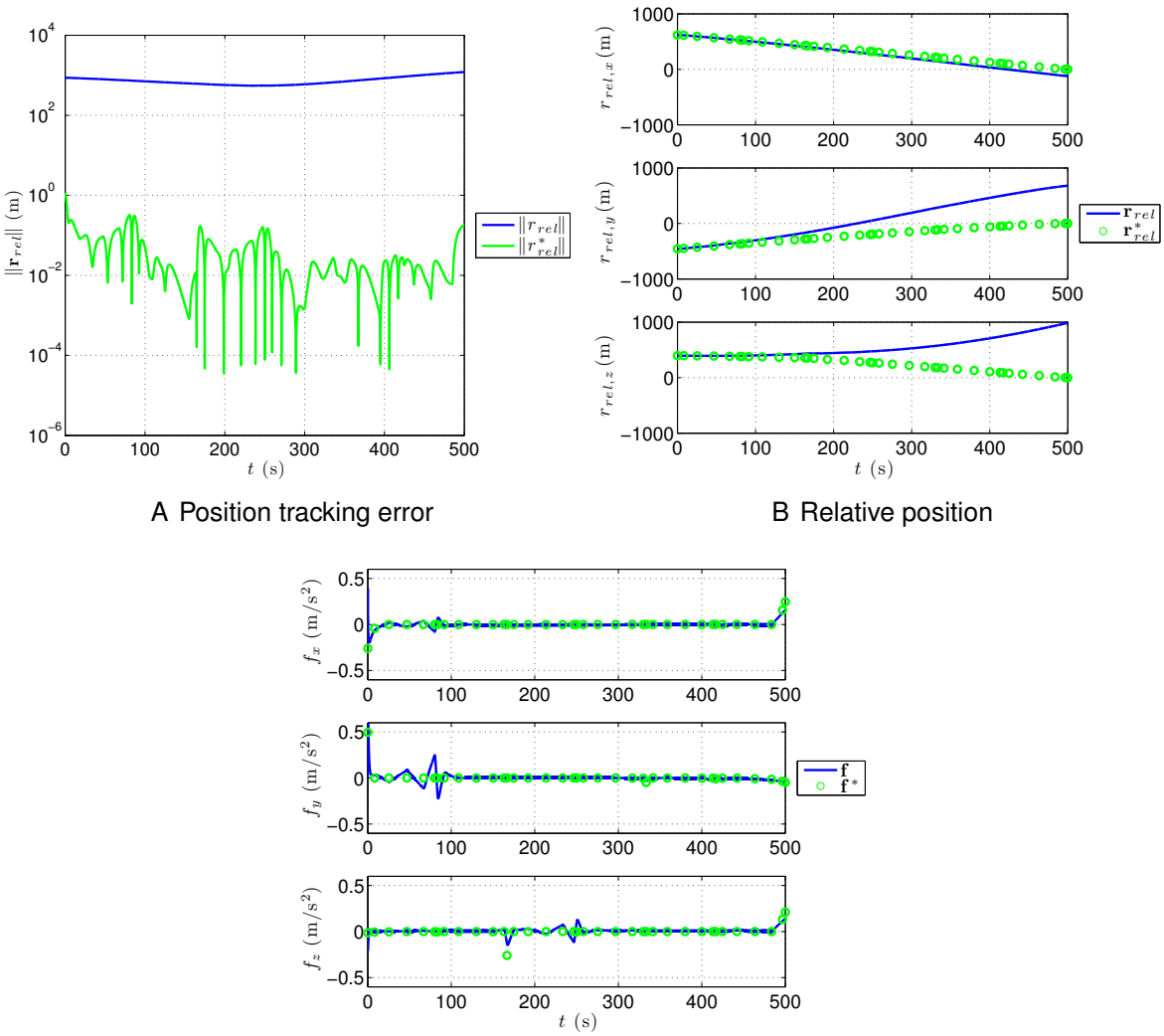

Figure 8-14. Constrained fixed time minimum control effort “trajectory tracking” results

Table 8-8. Constrained APF method parameters

Parameter	Value	Units
$\mathbf{r}_f$	$\mathbf{0}$	m
$\mathbf{P}$	$\mathbf{I} \in \mathbb{R}^{3\times3}$	s^{-2}
$\mathbf{N}$	$\mathbf{I} \in \mathbb{R}^{3\times3}$	s^{-2}
ψ	2.5×10^6	–
σ	2.5×10^3	m^2
k	0.004	–

The results obtained from implementing the APF method are shown in Figure 8-15 and Figure 8-16. The relative position trajectories of the chaser are shown at different instances in Figure 8-15A thru Figure 8-15D. These figures indicate that the chaser is able to rendezvous with the target while avoiding the obstacle. Figure 8-15A shows that the chaser encounters the obstacle after approximately 250 s and performs a maneuver to avoid it.

The magnitude of the relative position between the chaser and the target is shown in Figure 8-16A. This figure shows that the chaser continues to approach the target and gets within 8 m of the target after 1000 s. The relative position plots are shown in Figure 8-16B and the corresponding control histories are shown in Figure 8-16C. These force plot shows the avoidance maneuver that occurred at approximately 150 s. As a result, the relative position plot shows that this avoidance maneuver keeps the chaser from approaching the target until the next maneuver.

The parameters used for implementing the AAPF method for close-range rendezvous with obstacle avoidance are shown in Table 8-9. The same parameters for the repulsive potential are used for this simulation. The gain k is smaller since it is only applied to the gradient of the repulsive potential and the scaling between the attractive and repulsive potentials is different than the APF method.

Table 8-9. Constrained AAPF method parameters

Parameter	Value	Units
$\mathbf{r}_f$	$\mathbf{0}$	m
$\boldsymbol{\theta}_0$	$0.002 \times \begin{bmatrix} 1 & 0 & 0 & 1 & 0 & 1 \end{bmatrix}^T$	s^{-2}
T	200	s
$\mathbf{N}$	$\mathbf{I} \in \mathbb{R}^{3\times 3}$	s^{-2}
ψ	2.5×10^6	–
σ	2.5×10^3	m^2
k	0.001	–

The results obtained from implementing the AAPF method are shown in Figure 8-17 and Figure 8-18. The relative position trajectories of the chaser are shown at different instances in Figure 8-17A thru Figure 8-17D. These figures show that the chaser is able

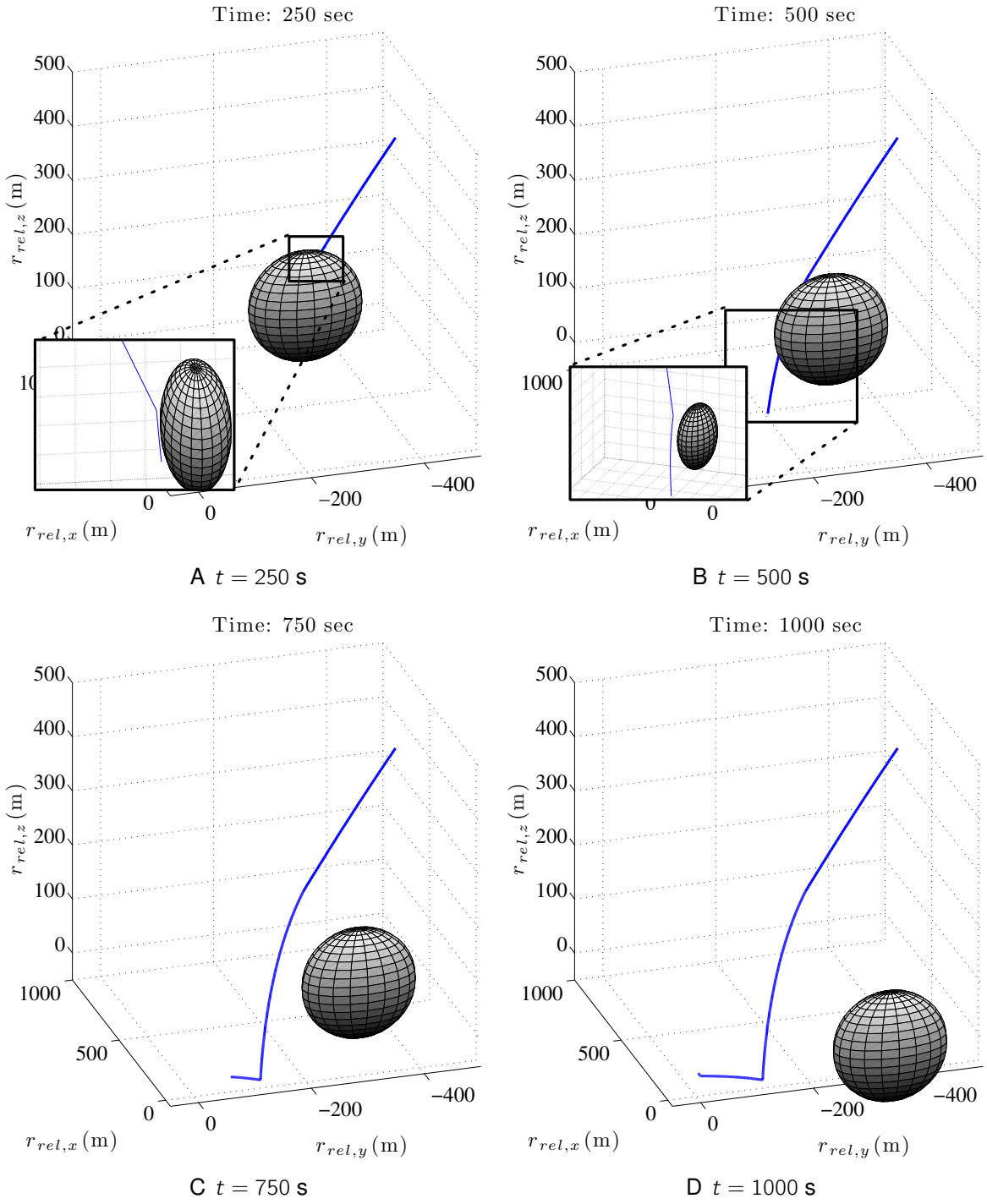

A $t = 250$ s

B $t = 500$ s

C $t = 750$ s

D $t = 1000$ s

Figure 8-15. Constrained APF method trajectories

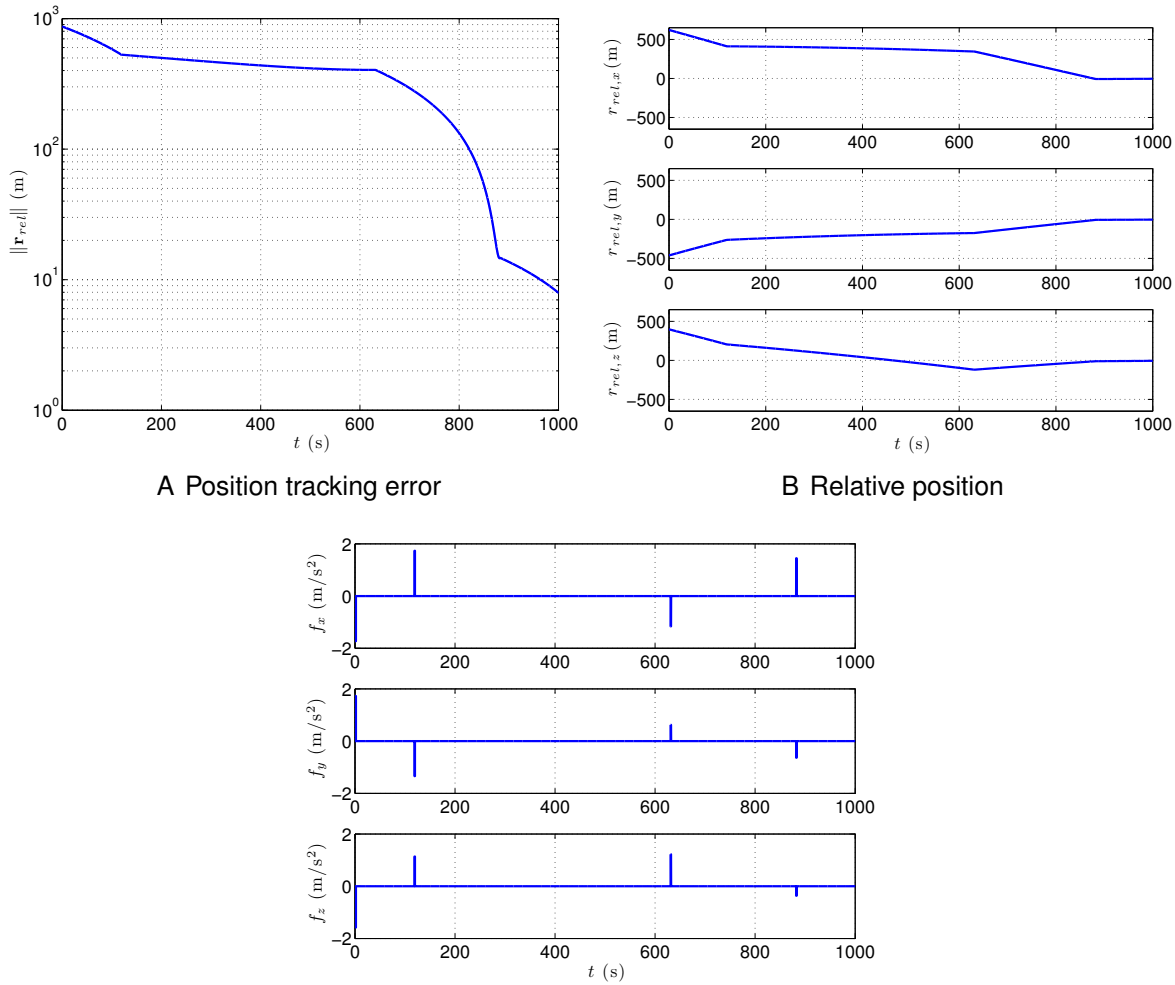

A Position tracking error

B Relative position

C Force history

Figure 8-16. Constrained APF method results

to rendezvous with the target while avoiding the obstacle. In this case, the obstacle is sensed sooner than the APF method. This is due to the different scaling between the attractive and repulsive potentials. Smaller values of ψ and σ can be used to reduce the effect of the repulsive potentials and to allow the chaser to converge to the target at a faster rate.

The magnitude of the relative position between the chaser and target is shown in Figure 8-18A. This figure shows that the chaser approaches the target at a faster rate than the APF method. This is expected since it was shown that convergence times are improved with the AAPF method. The relative position plots are shown in Figure 8-18B

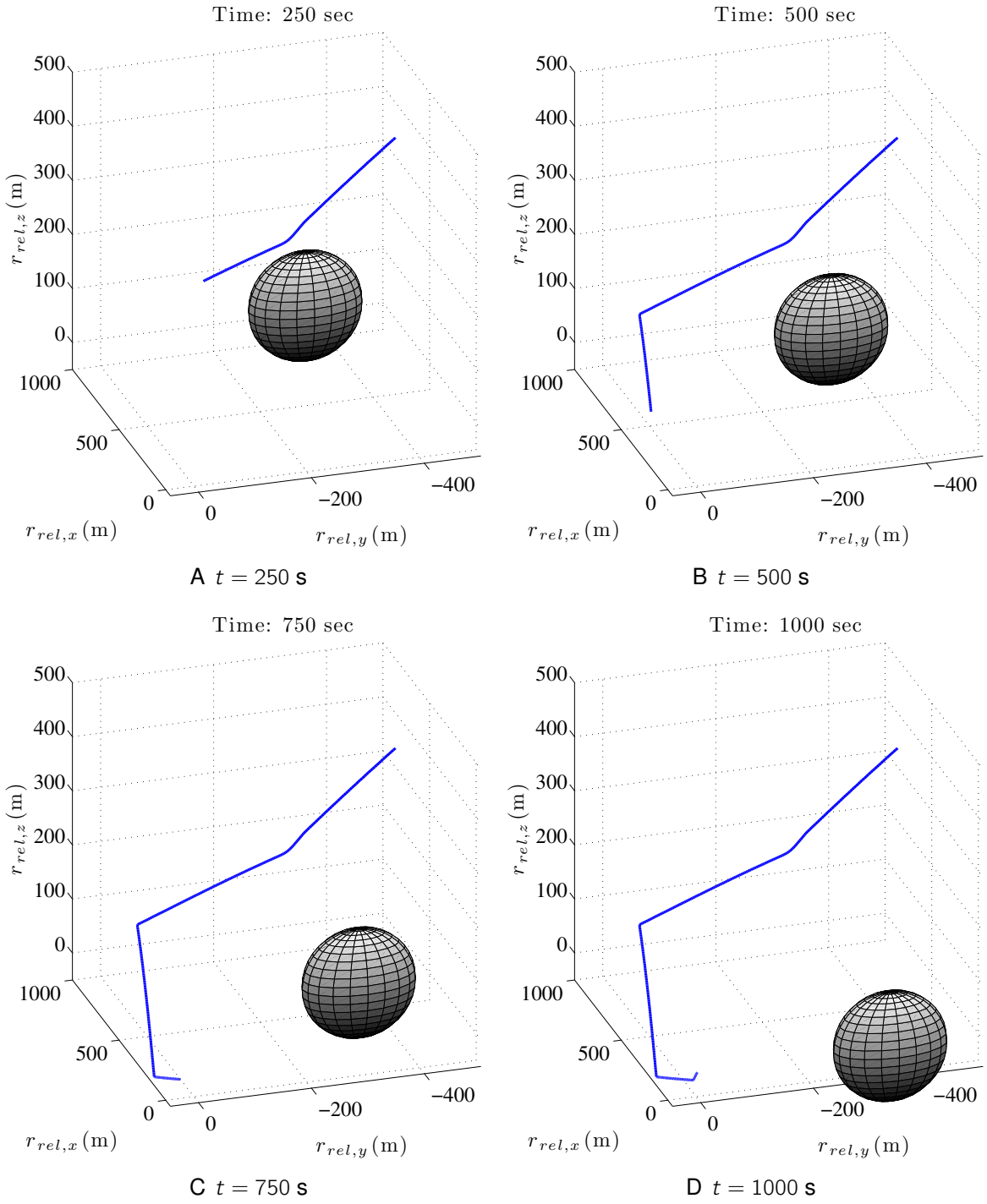

A $t = 250$ s

B $t = 500$ s

C $t = 750$ s

D $t = 1000$ s

Figure 8-17. Constrained AAPF method trajectories

and the corresponding control histories are shown in Figure 8-18C. The force plot shows that the avoidance maneuver occurs at approximately 100 s. As a result, the relative position plot shows that the obstacle is avoided yet the chaser continues to approach the target.

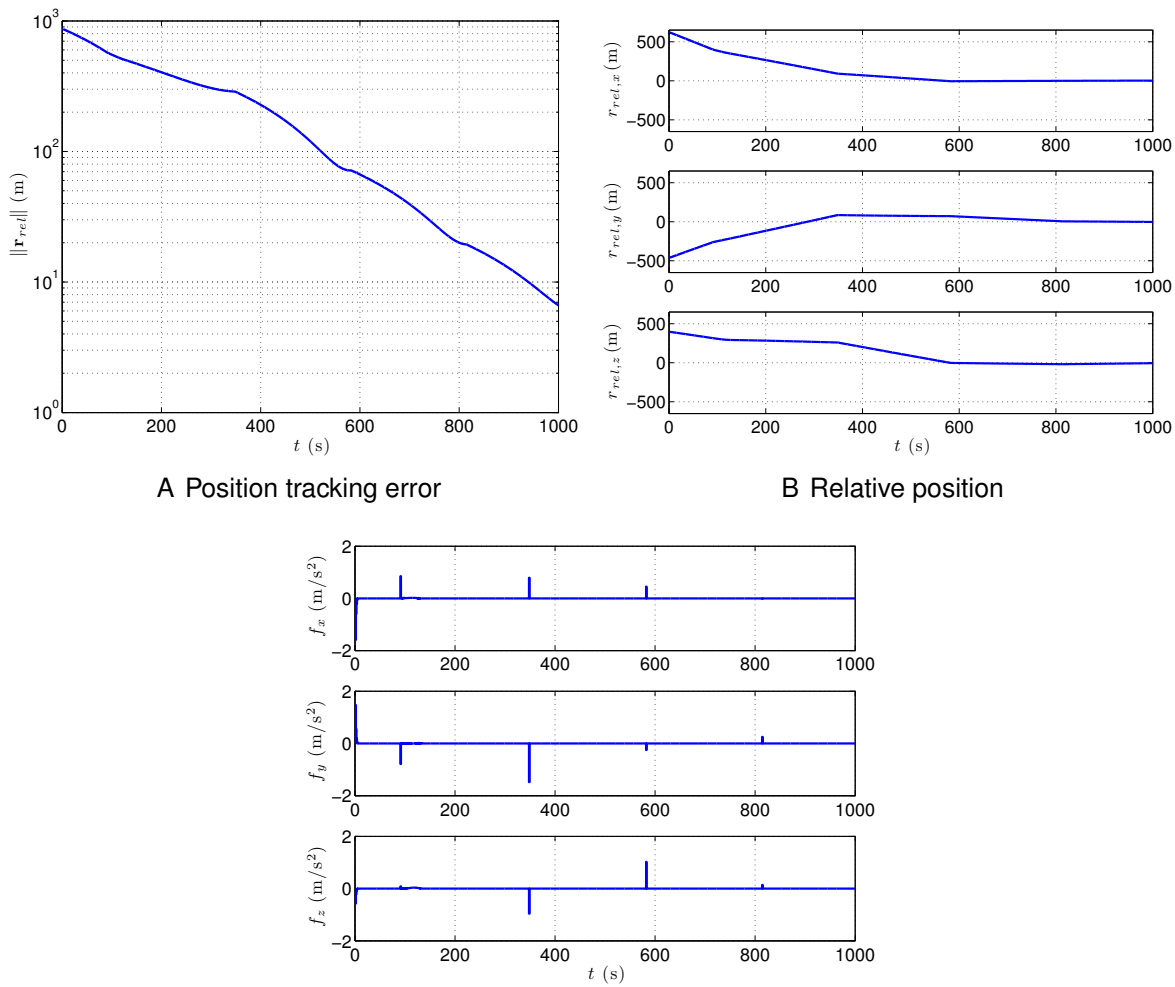

A Position tracking error

B Relative position

C Force history

Figure 8-18. Constrained AAPF method results

8.2.8 Final Approach Trajectory

The results obtained for the final approach scenario are presented in this section. The final approach is performed using the finite horizon LQ control law. The CWH equation from Appendix A is used in the LQ problem and the Riccati matrix is obtained using the STM representation. The parameters used are given in Table 8-10 which

include the parameters defining the Riccati matrix and a new set of initial positions and velocities for the chaser and target.

Table 8-10. Final approach parameters

Parameter	Value	Units
$\mathbf{r}_t(t_0)$	$\begin{bmatrix}-1005.448303 & 5813.480084 & 3725.077734\end{bmatrix}^T$	km
$\mathbf{v}_t(t_0)$	$\begin{bmatrix}0.697715 & -3.976259 & 6.387082\end{bmatrix}^T$	km/s
$\mathbf{r}_t(t_0)$	$\begin{bmatrix}-1005.453976 & 5813.510411 & 3725.067550\end{bmatrix}^T$	km
$\mathbf{v}_t(t_0)$	$\begin{bmatrix}0.697738 & -3.976498 & 6.386375\end{bmatrix}^T$	km/s
$\mathbf{S}_f$	$\begin{bmatrix}10^{-1}\times\mathbf{I} & \mathbf{0} \\ \mathbf{0} & 10^{-1}\times\mathbf{I}\end{bmatrix} \in \mathbb{R}^{6\times 6}$	–
$\mathbf{Q}$	$\begin{bmatrix}10^{-1}\times\mathbf{I} & \mathbf{0} \\ \mathbf{0} & 10^{-1}\times\mathbf{I}\end{bmatrix} \in \mathbb{R}^{6\times 6}$	–
$\mathbf{R}$	$10^2\times\mathbf{I}\in\mathbb{R}^{3\times 3}$	–
t_f	50	s

The results of implementing the finite horizon LQ feedback control law are shown in Figure 8-19. The magnitude of the relative position between the chaser and the target is shown in Figure 8-19A. This figure shows that the chaser is able to perform the final approach with the target and gets within 0.2 m. The relative position and relative velocity plots are shown in Figure 8-19B and Figure 8-19C, respectively. These plots show that using a linearized model to develop a control law for the final approach is valid. The corresponding control histories are shown in Figure 8-19D. The effects of the deadband constraints on the actuator are seen in this figure when the control values are near zero. This is also seen in Figure 8-19A since the deadband limits do not allow the relative position to decrease below 0.2 m.

In conclusion, the MCSs presented in this chapter suggest that the AAPF method developed in Chapter 6 is more easily tuned than the APF method. A single scalar parameter is required to tune the AAPF method where this parameter balances the transfer time versus the control effort. Also, faster convergence times with less control effort are seen since the dynamics are embedded in the formulation of the AAPF method.

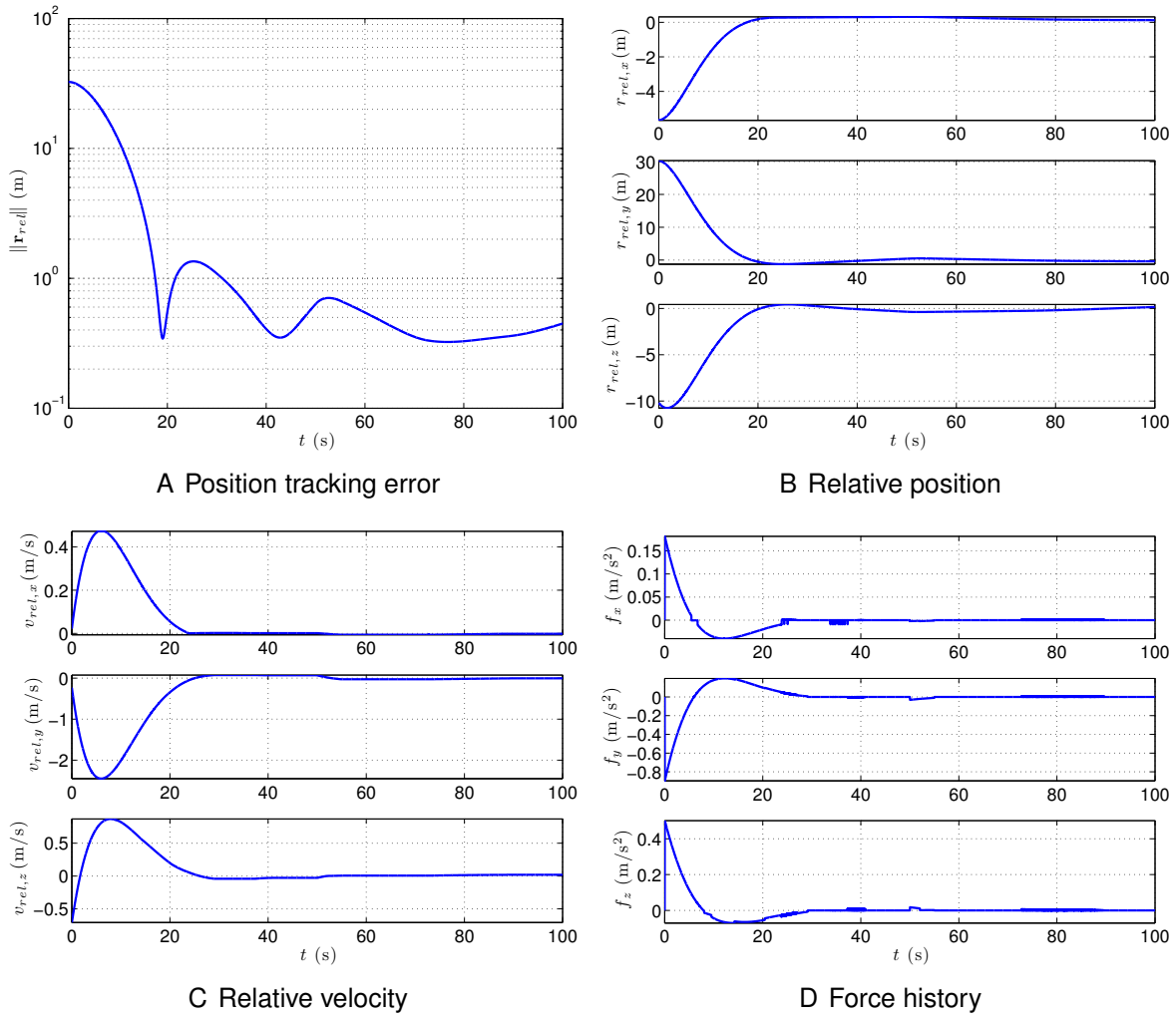

Figure 8-19. Final approach results

The high fidelity simulation results suggest that using implementing planned trajectories is only suitable for a certain classes of problems. The rotational motion in the close-range rendezvous scenario yielded favorable results for the three pertinent problems (at most a 10° error). The translational motion only yielded favorable results for the minimum time problems since the transfer time was short. The cases with a long transfer time (e.g., minimum control effort and finite horizon quadratic cost examples) experienced secular disturbing effects which greatly affected the performance and terminal conditions. Moreover, inaccuracies are introduced since the optimal solution is only known at the collocation points. An interpolation scheme is used to obtain a

continuous solution; however, the interpolated points are not necessarily part of the optimal solution.

The APF and AAPF methods are also implemented in the high fidelity model. The results indicate that these methods can be used for close-range rendezvous scenarios (with and without obstacles). In particular, the AAPF method is able to converge faster than the APF method despite it being developed using a linearized model. A final approach scenario is also simulated using the finite horizon LQ control law. This method also performed favorably despite the control law being developed using a linearized model.

CHAPTER 9
CONCLUSIONS

The technology for enabling path-planning on board space systems for autonomous proximity operations (APOs) is developed in this manuscript. Proximity operations are bifurcated into two phases: (i) close-range rendezvous and (ii) final approach or endgame. The motivation for developing algorithms that compute trajectories in real-time is developed since this must be to done to account for “unmodeled” events. As a result, autonomous space systems must have the capability of planning or correcting trajectories on-demand while optimizing the solutions (with respect to a performance index).

The adaptive artificial potential function (AAPF) method was developed for the close-range rendezvous scenario. This method is a modification to the artificial potential function (APF) method which embeds the dynamics and a performance criterion in the formulation. This modification was done since the APF method is not well-suited for a conservative system (with respect to resources) such as a spacecraft. The AAPF method was shown to have improved performance and convergence times over the APF method through Monte Carlo simulations (MCSs).

It is also shown through extensive numerical analyses that tracking planned trajectories is ineffective for APOs when the transfer times of the trajectories are long. This implies that using short time horizons to plan trajectories must be done to account for all disturbances or “unmodeled” events. Moreover, the short time horizon framework lends itself well to using the AAPF method since it is developed using a linearized model which is accurate for short time horizons. This was demonstrated in simulation which proves that the AAPF method can be used with a high fidelity model.

Final approach trajectories are conventionally obtained by solving a finite horizon linear quadratic (LQ) problem which essentially is solved as a final value problem with a Differential Riccati equation (DRE). It is shown that if the Hamiltonian matrix is

linear time invariant (LTI), then the solution is obtained using a state transition matrix. However, this can not be done (in general) when the Hamiltonian matrix is linear time varying (LTV). As a result, two mathematical tools were utilized to avoid solving a final value problem and in turn obtain the solution to the DRE in real-time. Namely, these tools are the Picard Iteration (PI) and the Homotopy Continuation (HC). The parametric solution structure obtained using the PI and the HC allow for updates to be easily made in the time horizon, dynamics model, and/or performance index. A numerical example was presented to demonstrate how solutions are obtained using the PI and HC. In addition, an example of a final approach scenario in an elliptic orbit (i.e., using the Yamanaka-Ankerson-Tschauner-Hempel equation) was presented with the HC method. Lastly, a final approach trajectory is implemented in the high fidelity model using an LQ control law which demonstrated how using a linear model is valid for this scenario.

In conclusion, the methods developed in this manuscript are well-suited for autonomous space systems. The methods developed compute optimized trajectories through functional evaluations rather than through iterative techniques. To further increase the range of applicability, different models can be used in the development (like those described in [98, 99, 101]) which are amenable with the methods developed. An instructional effect from developing these methodologies is that path-planning can be done as the properties of the dynamics become more well-established.

APPENDIX A
RELATIVE MOTION MODELS

The models to describe relative motion of two spacecraft are discussed in this appendix. The translational relative motion model is derived using the two body model on both the chaser and target. Using the close proximity assumption, the model results in a linear form. Two sets of equations are presented to describe relative translational motion when the target's orbit is: (i) circular and (ii) eccentric. The rotational relative motion model is derived using a small angle approximation (SAA) which also results in a linear form.

A.1 Relative Translation

The position of the chaser relative to the target is

$$\mathbf{r} = \mathbf{r}_c - \mathbf{r}_t \ ,$$

where $\mathbf{r}_c$ is the position of the chaser and $\mathbf{r}_t$ is the position of the target. If both spacecraft are governed by the two body relative motion model

$$\begin{aligned}
\ddot{\mathbf{r}}_t &= -\frac{\mu_\oplus}{\|\mathbf{r}_t\|^3}\mathbf{r}_t \\
\ddot{\mathbf{r}}_c &= -\frac{\mu_\oplus}{\|\mathbf{r}_c\|^3}\mathbf{r}_c + \mathbf{f} \ ,
\end{aligned}$$

and the chaser is the only spacecraft with control thrust $\mathbf{f}$, then the relative position is differentiated twice to yield

$$\begin{aligned}
&\ddot{\mathbf{r}} = \ddot{\mathbf{r}}_c - \ddot{\mathbf{r}}_t \\
\Rightarrow\ &\ddot{\mathbf{r}} = -\frac{\mu_\oplus}{\|\mathbf{r}_c\|^3}\mathbf{r}_c + \mathbf{f} + \frac{\mu_\oplus}{\|\mathbf{r}_t\|^3}\mathbf{r}_t \\
\Rightarrow\ &\ddot{\mathbf{r}} = -\frac{\mu_\oplus}{\|\mathbf{r}+\mathbf{r}_t\|^3}(\mathbf{r}+\mathbf{r}_t) + \mathbf{f} + \frac{\mu_\oplus}{\|\mathbf{r}_t\|^3}\mathbf{r}_t \ . \qquad \text{(A–1)}
\end{aligned}$$

Note that the value $\|\mathbf{r}+\mathbf{r}_t\|$ can be simplified as

$$\|\mathbf{r}+\mathbf{r}_t\| = \left[(\mathbf{r}+\mathbf{r}_t)^T(\mathbf{r}+\mathbf{r}_t)\right]^{\frac{1}{2}} = \left[\|\mathbf{r}_t\|^2 + 2\mathbf{r}^T\mathbf{r}_t + \|\mathbf{r}\|^2\right]^{\frac{1}{2}}$$
$$\Rightarrow \|\mathbf{r}+\mathbf{r}_t\|^3 = \|\mathbf{r}_t\|^3\left[1+2\frac{\mathbf{r}^T\mathbf{r}_t}{\|\mathbf{r}_t\|^2}+\frac{\|\mathbf{r}\|^2}{\|\mathbf{r}_t\|^2}\right]^{\frac{3}{2}} .$$

This identity is substituted into equation (A–1) to yield

$$\ddot{\mathbf{r}} = -\frac{\mu_\oplus}{\|\mathbf{r}_t\|^3}\left[1+2\frac{\mathbf{r}^T\mathbf{r}_t}{\|\mathbf{r}_t\|^2}+\frac{\|\mathbf{r}\|^2}{\|\mathbf{r}_t\|^2}\right]^{-\frac{3}{2}}(\mathbf{r}+\mathbf{r}_t)+\mathbf{f}+\frac{\mu_\oplus}{\|\mathbf{r}_t\|^3}\mathbf{r}_t . \tag{A–2}$$

Moreover, the polynomial expansion

$$(1+x)^k = 1+kx+\frac{k(k-1)}{2!}x^2+\cdots$$

is used to expand

$$\left[1+\left(2\frac{\mathbf{r}^T\mathbf{r}_t}{\|\mathbf{r}_t\|^2}+\frac{\|\mathbf{r}\|^2}{\|\mathbf{r}_t\|^2}\right)\right]^{-\frac{3}{2}} = 1-\frac{3}{2}\left(2\frac{\mathbf{r}^T\mathbf{r}_t}{\|\mathbf{r}_t\|^2}+\frac{\|\mathbf{r}\|^2}{\|\mathbf{r}_t\|^2}\right)+\cdots .$$

Using the close proximity assumption (i.e., $\mathbf{r}_t \gg \mathbf{r}$) and the polynomial expansion above, equation (A–2) is simplified as

$$\ddot{\mathbf{r}} = -\frac{\mu_\oplus}{\|\mathbf{r}_t\|^3}\left(\mathbf{r}+\mathbf{r}_t-3\frac{\mathbf{r}^T\mathbf{r}_t}{\|\mathbf{r}_t\|^2}\mathbf{r}_t\right)+\mathbf{f}+\frac{\mu_\oplus}{\|\mathbf{r}_t\|^3}\mathbf{r}_t$$
$$\Rightarrow \ddot{\mathbf{r}} = -\frac{\mu_\oplus}{\|\mathbf{r}_t\|^3}\left(\mathbf{r}-3\frac{\mathbf{r}^T\mathbf{r}_t}{\|\mathbf{r}_t\|^2}\mathbf{r}_t\right)+\mathbf{f} . \tag{A–3}$$

This relative motion model in equation (A–3) expressed in the target's orbital frame is

$$\Rightarrow \ddot{\mathbf{r}} = -n^2\left(\mathbf{r}-3\frac{\mathbf{r}^T\mathbf{r}_t}{\|\mathbf{r}_t\|^2}\mathbf{r}_t\right)+\mathbf{f}-\dot{\boldsymbol{\omega}}_o\times\mathbf{r}-2\boldsymbol{\omega}_o\times\dot{\mathbf{r}}-\boldsymbol{\omega}_o\times(\boldsymbol{\omega}_o\times\mathbf{r}) . \tag{A–4}$$

where the derivatives are derivates in the target's rotating orbital frame. The target position can be expressed in the target's orbital frame as

$$\mathbf{r}_t = \begin{bmatrix} r_t & 0 & 0 \end{bmatrix}^T .$$

where r_t is the distance from the Earth's center to the target. In addition, the angular velocity of the target's orbital frame is expressed in the target's orbital frame as

$$\boldsymbol{\omega}_o = \begin{bmatrix} 0 & 0 & \omega \end{bmatrix}^T ,$$

where ω is the target's orbital rate. Letting the relative position vector be defined as

$$\mathbf{r} = \begin{bmatrix} x & y & z \end{bmatrix}^T ,$$

then the cross product terms are simplified as

$$\begin{aligned}
\boldsymbol{\omega}_o \times \dot{\mathbf{r}} &= \begin{bmatrix} -\omega\dot{y} & \omega\dot{x} & 0 \end{bmatrix}^T \\
\dot{\boldsymbol{\omega}}_o \times \mathbf{r} &= \begin{bmatrix} -\dot{\omega}y & \dot{\omega}x & 0 \end{bmatrix}^T \\
\boldsymbol{\omega}_o \times (\boldsymbol{\omega}_o \times \mathbf{r}) &= \begin{bmatrix} -\omega^2 x & \omega^2 y & 0 \end{bmatrix}^T \\
\mathbf{r} - 3\frac{\mathbf{r}^T\mathbf{r}}{\|\mathbf{r}\|^2}\mathbf{r}_t &= \begin{bmatrix} -2x & y & z \end{bmatrix}^T
\end{aligned}$$

From the orbital angular momentum relationship

$$r_t^2\omega = h ,$$

the simplification can be made

$$\frac{\mu_\oplus}{\|\mathbf{r}_t\|^3} = \frac{\mu_\oplus}{h^{\frac{3}{2}}}\omega^{\frac{3}{2}} = k\omega^{\frac{3}{2}} ,$$

where

$$k = \frac{\mu}{h^{\frac{3}{2}}}$$

is a constant. As a result, equation (A–4) simplifies to

$$\begin{aligned} \ddot{x} - 2k\omega^{\frac{3}{2}}x - \omega^2 x - \dot{\omega}y - 2\omega\dot{y} &= f_x \\ \ddot{y} + k\omega^{\frac{3}{2}}y - \omega^2 y + \dot{\omega}x + 2\omega\dot{x} &= f_y \\ \ddot{z} + k\omega^{\frac{3}{2}}z &= f_z \ , \end{aligned} \tag{A–5}$$

where f_x, f_y, f_z are the components of the control acceleration $\mathbf{f}$ in the target's orbital frame.

A.1.1 Clohessy-Wiltshire-Hill Equation

Assuming the target is in a circular orbit, then

$$\begin{aligned} \dot{\omega} &= 0 \\ k &= \omega^{\frac{1}{2}} \ . \end{aligned}$$

Simplifying equation (A–5) results in the Clohessy-Wiltshire-Hill (CWH) equation which describes the relative translational motion between two spacecraft [39, 55]

$$\begin{aligned} \ddot{x} - 3n^2 x - 2n\dot{y} &= f_x \\ \ddot{y} + 2n\dot{x} &= f_y \\ \ddot{z} + n^2 z &= f_z \ , \end{aligned} \tag{A–6}$$

where $n = \omega$ is the mean motion of the target's orbital frame. Equation (A–6) can be written in state space form

$$\begin{bmatrix} \dot{\mathbf{r}} \\ \dot{\mathbf{v}} \end{bmatrix} = \begin{bmatrix} \mathbf{0} & \mathbf{I} \\ \mathbf{A}_{21} & \mathbf{A}_{22} \end{bmatrix} \begin{bmatrix} \mathbf{r} \\ \mathbf{v} \end{bmatrix} + \begin{bmatrix} \mathbf{0} \\ \mathbf{I} \end{bmatrix} \mathbf{u} \ ,$$

where

$$\mathbf{r} = \begin{bmatrix} x & y & z \end{bmatrix}^T ,$$
$$\mathbf{v} = \begin{bmatrix} \dot{x} & \dot{y} & \dot{z} \end{bmatrix}^T ,$$
$$\mathbf{u} = \begin{bmatrix} f_x & f_y & f_z \end{bmatrix}^T ,$$

and $\mathbf{A}_{21}, \mathbf{A}_{22}$ are blocks of the state matrix and are defined as

$$\mathbf{A}_{21} = \begin{bmatrix} 3n^2 & 0 & 0 \\ 0 & 0 & 0 \\ 0 & 0 & -n^2 \end{bmatrix}$$

$$\mathbf{A}_{22} = \begin{bmatrix} 0 & 2n & 0 \\ -2n & 0 & 0 \\ 0 & 0 & 0 \end{bmatrix} .$$

A.1.2 Yamanaka-Ankerson-Tschauner-Hempel Equation

By relaxing the circular orbit assumption, a different set of equations can be obtained. [98, 99] First, the independent variable is changed from time to the true anomaly of the target (i.e., θ). Through the chain rule, the time derivative of an arbitrary scalar parameter a now becomes

$$\frac{da}{dt} = \frac{da}{d\theta}\frac{d\theta}{dt}$$
$$\Rightarrow \frac{da}{dt} = \omega a' ,$$

and the second time derivative becomes

$$\begin{aligned}
\frac{d^2a}{dt^2} &= \frac{d\omega}{dt}a' + \omega\frac{da'}{dt} \\
\Rightarrow \frac{d^2a}{dt^2} &= \frac{d\omega}{d\theta}\frac{d\theta}{dt}a' + \omega\frac{da'}{d\theta}\frac{d\theta}{dt} \\
\Rightarrow \frac{d^2a}{dt^2} &= \omega\omega' a' + \omega^2 a'' \ .
\end{aligned}$$

Using these relationships, equation (A–5) can be written as

$$\begin{aligned}
\omega^2 x'' + \omega\omega' x' - 2k\omega^{\frac{3}{2}}x - \omega^2 x - \omega\omega' y - 2\omega^2 y' &= f_x \\
\omega^2 y'' + \omega\omega' y' + k\omega^{\frac{3}{2}}y - \omega^2 y + \omega\omega' x + 2\omega^2 x' &= f_y \\
\omega^2 z'' + \omega\omega' z' + k\omega^{\frac{3}{2}}z &= f_z \ ,
\end{aligned} \tag{A–7}$$

Recall that the position magnitude in terms of the true anomaly can be written as

$$r_t = \frac{p}{1 + e\cos\theta} \ ,$$

where p is the semi-latus rectum of the target's orbit and e is the eccentricity of the target's orbit. [40] Similarly, from the conservation of orbital angular momentum, the semi-latus rectum can be written as

$$p = \frac{h^2}{\mu_\oplus} \ . \tag{A–8}$$

As a result, the orbital rate of the target can be written as

$$\omega = \frac{h}{r_t^2} = \frac{h}{p^2}(1 + e\cos\theta)^2 = k^2(1 + e\cos\theta)^2 \ , \tag{A–9}$$

and the derivative of the orbital rate with respect to the true anomaly is

$$\omega' = -2k^2 e\sin\theta(1 + e\cos\theta) \ . \tag{A–10}$$

Substituting equation (A–9) and equation (A–10) into equation (A–7) and dividing by ω^2 yields the Yamanaka-Ankerson-Tschauner-Hempel (YATH) equations which describe the

relative translational motion between two spacecraft

$$
\begin{aligned}
x'' - \left(1 + \frac{2}{1+e\cos\theta}\right)x + \frac{2e\sin\theta}{1+e\cos\theta}y - \frac{2e\sin\theta}{1+e\cos\theta}x' - 2y' &= \frac{1}{k^4(1+e\cos\theta)^4}f_x \\
y'' - \frac{2e\sin\theta}{1+e\cos\theta}x - \left(1 - \frac{1}{1+e\cos\theta}\right)y + 2x' - \frac{2e\sin\theta}{1+e\cos\theta}y' &= \frac{1}{k^4(1+e\cos\theta)^4}f_y \\
z'' + \frac{1}{1+e\cos\theta}z - \frac{2e\sin\theta}{1+e\cos\theta}z' &= \frac{1}{k^4(1+e\cos\theta)^4}f_z \ .
\end{aligned}
$$

These set of equations can be written in state space form

$$
\begin{bmatrix} \mathbf{r}' \\ \mathbf{v}' \end{bmatrix} = \begin{bmatrix} \mathbf{0} & \mathbf{I} \\ \mathbf{A}_{21} & \mathbf{A}_{22} \end{bmatrix} \begin{bmatrix} \mathbf{r} \\ \mathbf{v} \end{bmatrix} + \frac{1}{k^4(1+e\cos\theta)^4} \begin{bmatrix} \mathbf{0} \\ \mathbf{I} \end{bmatrix} \mathbf{f}
$$

where

$$
\begin{aligned}
\mathbf{r} &= \begin{bmatrix} x & y & z \end{bmatrix}^T \\
\mathbf{v} &= \begin{bmatrix} x' & y' & z' \end{bmatrix}^T \\
\mathbf{f} &= \begin{bmatrix} f_x & f_y & f_z \end{bmatrix}^T
\end{aligned}
$$

and $\mathbf{A}_{21}, \mathbf{A}_{22}$ are blocks of the state matrix and are defined as

$$
\mathbf{A}_{21} = \frac{1}{1+e\cos\theta} \begin{bmatrix} 3+e\cos\theta & -2e\sin\theta & 0 \\ 2e\sin\theta & e\cos\theta & 0 \\ 0 & 0 & -1 \end{bmatrix}
$$

$$
\mathbf{A}_{22} = \frac{1}{1+e\cos\theta} \begin{bmatrix} 2e\sin\theta & 2 & 0 \\ -2 & 2e\sin\theta & 0 \\ 0 & 0 & 2e\sin\theta \end{bmatrix} .
$$

A.2 Relative Orientation

A small angle approximation (SAA) can be used to describe the relative orientation of the chaser with respect to the target. The underlying assumptions here are small

angular displacements between the two body frames and a passively tumbling target target with constant angular velocity $\boldsymbol{\omega}_t$ relative to an inertial frame. [65] Figure A-1 illustrates the small angular displacement assumption, where $\{\mathbf{b}_{t,1}, \mathbf{b}_{t,2}, \mathbf{b}_{t,3}\}$ is the basis associated with the target's body frame $\mathcal{B}_t$ and $\{\mathbf{b}_{c,1}, \mathbf{b}_{c,2}, \mathbf{b}_{c,3}\}$ is the basis associated with the chaser's body frame $\mathcal{B}_c$. Using an antisymmetric Euler sequence to relate the orientation of the target body frame to the chaser body frame, the rotation matrix to relate two reference frames is approximated as

$$\mathbf{C}_{\mathcal{B}_c\mathcal{B}_t} \approx \mathbf{I} - \boldsymbol{\alpha}^{\times} \ ,$$

where

$$\boldsymbol{\alpha} = \begin{bmatrix} \alpha_1 & \alpha_2 & \alpha_3 \end{bmatrix}^T$$

and $\alpha_1, \alpha_2, \alpha_3$ are the angles associated with the rotations in the antisymmetric Euler sequence. [65] As a result, the relative angular velocity is $\dot{\boldsymbol{\alpha}}$ and the angular velocity of the chaser body frame relative to an inertial frame is approximated as

$$\boldsymbol{\omega}_c = \dot{\boldsymbol{\alpha}} + (\mathbf{I} - \boldsymbol{\alpha}^{\times})\boldsymbol{\omega}_t \ .$$

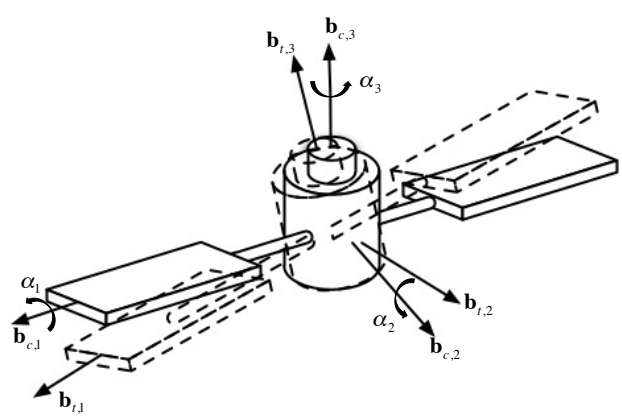

Figure A-1. Relative orientation between chaser and target

Applying Euler's second law, the governing equations for small angular displacements of the chaser body frame relative to the target body frame is

$$\mathbf{J}\left(\ddot{\boldsymbol{\alpha}} - \dot{\boldsymbol{\alpha}}^{\times}\boldsymbol{\omega}_t\right) + \left(\dot{\boldsymbol{\alpha}} + \left[\left(\mathbf{I} - \boldsymbol{\alpha}^{\times}\right)\boldsymbol{\omega}_t\right]\right)^{\times}\mathbf{J}\left(\dot{\boldsymbol{\alpha}} + \left[\mathbf{I} - \boldsymbol{\alpha}^{\times}\right]\boldsymbol{\omega}_t\right) = \boldsymbol{\tau}\ , \tag{A–11}$$

where $\mathbf{J}$ is the inertia matrix of the chaser. Considering only the first order terms, equation (A–11) reduces to

$$\mathbf{J}\ddot{\boldsymbol{\alpha}} = \left[\boldsymbol{\omega}_t\boldsymbol{\omega}_t^T\mathbf{J} - \boldsymbol{\omega}_t^{\times}\mathbf{J}\boldsymbol{\omega}_t^{\times} - \left(\boldsymbol{\omega}_t^T\mathbf{J}\boldsymbol{\omega}_t\right)\mathbf{I}\right]\boldsymbol{\alpha} + \left[\left(\mathbf{J}\boldsymbol{\omega}_t\right)^{\times} - \boldsymbol{\omega}_t^{\times}\mathbf{J} - \mathbf{J}\boldsymbol{\omega}_t^{\times}\right]\dot{\boldsymbol{\alpha}} - \boldsymbol{\omega}_t^{\times}\mathbf{J}\boldsymbol{\omega}_t + \boldsymbol{\tau}\ . \tag{A–12}$$

Equation (A–12) can be written in state space form

$$\begin{bmatrix}\dot{\boldsymbol{\alpha}}\\ \ddot{\boldsymbol{\alpha}}\end{bmatrix} = \begin{bmatrix}\mathbf{0} & \mathbf{I}\\ \mathbf{A}_{21} & \mathbf{A}_{22}\end{bmatrix}\begin{bmatrix}\boldsymbol{\alpha}\\ \dot{\boldsymbol{\alpha}}\end{bmatrix} + \begin{bmatrix}\mathbf{0}\\ \mathbf{J}^{-1}\end{bmatrix}\mathbf{u}\ ,$$

where $\mathbf{u} = \boldsymbol{\tau} - \boldsymbol{\omega}_t^{\times}\mathbf{J}\boldsymbol{\omega}_t$ and $\mathbf{A}_{21}, \mathbf{A}_{22}$ are blocks of the state matrix and are defined as

$$\mathbf{A}_{21} = \mathbf{J}^{-1}\left[\boldsymbol{\omega}_t\boldsymbol{\omega}_t^T\mathbf{J} - \boldsymbol{\omega}_t^{\times}\mathbf{J}\boldsymbol{\omega}_t^{\times} - \left(\boldsymbol{\omega}_t^T\mathbf{J}\boldsymbol{\omega}_t\right)\mathbf{I}\right]$$

$$\mathbf{A}_{22} = \mathbf{J}^{-1}\left[\left(\mathbf{J}\boldsymbol{\omega}_t\right)^{\times} - \boldsymbol{\omega}_t^{\times}\mathbf{J} - \mathbf{J}\boldsymbol{\omega}_t^{\times}\right]\ .$$

It is interesting to note that a constant force term appears in this set of equations due to the constant tumbling rate of the target.

APPENDIX B
TWO POINT BOUNDARY VALUE PROBLEM SOLUTION

The two point boundary value problem (TPBVP) is stated as: "*Given a dynamical system* $\dot{\mathbf{x}} = \mathbf{f}(\mathbf{x}, \mathbf{u}, t)$*, an initial condition* $\mathbf{x}(t_0) = \mathbf{x}_0$*, and a desired final condition* $\mathbf{x}(t_f) = \mathbf{x}_f$ *obtained at time* $t = t_f$*, determine the control action* $\mathbf{u}(t)$ *that satisfies these conditions.*" The problem of interest is to determine an initial change in velocity $\Delta\dot{\mathbf{x}}_i$ to reach a final position $\mathbf{x}_f$ in time T with arbitrary final velocity. Solving a TPBVP can be cumbersome, but this is not the case for linear systems. Since the relative motion equations are linear, they can be written using a block form of the state transition matrix (STM) representation as [71]

$$\begin{bmatrix} \mathbf{x}(t) \\ \dot{\mathbf{x}}(t) \end{bmatrix} = \begin{bmatrix} \mathbf{\Phi}_{11}(t) & \mathbf{\Phi}_{12}(t) \\ \mathbf{\Phi}_{21}(t) & \mathbf{\Phi}_{22}(t) \end{bmatrix} \begin{bmatrix} \mathbf{x}_0 \\ \dot{\mathbf{x}}_0 \end{bmatrix} + \int_{t_0}^{t} \begin{bmatrix} \mathbf{\Phi}_{11}(t-\varepsilon) & \mathbf{\Phi}_{12}(t-\varepsilon) \\ \mathbf{\Phi}_{21}(t-\varepsilon) & \mathbf{\Phi}_{22}(t-\varepsilon) \end{bmatrix} \mathbf{B}\mathbf{u}(\varepsilon)\, d\varepsilon \,. \tag{B–1}$$

Thus, the solution of the TPBVP of interest is obtained by letting

$$\dot{\mathbf{x}}_0 = \dot{\mathbf{x}}_0 + \Delta\dot{\mathbf{x}}_i$$

and solving a system of algebraic equations for $\Delta\dot{\mathbf{x}}_i$.

The TPBVP solution is obtained for both the CWH equation and SAA equation. Since the SAA equation has a constant forcing term, the associated TPBVP problem includes a general constant forcing term $\mathbf{u} = -\boldsymbol{\omega}_t^{\times}\mathbf{J}\boldsymbol{\omega}_t$. Also, note that for both relative motion equations the input matrix is of the form

$$\mathbf{B} = \begin{bmatrix} \mathbf{0} \\ \mathbf{B}_2 \end{bmatrix} \,.$$

Thus, considering the first row of equation (B–1), the initial change in velocity required to reach a final position $\mathbf{x}_f$ in time T is solved for as

$$\Delta\dot{\mathbf{x}}_i = \mathbf{\Phi}_{12}^{-1}(T)\left[\mathbf{x}_f - \mathbf{x}_t - \mathbf{\Phi}_{11}(T)\mathbf{x}_0\right] - \dot{\mathbf{x}}_0 \,, \tag{B–2}$$

where

$$\mathbf{x}_t = \int_{t_0}^{T} \mathbf{\Phi}_{12}(T-t)\mathbf{B}_2\mathbf{u}\, dt \ .$$

This is for the application of interception since the only condition is for $\mathbf{x} \to \mathbf{x}_f$ as $t \to T$.

Substituting equation (B–2) into equation (B–1) and considering the second row of equation (B–1) yields the velocity profile

$$\begin{aligned}\dot{\mathbf{x}}_d(t) = \mathbf{\Phi}_{12}(t)\mathbf{x}_0 + \mathbf{\Phi}_{22}(t)\left[\dot{\mathbf{x}}_0 + \mathbf{\Phi}_{12}^{-1}(T)\left(\mathbf{x}_f - \mathbf{x}_t - \mathbf{\Phi}_{11}(T)\mathbf{x}_0\right) - \dot{\mathbf{x}}_0\right] \ldots \\ + \int_{t_0}^{t} \mathbf{\Phi}_{22}(T-\varepsilon)\mathbf{B}_2\mathbf{u}\, d\varepsilon\end{aligned}$$

$$\begin{aligned}\Rightarrow \dot{\mathbf{x}}_d(t) = \left[\mathbf{\Phi}_{21}(t) - \mathbf{\Phi}_{22}(t)\mathbf{\Phi}_{12}^{-1}(T)\mathbf{\Phi}_{11}(T)\right]\mathbf{x}_0 + \mathbf{\Phi}_{22}(t)\mathbf{\Phi}_{12}^{-1}(T)\left[\mathbf{x}_f - \mathbf{x}_t\right] \ldots \\ + \int_{t_0}^{t} \mathbf{\Phi}_{22}(T-\varepsilon)\mathbf{B}_2\mathbf{u}\, d\varepsilon \ . \qquad \text{(B–3)}\end{aligned}$$

Recall the STM property [71]

$$\mathbf{\Phi}(t_1)\mathbf{\Phi}(t_2) = \mathbf{\Phi}(t_1 + t_2) \ .$$

Using the block form of the STM and letting $t_1 = T$ and $t_2 = -T$, the $(1,2)$ block of this STM property is

$$\mathbf{\Phi}_{11}(T)\mathbf{\Phi}_{12}(-T) + \mathbf{\Phi}_{12}(T)\mathbf{\Phi}_{22}(-T) = \mathbf{0} \ .$$

Multiplying on the left by $\mathbf{\Phi}_{12}^{-1}(T)$ and multiplying on the right by $\mathbf{\Phi}_{12}^{-1}(-T)$, the equation reduces to

$$\mathbf{\Phi}_{12}^{-1}(T)\mathbf{\Phi}_{11}(T) = -\mathbf{\Phi}_{22}(-T)\mathbf{\Phi}_{12}^{-1}(-T) \ . \qquad \text{(B–4)}$$

Using the same STM property and letting $t_1 = t$ and $t_2 = -T$, the $(2,2)$ block of the STM property for this case is

$$\begin{aligned} \mathbf{\Phi}_{21}(t)\mathbf{\Phi}_{12}(-T) + \mathbf{\Phi}_{22}(t)\mathbf{\Phi}_{22}(-T) &= \mathbf{\Phi}_{22}(t-T) \\ \Rightarrow \mathbf{\Phi}_{22}(t)\mathbf{\Phi}_{22}(-T) &= \mathbf{\Phi}_{22}(t-T) - \mathbf{\Phi}_{21}(t)\mathbf{\Phi}_{12}(-T)\ . \end{aligned} \tag{B–5}$$

Substituting equation (B–4) into equation (B–3) results in equation(B–3)

$$\begin{aligned} \dot{\mathbf{x}}_d(t) = \left[\mathbf{\Phi}_{21}(t) - \mathbf{\Phi}_{22}(t)\mathbf{\Phi}_{22}^{-1}(-T)\mathbf{\Phi}_{12}^{-1}(-T)\right]\mathbf{x}_0 + \mathbf{\Phi}_{22}(t)\mathbf{\Phi}_{12}^{-1}(T)\left[\mathbf{x}_f - \mathbf{x}_t\right] \ldots \\ + \int_{t_0}^{t} \mathbf{\Phi}_{22}(T-\varepsilon)\mathbf{B}_2\mathbf{u}\ d\varepsilon\ . \end{aligned}$$

Substituting equation (B–5) into this equation results in

$$\begin{aligned} \dot{\mathbf{x}}_d(t) = \left[\mathbf{\Phi}_{21}(t) - \left(\mathbf{\Phi}_{22}(t-T) - \mathbf{\Phi}_{21}(t)\mathbf{\Phi}_{12}(-T)\right)\mathbf{\Phi}_{12}^{-1}(-T)\right]\mathbf{x}_0 + \mathbf{\Phi}_{22}(t)\mathbf{\Phi}_{12}^{-1}(T)\left[\mathbf{x}_f - \mathbf{x}_t\right] \ldots \\ + \int_{t_0}^{t} \mathbf{\Phi}_{22}(T-\varepsilon)\mathbf{B}_2\mathbf{u}\ d\varepsilon \end{aligned}$$

$$\Rightarrow \dot{\mathbf{x}}_d(t) = \mathbf{\Phi}_{22}(t-T)\mathbf{\Phi}_{12}^{-1}(-T)\mathbf{x}_0 + \mathbf{\Phi}_{22}(t)\mathbf{\Phi}_{12}^{-1}(T)\left[\mathbf{x}_f - \mathbf{x}_t\right] + \int_{t_0}^{t} \mathbf{\Phi}_{22}(T-\varepsilon)\mathbf{B}_2\mathbf{u}\ d\varepsilon\ . \tag{B–6}$$

This velocity profile gives the velocity history of the trajectory from the initial condition to the final position.

Equation (B–6) can also be used to define the velocity change $\Delta\dot{\mathbf{x}}_f$ needed at position $\mathbf{x}_f$ so that the velocity at time T is zeroed out. This velocity change is the negative of the velocity profile at time $t = T$.

$$\Delta\dot{\mathbf{x}}_f = -\mathbf{\Phi}_{12}^{-1}(-T)\mathbf{x}_0 - \mathbf{\Phi}_{22}(T)\mathbf{\Phi}_{12}^{-1}(T)\left[\mathbf{x}_f - \mathbf{x}_t\right] - \int_{t_0}^{T} \mathbf{\Phi}_{22}(T-t)\mathbf{B}_2\mathbf{u}\ dt$$

This is for the application of rendezvous since $\mathbf{x} \to \mathbf{x}_f$, $\dot{\mathbf{x}} \to \mathbf{0}$ as $t \to T$.

Obtaining these two velocity changes is particularly useful when considering a minimum control effort OCP. The solution to the minimum control effort optimal control

problem (OCP) can be approximated as the two burn solution, with one burn at the initial time and one burn at the final time. [72] Thus, the cost for this problem is also approximated as

$$J \approx \|\Delta\dot{\mathbf{x}}_i\|_1 + \|\Delta\dot{\mathbf{x}}_f\|_1 \ .$$

It should be noted that the matrix $\mathbf{\Phi}_{12}(T)$ can be singular for certain values of T. To illustrate this, two interception examples are performed using the CWH and SAA equations. The parameters used for the CWH example are in Table B-1, and the parameters for the SAA example are in Table B-2.

Table B-1. Relative orientation parameters

Parameter	Value	Units
n	0.001	rad/s
$\mathbf{r}_0$	$\begin{bmatrix}500 & 500 & 500\end{bmatrix}^T$	m
$\mathbf{v}_0$	$\begin{bmatrix}0 & 0 & 0\end{bmatrix}^T$	m/s
$\mathbf{r}_f$	$\begin{bmatrix}0 & 0 & 0\end{bmatrix}^T$	m

Table B-2. Relative orientation parameters

Parameter	Value	Units
$\mathbf{J}$	$\begin{bmatrix}300 & 0 & 0 \\ 0 & 100 & 0 \\ 0 & 0 & 200\end{bmatrix}$	$\mathrm{kg} \cdot \mathrm{m}^2$
$\boldsymbol{\omega}_t$	$\begin{bmatrix}0.1 & 0.1 & 0.1\end{bmatrix}^T$	rad/s
$\boldsymbol{\alpha}_0$	$\begin{bmatrix}0.1 & 0.1 & 0.1\end{bmatrix}^T$	rad
$\dot{\boldsymbol{\alpha}}_0$	$\begin{bmatrix}0 & 0 & 0\end{bmatrix}^T$	rad/s
$\boldsymbol{\alpha}_f$	$\begin{bmatrix}0 & 0 & 0\end{bmatrix}^T$	rad

Figure B-1A shows a set of TPBVP trajectories for the CWH equation with different values of T. Figure B-1B shows a plot of $\|\Delta\mathbf{v}_i\|_1$ for different values of T and depicts the values where $\mathbf{\Phi}_{12}(T)$ becomes singular (i.e., the vertical asymptotes). For this example, the matrix $\mathbf{\Phi}_{12}(T)$ becoming singular physically signifies an infinite impulse that is pointed directly at the desired position or in the opposite direction.

Figure B-1C shows a set of TPBVP trajectories for the SAA equation with different values of T. Figure B-1D shows a plot of $\|\Delta\dot{\boldsymbol{\alpha}}_i\|_1$ for different values of T and depicts the values where $\boldsymbol{\Phi}_{12}(T)$ becomes singular (i.e., the vertical asymptotes). For this example, the matrix $\boldsymbol{\Phi}_{12}(T)$ becoming singular physically signifies an infinite impulse to reach the desired orientation.

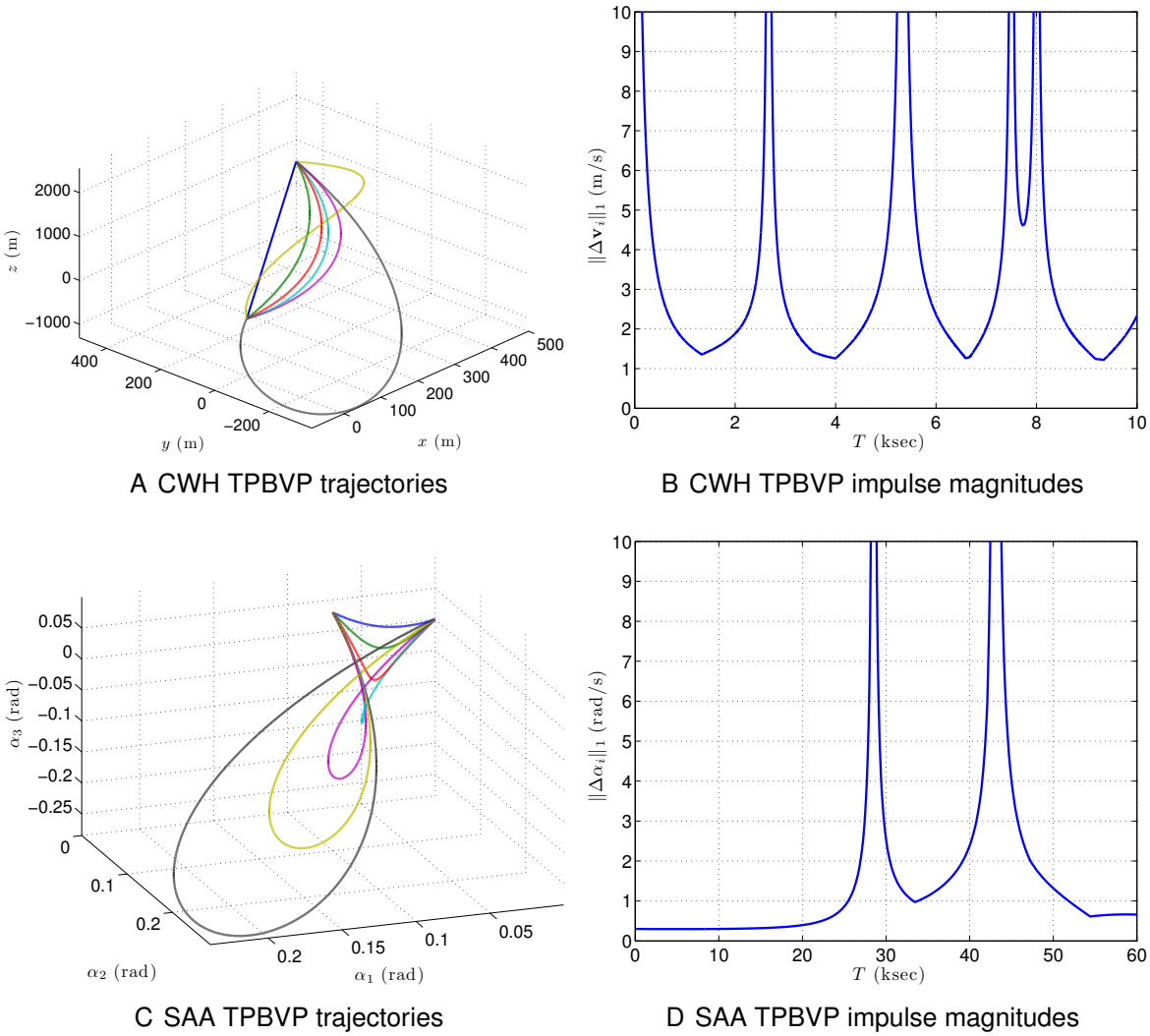

A CWH TPBVP trajectories

B CWH TPBVP impulse magnitudes

C SAA TPBVP trajectories

D SAA TPBVP impulse magnitudes

Figure B-1. Two point boundary value problem examples

APPENDIX C
HOMOTOPY WITH RICCATI EQUATION - $L(\mathbf{S}) = \dot{\mathbf{S}}$

The derivation for solving the nonlinear operator

$$N(\mathbf{S}) = \dot{\mathbf{S}} + \mathbf{Q} - \mathbf{S}\mathbf{B}\mathbf{R}^{-1}\mathbf{B}^T\mathbf{S} + \mathbf{A}^T\mathbf{S} + \mathbf{S}\mathbf{A} = \mathbf{0}\ ,\ \ \mathbf{S}(t_f) = \mathbf{S}_f\ , \tag{C–1}$$

using the Homotopy Continuation (HC) method is presented in this Appendix. First, the convex homotopy is defined as

$$H(\mathbf{S}, p) = (1-p)\left[L(\mathbf{S}) - L(\mathbf{Y}_0)\right] - ph\mathbf{\Psi}(t)\left[N(\mathbf{S})\right] = \mathbf{0}\ , \tag{C–2}$$

where $p \in \{\nu \in \mathbb{R} \mid 0 \leq \nu \leq 1\}$ is the embedding parameter, $h \in \mathbb{R} - \{0\}$ is the auxiliary parameter, $\mathbf{\Psi}(t) \neq \mathbf{0}\ \forall\ t$ is the auxiliary function, $\mathbf{Y}_0$ is an initial guess, and

$$L(\mathbf{S}) = \dot{\mathbf{S}}\ .$$

Next, the Maclaurin Series Expansion (MSE) of $\mathbf{S}$ is obtained as

$$\mathbf{S} = \mathbf{S}_0 + p\mathbf{S}_1 + p^2\mathbf{S}_2 + \cdots\ , \tag{C–3}$$

Substituting equation (C–3) into equation (C–2) yields,

$$\begin{aligned} H(\mathbf{S}_0, \mathbf{S}_1, \mathbf{S}_2, \ldots, p) = (1-p)\left[L(\mathbf{S}_0 + p\mathbf{S}_1 + p^2\mathbf{S}_2 + \cdots) - L(\mathbf{Y}_0)\right] - \ldots \\ ph\mathbf{\Psi}(t)N(\mathbf{S}_0 + p\mathbf{S}_1 + p^2\mathbf{S}_2 + \cdots) \end{aligned} \tag{C–4}$$

The operator $L(\mathbf{S})$ is easily decomposed as

$$L(\mathbf{S}_0 + p\mathbf{S}_1 + p^2\mathbf{S}_2 + \ldots) = L(\mathbf{S}_0) + pL(\mathbf{S}_1) + p^2L(\mathbf{S}_2) + \cdots\ , \tag{C–5}$$

since it is a linear operator. The operator $N(\mathbf{S})$ defined in equation (C–1) is nonlinear and must be decomposed manually. Direct substitution of the MSE into equation (C–1)

results in

$$
\begin{aligned}
N(\mathbf{S}_0, \mathbf{S}_1, \mathbf{S}_2, \dots, p) = \left[\dot{\mathbf{S}}_0 + p\dot{\mathbf{S}}_1 + p^2\dot{\mathbf{S}}_2 + \cdots\right] + \mathbf{Q} - \dots \\
\left[\mathbf{S}_0 + p\mathbf{S}_1 + p^2\mathbf{S}_2 + \cdots\right] \mathbf{B}\mathbf{R}^{-1}\mathbf{B}^T \left[\mathbf{S}_0 + p\mathbf{S}_1 + p^2\mathbf{S}_2 + \cdots\right] + \dots \\
\mathbf{A}^T \left[\mathbf{S}_0 + p\mathbf{S}_1 + p^2\mathbf{S}_2 + \cdots\right] + \left[\mathbf{S}_0 + p\mathbf{S}_1 + p^2\mathbf{S}_2 + \cdots\right] \mathbf{A} = \mathbf{0}\ .
\end{aligned}
$$

The result is rewritten such that coefficients are grouped for the different powers of the embedding parameter,

$$
N(\mathbf{S}) = \mathbf{G}_0 + p\mathbf{G}_1 + p^2\mathbf{G}_2 + \cdots \tag{C–6}
$$

where

$$
\begin{aligned}
\mathbf{G}_0 &= \dot{\mathbf{S}}_0 + \mathbf{Q} - \mathbf{S}_0\mathbf{B}\mathbf{R}^{-1}\mathbf{B}^T\mathbf{S}_0 + \mathbf{A}^T\mathbf{S}_0 + \mathbf{S}_0\mathbf{A} \\
\mathbf{G}_1 &= \dot{\mathbf{S}}_1 - \mathbf{S}_0\mathbf{B}\mathbf{R}^{-1}\mathbf{B}^T\mathbf{S}_1 - \mathbf{S}_1\mathbf{B}\mathbf{R}^{-1}\mathbf{B}^T\mathbf{S}_0 + \mathbf{A}^T\mathbf{S}_1 + \mathbf{S}_1\mathbf{A} \\
\mathbf{G}_2 &= \dot{\mathbf{S}}_2 - \mathbf{S}_0\mathbf{B}\mathbf{R}^{-1}\mathbf{B}^T\mathbf{S}_2 - \mathbf{S}_1\mathbf{B}\mathbf{R}^{-1}\mathbf{B}^T\mathbf{S}_1 - \mathbf{S}_2\mathbf{B}\mathbf{R}^{-1}\mathbf{B}^T\mathbf{S}_0 + \mathbf{A}^T\mathbf{S}_2 + \mathbf{S}_2\mathbf{A} \\
\mathbf{G}_3 &= \dot{\mathbf{S}}_3 - \mathbf{S}_0\mathbf{B}\mathbf{R}^{-1}\mathbf{B}^T\mathbf{S}_3 - \mathbf{S}_1\mathbf{B}\mathbf{R}^{-1}\mathbf{B}^T\mathbf{S}_2 - \mathbf{S}_2\mathbf{B}\mathbf{R}^{-1}\mathbf{B}^T\mathbf{S}_1 - \mathbf{S}_3\mathbf{B}\mathbf{R}^{-1}\mathbf{B}^T\mathbf{S}_0 + \mathbf{A}^T\mathbf{S}_3 + \mathbf{S}_3\mathbf{A}\ . \\
&\vdots
\end{aligned}
$$

Equation (C–5) and equation (C–6) are substituted into equation (C–4) to obtain,

$$
\begin{aligned}
H(\mathbf{S}_0, \mathbf{S}_1, \mathbf{S}_2, \dots, p) = (1-p)\left[L(\mathbf{S}_0) + pL(\mathbf{S}_1) + p^2L(\mathbf{S}_2) + \cdots\right] - (1-p)L(\mathbf{Y}_0) - \dots \\
ph\mathbf{\Psi}(t)\left[\mathbf{G}_0 + p\mathbf{G}_1 + p^2\mathbf{G}_2 + \cdots\right] = \mathbf{0}
\end{aligned}
$$

The coefficients for the different powers of the embedding parameter are grouped, which results in

$$
\begin{aligned}
p^0 \text{ terms} &: \quad L(\mathbf{S}_0) - L(\mathbf{Y}_0) \\
p^1 \text{ terms} &: \quad L(\mathbf{S}_1) - h\boldsymbol{\Psi}\mathbf{G}_0 - L(\mathbf{S}_0) + L(\mathbf{Y}_0) \\
p^2 \text{ terms} &: \quad L(\mathbf{S}_2) - h\boldsymbol{\Psi}\mathbf{G}_1 - L(\mathbf{S}_1) \\
p^3 \text{ terms} &: \quad L(\mathbf{S}_3) - h\boldsymbol{\Psi}\mathbf{G}_2 - L(\mathbf{S}_2) \ . \\
&\quad \vdots
\end{aligned}
$$

The trend for obtaining the subsequent group of terms is the same. The coefficients are individually set to zero to solve for the parameters $\mathbf{S}_0, \mathbf{S}_1, \mathbf{S}_2, \ldots$. The result is a system of differential equations. For the derivation presented in this Appendix, the auxiliary function used is $\boldsymbol{\Psi}(t) = \mathbf{I}$, however, this function is free to choose.

The equation for the zeroth order term suggests

$$
\begin{aligned}
L(\mathbf{S}_0) - L(\mathbf{Y}_0) &= \mathbf{0} \\
\Rightarrow \dot{\mathbf{S}}_0 - \dot{\mathbf{Y}}_0 &= \mathbf{0} \ .
\end{aligned}
$$

The most easily obtainable solution is to let $\mathbf{S}_0 = \mathbf{Y}_0$ where $\mathbf{Y}_0$ is free to choose. The chosen parameter is $\mathbf{Y}_0 = \mathbf{C}_0 = \mathbf{S}_f$ since this would satisfy the equation

$$
L(\mathbf{Y}_0) = \mathbf{0} \ ,
$$

and the boundary condition $\mathbf{Y}_0(t_f) = \mathbf{S}_f$. Thus, the solution for the zeroth parameter is

$$
\mathbf{S}_0 = \mathbf{C}_0 = \mathbf{S}_f \ .
$$

The equation for the first order term suggests

$$
\begin{aligned}
L(\mathbf{S}_1) - h\mathbf{G}_0 - L(\mathbf{S}_0) + L(\mathbf{Y}_0) &= \mathbf{0} \\
\Rightarrow \dot{\mathbf{S}}_1 - h\mathbf{G}_0 &= \mathbf{0} \ .
\end{aligned}
$$

Note that the term $\mathbf{G}_0$ only depends on $\mathbf{S}_0$ which has already been solved for. To solve for the parameter $\mathbf{S}_1$, the homogeneous solution is first obtained

$$\mathbf{S}_{1,h} = \mathbf{C}_1 \ ,$$

where $\mathbf{C}_1$ is a constant. The particular solution is determined by employing the variation of parameters technique. That is, the integration constant is assumed to be time dependent (i.e., $\mathbf{C}_1 = \mathbf{C}_1(t, t_f)$) and the homogeneous solution is substituted into the original differential equation. Thus, the resulting differential equation for the particular solution is

$$\dot{\mathbf{C}}_1 = h\mathbf{G}_0 \ .$$

Notice that this equation only depends on $\mathbf{S}_0$, which has already been solved for. The solution for the constant is

$$\mathbf{C}_1(t, t_f) = h \int_{t_f}^{t} \mathbf{G}_0 \ d\varepsilon \ .$$

Also, note that $\mathbf{C}_1(t_f, t_f) = \mathbf{0}$ in order to maintain the boundary condition of $\mathbf{S}(t_f) = \mathbf{S}_f$. Thus, the solution for the first parameter is

$$\mathbf{S}_1 = \mathbf{C}_1(t, t_f) \ .$$

The equation for the second order term suggests

$$\begin{aligned} L(\mathbf{S}_2) - h\mathbf{G}_1 - L(\mathbf{S}_1) &= \mathbf{0} \\ \Rightarrow \dot{\mathbf{S}}_2 - h\mathbf{G}_1 - \dot{\mathbf{S}}_1 &= \mathbf{0} \ . \end{aligned}$$

Note again that the term $\mathbf{G}_1$ only depends on $\mathbf{S}_0$ and $\mathbf{S}_1$ which have already been solved for. It should be noted that the subsequent differential equations to be solved are of the

same form

$$\dot{\mathbf{S}}_{i+1} - h\mathbf{G}_i - \dot{\mathbf{S}}_i = \mathbf{0} \text{ for } i = 1, 2, 3, \ldots \ .$$

Thus, for the remaining derivation is done for the $(i+1)^{\text{th}}$ term. The homogeneous solution of $\mathbf{S}_{i+1}$ is first found and is of the form

$$\mathbf{S}_{i+1,h} = \mathbf{C}_{i+1} \text{ for } i = 1, 2, 3, \ldots \ ,$$

where $\mathbf{C}_{i+1}$ is a constant. The variation of parameters technique is again employed to solve for the particular solution. The resulting differential equation for the particular solution is

$$\dot{\mathbf{C}}_{i+1} = \dot{\mathbf{C}}_i + h\mathbf{G}_i \text{ for } i = 1, 2, 3, \ldots \ .$$

This equation is integrated to obtain the solution

$$\mathbf{C}_{i+1}(t, t_f) = \mathbf{C}_i + h \int_{t_f}^{t} \mathbf{G}_i \ d\varepsilon \text{ for } i = 1, 2, 3, \ldots \ .$$

Note again that $\mathbf{C}_{i+1}(t_f, t_f) = \mathbf{0}$ to maintain the boundary condition of $\mathbf{S}(t_f) = \mathbf{S}_f$. The solution for the $(i+1)^{\text{th}}$ parameter is

$$\mathbf{S}_{i+1} = \mathbf{C}_{i+1}(t, t_f) \text{ for } i = 1, 2, 3, \ldots \ .$$

As a result, the kth order approximation of the homotopy solution is given by

$$\mathbf{S}^{(k)} = \sum_{i=0}^{k} \mathbf{S}_i \ .$$

APPENDIX D
HOMOTOPY WITH TRANSFORMED RICCATI EQUATION - $L(\mathbf{X}) = \dot{\mathbf{X}}$

The derivation for solving the linear time varying (LTV) differential equation

$$N(\mathbf{X}) = \dot{\mathbf{X}} - \mathbf{H}_t\mathbf{X} = \mathbf{0} \ , \quad \mathbf{X}(t_f) = \mathbf{X}_f \ ,$$

using the Homotopy Continuation (HC) method is presented in this Appendix. First, the convex homotopy is defined as

$$H(\mathbf{X}, p) = (1-p)\left[L(\mathbf{X}) - L(\mathbf{Y}_0)\right] - ph\mathbf{\Psi}(t)\left[N(\mathbf{X})\right] = \mathbf{0} \ , \tag{D–1}$$

where $p \in \{\nu \in \mathbb{R} \mid 0 \leq \nu \leq 1\}$ is the embedding parameter, $h \in \mathbb{R} - \{0\}$ is the auxiliary parameter, $\mathbf{\Psi}(t) \neq \mathbf{0} \ \forall \ t$ is the auxiliary function, $\mathbf{Y}_0$ is an initial guess, and

$$L(\mathbf{X}) = \dot{\mathbf{X}} \ .$$

Next, the Maclaurin Series Expansion (MSE) of $\mathbf{X}$ is obtained as

$$\mathbf{X} = \mathbf{X}_0 + p\mathbf{X}_1 + p^2\mathbf{X}_2 + \cdots \ , \tag{D–2}$$

Substituting equation (D–2) into equation (D–1) yields

$$\begin{aligned} H(\mathbf{X}_0, \mathbf{X}_1, \mathbf{X}_2, \dots, p) = (1-p)\left[L(\mathbf{X}_0 + p\mathbf{X}_1 + p^2\mathbf{X}_2 + \cdots) - L(\mathbf{Y}_0)\right] - \dots \\ ph\mathbf{\Psi}(t)N(\mathbf{X}_0 + p\mathbf{X}_1 + p^2\mathbf{X}_2 + \cdots) \ . \end{aligned} \tag{D–3}$$

Note that both $L(\mathbf{X})$ and $N(\mathbf{X})$ are linear operators and are easily decomposed as

$$L(\mathbf{S}_0 + p\mathbf{S}_1 + p^2\mathbf{S}_2 + \dots) = L(\mathbf{S}_0) + pL(\mathbf{S}_1) + p^2L(\mathbf{S}_2) + \cdots \tag{D–4}$$

$$N(\mathbf{S}_0 + p\mathbf{S}_1 + p^2\mathbf{S}_2 + \dots) = N(\mathbf{S}_0) + pN(\mathbf{S}_1) + p^2N(\mathbf{S}_2) + \cdots \ . \tag{D–5}$$

Equation (D–4) and equation (D–5) are substituted into equation (D–3) to obtain

$$H(\mathbf{X}_0, \mathbf{X}_1, \mathbf{X}_2, \dots, p) = (1-p)\left[L(\mathbf{X}_0) + pL(\mathbf{X}_1) + p^2 L(\mathbf{X}_2) + \cdots\right] - (1-p)L(\mathbf{Y}_0) - \dots$$
$$ph\mathbf{\Psi}(t)\left[N(\mathbf{X}_0) + pN(\mathbf{X}_1) + p^2 N(\mathbf{X}_2) + \cdots\right] = \mathbf{0}\ .$$

The coefficients for the different powers of the embedding parameter are grouped which results in

$$\begin{aligned}
p^0 \text{ terms } &: \quad L(\mathbf{X}_0) - L(\mathbf{Y}_0) \\
p^1 \text{ terms } &: \quad L(\mathbf{X}_1) - h\mathbf{\Psi}(t)N(\mathbf{X}_0) - L(\mathbf{X}_0) + L(\mathbf{Y}_0) \\
p^2 \text{ terms } &: \quad L(\mathbf{X}_2) - h\mathbf{\Psi}(t)N(\mathbf{X}_1) - L(\mathbf{X}_1) \\
p^3 \text{ terms } &: \quad L(\mathbf{X}_3) - h\mathbf{\Psi}(t)N(\mathbf{X}_2) - L(\mathbf{X}_2)\ . \\
&\quad\ \vdots
\end{aligned} \tag{D–6}$$

The trend for obtaining the subsequent group of terms is the same. The coefficients are individually set to zero to solve for the parameters $\mathbf{X}_1, \mathbf{X}_2, \mathbf{X}_2, \dots$. The result is a system of differential equations. For the derivation presented in this Appendix, the auxiliary function used is $\mathbf{\Psi}(t) = \mathbf{I}$, however, this function is free to choose.

The equation for the zeroth order term suggests

$$L(\mathbf{X}_0) - L(\mathbf{Y}_0) = \mathbf{0}$$
$$\Rightarrow \dot{\mathbf{X}}_0 - \dot{\mathbf{Y}}_0 = \mathbf{0}\ .$$

The most easily obtainable solution is to let $\mathbf{X}_0 = \mathbf{Y}_0$ where $\mathbf{Y}_0$ is free to choose. The chosen parameter is $\mathbf{Y}_0 = \mathbf{C}_0 = \mathbf{S}_f$ since this would satisfy the equation

$$L(\mathbf{Y}_0) = \mathbf{0}\ ,$$

and the boundary condition $\mathbf{Y}_0(t_f) = \mathbf{X}_f$. Thus, the solution for the zeroth parameter is

$$\mathbf{S}_0 = \mathbf{C}_0 = \mathbf{X}_f\ . \tag{D–7}$$

The equation for the first order term suggests

$$L(\mathbf{X}_1) - hN(\mathbf{X}_0) - L(\mathbf{X}_0) + L(\mathbf{Y}_0) = \mathbf{0}$$
$$\Rightarrow \dot{\mathbf{X}}_1 - h\left[\dot{\mathbf{X}}_0 - \mathbf{H}_t\mathbf{X}_0\right] = \mathbf{0}\ .$$

To solve for the parameter $\mathbf{X}_1$, the homogeneous solution is first obtained

$$\mathbf{X}_{1,h} = \mathbf{C}_1\ ,$$

where $\mathbf{C}_1$ is a constant. The particular solution is determined by employing the variation of parameters technique. That is, the integration constant is assumed to be time dependent (i.e., $\mathbf{C}_1 = \mathbf{C}_1(t, t_f)$) and the homogeneous solution is substituted into the original differential equation. Thus, the resulting differential equation for the particular solution is

$$\dot{\mathbf{C}}_1 = -h\mathbf{H}_t\mathbf{C}_0\ ,$$

Notice that this equation only depends on $\mathbf{S}_0$, which has already been solved for. The solution for the constant is

$$\mathbf{C}_1(t, t_f) = -h\int_{t_f}^{t} \mathbf{H}_t\mathbf{C}_0\ d\varepsilon\ .$$

Note that $\mathbf{C}_1(t_f, t_f) = \mathbf{0}$ in order to maintain the boundary condition of $\mathbf{X}(t_f) = \mathbf{X}_f$. Thus, the solution for the first parameter is

$$\mathbf{X}_1 = \mathbf{C}_1(t, t_f)\ .$$

The equation for the second order term suggests

$$L(\mathbf{X}_2) - hN(\mathbf{X}_1) - L(\mathbf{X}_1) = \mathbf{0}$$
$$\Rightarrow \dot{\mathbf{X}}_2 - h\left[\dot{\mathbf{X}}_1 - \mathbf{H}_t\mathbf{X}_1\right] - \dot{\mathbf{X}}_1 = \mathbf{0}\ .$$

Note again that the equation only depends on $\mathbf{X}_0$ and $\mathbf{X}_1$ which have already been solved for. It should also be noted that the subsequent differential equations to be solved are of the same form,

$$\dot{\mathbf{X}}_{i+1} - h\left[\dot{\mathbf{X}}_i - \mathbf{H}_t\mathbf{X}_i\right] - \dot{\mathbf{X}}_i = \mathbf{0} \text{ for } i = 1, 2, 3, \ldots \ .$$

Thus the remaining derivation is done for the $(i+1)^{\text{th}}$ term. The homogeneous solution of $\mathbf{X}_{i+1}$ is first found and is of the form

$$\mathbf{X}_{i+1,h} = \mathbf{C}_{i+1} \text{ for } i = 1, 2, 3, \ldots \ ,$$

where $\mathbf{C}_{i+1}$ is a constant. The variation of parameters technique is again employed to solve for the particular solution. The resulting differential equation for the particular solution is

$$\dot{\mathbf{C}}_{i+1} = (h+1)\dot{\mathbf{C}}_i - h\mathbf{H}_t\mathbf{C}_i \text{ for } i = 1, 2, 3, \ldots \ .$$

This equation is integrated to obtain the solution

$$\mathbf{C}_{i+1}(t, t_f) = (h+1)\mathbf{C}_i - h\int_{t_0}^{t} \mathbf{H}_t\mathbf{C}_i \, d\varepsilon, \text{ for } i = 1, 2, 3, \ldots \ .$$

Notice again that $\mathbf{C}_{i+1}(t_f, t_f) = \mathbf{0}$ to maintain the boundary condition of $\mathbf{X}(t_f) = \mathbf{X}_f$. Therefore the solution for the $(i+1)^{\text{th}}$ parameter is

$$\mathbf{X}_{i+1} = \mathbf{C}_{i+1}(t, t_f) \text{ for } i = 1, 2, 3, \ldots \ .$$

As a result, the kth order approximation of the homotopy solution is given by

$$\mathbf{X}^{(k)} = \sum_{i=0}^{k} \mathbf{X}_i \ .$$

APPENDIX E
HOMOTOPY WITH TRANSFORMED RICCATI EQUATION - $L(\mathbf{X}) = \dot{\mathbf{X}} - \mathbf{X}$

The derivation for solving the linear time varying (LTV) differential equation

$$N(\mathbf{X}) = \dot{\mathbf{X}} - \mathbf{H}_t\mathbf{X} = \mathbf{0} \ , \quad \mathbf{X}(t_f) = \mathbf{X}_f \ ,$$

using the Homotopy Continuation (HC) method is presented in this Appendix. First, the convex homotopy in equation (D–1) is defined with

$$L(\mathbf{X}) = \dot{\mathbf{X}} - \mathbf{X} \ .$$

Next, the Maclaurin Series Expansion (MSE) of $\mathbf{X}$ in equation (D–2) is obtained. Substituting equation (D–2) into equation (D–1) yields equation (D–3). Since $L(\mathbf{X})$ and $N(\mathbf{X})$ are linear operators, they can easily be decomposed as shown in equation (D–4) and equation (D–5), respectively. As a result, the coefficients for the different powers of the embedding parameter are grouped and result in the same form as equation (D–6). For the derivation presented in this Appendix, the auxiliary function used is $\mathbf{\Psi}(t) = \mathbf{I}$, however, this function is free to choose.

The equation for the zeroth order term suggests

$$L(\mathbf{X}_0) - L(\mathbf{Y}_0) = \mathbf{0}$$
$$\Rightarrow \left[\dot{\mathbf{X}}_0 - \dot{\mathbf{Y}}_0\right] - \mathbf{H}_c\left[\mathbf{X}_0 - \mathbf{Y}_0\right] = \mathbf{0} \ .$$

The most easily obtainable solution is to let $\mathbf{X}_0 = \mathbf{Y}_0$ where $\mathbf{Y}_0$ is free to choose. The chosen parameter is

$$\mathbf{Y}_0 = \exp((t - t_f)\mathbf{I})\mathbf{C}_0 = \exp((t - t_f)\mathbf{I})\mathbf{X}_f \ ,$$

since this would satisfy the equation

$$L(\mathbf{Y}_0) = \mathbf{0} \ ,$$

and the boundary condition $\mathbf{Y}_0(t_f) = \mathbf{X}_f$. Thus, the solution for the zeroth parameter is

$$\mathbf{X}_0 = \exp((t - t_f)\mathbf{I})\mathbf{C}_0 = \exp((t - t_f)\mathbf{I})\mathbf{X}_f \ .$$

The equation for the first order terms suggests,

$$\begin{aligned} L(\mathbf{X}_1) - hN(\mathbf{X}_0) - L(\mathbf{X}_0) + L(\mathbf{Y}_0) &= \mathbf{0} \\ \Rightarrow \left[\dot{\mathbf{X}}_1 - \mathbf{H}_c\mathbf{X}_1\right] - h\left[\dot{\mathbf{X}}_0 - \mathbf{H}_t\mathbf{X}_0\right] &= \mathbf{0} \ . \end{aligned}$$

To solve for the parameter $\mathbf{X}_1$, the homogeneous solution is first obtained

$$\mathbf{X}_{1,h} = \exp((t - t_f)\mathbf{I})\mathbf{C}_1 \ ,$$

where $\mathbf{C}_1$ is a constant. The particular solution is determined by employing the variation of parameters technique. That is, the integration constant is assumed to be time dependent (i.e., $\mathbf{C}_1 = \mathbf{C}_1(t, t_f)$) and the homogeneous solution is substituted into the original differential equation. Thus, the resulting differential equation for the integration constant is

$$\begin{aligned} \exp((t - t_f))\dot{\mathbf{C}}_1 &= h\left[\exp((t - t_f)\mathbf{I})\mathbf{C}_0 - \mathbf{H}_t \exp((t - t_f)\mathbf{I})\mathbf{C}_0\right] \\ \Rightarrow \dot{\mathbf{C}}_1 &= h\left[\mathbf{I} - \mathbf{H}_t\right]\mathbf{C}_0 \ . \end{aligned}$$

Note that the matrix exponential term is a diagonal term, thus it commutes with the matrix multiplication operation. The solution for the constant is

$$\mathbf{C}_1(t, t_f) = h\int_{t_f}^{t} \left[\mathbf{I} - \mathbf{H}_t\right]\mathbf{C}_0 \ d\varepsilon \ .$$

Note that $\mathbf{C}_1(t_f, t_f) = \mathbf{0}$ in order to maintain the boundary condition of $\mathbf{X}(t_f) = \mathbf{X}_f$. Thus, the solution for the first parameter is

$$\mathbf{X}_1 = \exp((t - tf)\mathbf{I})\mathbf{C}_1(t, t_f) \ .$$

The equation for the second order term suggests

$$L(\mathbf{X}_2) - hN(\mathbf{X}_1) - L(\mathbf{X}_1) = \mathbf{0}$$
$$\Rightarrow \left[\dot{\mathbf{X}}_2 - \mathbf{X}_2\right] - h\left[\dot{\mathbf{X}}_1 - \mathbf{H}_t\mathbf{X}_1\right] - \left[\dot{\mathbf{X}}_1 - \mathbf{X}_1\right] = \mathbf{0}\ .$$

It should be noted that the subsequent differential equations to be solved are of the form

$$\left[\dot{\mathbf{X}}_{i+1} - \mathbf{X}_{i+1}\right] - h\left[\dot{\mathbf{X}}_i - \mathbf{H}_t\mathbf{X}_i\right] - \left[\dot{\mathbf{X}}_i - \mathbf{X}_i\right] = \mathbf{0} \ \text{ for } i = 1, 2, 3, \dots\ .$$

The remaining derivation are done for the $(i+1)^{\text{th}}$ term. The homogeneous solution of $\mathbf{X}_{i+1}$ is first found and is of the form

$$\mathbf{X}_{i+1,h} = \exp((t - t_f)\mathbf{I})\mathbf{C}_{i+1} \ \text{ for } i = 1, 2, 3, \dots\ ,$$

where $\mathbf{C}_{i+1}$ is a constant. The variation of parameters technique is again employed to solve for the particular solution. The resulting differential equation for the particular solution is

$$\exp((t - t_f)\mathbf{I})\dot{\mathbf{C}}_{i+1} = \exp((t - t_f)\mathbf{I})\dot{\mathbf{C}}_i + h\left[\exp((t - t_f)\mathbf{I})\left(\mathbf{C}_i + \dot{\mathbf{C}}_i\right) - \mathbf{H}_t\exp((t - t_f)\mathbf{I})\mathbf{C}_i\right]$$
$$\Rightarrow \dot{\mathbf{C}}_{i+1} = (1 + h)\dot{\mathbf{C}}_i + h\left[\mathbf{I} - \mathbf{H}_t\right]\mathbf{C}_i \ \text{ for } i = 1, 2, 3, \dots\ .$$

This equation is integrated to obtain the solution

$$\mathbf{C}_{i+1}(t, t_f) = (1 + h)\mathbf{C}_i + h\int_{t_f}^{t}\left[\mathbf{I} - \mathbf{H}_t\right]\mathbf{C}_i\ d\varepsilon \ \text{ for } i = 1, 2, 3, \dots\ .$$

Notice again that $\mathbf{C}_{i+1}(t_f, t_f) = \mathbf{0}$ to maintain the boundary condition of $\mathbf{X}(t_f) = \mathbf{X}_f$. Therefore, the solution for the $(i+1)^{\text{th}}$ parameter is

$$\mathbf{X}_{i+1} = \exp((t - t_f)\mathbf{I})\mathbf{C}_{i+1} \ \text{ for } i = 1, 2, 3, \dots\ .$$

As a result, the kth order approximation of the homotopy solution is given by

$$\mathbf{X}^{(k)} = \sum_{i=0}^{k}\mathbf{X}_i\ .$$

REFERENCES

[1] "National Space Policy of the United States of America," June 2010.

[2] Space-Travel.com, "Tugboats in Space," http://www.space-travel.com/reports/Tugboats_in_Space_999.html, April 2011.

[3] Lanzerotti, L. J., *Assessment of Options for Extending the Life of the Hubble Space Telescope: Final Report*, National Academy Press, 2005.

[4] Polites, M. E., "Technology of Automated Rendezvous and Capture in Space," *Journal of Spacecraft and Rockets*, Vol. 36, 1999, pp. 280–291.

[5] Kelso, T. S., Vallado, D. A., Chan, J., and Buckwalter, B., "Improved Conjunction Analysis Via Collaborative Space Situational Awareness," *AAS/AIAA Space Flight Mechanics Meeting*, 2008.

[6] Kelso, T. S., "Analysis of the Iridium 33 Cosmos 2251 Collision," Tech. rep., Center for Space Standards & Innovation, 2009.

[7] Carrico, T., Langster, T., Carrico, J., Alfano, S., Loucks, M., and Vallado, D., "Proximity Operations for Space Situational Awareness Spacecraft Rendezvous and Maneuvering using Numerical Simulations and Fuzzy Logic," *The Advanced Maui Optical and Space Surveillance Technologies Conference*, 2006.

[8] Cebrowski, A. K., "Operationally Responsive Space: A New Defense Business Model," Tech. rep., U.S. Army War College, 2005.

[9] Richards, M. G., Viscito, L., Ross, A. M., and Hastings, D. E., "Distinguishing Attributes for the Operationally Responsive Space Paradigm," *Responsive Space*, Vol. 6, 2008.

[10] Brown, O., "Fractionated space architectures: A vision for responsive space," Tech. rep., Defense Advanced Research Projects Agency, 2006.

[11] Siewert, S., McClure, L. H., and Hansen, E., "A System Architecture to Advance Small Satellite Mission Operations Autonomy," *AIAA Conference on Small Satellites*, 1995.

[12] Tatsch, A. R., Fitz-Coy, N., and Gladun, S., "On-Orbit Servicing: A Brief Survey," *Performance Metrics for Intelligent Systems Conference*, 2006.

[13] Gralla, E. L., Shull, S., and de Weck, O., "On-Orbit Assembly Strategies for Next-Generation Space Exploration," *The 57th International Astronautical Congress*, 2006.

[14] Antsaklis, P. J., Passino, K. M., and Wang, S. J., "Towards Intelligent Autonomous Control Systems: Architecture and Fundamental Issues," *Journal of Intelligent and Robotic Systems*, Vol. 1, No. 4, 1989, pp. 315–342.

[15] Zeigler, B. P., "High Autonomy Systems: Concepts and Models," *Proceedings in AI, Simulation, and Planning in High Autonomy Systems*, 1990, pp. 2–7.

[16] Huang, H. M., Messina, E., and Albus, J., "Toward a Generic Model for Autonomy Levels for Unmanned Systems (ALFUS)," *Performance Metrics for Intelligent Systems*, 2003.

[17] Huang, H. M., Pavek, K., Albus, J., and Messina, E., "Autonomy Levels for Unmanned Systems (ALFUS) Framework: An Update," *Proceedings of the 2005 SPIE Defense and Security Symposium*, 2005.

[18] Clough, B. T., "Metrics, Schmetrics! How the Heck Do You Determine a UAV's Autonomy Anyway," Tech. rep., Air Force Research Lab/Wright-Patterson AFB, OH, 2002.

[19] Lavery, D., "Perspectives on Future Space Robotics," *Aerospace America*, Vol. 32, No. 5, 1994, pp. 32–37.

[20] Fehse, W., *Automated Rendezvous and Docking of Spacecraft*, Cambridge, 2003.

[21] Bajracharya, M., Maimone, M. W., and Helmick, D., "Autonomy for Mars Rovers: Past, Present, and Future," *IEEE Computer Society*, Vol. 41, No. 12, 2008, pp. 44–50.

[22] Yamanaka, K., "Rendezvous Strategy of the Japanese Logistics Support Vehicle to the International Space Station," *Spacecraft Guidance, Navigation, and Control Systems*, Vol. 381, 1997, p. 103.

[23] Kawano, I., Mokuno, M., Kasai, T., and Suzuki, T., "Result of Autonomous Rendezvous Docking Experiment of Engineering Test Satellite-VII," *Journal of Spacecraft and Rockets*, Vol. 38, No. 1, 2001, pp. 105–111.

[24] Miki, Y., Abe, N., Matsuyama, K., Masuda, K., Fukuda, N., and Sasaki, H., "Development of the H-II Transfer Vehicle (HTV)," *Mitsubishi Heavy Industries Technical Review*, Vol. 47, No. 1, 2010, pp. 58–64.

[25] Gladun, S. A., *Investigation of Close-Proximity Operations of an Autonomous Robotic On-Orbit Servicer Using Linearized Orbit Mechanics*, Master's thesis, University of Florida, 2005.

[26] Woffinden, D. C. and Geller, D. K., "Navigating the Road to Autonomous Orbital Rendezvous," *Journal of Spacecraft and Rockets*, Vol. 44, No. 4, 2007, pp. 898–909.

[27] Croomes, S., "Demonstration of Autonomous Rendezvous Technology Mishap Investigation Board Review," Tech. rep., National Aeronautics and Space Administration, 2006.

[28] Davis, T. M. and Melanson, D., "XSS-10 Micro-Satellite Flight Demonstration," *Paper No. GT-SSEC. D.3*, 2005.

[29] AFRL, "XSS-11 Micro-Satellite," http://www.kirtland.af.mil/shared/media/document/AFD-070404-108.pdf, December 2005.

[30] Weismuller, T. and Leinz, M., "GNC Technology Demonstrated by the Orbital Express Autonomous Rendezvous and Capture Sensor System," *AAS Guidance and Control Conference*, 2006.

[31] SatNews.com, "Orbital Express Conducts History's First Satellite-to-Satellite Hardware Transfer," http://www.satnews.com/stories2007/4315/, April 2007.

[32] Prisma, "Prisma Satellites," http://www.prismasatellites.se/?sid=9028.

[33] SSC, "Swedish Space Corporation," http://www.ssc.se/?id=7611.

[34] Bodin, P., Larsson, R., Nilsson, F., Chasset, C., Noteborn, R., and Nylund, M., "PRISMA: An In-Orbit Test Bed for Guidance, Navigation, and Control Experiments," *Journal of Spacecraft and Rockets*, Vol. 46, No. 3, 2009.

[35] Bosse, A. B., Barnds, W. J., Brown, M. A., Creamer, N. G., Feerst, A., Henshaw, C. G., Hope, A. S., Kelm, B. E., Klein, P. A., Pipitone, F., et al., "SUMO: Spacecraft for the Universal Modification of Orbits," *Proceedings of SPIE*, 2004.

[36] Space.com, "Air Force ANGELS: Satellite Escorts to Take Flight," http://www.space.com/1816-air-force-angels-satellite-escorts-flight.html, November 2007.

[37] SpaceDaily.com, "ViviSat Launched," http://www.spacedaily.com/reports/ViviSat_Launched_999.html, January 2011.

[38] Henshaw, C. G. and Sanner, R. M., "Variational Technique for Spacecraft Trajectory Planning," *Journal of Aerospace Engineering*, Vol. 23, No. 2, 2010, pp. 147–156.

[39] Vallado, D. A. and McClain, W. D., *Fundamentals of Astrodynamics and Applications*, Kluwer Academic Publishers, 2001.

[40] Battin, R. H., *An Introduction to the Mathematics and Methods of Astrodynamics*, AIAA, 1999.

[41] Lawden, D. F., *Optimal Trajectories for Space Navigation*, Butterworths, 1963.

[42] Marec, J. P., *Optimal Space Trajectories*, Elsevier, 1979.

[43] Bryson, A. E. and Ho, Y. C., *Applied Optimal Control*, John Wiley & Sons Inc, 1975.

[44] Kirk, D. E., *Optimal Control Theory: An Introduction*, Dover Publications, 2004.

[45] Henshaw, C. G., *A Variational Technique for Spacecraft Trajectory Planning*, Ph.D. thesis, University of Maryland, 2003.

[46] Rosell, J. and Iniguez, P., "Path Planning Using Harmonic Functions and Probabilistic Cell Decomposition," *IEEE International Conference on Robotics and Automation*, 2005, pp. 1803–1808.

[47] Phillips, J., Kavraki, L., and Bedrossian, N., "Probabilistic Optimization Applied to Spacecraft Rendezvous and Docking," *Advances in the Astronautical Sciences*, Vol. 114, 2003, pp. 261–274.

[48] Phillips, J. M., Bedrossian, N., and Kavraki, L. E., "Guided Expansive Spaces Trees: A Search Strategy for Motion- and Cost-Constrained State Spaces," *IEEE International Conference on Robotics and Automation*, Vol. 4, 2004, pp. 3968–3973.

[49] Benson, D., *A Gauss Pseudospectral Transcription for Optimal Control*, Ph.D. thesis, Massachusetts Institute of Technology, 2005.

[50] Huntington, G. T., *Advancement and Analysis of a Gauss Pseudospectral Transcription for Optimal Control Problems*, Ph.D. thesis, Massachussets Institute of Technology, 2007.

[51] Boyarko, G. A., *Spacecraft Guidance Strategies for Proximity Maneuvering and Close Approach with a Tumbling Object*, Ph.D. thesis, Naval Postgraduate School, 2010.

[52] Henshaw, C. G., "A Unification of Artificial Potential Function Guidance and Optimal Trajectory Planning," Tech. rep., Naval Center for Space Technology, U.S. Naval Research Laboroatory, 2005.

[53] Martinson, N. S., *Obstacle Avoidance Guidance and Control for Autonomous Satellites*, Ph.D. thesis, University of Florida, 2009.

[54] Hablani, H. B., Tapper, M. L., and Dana-Bashian, D. J., "Guidance and Relative Navigation for Autonomous Rendezvous in a Circular Orbit," *Journal of Guidance, Control, and Dynamics*, Vol. 25, No. 3, 2002, pp. 553–562.

[55] Clohessy, W. H. and Wiltshire, R. S., "Terminal Guidance System for Satellite Rendezvous," *Journal of the Aerospace Sciences*, Vol. 27, No. 9, 1960, pp. 653–658.

[56] Khatib, O., “Real-Time Obstacle Avoidance for Manipulators and Mobile Robots,” *The International Journal of Robotics Research*, Vol. 5, No. 1, 1986, pp. 90–98.

[57] Lopez, I. and McInnes, C. R., “Autonomous Rendezvous Using Artificial Potential Function Guidance,” *Journal of Guidance, Control, and Dynamics*, Vol. 18, No. 2, 1995, pp. 237–241.

[58] Ge, S. S. and Cui, Y. J., “Dynamic Motion Planning for Mobile Robots Using Potential Field Method,” *Autonomous Robots*, Vol. 13, No. 3, 2002, pp. 207–222.

[59] McInnes, C. R., “Autonomous Path-planning for On-orbit Servicing Vehicles,” *Journal of the British Interplanetary Society*, Vol. 53, No. 1/2, 2000, pp. 26–38.

[60] Huang, W. H., Fajen, B. R., Fink, J. R., and Warren, W. H., “Visual Navigation and Obstacle Avoidance Using a Steering Potential Function,” *Robotics and Autonomous Systems*, Vol. 54, No. 4, 2006, pp. 288–299.

[61] Gazi, V., “Swarm Aggregations Using Artificial Potentials and Sliding-Mode Control,” *IEEE Transactions on Robotics*, Vol. 21, No. 6, 2005, pp. 1208–1214.

[62] Strizzi, J., Ross, I. M., and Fahroo, F., “Towards Real-Time Computation of Optimal Controls for Nonlinear Systems,” *AIAA Guidance, Navigation, and Control Conference*, 2002.

[63] Wertz, J. R. and Bell, R., “Autonomous Rendezvous and Docking Technologies - Status and Prospects,” *Proceedings of SPIE*, Vol. 5088, 2003, pp. 20–30.

[64] Wertz, J. R., *Spacecraft Attitude Determination and Control*, Kluwer Academic Publishers, 1978.

[65] Hughes, P. C., *Spacecraft Attitude Dynamics*, John Wiley & Sons Inc, 1986.

[66] Shuster, M. D., “Survey of Attitude Representations,” *Journal of the Astronautical Sciences*, Vol. 41, 1993, pp. 439–517.

[67] Kuipers, J. B., *Quaternions and Rotation Sequences*, Princeton University Press, 1999.

[68] Crassidis, J. L. and Junkins, J. L., *Optimal Estimation of Dynamic Systems*, Chapman & Hall, 2004.

[69] Zipfel, P. H., *Modeling and Simulation of Aerospace Vehicle Dynamics*, AIAA, 2000.

[70] Wie, B., *Space Vehicle Dynamics and Control*, AIAA, 1998.

[71] Ogata, K., *Modern control Engineering*, Prentice Hall, 2009.

[72] Lembeck, C. A. and Prussing, J. E., "Optimal Impulsive Intercept with Low-Thrust Rendezvous Return," *Journal of Guidance, Control, and Dynamics*, Vol. 16, 1993, pp. 426–433.

[73] Atkinson, K. E., *An Introduction to Numerical Analysis*, John Wiley & Sons Inc, 1989.

[74] Benson, D. A., Huntington, G. T., Thorvaldsen, T. P., and Rao, A. V., "Direct Trajectory Optimization and Costate Estimation Via an Orthogonal Collocation Method," *Journal of Guidance, Control, and Dynamics*, Vol. 29, No. 6, 2006, pp. 1435–1440.

[75] Bertsekas, D. P., Hager, W. W., and Mangasarian, O. L., *Nonlinear Programming*, Athena Scientific, 1999.

[76] Rao, A. V., Benson, D. A., Darby, C., Patterson, M. A., Francolin, C., Sanders, I., and Huntington, G. T., "Algorithm 902: GPOPS, A MATLAB Software for Solving Multiple-Phase Optimal Control Problems Using the Gauss Pseudospectral Method," *ACM Transactions on Mathematical Software*, Vol. 37, No. 2, 2010, pp. 1–39.

[77] Rao, A. V., Benson, D. A., Huntington, G. T., Origin, B., Seattle, L., Francolin, C., Darby, C. L., Patterson, M. A., and Sanders, I., *Users Manual for GPOPS Version 3.0: A MATLAB R Software for Solving Multiple-Phase Optimal Control Problems Using Pseudospectral Methods*, 2010.

[78] Badawy, A. and McInnes, C. R., "On-Orbit Assembly Using Superquadric Potential Fields," *Journal of Guidance, Control, and Dynamics*, Vol. 31, No. 1, 2008, pp. 30–43.

[79] Kim, J. O. and Khosla, P. K., "Real-Time Obstacle Avoidance Using Harmonic Potential Functions," *IEEE Transactions on Robotics and Automation*, Vol. 8, No. 3, 1992, pp. 338–349.

[80] Rimon, E. and Koditschek, D. E., "Exact Robot Navigation Using Artificial Potential Functions," *IEEE Transactions on Robotics and Automation*, Vol. 8, No. 5, 1992, pp. 501–518.

[81] Waydo, S. and Murray, R. M., "Vehicle Motion Planning Using Stream Functions," *IEEE International Conference on Robotics and Automation*, 2003.

[82] Koditschek, D., "Exact Robot Navigation by Means of Potential Functions: Some Topological Considerations," *IEEE International Conference on Robotics and Automation*, 1987.

[83] Mabrouk, M. H. and McInnes, C. R., "Solving the Potential Field Local Minimum Problem Using Internal Agent States," *Robotics and Autonomous Systems*, Vol. 56, No. 12, 2008, pp. 1050–1060.

[84] Tatsch, A. R., *Artificial Potential Function Guidance for Autonomous In-Space Operations*, Ph.D. thesis, University of Florida, 2006.

[85] Izzo, D. and Pettazzi, L., "Autonomous and Distributed Motion Planning for Satellite Swarm," *Journal of Guidance, Control, and Dynamics*, Vol. 30, No. 2, 2007, pp. 449–459.

[86] McCamish, S. B., *Distributed Autonomous Control of Multiple Spacecraft During Close Proximity Operations*, Ph.D. thesis, Naval Postgraduate School, 2007.

[87] Dixon, W. E., Behal, A., Dawson, D. M., and Nagarkatti, S. P., *Nonlinear Control of Engineering Systems: A Lyapunov-Based Approach*, Birkhauser, 2003.

[88] Yao, B. and Tomizuka, M., "Smooth Robust Adaptive Sliding Mode Control of Manipulators with Guaranteed Transient Performance," *IEEE American Control Conference*, Vol. 1, 1994, pp. 1176–1180.

[89] Khalil, H. K. and Grizzle, J. W., *Nonlinear systems*, Prentice Hall, 2002.

[90] Martinson, N., Munoz, J. D., and Wiens, G. J., "A New Method of Guidance Control for Autonomous Rendezvous in a Cluttered Space Environment," *AIAA Guidance, Navigation, and Control Conference*, 2007.

[91] Reid, W. T., *Riccati Differential Equations*, Academic Press, 1972.

[92] Engwerda, J. C., *LQ Dynamic Optimization and Differential Games*, John Wiley & Sons Inc, 2005.

[93] Jodar, L. and Navarro, E., "Closed Analytical Solution of Riccati Type Matrix Differential Equations," *Indian Journal of Pure Applied Mathematics*, Vol. 23, No. 3, 1992, pp. 185–187.

[94] Razzaghi, M., "Solution of the Matrix Riccati Equation in Optimal Control," *Information Sciences*, Vol. 16, No. 1, 1978, pp. 61–73.

[95] Bellman, R., *Stability Theory of Differential Equations*, McGraw-Hill, 1953.

[96] Liao, S. J., *Beyond Perturbation: Introduction to the Homotopy Analysis Method, Vol. 2 of CRC Series: Modern Mechanics and Mathematics*, Chapman & Hall, 2004.

[97] Allgower, E. L. and Georg, K., *Numerical Continuation Methods: An Introduction*, Springer, 1990.

[98] Tschauner, J. and Hempel, P., "Optimale Beschleunigeungsprogramme fur das Rendezvous-Manover," *Astronautica Acta*, Vol. 10, 1964, pp. 296–307.

[99] Yamanaka, K. and Ankersen, F., "New State Transition Matrix for Relative Motion on an Arbitrary Elliptical Orbit," *Journal of Guidance, Control, and Dynamics*, Vol. 25, No. 1, 2002, pp. 60–66.

[100] Wie, B., Weiss, H., and Arapostathis, A., “Quaternion Feedback Regulator for Spacecraft Eigenaxis Rotations,” *Journal of Guidance and Control*, Vol. 12, No. 3, 1989, pp. 375–380.

[101] Schweighart, S. A. and Sedwick, R. J., “High-Fidelity Linearized J2 Model for Satellite Formation Flight,” *Journal of Guidance, Control, and Dynamics*, Vol. 25, No. 6, 2002, pp. 1073–1080.

BIOGRAPHICAL SKETCH

Josue David Muñoz was born in Guatemala City, Guatemala in 1982. He moved to Miami, Florida at the ripe age of five years old and was raised there. He received his Bachelors of Science in aerospace engineering from the University of Florida in December 2005 and graduated Cum Laude. He was then accepted to the Ph.D. direct program at the University of Florida and obtained his Masters of Science in aerospace engineering in December 2008. He also had the honor of being awarded the South East Alliance for Graduate Education of the Professoriate Fellowship as well as the Science, Math, and Research Transformation Scholarship.

He had the pleasure of being a graduate teaching assistant as well as a graduate research assistant, working on projects for agencies like Defense Advanced Research Agency Projects and the Lockheed Martin Corporation. He was also Space Scholar at the Air Force Research Lab/Space Vehicles Directorate for the Summers of 2009 and 2010. He was also able to be part of the Student Temporary Employment Program at the Air Force Research Lab for the Fall 2009 semester, where he was able to contribute with his research. He was a member of the Space Systems Group and Small Satellite Design Club at the University of Florida, and is a member of the American Institute of Aeronautics and Astronautics, and American Astronautics Society.